TUDelft

Delft University of Technology

Assessing and improving trailing-edge noise reduction technologies for industrial wind-turbine applications

Luesutthiviboon, S.

DOI
10.4233/uuid:23e2f72e-2502-4f4a-9504-ba607bae0364

Publication date
2022

Document Version
Final published version

Citation (APA)
Luesutthiviboon, S. (2022). *Assessing and improving trailing-edge noise reduction technologies for industrial wind-turbine applications.* [Dissertation (TU Delft), Delft University of Technology]. https://doi.org/10.4233/uuid:23e2f72e-2502-4f4a-9504-ba607bae0364

Important note
To cite this publication, please use the final published version (if applicable).
Please check the document version above.

ASSESSING AND IMPROVING TRAILING-EDGE NOISE REDUCTION TECHNOLOGIES FOR INDUSTRIAL WIND-TURBINE APPLICATIONS

ASSESSING AND IMPROVING TRAILING-EDGE NOISE REDUCTION TECHNOLOGIES FOR INDUSTRIAL WIND-TURBINE APPLICATIONS

Dissertation

for the purpose of obtaining the degree of doctor
at Delft University of Technology
by the authority of the Rector Magnificus, prof. dr. ir. T.H.J.J. van der Hagen,
chair of the Board for Doctorates
to be defended publicly on
Friday 14 October 2022 at 12:30 o'clock

by

Salil LUESUTTHIVIBOON

Master of Science in Aerospace Engineering,
Delft University of Technology, the Netherlands
born in Bangkok, Thailand

This dissertation has been approved by the promotors.

Composition of the doctoral committee:

Rector Magnificus	chairperson
Prof. dr. ir. M. Snellen	Delft University of Technology, promotor
Prof. dr. D. G. Simons	Delft University of Technology, promotor
Dr. D. Ragni	Delft University of Technology, promotor

Independent members:

Prof. dr. S. J. Watson	Delft University of Technology
Prof. dr. ir. J.W. van Wingerden	Delft University of Technology
Prof. dr. -ing. E. Sarradj	Technische Universität Berlin, Germany
PD dr. -ing. habil. T. F. Geyer	German Aerospace Center (DLR), Germany

Growth happens outside of your comfort zone.

CONTENTS

SUMMARY

Nowadays wind turbines with large rotor sizes are required to be installed and operated close to residential areas due to growing demands for sustainable energy. Noise constraints have been hindering this development.

Turbulent Boundary Layer Trailing-Edge (TBL–TE) noise originating close to the wind-turbine blade tip is mainly responsible for the wind turbine noise emission. This broadband swishing noise results from scattering of the surface pressure fluctuations, induced by the TBL, approaching the blade TE.

Researchers have been developing add-on devices to help mitigate this noise. One classical strategy is by installing TE serrations. The TE serrations help to mitigate the TBL–TE noise by promoting destructive interference of the surface pressure fluctuations having different phases at the edge, hence reducing the scattered noise levels. The TE serrations are now the default design option for modern wind turbines and are known to help mitigate 3 dB(A) of noise. Another potential TBL–TE noise reduction add on is the permeable material. By making the region in proximity to the TE permeable, communication of the pressure fluctuations upstream of the TE takes place. This mechanism minimizes the sound scattering at the TE tip and is known as the *pressure release* mechanism. Airfoils with permeable TEs have shown more than 10 dB of noise reduction in laboratory tests. However, despite this potential, they have not been applied on real wind turbines. This is partially due to some well-known shortcomings of the permeable materials, namely, tonal noise and roughness noise increases, and aerodynamic disadvantages such as friction drag increase due to their commonly rough surfaces.

This thesis objective is to assess and improve the permeable TE technology to ultimately raise its technological readiness level for industrial wind-turbine applications. In order to assess performances of current TBL–TE noise reduction technologies, wind-tunnel tests of representative wind turbine airfoils were carried out. Aerodynamic performance was quantified by computing the lift and drag coefficients. To enable accurate and exclusive quantification of noise originating from the TE, a microphone array and acoustic beamforming techniques were employed.

Wind-tunnel tests of a NACA 63_3–018 airfoil were carried out. The airfoil was equipped with several different TE serration geometries and permeable TE inserts. For a constant airfoil lift, noise reduction provided by the TE serrations is found to depend on the serrations geometry. The iron-shaped serrations provided approximately 2.5 dB extra maximum TBL–TE noise reduction than the more conventional sawtooth-shaped serrations. For permeable TEs, represented by simple perforated channels, the maximum noise reduction increases with increasing permeability, i.e. number of pores per unit area. The perforated channels provide about 3 dB higher maximum TBL–TE noise reduction than the serrations, confirming their potential for industrial applications. However, for both technologies, the TBL–TE noise reduction capability worsens as the airfoil load-

ing increases. Furthermore, surface roughness of the perforated channels also causes roughness noise increase at high frequencies as well as increase in aerodynamic drag.

To counteract the shortcomings of the permeable TE, an alternative design concept was investigated. In the direction normal to the chord, the permeable material has a high permeability K (low resistivity r) and a high form drag coefficient C. This is an unconventional characteristic because C generally varies inversely with K. To realize this concept, a Kevlar-covered highly permeable perforated channel was installed on the TE region of a NACA 0018 airfoil. The objective of treating the surface with the Kevlar fabric was twofold: first, to exploit the Kevlar's acoustically transparent, yet flow impermeable, property to achieve a relatively higher C; second, the smooth Kevlar surface was intended to mitigate the roughness of the 3D-printed perforated channels and the possible tonal noise. The airfoil was tested in an open-jet wind tunnel and the results were compared to tests of the same airfoil with porous metal-foam TE inserts. Results have shown that the new TE concept can provide broadband noise mitigation without roughness noise increase. Variation of the noise reduction with the increasing airfoil loading is lower than 1 dB. It has further been shown that when compared to metal foams, the maximum noise reduction and its variability varies inversely with C, not with the resistivity r as usually reported in literature. The latter seems to only be valid when permeable materials of the same type are considered. This motivates the need to identify a more generic parameter to help design future permeable materials for TBL–TE noise attenuation.

Therefore, it is motivated to carry out a data-driven analysis, based on collected wind-tunnel experimental data, to identify a set of relevant flow parameters that determines the maximum TBL–TE noise attenuation. Symbolic regression modeling supported by genetic programming was employed to formulate mathematical expressions that relate the maximum noise attenuation to relevant parameters. The program was allowed to freely select any user-provided parameters to formulate expressions that fit the best to experimental data. In this study, the flow permeability in the streamwise K_x and chord-normal K_y directions were uncoupled. Additionally, a parameter that accounts for the slenderness of the TE shape was included. Experimental data from two airfoils and three permeable material types were considered. Outcomes have confirmed that the maximum TBL–TE noise reduction is achieved when the TE shape is long and thin to facilitate the pressure release mechanism. Additionally, the maximum noise reduction varies with $\sqrt{K_x}$, known as the Brinkman's screening distance. A general guideline is derived: it is desirable to maximize $\sqrt{K_x}$ to maximize the TBL–TE noise reduction.

Finally, as the first step toward the full-scale application of a permeable TE, a prototype permeable TE extension was tested on a real wind turbine. Counterintuitively, 1.5 dB(A) of noise increase was found. Further analysis of the spectra showed evidence that flow separation might have occurred.

Overall, this thesis has addressed the common shortcomings of the permeable TE. Alternative concepts have been demonstrated in extensive wind tunnel tests. Generic parameters related to material properties and airfoil geometry that govern the maximum noise attenuation are defined. It is recommended to exploit and optimize further anisotropic materials, i.e. permeable materials with unequal K_y and K_x. Additionally, constant proof-of-concept validations should regularly be carried out along with wind-tunnel tests to help accelerate the technological readiness level of the permeable TEs.

SAMENVATTING

Tegenwoordig moeten windturbines met grote rotorafmetingen door toenemende vraag naar duurzame energie geïnstalleerd en bediend worden in de buurt van woongebieden. Geluidsbeperkingen belemmeren deze ontwikkeling.

Turbulente grenslaag achterrand (in het Engels: *Turbulent Boundary Layer Trailing-Edge, TBL–TE*) geluid aan de punt van het windturbineblad is voornamelijk verantwoordelijk voor de geluidsemissie van de windturbine. Dit breedbandige zwiepende geluid is het gevolg van verstrooiing van de fluctuaties van de oppervlaktedruk, geïnduceerd door de turbulente grenslaag, die de TE van het blad nadert.

Onderzoekers hebben toevoegingen ontwikkeld om dit geluid te verminderen. Een klassieke strategie is door zaagtanden op de TE te installeren. De zaagtanden helpen het TBL–TE geluid te verminderen door destructieve interferentie van de fluctuaties van de oppervlaktedruk te bevorderen die verschillende fasen heeft aan de rand, waardoor de verspreide geluidsniveaus worden verminderd. De TE zaagtanden zijn nu de standaard ontwerpoptie voor moderne windturbines en verminderen 3 dB(A) aan geluid. Een andere mogelijke toevoeging voor TBL–TE geluidsvermindering is permeabel materiaal. Door het gebied in de buurt van de TE permeabel te maken, zal interactie van de druk fluctuaties stroomopwaarts van de TE plaatsvinden. Dit mechanisme minimaliseert de geluidsverstrooiing aan het uiteinde van het blad en staat bekend als het drukontlastingsmechanisme (in het Engels: *Pressure release mechanism*). Vleugelprofielen met permeabele TE's lieten meer dan 10 dB geluidsreductie zien in laboratoriumtests. Echter, ondanks dit potentieel, zijn ze niet toegepast op echte windturbines. Dit is gedeeltelijk te wijten aan een aantal bekende tekortkomingen van het permeabele materiaal, zoals het toenemen van tonale en ruwe geluid, en daarnaast aerodynamische nadelen zoals hogere wrijvingsweerstand als gevolg van de vaak ruwe oppervlakken.

Dit proefschrift heeft tot doel de permeabele TE-technologie te beoordelen en te verbeteren om uiteindelijk het technologische gereedheidsniveau voor industriële windturbinetoepassingen te verhogen. Om de prestaties van de huidige TBL–TE geluidsreductietechnologieën te beoordelen, werden windtunneltests van representatieve vleugelprofielen van windturbines uitgevoerd. Aerodynamische prestaties werden gekwantificeerd door de lift en luchtweerstandscoëfficiënten te berekenen. Om nauwkeurige en exclusieve kwantificering van het geluid van de TE mogelijk te maken, werden een microfoonarray en akoestische bundelvormingstechnieken gebruikt. Windtunneltests aan een NACA 63$_3$–018 vleugelprofiel werden uitgevoerd. Het vleugelprofiel was uitgerust met verschillende zaagtandgeometrieën en permeabele TE-inzetstukken. Voor een constante vleugellift, blijkt de geluidsreductie door de TE zaagtanden af te hangen van de zaagtandgeometrie. De strijkijzervormige tanden zorgden voor ongeveer 2,5 dB extra maximale TBL–TE geluidsreductie dan de meer conventionele zaagtandvormige vertandingen. Voor permeabele TE's, weergegeven door eenvoudig geperforeerde kanalen, neemt de maximale geluidsreductie toe met toenemende doorlaatbaarheid, d.w.z.

het aantal poriën per oppervlakte-eenheid. De geperforeerde kanalen zorgen voor een ongeveer 3 dB hogere maximale TBL–TE geluidsreductie dan de zaagtanden, wat hun potentieel voor industriële toepassingen bevestigt. Echter, voor beide technologieën, verslechtert de TBL–TE geluidsreductiemogelijkheden naarmate de vleugelbelasting toe neemt. Bovendien veroorzaakt de oppervlakteruwheid van de geperforeerde kanalen ook een toename van ruwheidsgeluid bij hoge frequenties en ook een toename van de aerodynamische weerstand.

Om de tekortkomingen van de permeabele TE tegen te gaan, wordt een alternatief ontwerpconcept onderzocht. In de richting loodrecht op de koorde heeft het permeabele materiaal een hoge permeabiliteit K (lage soortelijke weerstand r) en een hoge vormweerstandscoëfficiënt C. Dit is een onconventionele eigenschap omdat C in het algemeen omgekeerd evenredig is met K. Om dit onconventionele concept te realiseren, is een met Kevlar bedekt, zeer doorlatend geperforeerd kanaal geïnstalleerd op het TE-gebied van een NACA 0018-vleugelprofiel. Het doel van het behandelen van het oppervlak met de Kevlar-stof was tweeledig: ten eerste om gebruik te maken van de akoestisch doorlaatbare, doch stroming ondoordringbare, eigenschap van Kevlar om een relatief hogere C te bereiken; ten tweede is het gladde Kevlar oppervlak bedoeld om de ruwheid van de 3D-geprinte geperforeerde kanalen en het mogelijke tonale geluid te dempen. Het vleugelprofiel werd getest in een open-jet windtunnel en de resultaten zijn vergeleken met tests van hetzelfde vleugelprofiel met TE-inzetstukken van poreus metaalschuim. De resultaten hebben aangetoond dat het nieuwe TE-concept breedbandige geluidsreductie kan bieden zonder ruwheid geluid toe te laten nemen. De variatie van de geluidsreductie met de toenemende vleugelprofielbelasting is minder dan 1 dB. Verder is aangetoond dat in vergelijking met metaalschuim, de maximale geluidsreductie en de variabiliteit ervan omgekeerd evenredig is met C, en niet met de soortelijke weerstand r zoals gewoonlijk gerapporteerd in literatuur. Dit laatste lijkt alleen geldig wanneer permeabele materialen van hetzelfde type worden overwogen. Dit motiveert de noodzaak om een meer generieke parameter te identificeren om te helpen bij het ontwerpen van toekomstige permeabele materialen voor TBL–TE geluidsreductie.

Daarom is het gemotiveerd om een datagedreven analyse uit te voeren, gebaseerd op verzamelde experimentele windtunnelgegevens, om een reeks relevante stroomparameters te identificeren die de maximale TBL–TE geluidsreductie bepalen. Symbolische regressiemodellering ondersteund door genetische programmering werd gebruikt om wiskundige uitdrukkingen te formuleren die de relatie aangeven tussen de maximale geluidsreductie en de relevante parameters. Het programma mocht vrijelijk alle door de gebruiker verstrekte parameters selecteren om uitdrukkingen te formuleren die het beste passen bij de experimentele gegevens. In deze studie waren de stromingspermeabiliteit in de stroomrichting K_x- en koorde-normale K_y-richting ontkoppeld. Bovendien werd een parameter opgenomen die de slankheid van de TE-vorm in acht neemt. Experimentele data van twee vleugelprofielen en drie permeabele materiaalsoorten zijn meegenomen. De resultaten hebben bevestigd dat de maximaal TBL–TE geluidsreductie bereikt wordt wanneer de TE-vorm lang en dun is om het drukontlastingsmechanisme te faciliteren. Bovendien varieert de maximale geluidsreductie met $\sqrt{K_x}$, ook wel de *Brinkman's screening distance* genoemd. Een generieke richtlijn is afgeleid: het is wenselijk om $\sqrt{K_x}$ te maximaliseren om de TBL–TE geluidsreductie te maximaliseren.

Tot slot, als eerste stap naar grootschalige toepassing van een permeabele TE, werd een prototype permeabele TE-verlenging getest op een echte windturbine. Contra-intuïtief, een toename van 1,5 dB(A) werd geconstateerd. Verdere analyse van de spectra toonde bewijs dat stroom loslating zou hebben plaatsgevonden.

Over het algemeen heeft dit proefschrift de veelvoorkomende tekortkomingen van de permeabele TE behandeld. Alternatieve concepten zijn gedemonstreerd in uitgebreide windtunneltests. Generieke parameters gerelateerd aan materiaaleigenschappen en vleugelprofielgeometrie die de maximale geluidsreductie bepalen, zijn gedefinieerd. Het wordt aanbevolen om anisotrope materialen, d.w.z. permeabele materialen met ongelijke K_y en K_x, verder te exploiteren en te optimaliseren. Bovendien, constante *proof-of-concept* validaties moeten regelmatig worden uitgevoerd samen met windtunnel tests om het technologische gereedheidsniveau van de permeabele TE's te helpen versnellen.

NOMENCLATURE

ACRONYMS

BANC	Benchmark Problems for Airframe Noise Computations
CFDBF	Conventional Frequency Domain Beamforming
CTDBF	Conventional Time Domain Beamforming
CNC	Computer Numerical Control
CSM	Cross-Spectral Matrix
DLR	German Aerospace Center
FS	Frequency Scaling
HAWT	Hybrid Anechoic Wind Tunnel
ISO	International Standard Organization
KNMI	Koninklijk Nederlands Meteorologisch Instituut (Royal Netherlands Meteorological Institute)
LTT	Low-Turbulence Tunnel
MLW	Main Lobe Width
MSEM	Mimetic Spectral Element Method
MSL	Maximum Sidelobe Level
NI	National Instruments
PIV	Particle-Image Velocimetry
PLA	Polylactic Acid
PSF	Point Spread Function
ROI	Region Of Integration
ROSI	ROtational Source Identifier
RPM	Rotations Per Minute
SEL	Sound Exposure Level
SPI	Source Power Integration
[O(A)]SPL	[Overall (A-weighted)] Sound Pressure Level
SS	Spectral Scaling
SSE	Sum of Squared Error
TBL	Turbulent Boundary Layer
TE	Trailing Edge
TL	Transmission Loss
VPM	Vortex Panel Method
WHO	World Health Organization

LATIN SYMBOLS

A	Area	(m^2)
$\tilde{A}$	Source power	(Pa^2)
a_i	Surface pressure spectra modeling parameters	(-)
B	Cole's fitting coefficient	(-)
b	Clean beam shape parameter	(-)
C	Form drag coefficient	(m^{-1})
$\mathbf{C}$	Cross-Spectral Matrix	(Pa^{2}Hz^{-1})
c	Airfoil chord	(m)
c_0	Speed of sound	(ms^{-1})
c_d	Drag coefficient	(-)
c_l	Lift coefficient	(-)
c_p	Pressure coefficient	(-)
$c_{p,s}$	Static pressure coefficient	(-)
$c_{p,t}$	Total pressure coefficient	(-)
D	Array aperture	(m)
D_c	Unit cell size	(m)
d	Distance on the scan plane	(m)
d_c	Nominal cell diameter	(m)
d_h	Cylindrical channel diameter	(m)
d_p	Mean pore size	(m)
f	Frequency	(Hz)
G_{pp}	Auto-spectral density of the surface pressure fluctuation	(Pa^{2}Hz^{-1})
$\mathbf{g}_j$	Steering vector to grid point j	(-)
$g_{j,n}$	Component of $\mathbf{g}_j$ from microphone n	(-)
H	Shape factor	(-)
$\mathbf{h}$	Source component	(-)
h	Serrations amplitude	(m)
I_r	Far-field acoustic intensity	(Wm^{-2})
i	Imaginary unit	(-)
J	Number of grid point	(-)
j	Grid point index	(-)
$K, (K_x, K_y)$	Permeability (in the x and y directions)	(m^2)
K_B	Brooks angle of attack correction factor	(-)
$K_{\delta_{99}}$	Boundary layer thickness factor	(-)
K_{TL}	Transmission loss factor	(-)
$\mathbb{K}$	Permeability tensor	(m^2)
k_x, k_z	Wavenumber in the x and z directions	(-)
L	Airfoil span	(m)
l_h	Hole spacing	(m)
l_z	Spanwise correlation length	(m)
$\mathbf{M} = [M_x, M_y, M_z]$	Mach number vector	(-)
$\mathbf{M}_0$ $= [M_{x,0}, M_{y,0}, M_{z,0}]$	Mach number vector of the incoming wind	(-)
M	Mach number	(-)

M_c	Convective Mach number	(-)
m	Summation index	(-)
N	Number of microphones	(-)
N_s	Number of sources	(-)
N_v	Number of variables	(-)
$\mathbf{n}_a$	Unit vector in a direction	(-)
n	Microphone index	(-)
$\mathbf{p}$	Vector containing Fourier transforms of microphone signals	$(\mathrm{Pa^2Hz^{-1}})$
P	Sound power	$(\mathrm{Pa^2})$
P_0	Incident pressure amplitude	(Pa)
P_1	Scattered pressure amplitude	(Pa)
p_0	Reference pressure	(Pa)
p_a	Far-field acoustic pressure	(Pa)
p_i	Incident presssure gust spectral component	(Pa)
Q	Consecutive timestamp sample number	(-)
R	Observer's distance	(m)
R_T	Reynolds-number-dependent timescale ratio	(-)
R_t	Sound propagation path distance	(m)
Re_a	Reynolds number based on a length a	(-)
r	Resistivity	$(\mathrm{Nsm^{-4}})$
$r_{j,n}$	Distance from microphone n to grid point j	(m)
S	Direction along the surface	(-)
S_{pp}	Auto-spectral density of the far-field sound pressure	$(\mathrm{Pa^2Hz^{-1}})$
St_a	Strouhal number based on a length a	(-)
$\mathbb{S}$	Set of source indices	(-)
s	Source index of interest	(-)
T	Time interval	(sec.)
t	Time	(sec.)
$t_{\mathrm{junc.}}$	Airfoil thickness at the solid–permeable junction	(m)
t_s	Sample thickness	(m)
t_{TE}	Trailing-edge thickness	(m)
$\mathbf{u}_j$	Weight vector replacement	(-)
u, v	Velocity components	$(\mathrm{ms^{-1}})$
u_c	Convection velocity	$(\mathrm{ms^{-1}})$
u_e	Edge velocity	$(\mathrm{ms^{-1}})$
u_∞	Free-stream flow speed	$(\mathrm{ms^{-1}})$
u_τ	Friction velocity	$(\mathrm{ms^{-1}})$
V_a^b	Variability of a with b	(unit of a)
V_s	Base (solid) material volume	$(\mathrm{m^3})$
V_t	Total material volume	$(\mathrm{m^3})$
v_D	Darcy velocity	$(\mathrm{ms^{-1}})$
v_S	Slip velocity	$(\mathrm{ms^{-1}})$
$\mathbf{w}_j$	Weight vector	(-)
X_i	Generic input variable	(-)
$\mathbf{x} = [x, y, z]$	Location vector	(m)

$\mathbf{x}_c = [x_c, y_c, z_c]$	Wind-turbine hub location vector	(m)
$\mathbf{x}_j = [x_j, y_j, z_j]$	Grid point j location vector	(m)
$\mathbf{x}_n = [x_n, y_n, z_n]$	Microphone n location vector	(m)
$\mathbf{x}_o = [x_o, y_o, z_o]$	Observer's location vector	(m)
$x, (\bar{x})$	Airfoil, flat plate: chordwise (averaged) location	(m)
	Wind turbine: direction along the incoming wind	(m)
$x_{\text{tr.}}$	Transition location	(m)
$Y_i, (\hat{Y}_i)$	Generic (predicted) output variable	(-)
y	Airfoil, flat plate: chord-normal location	(m)
	Wind turbine: lateral location	(m)
z	Airfoil, flat plate: spanwise location	(m)
	Wind turbine: vertical location	(m)

GREEK SYMBOLS

α	Angle of attack	(deg.)
β	$\sqrt{1 - M^2}$	(-)
γ	Fitting coefficient for the Corcos model	(-)
δ	Turbulence length scale	(m)
$(\bar{\delta^*}), \delta^*$	(Averaged) displacement thickness	(m)
δ_{99}	Boundary layer thickness	(m)
δ_i	Interface boundary layer thickness	(m)
$\Delta\ell$	Rayleigh resolution limit	(m)
Δl_e	Euclidian distance through a material sample	(m)
Δl_v	Shortest path through a material sample	(m)
Δp	Pressure drop	(Pa)
Δp_i	Incident pressure jump	(Pa)
Δp_s	Scattered pressure jump	(Pa)
Δp_t	Total pressure jump	(Pa)
Δt_e	Emission time delay	(sec.)
$\Delta\mathbf{x}$	Separation distance vector	(-)
ϵ	Angle offset	(deg.)
ε	CSM factor	(-)
ζ	Angle between the Mach number perceived by the blade and the source-observer line	(deg.)
η	Source marker constraint	(-)
Θ	Observer's angle	(deg.)
θ	Momentum thickness	(m)
ϑ_0	Blade starting azimuth angle	(deg.)
κ	von Kármán constant	(-)
λ	Serrations wavelength	(m)
λ_0	Acoustic wavelength	(m)
μ	Dynamic viscosity	(Nm^{-2}s)
ν	Kinematic viscosity	(m^{2}s^{-1})

ξ	Angle between the blade planform plane and the chord-observer plane	(deg.)
Π	Wake parameter	(-)
Π_0	Wavenumber-frequency spectrum	(-)
Π_{P_0}	Cross spectral density of the incident pressure P_0	$(\mathrm{Pa}^2\mathrm{Hz}^{-1})$
ρ_0	Air density	(kgm^{-3})
ρ_s	Base (solid) material density	(kgm^{-3})
ρ_t	Permeable material sample density	(kgm^{-3})
σ	See Eq. (2.8)	(m)
τ	Tortuousity	(-)
Φ	Loop gain	(-)
Φ_{pp}	Cross-spectral density of the surface pressure fluctuation between any given points	$(\mathrm{Pa}^2\mathrm{Hz}^{-1})$
ϕ	Porosity	(-)
φ	Serrations flap angle	(deg.)
χ	Recorded pressure-time signal	(Pa)
Ψ	Azimuth angle	(deg.)
Ω	Rotational speed	(rads^{-1})
ω	Angular frequency	(rads^{-1})

SUBSCRIPTS AND SUPERSCRIPTS

1/3	One-third octave band
corr.	Corrected
degraded	Degraded CSM
eff.	Effective value
geom.	Geometrical value
j	Evaluated at grid point j
junc.	Solid–permeable junction
k, k'	Related to source k or k'
l	Related to source other than k
lam.	Laminar
max.	Maximum value
meas.	Measured value
min.	Minimum value
o	Observer
per.	Permeable extent
q	Timestamp index
ref.	Reference value
s	Source index of interest
s.l.	Shear layer
sim.	Simulated
tot.	Total

FUNCTIONS AND MATHEMATICAL OPERATORS

$|.|$	Absolute value of a real number or vector
$\|.\|$	Norm of a vector
$(.)^*$	Complex conjugate transpose
$\Delta(.)$	Difference
$\mathrm{E}(.)$	Fresnel function
$E[.]$	Ensemble average
$F(z)$	Serrations shape function
$g(.)$	Generic function
$G(.)$	Green's function
$I(.)$	Propagation term
$\mathscr{L}$	Aeroacoustic transfer function

1

INTRODUCTION
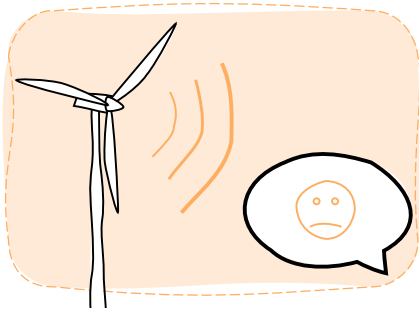
Nowadays, large wind turbines are installed and operated close to densely populated areas due to growing needs for renewable energy. Noise constraints are hampering this development. Measurement of noise from a real wind turbine shows that the broadband and swishing wind-turbine noise originates from the region close to the blade tip. The most relevant wind turbine noise source is the so-called Turbulent Boundary Layer Trailing-Edge (TBL–TE) noise. Many passive TBL–TE noise reduction technologies have been developed and tested in laboratories, yet only TE serrations are being implemented on real wind turbines. Some technologies, such as porous materials, have shown potential to achieve higher TBL–TE noise reduction than the TE serrations. This thesis aims to advance technological readiness level of such technologies.

1

1.1. Growth of wind energy and wind turbines

Renewable energy, such as solar and wind energy, is beneficial both economically and environmentally. The advantages of renewable energy come from their independence on the volatile fuel price and little-to-none harmful waste from energy production [1]. Wind energy is one of the fastest-growing renewable energy branches [2]. From 2010 to 2020, the total global wind power capacity has quadrupled to almost 800 GW [3, 4]. Accelerated by the commitment to reach net zero carbon dioxide emission in the middle of the 21st century, world leaders are facing ever-increasing pressure to maximize the renewable energy extraction. Therefore, the wind energy sector is expected to experience an unprecedented growth in the upcoming decades [5].

Figure 1.1: A horizontal-axis wind turbine close to Leidschendam, the Netherlands.

Wind turbines are used to capture the wind energy and convert it to electricity. Horizontal-axis wind turbines (See, for instance, Fig. 1.1) are the most common [6] due to their higher efficiency, compared to their vertical-axis counterparts [7]. Despite being a sophisticated system, engineers have been able to craft larger horizontal-axis wind turbines capable of producing more power [8]. The rotor diameter has grown from 20 meters in average in the 1980s to more than 120 m in the present [9]. In Europe, about 80 % of new wind turbines are installed on shore [5], both as a stand-alone structure or as wind farms. The average on-shore wind turbine rotor diameter and power rating have doubled between 2010 and 2018 [10] as visualized in Fig. 1.2. More recently in 2020, almost 900 new on-shore wind turbines, having an average power rating of 3 MW, were installed in Germany and France, according to WindEurope [5].

1.2. Noise constraints for new wind turbines

It is economically desirable to install new on-shore wind turbines in areas with consistently high wind speeds close to access roads and existing power lines [11, 12]. This could result in wind turbines being installed close to densely populated areas. As such, presence of wind turbines poses environmental and societal impacts. A wind turbine could cause many forms of nuisance [13], including noise nuisance. In 2018, the World Health Organization (WHO) published guidelines for wind turbine noise [14], which recommend the day-evening-night-weighted Sound Pressure Level (SPL) to be below 45 dB. The concern regarding noise is raised due to the proven health consequences of exposure to noise [15, 16].
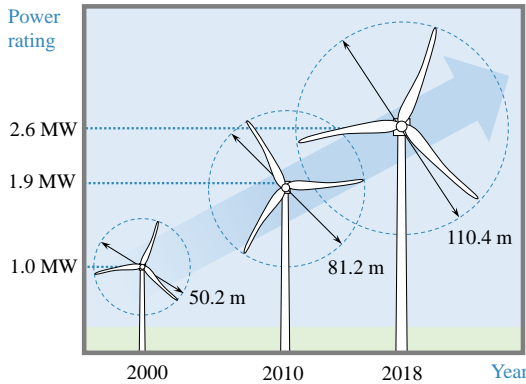
Figure 1.2: Growth of the average on-shore wind turbine rotor diameter and power rating from year 2010 to 2018, adapted from Renewable Energy Statistics 2019 by The International Renewable Energy Agency (IRENA) [10].
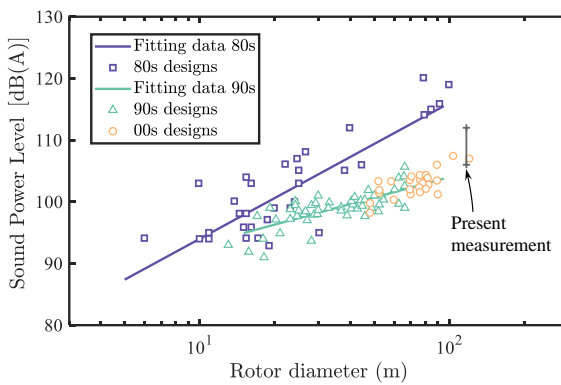
Figure 1.3: Sound power levels of wind turbines with different rotor diameters classified by the year they were designed. The 'Present measurement' refers to the measurement presented in Section 1.3.

Subsequent noise restrictions by local governments [17] have been enforced. The limits are more strict especially in rural and residential areas during nighttime. Such limits have been hampering installation and operation of new wind turbines for years [18, 19]. In fact, the noise restrictions go against the current growth of the wind-turbine technology because wind turbines with larger rotor diameter operating at high speeds are known to produce more noise [20]. Nevertheless, responses to the restrictions are visible in the past as shown for instance in Fig. 1.3. where noise data from a number of sample wind turbines in the USA designed between the 80s and the 00s are shown. There is a clear direct increase of the wind turbine sound power level and the rotor diameter. However, this data shows that newer wind turbines from the 90s and 00s, despite having equally large or even larger rotor diameters than those from the 80s, are clearly more quiet. This is because engineers have been actively developing technologies for mitigating various noise sources from wind turbines [21]. Given the current projection of the wind turbine growth and the pressure to utilize more renewable energy such as wind energy, the wind turbine noise constraint is still expected to persist. Research will therefore still be needed to understand the wind turbine noise sources and to develop noise mitigation technologies.

1.3. A REAL-LIFE EXAMPLE OF WIND-TURBINE NOISE

To help the readers envision the present characteristics of modern-day wind turbine noise and identify the relevant noise sources, this section presents acoustic measurement results of an actual wind turbine.

1.3.1. NOISE MEASUREMENT SET UP

In October 2021, LM Wind Power, an industrial partner in the present research project, has provided access to carry out noise measurements of a wind turbine at Windpark Wieringermeer administrated by ECN Wind Energy Facilities B.V. (EWEF) close to Wieringerwerf, the Netherlands. The considered wind turbine height from the base to the hub is 89 m and the rotor diameter is 117 m. The power rating of this turbine is 4.2 MW. A 4 m × 4 m array of microphone with a synchronized video camera was placed in the upwind direction of the turbine at a distance approximately the same as the base-to-hub height. A schematic is shown in Fig. 1.4a and a photograph of the set up is shown in Fig. 1.4b. Interested readers are referred to Chapter 4 for further technical details of the measurement system and the post-processing techniques.

During the present measurement, the wind turbine was rotating at a rotational speed of approximately 13.6 Rotations Per Minute (RPM). The turbine was facing a southerly wind. According to the open data from Royal Netherlands Meteorological Institute (KNMI) [22] collected at the closest by weather station in De Kooy, the wind speed was approximately 9.5 m/s, the temperature was 15.8°C, and the relative humidity was 66%.
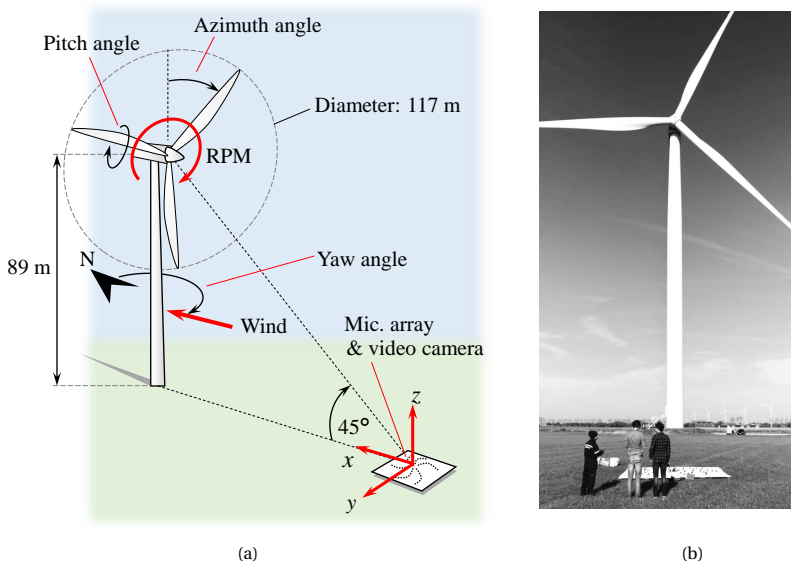

Figure 1.4: Wind turbine noise measurement set up: (a) A schematic (not to scale) and (b) a photograph.

1.3.2. Characterizing the wind turbine noise and localizing the sources

The results are presented in Fig. 1.5 for a 20-second extract of the measurement. First, the time-series data of the Overall A-Weighted Sound Pressure Level (OASPL) is presented in Fig. 1.5a. This A-weighted result represents human ear perception which is the most sensitive to sound frequencies around 1 kHz. A clear periodic pattern of the OASPL varying between 53 and 59 dB(A) can be seen. This OASPL translates to the sound power level range of 106 to 112 dB(A). This range is visualized in Fig. 1.3. In comparison to other modern wind turbines, the approximated sound power levels of this wind turbine fall within the expected trend.

The period of the OASPL pattern is approximately 1.5 s which, according to the RPM, translates to every time a blade passes a certain azimuthal location. In other words, for a stationery observer, the amplitude of the OASPL is modulated by the blade movement. This periodic character, i.e. changing between loud and quiet synchronizing with the blade movement, is also (in)famously known as the *swishing* character [23, 24].

Figure 1.5b presents the A-weighted spectrogram of this measurement, hence reveals the frequency content of this periodic noise. The periodic pattern can still be seen in the time domain (horizontal axis). In the frequency domain (vertical axis), it can be seen that the Sound Pressure Level (SPL) is distributed over a broad frequency range with the highest A-weighted SPL between the sound frequency of 100 and 1,000 Hz. Therefore, the noise from the wind turbine is broadband sound.

To locate the origin of this noise, the ROtational Source Identifier (ROSI) beamforming technique [25] (See Chapter 4) is applied to the microphone array data. Four source maps visualizing the SPL and the location of the sound sources are overlaid over instantaneous photographs of the wind turbine. The brighter colors in the maps mean the louder noise. The four selected time instances are chosen at various locations in the periodic pattern as marked in Fig. 1.5a. The frequencies considered are between 600 and 1,400 Hz as marked in the spectrogram in Fig. 1.5b.

From the source map, it is clear that the strongest noise emanates from the region close to the tip of the blade; more specifically, the downward-moving blade approaching the stationery observer on the ground. This phenomenon is examined in further detail in Chapter 4. Apart from the blade tip, one can observe a somewhat constant noise source from the tower close to the hub which could result from turbulent air flow interacting with the tower and/or mechanical noise from the hub [23, 26]. However, this noise source is approximately 3-4 dB lower than that from the blade.

1.4. Aerodynamic noise from a wind turbine

The present measurement has shown that the outboard region of the blade, i.e. close to the tip, contributes the most to noise emission from a wind turbine. This noise results from interaction between the blades and air and is known as the *aerodynamic noise*. A schematic in Fig. 1.6 focuses on this blade region and illustrates possible mechanisms that contribute to the aerodynamic noise emission. Wagner et al. [26] categorized aerodynamic noise mechanisms of a wind turbine in three groups. Their affiliating mechanisms
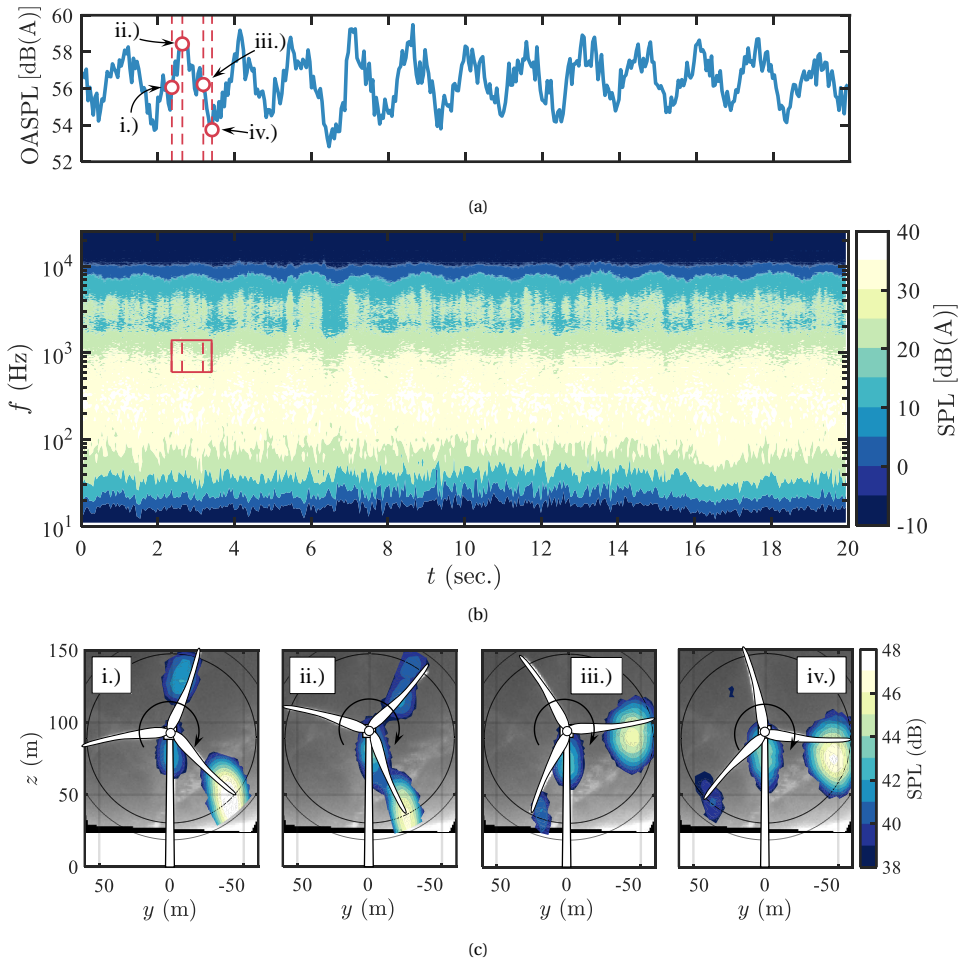
Figure 1.5: Wind turbine noise in a 20-second excerpt: (a) Time-series OASPL (b) spectrogram, and (c) instanteneous ROSI beamforming images at time instances and frequency range marked in (a) and (b).

and relevance are summarized in the following.

1. Low-frequency noise: This results from blade interaction with flow field around the tower or with wakes from other wind turbines (in a wind park). The frequency of this noise is close to the lower human hearing limit of approximately 20 Hz.

2. Inflow turbulent noise: This noise is governed by the turbulence intensity of the incoming wind experienced by the blade. This is associated to frequencies up to approximately 1 kHz. Research has shown that this noise can be mitigated by carefully optimizing the blade's leading-edge shape [28].
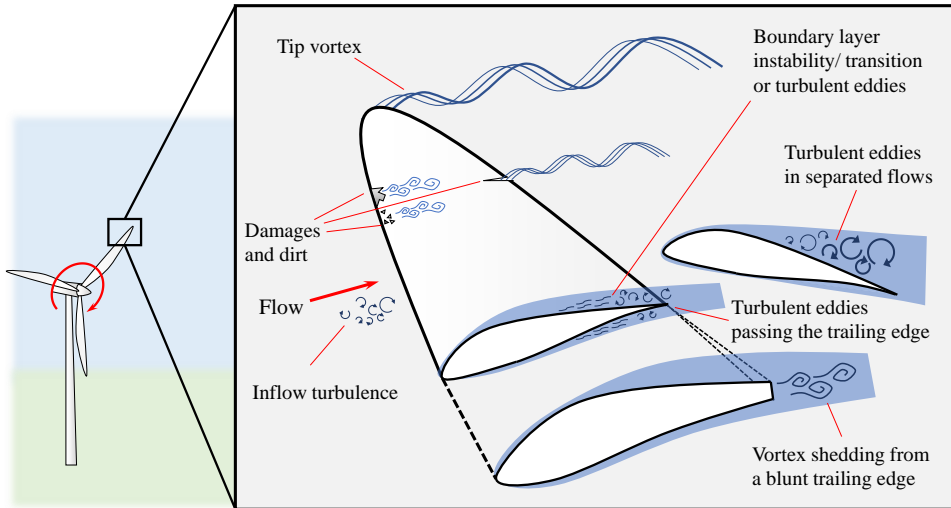
Figure 1.6: Schematic of possible flow-blade interaction mechanisms that contribute to aerodynamic noise emissions from a wind turbine (Adapted from Wagner et al. [26] and Blake [27]).

3. Airfoil self-noise [29]: This noise results from interaction between the blade and incoming air flow. The sub-categories of the airfoil self-noise are grouped based on their broadband and tonal characteristics as follows:

   (a) Broadband airfoil self-noise

      i. Trailing-edge (TE) noise: This is the noise emission from the TE tip where the boundary layer reaches the TE. For the chord-based Reynolds number range where the wind turbine operates, the boundary layer is usually turbulent and this noise is more specifically named as the Turbulent Boundary Layer Trailing-Edge (TBL–TE) noise. It is dominant in the audible frequency range between 750 and 2,000 Hz and is therefore the main focus of this thesis. Chapter 2 is dedicated to the mechanism and reduction technologies for this noise.

      ii. Tip noise: This noise occurs from cross-flow induced by the pressure difference at the blade tip. Vortices are formed due to this cross-flow and the blade movement. Blade tip designs are being investigated to mitigate this noise [30, 31].

      iii. Separation/ stall noise: During stall, unsteady flow separation containing large turbulence eddies occurs over the airfoil. In normal operating conditions, where the flow is attached, this noise is naturally avoided.

   (b) Tonal airfoil self-noise: This type of noise often arises when vortex shedding is triggered. This comprises of noise from a laminar boundary layer instability, a blunt TE, damages, dirt, and imperfections. These sources of noise can easily be avoided.

1

Among the noise sources mentioned above, the TBL–TE noise is mainly responsible for wind turbine noise annoyance. It still exists even in the case of non-turbulent inflow [29] or if the blade shape and surface are well-designed and smooth [32].

1.5. TBL–TE NOISE REDUCTION TECHNOLOGIES

It has been estimated by Oerlemans [18] that the energy production of a wind turbine could potentially increase by up to 4 % if its noise emission could be reduced by 1 dB. This signals that research and development of wind turbine noise reduction technologies are still lacking behind the progress of wind-turbine engineering. Researchers have been innovating technologies to abate the TBL–TE noise since the 1970s [33–38]. Unfortunately, many of these technologies have been developed and demonstrated only in a laboratory scale without actually entering the real-world scale. Given the current growth of the wind turbine industry, much more work is needed in order to raise the technological readiness level of the TE noise reduction technologies.
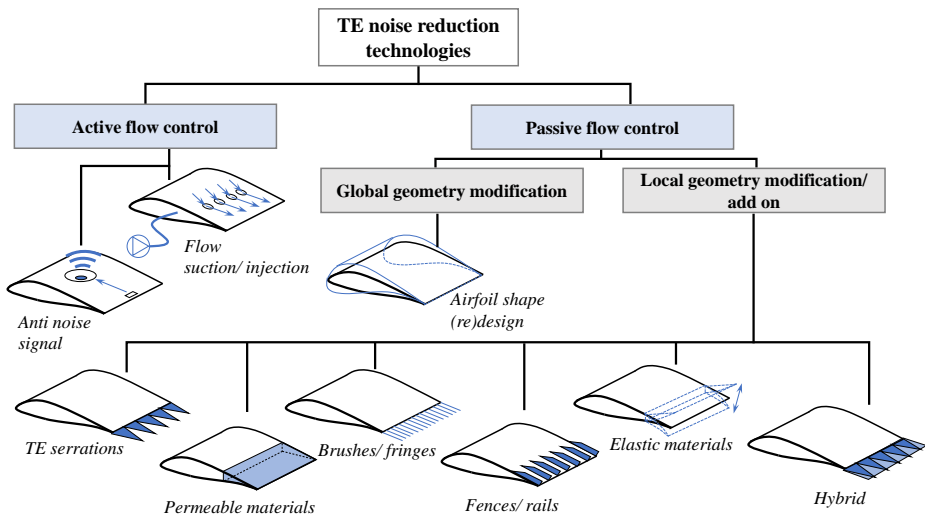
Figure 1.7: Traling-edge noise reduction approaches.

The noise mitigation technologies may first be subdivided into two main groups: active and passive flow control as shown in Fig. 1.7. The active techniques include, for instance, installation of speakers on the airfoil which emit anti-noise signals based on real-time unsteady pressure measurements at the TE [39], or suction or injection of flow to modify the TBL characteristics [40]. These techniques require external energy, e.g. electrical input, and therefore might not be practical. Due to this, passive techniques, usually realized by geometry modifications, are more desirable. The modifications may be done globally by modifying the entire airfoil shape [41, 42]. However, for already existing wind turbine blades, local geometry modifications and add-ons for noise mitigation are relatively more pragmatic. Such modifications and add-ons are summarized in Fig. 1.7.

Many of the present technologies are bio-inspired [34, 43, 44]. Generally, wind-tunnel tests of an airfoil, i.e. representative section of a wind-turbine blade, equipped with these add-ons are carried out. The tests are done as a preliminary proof of concept. Noise reduction performances of these concepts observed in wind-tunnel tests and selected references are summarized in Table 1.1 [45]. Applications of these technologies on real wind turbines are also summarized in Table 1.1. Table 1.1 shows that, among these technologies, only the TE serrations are the most mature since they are currently in use on real wind turbines. Given the current growth of the wind turbine industry, much more work is needed in order to raise the technological readiness level of the TE noise reduction technologies that can potentially attenuate more noise. From Table 1.1 the permeable materials are an attractive technology to investigate further due to their proven high noise reduction levels reported from wind-tunnel tests, compared to TE serrations.

1

Table 1.1: Review of TE noise reduction technologies, their wind-tunnel tests of concept, and application on real wind turbines.

Technology	Wind-tunnel tests of concept		Application on real wind turbines	
	Maximum reported noise reduction	References	Maximum reported noise reduction (if application exists)	References
TE serrations	7-10 dB	Dassen et al. (1996) [46] Gruber et al. (2011, 2013) [47, 48] Avallone et al. (2016) [49] Arce–León et al. (2016) [50] Zhou et al. (2020) [51]	Very common on modern wind turbines, known to give about 3 dB noise reduction	Oerlemans et al. (2009) [52] Oerlemans et al. (2016) [53]
Permeable materials	10-20 dB depending on chordwise extent of application	Geyer et al. (2010) [54] Herr and Reichenberger (2011) [55]	Not identified	Not identified
Brush/ fringes	7-10 dB	Herr and Dobrzynski (2005) [56] Herr (2007) [57] Finez et al. (2010) [35] Clark et al. (2017) [59]	0.5 dB noise reduction, sometimes noise increase	Schepers (2007) [58]
Fences/ rails	6-10 dB	Afshari (2019) [60] Fiscaletti et al. (2022) [61]	Not identified	Not identified
Elastic materials	No TBL–TE noise reduction Only suppresses tonal noise from blunt TE	Kamps et al. (2017) [62] Talboys et al. (2019) [63] Talboys et al. (2021) [64]	Not identified	Not identified
Hybrid method	Poro-serrated TE: 7 dB Flexible TE serrations: 2-3 dB addition to rigid TE serrations	Poro-serrated TE: Vathylakis et al. (2015) [65], Chong et al. (2016) [66], and Arce–León (2017) [67] Flexible TE serrations: Zhou et al. (2020) [51]	Combed TE serrations reduce 2 dB extra compared to regular TE serrations	Oerlemans et al. (2016) [53]

1.6. OBJECTIVES AND THESIS STRUCTURE

The title of this thesis is 'Assessing and improving trailing-edge noise reduction technologies for industrial wind-turbine applications'. This thesis comprises of eight chapters and the structure of this thesis is presented in Fig. 1.8.
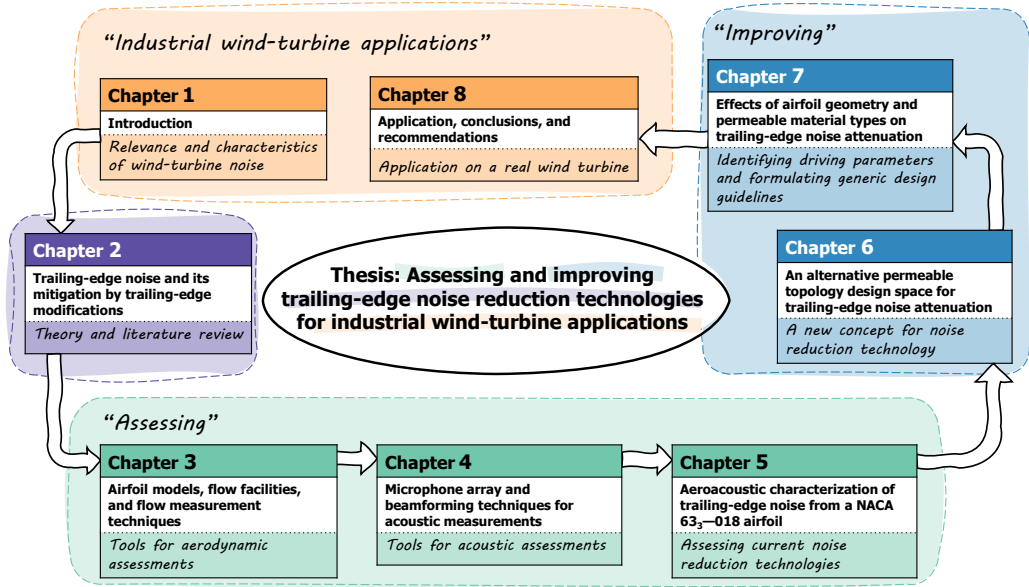
Figure 1.8: Overview of this thesis.

This thesis is a part of the 'Innovative PERmeable Materials for Airfoil Noise reduction' (IPER-MAN) project funded by academic in industrial partners, including LM Wind Power, through the Dutch Research Council (NWO). This thesis aims to advance the technological readiness level of the permeable materials for TE noise reduction for industrial wind-turbine applications by accurately assessing performance of current TE noise reduction technologies. For the assessment, this thesis focuses on two technologies: the TE serrations technology and the permeable materials using wind-tunnel measurements of airfoil models equipped with these technologies. Next, the thesis focuses on improving the current permeable TE technology because this technology shows the potential to achieve a considerable additional noise reduction compared to the TE serrations, but, unlike the TE serrations, has not been implemented on real wind turbines. This is partially because there are still some aeroacoustic disadvantages attributed to current permeable TE designs, such as the increase of high-frequency roughness noise and aerodynamic drag, that hinder implementation of them on real wind turbines. Based on the experimental data, an alternative design concept for a permeable TE for noise reduction is proposed. This design aims to improve the noise reduction performance while ensuring practicality on real wind turbine applications and addressing shortcomings of previous concepts. The experimental data are also used to identify design parameters that drive the noise reduction and to formulate a generic design guideline for future permeable TEs. Finally,

1

preliminary assessments of the TE noise reduction performance of a permeable TE on a real wind turbine are presented. Correspondingly, the remaining chapters in this thesis deal with the following:

- Chapter 2 provides theoretical description of the TE noise and discusses the noise reduction mechanisms attributed to the TE noise reduction devices.

- Chapters 3 to 5 present the experimental techniques for and the results of *assessing* the TBL–TE noise reduction technologies.

  – For aerodynamic assessments, Chapter 3 introduces the airfoil models, flow facilities, and measurement techniques employed in this thesis.

  – For acoustic assessments, Chapter 4 presents the experimental setups for acoustic measurements and discusses useful acoustic beamforming techniques for assessing the TE noise reduction technologies and quantifying the wind turbine noise.

  – Chapter 5 presents the measurement results of a representative airfoil for wind turbine blades equipped with TE serrations and permeable materials.

- Chapters 6 and 7 focus on *improving* the permeable material technologies.

  – Chapter 6 presents an alternative design for the permeable TE. Experimental results of the noise reduction and aerodynamic performances of an airfoil equipped with this alternative permeable TE design are compared to that with a conventional permeable TE.

  – Chapter 7 applies symbolic regression modeling on the collected experimental data to identify parameters that drive the noise reduction performance of a permeable TE and to suggest a design guideline.

- Finally, similar to the present chapter, Chapter 8 focuses on the real-world *industrial wind-turbine applications*. It concludes this thesis with a brief outlook on the first real wind-turbine implementation of a permeable TE extension for TE noise reduction. Finally, recommendations for future research are provided.

It is noteworthy that many chapters in this thesis have been adapted from the author's peer-reviewed journal articles. For the chapters where this is applicable, indications and citation guidelines are provided on the chapter title page. A list of the author's publications up to the date of defending this thesis is provided on page 173.

2

TRAILING-EDGE NOISE AND ITS MITIGATION BY TRAILING-EDGE SERRATIONS AND PERMEABLE MATERIALS[1]
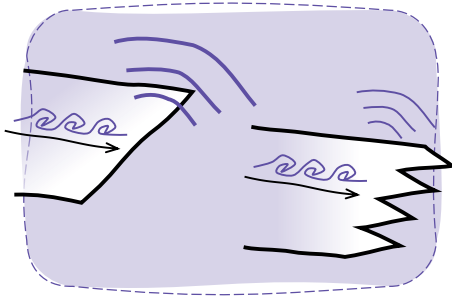
This chapter provides theoretical description of the Turbulent Boundary Layer Trailing-edge (TBL–TE) noise based on the framework of Amiet (1976). Physical quantities that govern the TBL–TE noise characteristics are pointed out. The two TBL–TE noise reduction technologies focused upon in this thesis, namely the permeable materials and the TE serrations, are discussed in more details. Physical mechanisms responsible for the TBL–TE noise mitigation by those devices are explained. Finally, state-of-the-art and current challenges associating to those devices are reviewed.

---

[1]Parts of Section 2.3.1 in this chapter have been published in the International Journal of Aeroacoustics. Please cite as shown in the list of peer-reviewed journal articles, number 5.

2.1. INTRODUCTION

The noise measurement of a real wind turbine shown in Chapter 1 has demonstrated that the main noise source is located at the region close to blade tip. This is the region where a high local relative flow speed is experienced [23]. The local chord-based Reynolds number Re_c is larger than one million [18] and the boundary layer is naturally turbulent. The turbulence-induced surface pressure fluctuations encounter a change in the boundary condition as they are convected towards the Trailing Edge (TE). This triggers acoustic scattering that radiates to the far-field. This is the underlying mechanism of the Turbulent Boundary Layer Trailing-edge (TBL–TE) noise introduced in Section 1.4. The TBL–TE noise is the dominant contributor to wind-turbine noise [23].

This chapter is dedicated to the theoretical description of the TBL–TE noise. An analytical model of Amiet [68, 69] is discussed. The intention is to introduce flow parameters responsible for TBL–TE noise characteristics. Subsequently, two passive TBL–TE noise mitigation technologies, namely TE serrations and permeable materials are discussed in detail. Their effects on the flow parameters, responsible for the TBL–TE noise, which contribute to noise reduction are presented. Finally, their state of the art and current challenges are discussed.

2.2. TBL–TE NOISE DESCRIBED BY ACOUSTIC ANALOGY

This section describes the TBL–TE noise by exploiting *acoustic analogies*. With acoustic analogies, determination of physical flow variables that contribute to sound generation, i.e. the *source*, such as pressure fluctuations and stress tensors, is done separately from the calculation of the acoustic *propagation*. The governing continuity and momentum conservation equations are rearranged in an inhomogeneous wave equation form. Subsequently, the far-field solution, i.e. the acoustic pressure at any arbitrary point and time resulting from the source, can be obtained by solving the inhomogeneous wave equation. This is done by integrating the source terms convoluted with the Green's function for the wave equation for a specified time/frequency and far-field location relative to the source.

There are several advantages of employing the acoustic analogy. For far-field noise predictions, it is computationally less expensive to confine high-resolution simulations or measurements to a small source region. The isolation of the source and the propagation is helpful for studying effects of different flow variables on the far-field acoustic characteristics as well as for tackling with the relevant physical quantity for noise mitigation.

By the end of this section, far-field acoustic characteristics of the TBL–TE noise will be linked to relevant physical flow variables that can easily be measured experimentally, modeled, or extracted from numerical flow simulations.

2.2.1. FAR-FIELD NOISE GENERATED BY TURBULENCE INTERACTION WITH A SOLID BODY

Curle [70] investigated far-field acoustic characteristics of sound generated by turbulence interacting with a solid body based on the classical Lighthill's analogy for a free jet in a quiescent field [71, 72]. In Curle's analogy, the solid body is assumed to be *acoustically compact*, meaning that the characteristic length of it, e.g. the chord c, is much smaller

than the acoustic wavelength of the radiated sound λ_0, i.e. $c/\lambda_0 \ll 1$. Curle argued that in low Mach number flows, unsteady normal forces acting on the body contribute more significantly to the far-field sound than quadrupole sources in the turbulence. As a result, the radiated far-field sound alters from that of the free-field turbulence scenario considered by Lighthill. The far-field acoustic intensity is proportional to the following variables (for an observer in the same plane as this solid body, i.e. two-dimensional consideration as sketched in Fig. 2.1):

$$I_r \propto \frac{\rho_0 u_\infty^6 c^2}{R^2 c_0^3} \sin^2\Theta \rightarrow I_r \propto u_\infty^6, \tag{2.1}$$

where ρ_0 is the medium density, u_∞ is the flow speed experienced by the body, R is the distance to the observer, c_0 is the speed of sound[2], and Θ is the observer's angle (See Fig. 2.1). This shows that in the acoustically compact case, the radiated sound is proportional to u_∞^6. The far-field Sound Pressure Level (SPL) [found by taking $10\log_{10}$ of $\rho_0 c_0 I_r/(\rho_0 c_0 I_{r,\text{ref.}})$, where $I_{r,\text{ref.}} = 10^{-12}$ W/m^2] increases with u_∞ with a slope of 6 as shown in Fig. 2.1. Furthermore, the radiation directivity is identical to that of a dipole source ($\propto \sin^2\Theta$) where the radiation efficiency is highest in the observer's direction normal to the body and lowest in the up– and downstream directions.
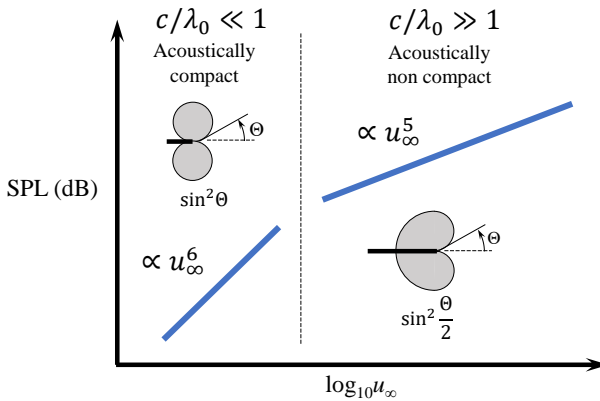
Figure 2.1: Theoretical noise emission of a turbulent flow with a solid body present.

To account for the acoustically non-compact cases where the acoustic wavelengths are much smaller than the chord of the solid body, i.e. $c/\lambda_0 \gg 1$, Ffwocs–Williams and Hall [20] derived a solution for the Lighthill's equation using a tailored Green's function where the boundary conditions account for the presence of a solid plate. The far-field sound intensity I_r resulting from this turbulence interaction with this plate at low Mach numbers, assuming inviscid and isentropic conditions in the source term (Lighthill's stress tensor), is proportional to the following variables (for a two-dimensional consideration):

---

[2]Throughout this thesis, c denotes the chord whereas c_0 denotes the sound speed.

$$I_r \propto \frac{\rho_0^2 u_\infty^5 c\delta}{R^2 c_0^2} \sin^2 \frac{\Theta}{2} \rightarrow I_r \propto u_\infty^5, \tag{2.2}$$

where δ is a length scale of the turbulence. This indicates that in the acoustically non-compact case, the radiated sound power is proportional to u_∞^5 (one exponent lower than the acoustically-compact case) as shown in Fig. 2.1. Furthermore, the radiation directivity has the so-called cardioid shape ($\propto \sin^2 \frac{\Theta}{2}$) where the strongest acoustic radiation is in the upstream direction.

Equation (2.2) is very representative for the TBL–TE noise radiation characteristics for wind-turbine applications, where the chord of the blade is much larger than the acoustic wavelengths.

2.2.2. AMIET'S THEORY FOR THE TBL–TE NOISE

The far-field TBL–TE noise of an airfoil is the result of sound scattering due to a turbulent flow passing the TE of a rigid flat plate. There exist several acoustic analogy approaches to describe the far-field acoustic characteristic of such setting. The presence of the plate introduces, as mentioned in the previous subsection, a modified boundary condition as compared to the classical analogy of Lighthill. The aforementioned work of Ffowcs–Williams and Hall [20] tailored the Green's function [73] according to this new boundary condition. The far-field acoustic characteristic is obtained by a volume integral of the transformed quadrupole source term convoluted with the tailored Green's function. Evaluation of this 3–D volume integral is very effortful because it requires all velocity components in time and space to construct the source term [74].

Alternatively, the source term is described using the so-called Wiener–Hopf technique [75] which performs a frequency decomposition of turbulence into single-frequency surface pressure waves. To alleviate the mathematical effort related to the Wiener–Hopf technique, Amiet [68, 69] further rearranged the governing equation and boundary conditions such that the so-called *Schwartzschild solution* [76] can be applied to solve for the source term. Subsequently, the far-field acoustic pressure can be obtained via Curle's analogy, i.e. integrating the source term convoluted with the propagation term (related to the Green's function) over the flat plate. This integration is applied to determine each frequency contribution to the overall far-field noise under the hypothesis that the problem formulation is linear. Generally, the scattered incident wave problem due to the presence of a plane is known as a *diffraction problem* [77].

This section adopts the classical Amiet's theory to discuss relevant physical flow parameters that affect the TBL–TE noise. For simplicity, advanced corrections of Amiet's theory, such as the leading-edge backscattering correction [78, 79], will not be mentioned, but will briefly be reviewed thereafter.

ACOUSTIC ANALOGY: ASSUMPTIONS FOR THE TBL–TE NOISE SOURCE

It is assumed that the contribution of quadrupole sources generated by the boundary layer to the far-field noise is insignificant compared to the dipole source generated by the unsteady loading force acting on the flat plate. Furthermore, the flat plate is assumed to be perfectly rigid, i.e. no fluid displacement is caused by the flat plate motion. As a

result, the Lighthill acoustic analogy in the formulation of Goldstein [80] in the frequency domain can be simplified; the volume integration of the quadrupole term as well as the surface integral of the source due to the fluid displacement are neglected, and one surface integral term remains.

Consider a flat plate with a chord c and span L where the reference coordinate system $\mathbf{x} = [x, y, z]$ originates from the TE at the midspan location as shown in Fig. 2.2. The x direction is parallel to the chord, the y direction is normal to the plate, and the z direction is parallel to the span. Let $p_a(\mathbf{x_o}, \omega)$ represent the far-field acoustic pressure resulting from a turbulent flow passing this flat plate TE, perceived at the observer location $\mathbf{x_o} = [x_o, y_o, z_o]$ at an angular frequency ω, $p_a(\mathbf{x_o}, \omega)$ can be calculated from the following simplified acoustic analogy [81]:

$$p_a(\mathbf{x_o}, \omega) = \int_S \Delta p_t(\mathbf{x}, \omega) I(\mathbf{x}, \mathbf{x_o}, \omega) \mathrm{d}S(\mathbf{x}). \tag{2.3}$$
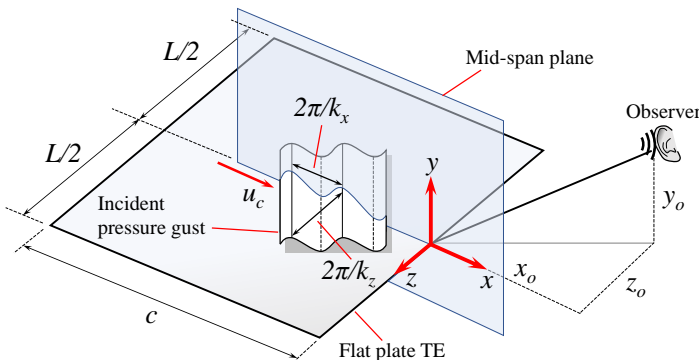
Figure 2.2: Schematic of an incident pressure gust approaching a straight TE of a flat plate.

The unsteady loading force acting per unit area on this flat plate may be represented by the total surface pressure jump $\Delta p_t(\mathbf{x}, \omega)$ at a location $\mathbf{x} = [x, y = 0, z]$ for a flat plate's surface. This $\Delta p_t(\mathbf{x}, \omega)$ term may therefore be regarded as the *source term*, while $I(\mathbf{x}, \mathbf{x_o}, \omega)$, containing the Green's function, accounts for the propagation to the far-field and may be regarded as the *propagation term*. The far-field acoustic pressure $p_a(\mathbf{x_o}, \omega)$ can be determined from the surface integral of the convolution of the source and propagation terms over the surface S.

From Eq. (2.3), one can already infer that the far-field acoustic pressure of the TBL–TE noise is directly proportional to the magnitude of the pressure jump between the upper and lower surfaces. For an airfoil, this is equivalent to the unsteady pressure jump between the suction and the pressure sides. The source and the propagation terms in the integrand in Eq. (2.3) are further elaborated upon in the following.

SOURCE TERM: PRESSURE JUMP

Equation (2.3) further implies that if the source term, i.e. pressure jump across the flat plate $\Delta p_t(\mathbf{x}, \omega)$ is known, the far-field acoustic pressure $p_a(\mathbf{x_o}, \omega)$ can be computed.

The pressure jump $\Delta p_t(\mathbf{x}, \omega)$ can be modeled as a summation of the incident pressure difference Δp_i and scattered pressure difference Δp_s, i.e. $\Delta p_t = \Delta p_i + \Delta p_s$ [33, 81]. The incident pressure p_i is modeled as a pressure gust traveling with a convection frequency u_c towards the TE of a flat plate. A schematic of this pressure gust is also shown in Fig. 2.2. It is assumed that the convective velocity u_c does not vary with the angular frequency ω. Then ω/u_c can be replaced by the wavenumber k_x. Supposing a two-dimensional case where $k_z = 0$, the spectral component of the incident pressure gust is described as follows:

$$p_i(x, \omega, u_c) = P_0(x)e^{-\mathrm{i}k_x x}, \tag{2.4}$$

where i is the imaginary unit.

Experimentally, the incident pressure amplitude P_0 can be retrieved by using, for instance, surface microphones [82, 83]. The scattered pressure p_s due to this gust must satisfy the convective wave equation as well as two boundary conditions: first, for $x > 0$ and $y = 0$, i.e. in the wake, $P_0(x)$ must be canceled out by the amplitude of the scattered pressure $P_1(x)$ to satisfy the Kutta condition, second, for $x \leq 0$ and $y = 0$, the derivative of $P_1(x)$ must be zero as the plate is impermeable.

The aforementioned convective wave equation and the boundary conditions are subjected to the Prandtl–Glauert coordinate transformation [84] and a change of variable (omitted for conciseness). The governing equations are then arranged in the canonical Helmholz equation for a diffraction problem. Consequently, the Schwarzschild solution of $P_1(x)$ can be found. Next, Δp_t is related to p_i via a transfer function g as follows:

$$\Delta p_t(x, \omega, u_c) = g(x, \omega, u_c)p_i(x, \omega, u_c). \tag{2.5}$$

The transfer function $g(x, \omega, u_c)$ reads:

$$g(x, \omega, u_c) = (1 + \mathrm{i})\mathrm{E}^*\left[-x\left(\frac{\omega}{c_0\beta^2} + k_x\right)\right] - 1, \text{ for } x < 0, \tag{2.6}$$

where $\mathrm{E}^*[*]$ is the Fresnel function, $\beta = \sqrt{1 - M^2}$, and the Mach number $M = u_\infty/c_0$. A full expression where $\Delta p_t(\mathbf{x}, \omega)$ is related to $p_i(\mathbf{x}, \omega)$ is obtained by substituting Eqs. (2.4) and (2.6) into Eq. (2.5) as shown here for completeness:

$$\Delta p_t(x, \omega, u_c) = \left((1 + \mathrm{i})\mathrm{E}^*\left[-x\left(\frac{\omega}{c_0\beta^2} + k_x\right)\right] - 1\right)P_0(x)e^{-\mathrm{i}k_x x}, \text{ for } x < 0. \tag{2.7}$$

PROPAGATION TERM

Another important term in Eq. (2.3) is the propagation term $I(\mathbf{x}, \mathbf{x_o}, \omega)$ which describes propagation of the sound generated by the source $\Delta p_t(\mathbf{x}, \omega)$ at a source location $\mathbf{x}$ and an angular frequency ω to a far-field observer's location $\mathbf{x_o}$. The propagation term $I(\mathbf{x}, \mathbf{x_o}, \omega)$ is related to the Fourier transform of the Green's function $G(\mathbf{x}, \mathbf{x_o}, \omega)$ which accounts for a uniform flow effect on the sound propagation, i.e. convection of the sound wave by the flow. It is further assumed that the observer is in the far-field where $|\mathbf{x_o}| \gg |\mathbf{x}|$. The expression for $I(\mathbf{x_o}, \mathbf{x}, \omega)$ is provided in Eq. (2.8) [81]. For conciseness, the sound propagation path distance, corrected for the convection, is denoted by R_t as shown:

$$I(\mathbf{x_o}, \mathbf{x}, \omega) = -\frac{\partial G(\mathbf{x_o}, \mathbf{x}, \omega)}{\partial \mathrm{x}_i} n_i \approx \frac{i\omega y_o}{4\pi c_0} e^{\frac{i\omega}{c_0 \beta^2} \left[\sigma - \frac{xx_o + \beta^2 zz_o}{\sigma} + M(x - x_o) \right]} = \frac{i\omega y_o}{4\pi c_0} e^{\frac{i\omega R_t}{c_0}}, \quad (2.8)$$

where n_i is a unit vector in the x_i direction and $\sigma = \sqrt{x_o^2 + \beta^2(y_o^2 + z_o^2)}$.

CLASSICAL AMIET'S THEORY

Having formulated the expressions for $\Delta p_t(\mathbf{x}, \omega)$ and $I(\mathbf{x}, \mathbf{x_o}, \omega)$, the far-field noise $p_a(\mathbf{x_o}, \omega)$ can be computed by evaluating the radiation integral given by Curle's acoustic analogy. Equation (2.3) becomes

$$p_a(\mathbf{x_o}, \omega) = \frac{-i\omega y_o}{4\pi c_0 \sigma^2} \int_{-c}^{0} \int_{-L/2}^{L/2} \Delta p_t e^{\frac{i\omega R_t}{c_0}} \, dz dx. \quad (2.9)$$

For turbulent flows, the auto spectral density of $p_a(\mathbf{x_o}, \omega)$, $S_{pp}(\mathbf{x_o}, \omega)$, is preferred [81]. This is obtained by multiplying $p_a(\mathbf{x_0}, \omega)$ in Eq. (2.9) with its complex conjugate $p_a^*(\mathbf{x_0}, \omega)$. For the assumed 2–D pressure gust, $S_{pp}(\mathbf{x_o}, \omega)$ reads

$$S_{pp}(\mathbf{x_o}, \omega) = \lim_{T \to \infty} \frac{\pi}{T} E[p_a(\mathbf{x_o}, \omega) p_a^*(\mathbf{x_o}, \omega)] \approx \left(\frac{\omega y_o}{4\pi c_0 \sigma^2} \right)^2 2\pi L |\mathcal{L}|^2 \Pi_0, \quad (2.10)$$

where $E[*]$ is the ensemble average and $|\mathcal{L}|$ contains the transfer function $g(\mathbf{x}, \omega)$ and part of $I(\mathbf{x}, \mathbf{x_o}, \omega)$. These functions are independent on the incoming pressure gust. For a simple case of $z_o = 0$, i.e. the observer in the mid-span, $|\mathcal{L}|$ is given by

$$|\mathcal{L}| = \left| \frac{2}{c} \int_{-c}^{0} g(x, \omega, u_c) e^{ik_x x} e^{-\frac{i\omega x}{c_0 \beta^2}(M - \frac{x_o}{\sigma})} dx \right|. \quad (2.11)$$

The function $|\mathcal{L}|$ is usually regarded as the *aeroacoustic transfer function* which describes the response of the flat plate to the pressure gust for a specified observer's location. A full expression for $|\mathcal{L}|$, including a solution for the Fresnel integral E^* within $g(x, \omega, u_c)$ in Eq. (2.6), can be found in literature [81, 85]. It can be seen that every term in Eq. (2.10) discussed so far up to and including $|\mathcal{L}|$ can be computed analytically based on the geometry of the problem. When the geometry of the problem changes, such as for the case of serrated, i.e. non-straight TE, $|\mathcal{L}|$ is modified. A modified version of Eq. (2.10) for TE serrations will be discussed later in Eq. (2.24) in Section 2.3.2.

The only remaining term Π_0 in Eq. (2.10) is the wavenumber–frequency spectrum which represents the TBL-induced incident pressure spectrum. For a given spanwise wavenumber, Π_0 is obtained by integrating the cross-spectral density of the incident pressure Π_{P_0}. Roger and Moreau [79] emphasized that the spanwise statistics of the pressure fluctuation is much more significant than the chordwise one. Therefore, Π_0 is simplified as follows:

$$\Pi_0 = \int_{-\infty}^{\infty} \Pi_{P_0}(k_x, k_z, \omega) dk_x \approx \frac{G_{pp}(\omega)}{2\pi} \int_{-\infty}^{\infty} \frac{\Phi_{pp}(\Delta x = 0, \Delta z, \omega)}{G_{pp}(\omega)} e^{ik_z \Delta z} d\Delta z, \quad (2.12)$$

where $G_{pp}(\omega)$ is the auto-spectrum of the surface pressure fluctuations. This quantity may be acquired experimentally by surface microphones or modeled using semi-empirical models which are discussed in Section 2.2.3. The variable Φ_{pp} is the cross-spectral density of the surface pressure fluctuation between a given point on the airfoil surface $\mathbf{x} = [x, y = 0, z]$ and another point $\mathbf{x} + \Delta\mathbf{x} = [x + \Delta x, y + \Delta y = 0, z + \Delta z]$.

Having defined $\Delta\mathbf{x}$, Π can also formally be related to $P_0(\mathbf{x})$ as [85]

$$\Pi_{P_0} = \lim_{T \to \infty} \frac{\pi}{T} E[P_0(\mathbf{x}, \omega) P_0^*(\mathbf{x} + \Delta\mathbf{x}, \omega)]. \tag{2.13}$$

Assuming that $k_z = 0$ the integral in Eq. (2.12) may conveniently be related to the spanwise correlation length $l_z(\omega)$ defined as

$$2l_z(\omega) = \int_{-\infty}^{\infty} \frac{\Phi_{pp}(\Delta x = 0, \Delta z, \omega)}{G_{pp}(\omega)} \mathrm{d}\Delta z, \tag{2.14}$$

which can also computed based on surface pressure fluctuation spectra acquired experimentally using multiple spanwise surface microphones. There also exists a semi-empirical formulation of $l_z(\omega)$ which will also be discussed in Section 2.2.3.

Correspondingly, Π_0 is

$$\Pi_0 = \frac{1}{\pi} G_{pp}(\omega) l_z(\omega), \tag{2.15}$$

Therefore, for a given flow condition and observer's location, the far-field TBL–TE noise is driven by the flow parameters within Π_0. It will also be shown further how TBL–TE noise reduction devices change these parameters to minimize the far–field noise level.

Inserting Π_0 from Eq. (2.15), the Amiet's theory in Eq. (2.10) reads:

$$S_{pp}(\mathbf{x_o}, \omega) \approx \left(\frac{\omega y_o}{2\pi c_0 \sigma^2}\right)^2 L |\mathscr{L}|^2 G_{pp}(\omega) l_z(\omega). \tag{2.16}$$

It is noteworthy that the Amiet's model in Eq. (2.16) for a highly simplified case of an observer in the midspan plane right above the TE, i.e. $\mathbf{x_o} = [0, y_o, 0]$, becomes

$$S_{pp}(\mathbf{x_o} = [0, y_o, 0], \omega) \approx \frac{L}{4} \left(\frac{1}{\pi\sigma}\right)^2 \frac{M_c}{1 - M_c} G_{pp}(\omega) l_z(\omega), \tag{2.17}$$

where $M_c = u_c / c_0$. This is also in accordance with the output of other TE noise calculation methods such as the one of Howe [33, 86, 87].

Finally, the far-field Sound Pressure Level (SPL) spectrum of the TBL–TE noise is calculated as:

$$\mathrm{SPL}(\mathbf{x_o}, \omega) = 10 \log_{10} \left[\frac{2\pi S_{pp}(\mathbf{x_o}, \omega) \Delta f}{p_0} \right] \mathrm{dB}, \tag{2.18}$$

where Δf is the frequency resolution of $S_{pp}(\mathbf{x_o}, \omega)$ and the reference pressure p_0 is 2×10^{-5} Pa.

FURTHER EXTENSIONS OF THE AMIET'S THEORY AND ADVANCES IN TE NOISE MODELS

Modifications to the enforced boundary conditions of the aforementioned flat plate–pressure gust interaction problem trigger further extensions to the presented Amiet's theory. In literature, a solution for a more generic three-dimensional gust problem [79, 88], i.e. $k_z \neq 0$, is provided. Amiet also later introduced a decay of the incident pressure complex amplitude towards the leading edge to account for the presence of flat plate leading edge, i.e. finite chord length [85]. This is done by adding a decay term to the transfer function $g(x, \omega, u_c)$ in Eq. (2.6) [81]. Roger and Moreau [78, 79] introduced the so-called *leading edge backscattering* correction to properly account for the presence of the leading edge, i.e. finite chord. This results in an additional term in the aeroacoustic transfer function $|\mathscr{L}|$ [74].

More recently, analytical solutions to problems involving sound scattering due to the incident pressure wave interaction with a flat plate have been developed for more complicated boundary conditions. For example, Jaworski and Peake [89] considered sound scattering of a poro-elastic plate instead of a solid and rigid plate. Such problems are usually solved by the Wiener–Hopf technique. Multiple boundary conditions that arise may require a matrix formulation that needs to be solved iteratively, such as the solid flat plate with a porous extension problem considered by Kisil and Ayton [90]. The solutions are then provided in terms of *Mathieu functions* in elliptical coordinates. The advantage of formulating the problem in a matrix form and incorporating the Mathieu function is the ability to handle unconventional boundary conditions, e.g. elastic or porous plates [33]. These techniques are currently being employed to analytically predict noise scattering from airfoils with unconventional TE treatments [91].

2.2.3. SEMI-EMPIRICAL MODELS FOR $G_{pp}(\omega)$ AND $l_z(\omega)$

The last two terms of Eq. (2.16), namely the auto-spectrum of the wall pressure fluctuation $G_{pp}(\omega)$ and the spanwise correlation length $l_z(\omega)$, are the only physical quantities that need to be computed or collected experimentally in order to determine the far-field noise autospectrum. Thanks to many experimental datasets that have rigorously been collected in the past, there are a number of semi-empirical models that may be employed to predict $G_{pp}(\omega)$ and $l_z(\omega)$ and hence the TBL–TE noise. This section presents examples of such models and discuss their implications on the TBL–TE noise characteristics with a focus on airfoil applications.

UNIVERSAL WALL PRESSURE SPECTRUM MODEL

The spectrum of the TBL-induced wall pressure fluctuation $G_{pp}(\omega)$ is a function of the TBL parameters. The spectrum features different regions [92–94]: low– and mid-frequency, overlap, and high-frequency. The low– and mid-frequency regions, where the slope is positive ($\propto \omega^2$), are governed by the edge velocity and the displacement thickness of the TBL, i.e. the outer region. On the other hand, the high-frequency region, where the slope is negative ($\propto \omega^{-7/3}$ to ω^{-5}), the spectra are governed by the near-wall parameters of the TBL, namely the friction velocity and the viscosity. Finally, the overlap region has a slightly less negative slope ($\propto \omega^{-0.7}$ to $\omega^{-1.1}$). The level of $G_{pp}(\omega)$ has been found to scale with the edge velocity, the wall friction, and the TBL displacement thickness. Therefore,

the aforementioned TBL-related parameters are taken into account to accurately predict $G_{pp}(\omega)$ spectral shape, i.e. slopes, and level.

Extra care must be taken when modeling $G_{pp}(\omega)$ for adverse-pressure-gradient flows, hence typical to an airfoil TE region, because a drastic increase of the $G_{pp}(\omega)$ level (10 dB at relatively low ω) has commonly been found in experiments when the pressure gradient is introduced [95]. A number of semi-empirical models for $G_{pp}(\omega)$ have been (and are still currently being) developed. These are, for example, the pioneering Rozenberg model [96] which modifies the zero-pressure-gradient formulation of Goody [97] by accounting for adverse-pressure-gradient effects, the Kamruzzaman model [98] which tunes the Rozenberg model further by more accurately modeling the spectral decay slope and the timescale ratio based on additional experimental data, and the recent model of Lee [93] which is robust for varying flow conditions.

Recently, Lee [93] expressed the wall pressure spectrum models developed in the past, including the models of Goody [97], Rozenberg [96], Kamruzzaman [98], Catlett [99], Hu [100], and Lee himself in a universal format:

$$G_{pp}(\omega)\text{SS} = \frac{a_1(\omega\text{FS})^{a_2}}{[a_9(\omega\text{FS})^{a_3} + a_4]^{a_5} + [(a_6 R_T^{a_7})(\omega\text{FS})^{a_8}]}, \tag{2.19}$$

where a_1, a_2, a_3, …, a_9 are modeling parameters that are used to tune the amplitude and the shape of the predicted spectrum. The parameter R_T is the Reynolds-number-dependent timescale ratio while SS and FS are the spectral and frequency scale factors, respectively. These parameters differ slightly for the different models. A comprehensive list of them is given by Lee [93]. The required inputs for these models are, in general, local TBL integral parameters and the wall shear stress, which can be obtained experimentally, and more simply by employing low-fidelity tools such as XFOIL [101].

To illustrate the dependence of $G_{pp}(\omega)$ on the input parameters, an example is given in Fig. 2.3a where predicted $G_{pp}(\omega)$ spectra at the TE region ($x = -0.02c$) of a symmetric NACA 0018 airfoil at chord-based Reynolds number $Re_c = 2.6 \times 10^5$ are shown. The model of Kamruzzaman [98] is chosen and the input parameters are obtained from XFOIL [101]. The figure shows $G_{pp}(\omega)$ on the suction side for varying angles of attack: 0°, 3°, and −3°, hence varying displacement thicknesses δ^* as specified in Fig. 2.3a. Additionally, the result for zero-degree angle of attack at a higher $Re_c = 4.6 \times 10^5$ is also shown.

For a given Re_c, an increase in the angle of attack, which causes also an increase in δ^*, makes $G_{pp}(\omega)$ shift to a lower frequency. This indicates that the low-frequency content of $G_{pp}(\omega)$ is associated with the relatively thick boundary layer while the high-frequency content is associated with the thin one. This result agrees with the sensitivity study of Lee [93] and is also analogous to the far-field acoustic pressure spectrum description of Oerlemans [102], where the frequency content of the far-field acoustic pressure spectrum inversely varies with the turbulent length scale (the TBL thickness in this case). Furthermore, an increase in the overall spectral level with an emphasis on the high-frequency content of $G_{pp}(\omega)$ is obtained when Re_c increases. This is reasonable since the flow speed increases while the boundary layer thickness reduces with the increasing Re_c.
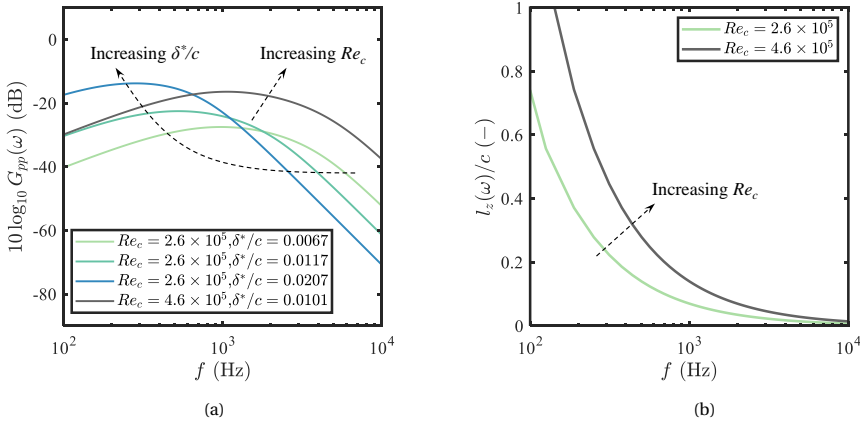
Figure 2.3: (a) Example of the predicted $G_{pp}(\omega)$ using the Kamruzzaman's model for a NACA 0018 airfoil at $x/c = -0.02$ for varying Re_c and δ^* and (b) Example of the predicted $l_z(\omega)$ using the Corcos' model for the same NACA airfoil.

CORCOS' SPANWISE CORRELATION LENGTH

Based mainly on the pressure fluctuation measurements below a TBL on the wind tunnel wall of Willmarth and Wooldridge [103], Corcos [104] proposed that the spanwise correlation length shall reduce exponentially with the angular frequency. Hence the following formula was proposed:

$$l_z(\omega) = \frac{u_c}{\gamma \omega}, \tag{2.20}$$

where γ is a fitting coefficient and u_c is usually chosen as $0.7 u_\infty$ [27].

For completeness, the predicted $l_z(\omega)$ for the same set up as described in Fig. 2.3a for $G_{pp}(\omega)$ is provided in Fig. 2.3b, only for zero-degree angle of attack. Here, γ is chosen as 1. The figure suggests a reduction of $l_z(\omega)$ as the frequency increases and an increase of $l_z(\omega)$ as Re_c, hence u_c, increases. These two figures therefore depict the required input parameters for predicting the far-field noise of a given airfoil.

2.3. TBL–TE NOISE REDUCTION TECHNOLOGIES

Having introduced the flow parameters that are relevant for the generation and the far-field characteristics of the TBL–TE, this section presents a summary of current TBL–TE noise mitigation strategies. Their effects on the flow parameters are discussed to illustrate the noise mitigation mechanism.

2.3.1. PERMEABLE MATERIALS

Permeable materials enable cross flow between the suction and the pressure sides of the airfoil. Many different types of material have been employed to this purpose, namely, porous (metal) foams [54, 105, 106], (3D printed) open-cell metamaterials [107, 108],

fibrous materials [109, 110], etc.

PERMEABLE MATERIAL CHARACTERIZATION

Porosity   The *porosity* ϕ of a certain material is defined as a ratio between the void volume V_v per total permeable material sample volume V_t [$V_s = V_t - V_v$, where V_s is the base (solid) material volume], whereas in some applications, where the voids are filled with air, the density is used:

$$\phi = \frac{V_v}{V_t} = 1 - \frac{V_s}{V_t} = 1 - \frac{\rho_t}{\rho_s} \tag{2.21}$$

where ρ_t and ρ_s are the densities of the permeable material sample and the base (solid) material, respectively. The porosity range is therefore $0 \leq \phi \leq 1$, with 0 meaning the material is fully solid, i.e. impermeable.

Tortuosity   Theoretically, the *tortuosity* τ is a ratio between the shortest path through the permeable domain Δl_v and the Euclidean distance between the start and the end point of the shortest path Δl_e [111]:

$$\tau = \frac{\Delta l_v}{\Delta l_e}. \tag{2.22}$$

However, determination of τ in practice is not as straightforward. Past literature argued that flow acceleration and deceleration when traveling through the porous domain with varying cross-sectional areas along the path, i.e. constrictions [112], should be accounted for. This resulted in modifications to Eq. (2.22), involving additional correction factors and coefficients [113]. A comprehensive overview is provided by Tjaden [111].

Alternatively, simulations and/or statistical approaches may be employed to determine τ. For the TBL–TE noise mitigation application, Rubio–Carpio et al. [108], for instance, employed the so-called random walk model [114] which simulates randomly distributed walkers within the digitized permeable material sample. Then, with a sufficient amount of walkers, the averaged τ was computed.

Permeability and form-drag coefficient   Additional characteristics of the permeable material may be characterized by measuring static pressure drops across a material sample according to the ISO 9053 standard [115, 116]. A schematic of a typical set up for such characterization of the permeable materials is given in Fig. 2.4. A cylindrical sample of the permeable material with a thickness t_s is subjected to air flow at multiple controlled Darcy velocities v_D. The static pressure drop Δp across the sample is recorded. The obtained $\Delta p / t_s$ is fitted by a quadratic function of v_D as

$$\frac{\Delta p}{t_s} = \frac{\mu}{K} v_D + \rho C v_D^2 = r v_D + \rho C v_D^2. \tag{2.23}$$

Equation (2.23) is typically known as the Forchheimer Equation [117] or the Hazen–Dupuit–Darcy Equation [118]. It describes that static pressure drop of a fluid having
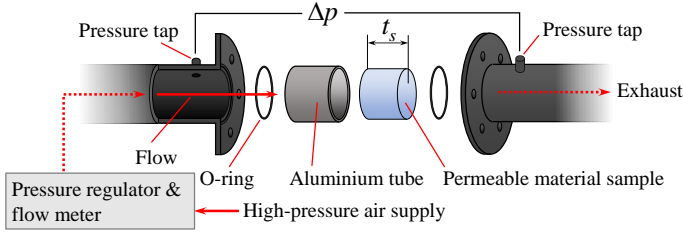
Figure 2.4: Schematic of the permeability test set up.

density ρ and dynamic viscosity μ attempting to pass through a permeable material sample with a thickness t_s depends on two material properties: the permeability K and the form drag coefficient C. When v_D is sufficiently low, the pressure drop is predominantly affected the viscosity [119]. In this regime, the quadratic term of Eq. (2.23) may be omitted, resulting in the well–known Darcy law [120], where the Δp varies linearly with v_D. Instead of K, the resistivity r, defined as $r = \mu/K$ is also widely used. For higher v_D, the intrinsic morphology of the permeable material dominates the pressure drop [121]. The streamline of flows are forced to slow down or change the directions when they encounter geometrical blockages, causing inertial losses [118]. The form drag coefficient C and the quadratic term of Eq. (2.23) account for this effect.

In this thesis, cylindrical samples of all the aforementioned permeable materials having a diameter of 55 mm and a representative thickness $t_s = 10$ mm are considered. An Aventics pneumatic regulator and a TSI 4040 volumetric flow meter are used to regulate the flow rate from a 10–bar air supply. The values of Δp are read by a Mensor 2101 differential pressure connected to pressure taps up– and downstream of the permeable material sample as shown schematically in Fig. 2.4.

PRESSURE RELEASE MECHANISM

On a solid airfoil, generation of the TBL–TE noise is attributed to scattering of TBL–induced surface pressure jump Δp_t at the TE as explained in Section 2.2.2. By introducing a finite permeability upstream of the TE, the incident TBL-induced surface pressure waves on the opposite sides of the airfoil partially interact and cancel, leading to a relatively weaker pressure jump close to the TE, and thus sound radiation [122, 123]. The aforementioned mechanism is the so-called *pressure release* mechanism [109, 110], which is, among others, the biggest contributor to the TBL–TE noise attenuation by the permeable TE [107]. Such a mechanism has been studied both experimentally and numerically [123] by correlations of the near-surface velocity [122] or pressure [107] fluctuations on the opposite surfaces of a permeable airfoil.

The pressure jump Δp_t may be viewed equivalently as the static pressure drop Δp across the permeable material in the Darcy–Forchheimer equation [Eq. (2.23)]. This equation states that Δp varies inversely with K, meaning that if the permeability increases, the pressure jump/drop reduces and further implies that the noise source strength reduces. This (partially) explains one of the most widely-known findings regarding TBL–TE noise attenuation of airfoils with permeable TE which states that the higher the permeability,

the more the noise is attenuated [54, 82, 106, 109, 110, 124]. Nevertheless, it is important to highlight that although it is theoretically possible to calculate Δp_t, directly employing the Amiet's model introduced to predict the far-field TBL–TE noise spectra for permeable airfoils may not yield accurate results. This is because application of these technologies may also modify the boundary conditions for the scattering, affecting also the Green's function (and thus the aeroacoustic transfer function $|\mathcal{L}|$) [107], or even introduce extra noise sources, e.g. roughness noise [109, 125], which will be demonstrated later in this section. Such alterations are beyond the scope of the pressure release mechanism and are, in fact, still a highly relevant topic for current research works [91].

It has further been shown that the pressure release mechanism does not occur uniformly along the chord when the permeable material is installed on the airfoil. Instead, it occurs very close to the TE tip [107, 123]. Teruna et al. [107] confirmed this statement in their simulation of a NACA 0018 airfoil with a permeable TE insert having diamond-lattice unit cells. They showed that noise attenuation at the last 4 % of the chord, i.e. very close to the TE, contributes substantially to the overall noise attenuation. Further analysis of the flow field showed that there exists a certain depth inside the permeable material where the pressure fluctuation magnitudes are comparable to that at the surface. This distance is the so-called *entrance length* [118, 126, 127] and is closely linked to the pore diameter for the foam-material type [126, 128]. Interactions of the surface pressure fluctuations between both sides, and therefore the aforementioned pressure release process, would occur most effectively only where the entrance lengths from the suction and the pressure sides of the airfoil overlap. Because of this, the region close to the TE, where the local airfoil geometry is thinner than approximately two times the entrance length, contributes the most to the overall noise attenuation [107].

State of the art and current challenges

Integration of permeable materials into the airfoil shape [54, 57, 105, 106, 109, 125, 129, 130] has been one of the most successful methods for attenuating the TBL–TE noise. Researchers have experimentally demonstrated an impressive capability of permeable airfoils of mitigating more than 10 dB of the TBL–TE noise. For instance, in research conducted by Geyer et al. [54], it was shown that the employment of porous materials, over the full extent of an SD7003 airfoil, could achieve up to 15 dB of noise reduction when compared to the solid airfoil.

Loss of lift and increase of drag   Balancing of the steady pressure difference between the suction and the pressure sides also occurs on permeable airfoils, leading to a loss of lift [131]. For instance, up to 75 % reduction of lift has been reported for highly permeable fully porous airfoils tested in a range of angles of attack between 12 and 24 degrees in the aforementioned work of Geyer et al. [54]. Studies from literature have, therefore, proposed to apply the permeable porous material only at the location where the TBL–TE noise is generated, i.e. as close as possible to the trailing edge. This approach gives a better compromise between the noise reduction and the preservation of the original aerodynamic performance, with respect to the fully porous airfoil [105, 125, 130, 132].

Apart from the loss of lift, Sarradj et al. [106] showed a clear increase of drag of a fully porous SD7003 airfoil with decreasing resistivity. This be attributed to the surface

roughness since cellular materials (i.e. open foams, generally metallic), which often entail high surface roughness, have been used in most of the previous research works.

Roughness and tonal noise increase   Increasing the pore size of porous materials increases the surface roughness, and hence the friction drag [109]. Increasing surface roughness also introduces the so-called *roughness noise* in a range of relatively high sound frequencies [109, 125]. The frequency above which the TBL–TE noise emission of the (partially) porous airfoil exceeds that of the reference solid airfoil is generally known as the *crossover frequency* [105, 125]. For instance, Herr et al. [109], found that the crossover frequency of the TBL–TE noise emission of the partially porous DLR F16 airfoil is around 9 to 12 kHz as shown in Fig. 2.5a. The crossover frequency has been found to vary inversely with the pore sizes [105, 106, 109, 125].
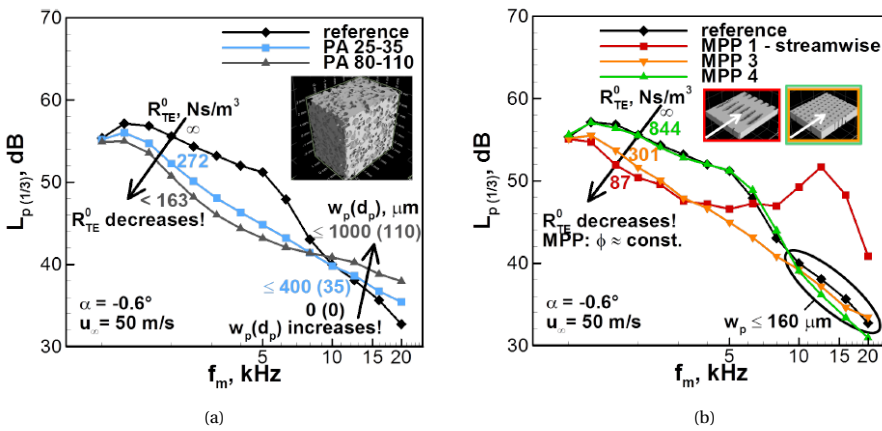

Figure 2.5: Far-field noise spectra of a DLR F16 airfoil with baseline and permeable trailing edges for different permeable material groups: (a) Porous Aluminum (PA) and (b) Micro Perforated Plates (MPP), reproduced from Herr et al. [109] with permission from the corresponding author. The notations used in this figures mean the following: R_{TE}^0: flow resistivity, w_p: pore width, d_p: effective pore size, ϕ: porosity, α: angle of attack, u_∞ free-stream flow speed, $L_{p,(1/3)}$: far-field noise level in 1/3-octave band, and f_m: middle frequency.

More recently, simplified perforated topologies comprising of an array of straight channels linking the suction and the pressure sides of the airfoil have also been employed as another alternative to the porous (metal) foam materials [57, 133]. The investigation by Herr et al. [109] discussed previously also featured a micro-perforated TE insert which could achieve a comparable noise attenuation of approximately 6 dB to more conventional porous topologies such as the porous aluminum. An example from their work is presented in Fig. 2.5b. A similar finding has been reported by Rubio–Carpio et al. [133] for a NACA 0018 airfoil with 3D-printed TE inserts. The authors found that, when a sufficiently low resistivity is reached by increasing the number of straight channels per unit area, a comparable TBL–TE noise attenuation to that achieved by a porous metal-foam TE insert is obtained. Nevertheless, care has to be taken when reducing the resistivity of such a perforated structure as tonal noise may appear. Herr et al. [109] and Rubio–Carpio et al. [133] have reported tonal noise increase found in their highly

permeable variants of the perforated structure. In the result of Herr et al. shown in Fig. [109], this phenomenon is found for the 'MPP1' case where a clear noise increase is detected at approximately 12.5 kHz. It has been hypothesized that the tonal noise is caused by vortex shedding across regions of regular perforation [108, 109], yet this issue has not further been addressed.

Practicality   Despite the promising noise attenuation capability of the porous materials proven by experimental results in literature, usage of such materials with large airfoils or in operating wind turbines could still be unappealing for industrial manufacturers. The permeable materials typically employed in the previous studies consist of randomized pore distribution resulting from the electrodeposition manufacturing processes [105, 106, 125]. Apart from the aforementioned drag and roughness noise increase due to the rough topology, large-scale realization, including manufacturing and maintenance, of such a complex topology could be very challenging.

Previous research works have recommended 'tailoring' [108, 109] the permeable material properties along the chord to overcome several downsides of the permeable materials discussed earlier, such as the tendency of the perforated channels to produce tonal noise. However, some issues such as the surface roughness may be mitigated only partially.

2.3.2. TE SERRATIONS

SERRATIONS GEOMETRY DEFINITION

TE serrations are non-straight geometric patterns that are periodic in the spanwise direction [36]. This section limits the consideration to only two-dimensional, i.e. flat, serrations. Consider a modified version of the schematic from Fig. 2.2. in Fig. 2.6 where the straight edge is replaced by the so-called *sawtooth* serrations. The serrations geometrical definition is governed by the wavelength λ and the peak amplitude h. These terminologies result from the wave-like consideration of the serrations geometry. Additionally, the most upstream and downstream parts of the serrations are denoted as the root and tip, respectively.

More generically, the serration geometry may also defined by a generic function $F(z)$. As a result, the TE of the flat plate considered varies along the span and is defined by $x = hF(z)$.

TE NOISE MITIGATION MECHANISM BY THE SERRATIONS AND DESIGN GUIDELINES

Consider the schematic of an incident pressure wave approaching the TE serrations in Fig. 2.6, and, for simplicity, assume that $k_z = 0$ the turbulence is frozen, one could envision different phases of the gust distributing along the serrations edge as the pressure wave approaches the edge. The coexisting different phase at the edge promotes destructive interference of the scattered pressure, and hence noise abatement [134–136].

Based on the previously introduced Amiet's approach, Lyu et al. [136] introduced a modified boundary condition for the scattered field, which is enforced at $x = hF(z)$ and $y = 0$, instead of at $x = 0$ and $y = 0$ for the straight TE case [91]. By further assuming that
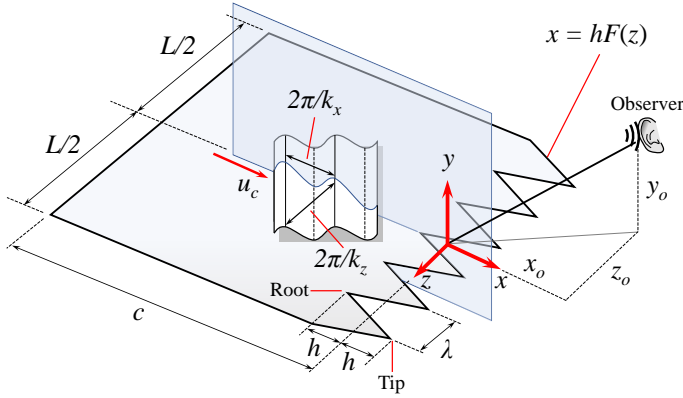
Figure 2.6: Schematic of an incident pressure gust approaching a straight TE of a flat plate.

the span L is large and the observer is in the midspan plane, i.e. $z_o = 0$, Eq. (2.10) modifies to

$$S_{pp}(\mathbf{x_o}, \omega) = \left(\frac{\omega y_o}{4\pi c_0 \sigma^2} \right)^2 2\pi L \sum_{m=-\infty}^{\infty} \left| \mathcal{L}\left(\omega, k_x, \frac{2m\pi}{\lambda} \right) \right|^2 \Pi_0\left(\omega, \frac{2m\pi}{\lambda} \right). \qquad (2.24)$$

It can be seen that the effect of the serrations geometry is only contained within the aeroacoustic transfer function $\mathcal{L}$ and the wavenumber-frequency spectrum Π_0. It is also noteworthy that although the infinite summation in Eq. (2.24) is similar to another well-known analytical model of Howe [134, 135], the model of Lyu is less likely to underestimate the noise emission of the serrated TE as that of Howe does. This is because the model of Howe is based on a compact Green's function which does not take into account coupling between the adjacent serrations edge [136]. Furthermore, as $k_x h \to 0$, Eq. (2.24) converges to the classical Amiet's theory for a straight TE [68, 69].

Having known that the noise reduction given by the serrations is due to the destructive interference of the scattered pressure at the serrations edge, the conceptual design goal for the serrations is to maximize the surface pressure phase difference within a correlation length along the serrations edge, so that the destructive interference occurs. Based on the proposed analytical model, Lyu [136] derived two necessary design conditions for the noise reduction: $k_x h \gg 1$ and $2h k_x l_z / \lambda \gg 1$. Similarly, Gruber [38] proposed a practical design guideline based on experimental results for noise reduction: $h > 2\delta$, where the boundary layer thickness δ is used to represent the turbulence length scale relative to the serrations. It is commonly known that a long and slender serration shape, i.e. large h/λ, is more likely to promote noise reduction as it maximizes the chance of having different phases along the serrations edge.

The aforementioned guidelines are strictly based on the frozen turbulence assumption. In fact, the surface pressure fluctuation as well as the flow structure also develop along the serration length. Avallone et al. [137] showed that the low-frequency noise reduction is contributed by the serrations root while the high-frequency one is governed by the tip. Therefore, the serrations root contributes more significantly to the overall noise reduction.

This can experimentally be demonstrated by chopped root and chopped tip serrations [51], where the root or the tip of the sawtooth serrations are straight. It was found that the high-frequency noise reduction by the chopped tip is absent. On the other hand, the low frequency noise reduction for the chopped root is not as pronounced as for the sawtooth serrations with a regular root.

STATE OF THE ART: OPTIMAL SERRATION SHAPE?

TE serrations are common on modern industrial wind turbines. Field measurements have shown noise reduction of up to 5 dB compared to untreated blades [138].

Based on the available analytical noise models [91, 136, 139] and a parametric definition of the serrations geometry $F(z)$, it is indeed possible to optimize the serrations geometry for the maximum TBL–TE noise mitigation. Kholodov and Moreau [140], for instance, have incorporated the analytical model of Lyu and Ayton [139] in their serration shape optimization. The results suggested that serrations with a slitted, i.e. sharp, root and relatively blunt tip are likely to maximize the noise reduction. A similar configuration is the so-called *iron*-shaped serrations introduced by Avallone et al [141]. This serration shape features very sharp and almost tangent roots as illustrated in comparison to the conventional sawtooth serration shape in Fig. 2.7. A computational study of Avallone showed an additional low-frequency noise reduction of 2 dB given by the iron serrations compared to the sawtooth serrations. This is also later confirmed by an experiment of Zhou at al. [51]. The additional noise reduction is found to be because the tangent root reduces noise scattering at that location by making flow interaction between the opposite sides more gradual along the streamwise direction, compared to the less tangent sawtooth serrations root.
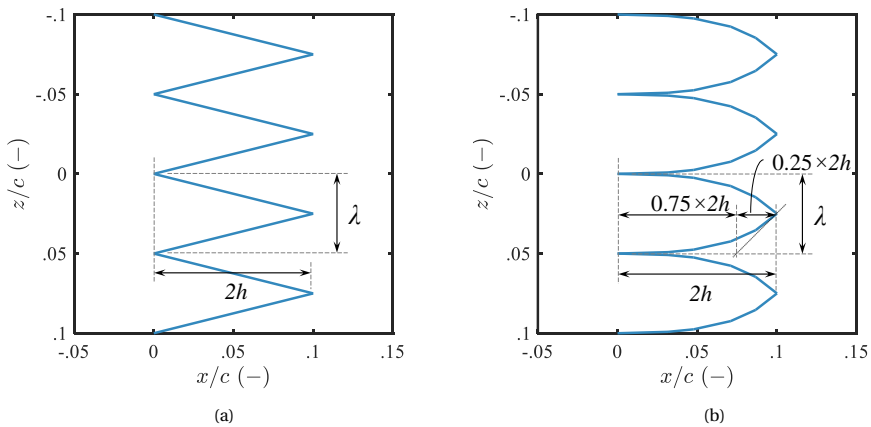
Figure 2.7: (a) Sawtooth serrations (b) Iron serrations.

Optimizing the serration shape design is still an ongoing research topic and the design possibilities seem endless. Many more sophisticated shapes have been proposed such as fractal shapes [142] and slitted serrations [140].

3

AIRFOIL MODELS, FLOW FACILITIES, AND FLOW MEASUREMENT TECHNIQUES[1]
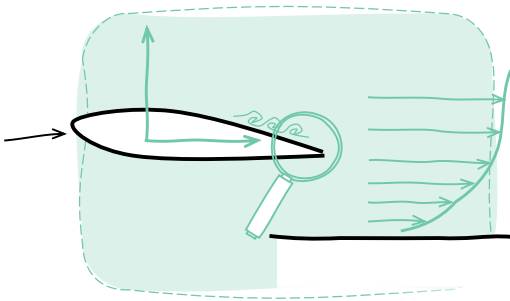
Wind-tunnel measurements featuring an airfoil, representing a wind-turbine blade section, are essential for research and development of wind-turbine blades and their noise reduction devices. In this thesis, two airfoil profiles are considered, namely the NACA 0018 and the NACA 63_3–018 profiles. The studies are conducted in two wind-tunnel facilities, covering a wide chord-based Reynolds number range. This chapter provides extensive descriptions of the airfoils and the wind-tunnel facilities. Aeroacoustic measurement techniques employed to assess boundary layer characteristics close to the trailing edge are described. Measurement techniques employed to assess aerodynamic coefficients, as well as necessary aerodynamic corrections, are discussed.

---

[1]Parts of this chapter will be published in the AIAA Journal. Please cite as shown in the list of peer-reviewed journal articles, number 6.

3.1. INTRODUCTION

Aerodynamic and acoustic testings in wind tunnels are essential steps for design and development of wind turbine blades [143] because they help to assess and predict the blades performance on a real wind turbine. A 2D airfoil with a cross-sectional profile representing that of a wind turbine blade is usually tested [144]. Correspondingly, for design and development of Trailing-Edge (TE) noise reduction technologies also involve wind-tunnel testing of such technology prototypes on the airfoil to assess their performance [41].

This chapter introduces airfoil models, wind-tunnel facilities, and flow measurement techniques employed for experimental TE noise studies in this thesis. The models, facilities, and measurement techniques are classified based on the following wind-tunnel facilities for tests in different chord-based Reynolds number Re_c ranges. In this chapter, the following terminologies are used:

- *A–Tunnel tests*: This refers to tests in the relatively lower Re_c range: $0.2 \times 10^6 \leq Re_c \leq 1 \times 10^6$, featuring two 0.2-m-chord airfoil models in the so-called *A–Tunnel*.

- *LTT tests*: This refers to tests in the relatively higher Re_c range: $1 \times 10^6 \leq Re_c \leq 3 \times 10^6$, featuring a 0.9-m-chord airfoil model in the so-called *Low Turbulence Tunnel* (LTT).

Details of the models and the wind-tunnel facilities are provided in the following subsections.

3.2. AIRFOIL MODELS

Airfoil profiles are used to represent a section of a wind-turbine blade. Two airfoil profiles are considered in this thesis, namely the NACA 0018 profile and NACA 63_3–018 profiles. Both airfoil profiles are symmetric and have the maximum thickness-to-chord ratio of 18 %. The profiles are shown in Fig. 3.1. Throughout this thesis, the following conventions are used: the x axis aligns with the direction along the chord, the y axis is normal to the chord, and the z axis is parallel to the span. The coordinate system originates from the TE at the midspan as shown in Fig. 3.1 and is normalized by the chord c.
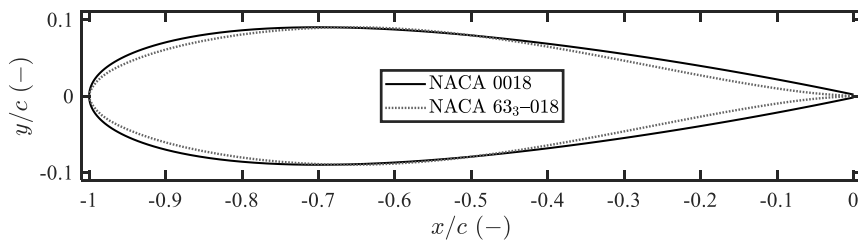

Figure 3.1: Airfoil profiles considered.

These airfoil profiles have well-characterized [145] and predictable [146, 147] aerodynamic characteristics. The symmetric geometry is advantageous for accurately setting

the zero-lift angle. Furthermore, these two NACA profiles belong to airfoil families that are commonly employed in wind-energy applications [144, 146].

3.2.1. AIRFOILS FOR THE A–TUNNEL (LOW-Re_c) TESTS

NACA 0018 AIRFOIL

The chord c of this NACA 0018 airfoil model is 200 mm and the span is two times the chord. The maximum thickness-to-chord ratio location is at $x/c = -0.661$ and the TE thickness is $1.5 \times 10^{-3} c$. The model was manufactured by computer-numerical-control machining of solid Aluminium blocks and comprises of three modular components: the suction side, the pressure side, and the interchangable TE insert. The interchangeable insert TE made up 20% of the chord (40 mm). A schematic of the model is shown in Fig 3.2a.

On the model surface, 30 pressure taps having a diameter of 0.4 mm are distributed. The pressure taps cover $-0.99 \le x/c \le -0.34$ on both sides of the airfoil. The pressure taps are distributed with a 15-degree angle with respect to the x axis to keep the flow over the downstream taps undisturbed by the flow pass the upstream ones. The pressure tap coordinates are provided in Appendix A.

It is worth mentioning that aerodynamic and acoustic measurements of this exact airfoil model have extensively been presented in many preceding studies such as in the work of Rubio–Carpio et al. [105].
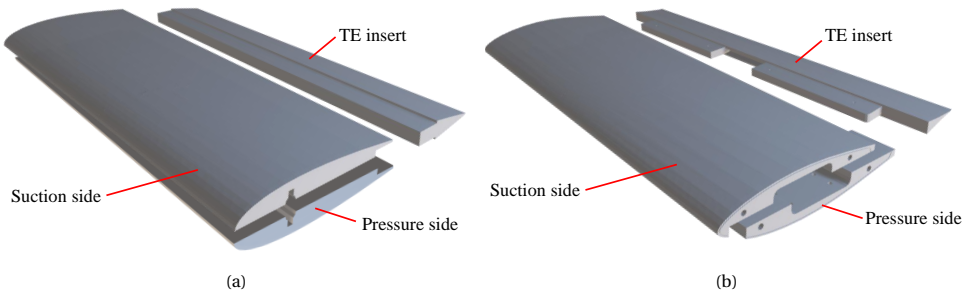
Figure 3.2: Components of the airfoil models for the A–Tunnel tests (a) NACA 0018 (b) NACA 63$_3$–018.

NACA 63$_3$–018 AIRFOIL

The chord and span of this airfoil model is identical to those of the NACA 0018 model. This model was also manufactured by the same method and is therefore modular. A schematic of the model is shown in Fig 3.2b. The maximum thickness-to-chord ratio location is at $x/c = -0.661$ and the TE thickness is $7.5 \times 10^{-4} c$. In addition to the baseline TE, 0.5-c-thick TE serrations can also be installed on this airfoil via dedicated TE serration clampers which replace the modular baseline TE insert (See Fig. 5.2).

On the model surface, 28 pressure taps having a diameter of 0.4 mm are distributed. The pressure taps cover $-0.98 \le x/c \le -0.175$ on the suction side and $-0.925 \le x/c \le$

−0.225 on the pressure side. For the same purpose as the NACA 0018 airfoil model, the pressure taps are distributed with a 15-degree angle with respect to the *x* axis. The pressure tap coordinates are provided in Appendix A.

Detailed wind-tunnel aerodynamic and acoustic measurement results of this airfoil model is presented in Chapter 5.

3.2.2. Airfoil the LTT (high-Re_c) tests

For the LTT tests, only the NACA 63_3–018 airfoil profile is considered. The model is the upscaled version of the aforementioned 63_3–018 airfoil with a chord $c = 900$ mm and a span $L = 2.22c$. The model was manufactured by *Deharde* using sheet metal skins covering rib and stringer structures [148], and is not modular.

There are multiple pressure tap rows on this model along the span. The main row is approximately in the middle of the span and comprises of 118 pressure taps covering the entire chord. The pressure tap coordinates for the main row are provided in Appendix A. The other pressure tap rows have fewer pressure taps and are useful for ensuring flow two-dimensionality over the airfoil. This topic is discussed in Section 3.4.2.

3.2.3. Forcing laminar-to-turbulent transition location

It is preferred trigger the transition at a specified chordwise rather than to let the transition occur naturally to ensure repeatability and comparibility of the results [149]. The transition was induced by a so-called *turbulator* which is a thin spanwise strip that adds roughness to the airfoil surface at a selected chordwise location. The roughness height was carefully selected based on the intended Re_c and angle of attack α ranges. The resulting turbulator selection and installation methods are specified in Table 3.1. Note that the dashed lines in the drawings indicate the chordwise location x/c where the turbulator strips were applied for both the suction and the pressure sides. For every test, effectiveness of the forced transition was verified by scanning a stethoscope probe (composed of a Brüel Kjær 4134 microphone and a Brüel Kjær 2619 pre-amplifier) downstream of the turbulator strip along the span. This stethoscope check also revealed that, when the turbulator was not applied, the boundary layer reaching the TE was also turbulent, whereas the transition occurred further downstream than where the turbulator would be applied.

3.3. Wind-tunnel facilities

3.3.1. A–Tunnel: $0.2 \times 10^6 \leq Re_c \leq 1 \times 10^6$

Facility descriptions

The A–Tunnel is an open-jet anechoic wind-tunnel facility of Delft University of Technology (TU Delft), where the jet is installed vertically within a room with acoustically absorbent foam wedges. A schematic of the A–Tunnel is presented in Fig. 3.3a. The cut-off frequency of the room is 200 Hz, and the room is characterized as *acoustically dead* according to the ISO 3382 standard [150]. Readers are referred to a paper of Merino–Martínez et al. [151] for further details on the A–Tunnel facility. Different velocity ranges

Table 3.1: Boundary layer forced-transition device parameters.

Airfoil model	Turbulator specifications		
	Transition element	Base tape	Drawing
NACA 0018 A–Tunnel tests ($c = 0.2$ m)	Randomly distributed 0.84-mm carborundum particles	Double-sided tape Thickness: 0.07 mm Width: 10 mm	
NACA 63_3–018 A–Tunnel tests ($c = 0.2$ m)	Glasfaser–Flugzeug– Service GmbH Zig-zag turbulator Thickness: 0.5 mm Width: 6 mm Angle: 70°	None	
NACA 63_3–018 LTT tests ($c = 0.9$ m)	Glasfaser–Flugzeug– Service GmbH Zig-zag turbulator Thickness: 0.4 mm Width: 12 mm Angle: 60°	Aerovac blue flash tape Thickness: 0.08 mm Width: 25.4 mm	
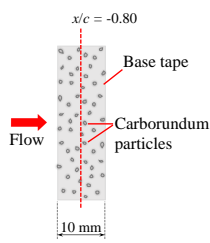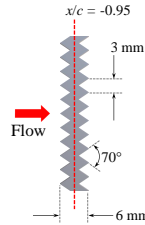
3
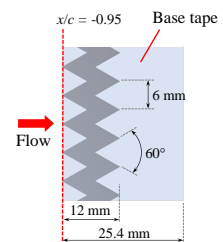
can be achieved by installing outlet nozzles of different contraction ratios. To achieve Re_c between 0.2×10^6 and 1.0×10^6, two nozzles were employed, namely nozzles with a rectangular opening of $y \times z = 3.5c \times 2c$ (700 × 400 mm) for $6 \times 10^4 \le Re_c \le 4.6 \times 10^5$, and $y \times z = 1.25c \times 2c$ (250 × 400 mm) for $3.9 \times 10^5 \le Re_c \le 1.0 \times 10^6$. For the whole range of flow speeds tested, the turbulence intensity of the free stream is below 0.15% [151].

AIRFOIL INSTALLATION

The airfoils were mounted between rectangular side plates, installed and centered downstream from the nozzle outlet (placed at $x = -2.9c$ for both nozzles tested). A photograph of the set up is shown in Fig. 3.4a. The test section is semi-open to allow for acoustic measurements. The angle of attack was controlled with a stepper motor with 0.001° precision, while the angle bias with respect to the floor was measured by a Wyler Clinotonic PLUS inclinometer with 0.01° precision. Due to the semi-open test section, the geometric and effective angles of attack are prone to deviate significantly at high lift conditions [152]. Corrections for the effective angle of attack based on the geometrical one are presented in Section 3.4.2.
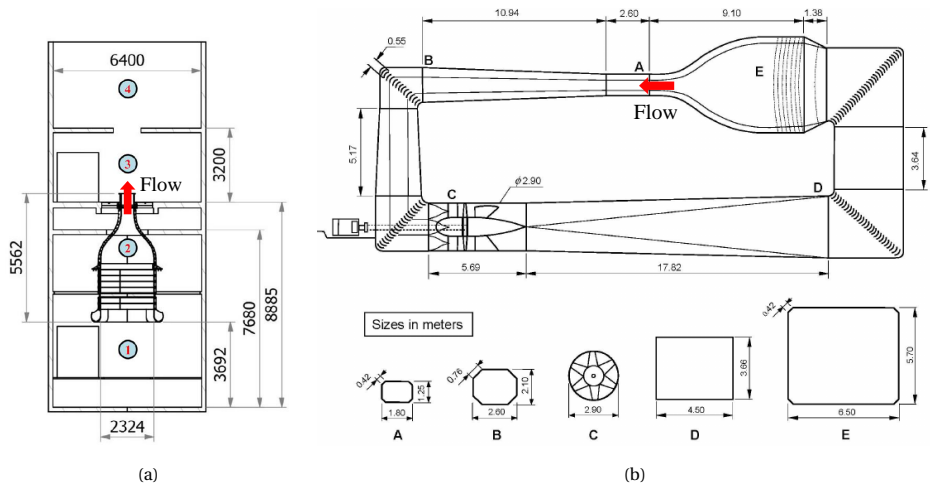
Figure 3.3: Schematics of the wind tunnels The arrow specifies the flow direction towards the location where the airfoil model is installed (a) A–Tunnel, the numbers label ① the settling chamber, ② the 3D-printed contraction, ③ the anechoic chamber, and ④ the fan and collector room (Scales in mm), reproduced from Merino–Martínez et al. [151] with permission from the corresponding author (b) LTT (Scales in m), reproduced from Timmer [147] with permission from the author.
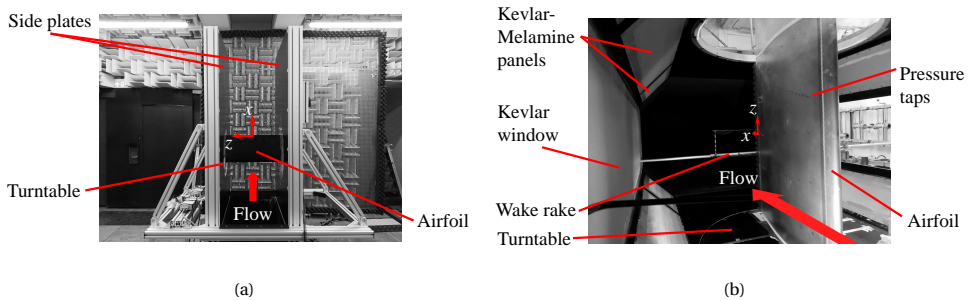
Figure 3.4: NACA 63_3–018 airfoil models installed in (a) the A-Tunnel and (b) the LTT.

3.3.2. LOW-TURBULENCE TUNNEL (LTT): $1 \times 10^6 \leq Re_c \leq 3 \times 10^6$

FACILITY DESCRIPTIONS

The Low-Turbulence Tunnel (LTT) facility of TU Delft is a closed-circuit wind tunnel with a contraction ratio of 17.8. In the free-stream envelope of the current study between 20 and 70 m/s, the turbulence intensity varies from 0.015% to 0.07% [144, 147]. A schematic of the LTT circuit is shown in Fig. 3.3b. The octagonal test section part of the circuit where the airfoil model is installed is exchangable. The test section has the width, height, and length of $2.00c$, $1.39c$, and $2.88c$, respectively. For aerodynamic and acoustic measurements in this thesis, a specially made test section where the wall panels were treated with Kevlar-covered melamine wedges to minimize acoustic reflections was used. An acoustically transparent Kevlar window [153] was installed on the side panel of the section where a

microphone array (see Section 4.2) was placed. The Aviation-standard Kevlar 49 T 965, with a thickness of 0.12 mm and a weight-to-area ratio of 61 g/m^2 [154] was used in combination with Foam S.T.O.P. open-cell anachoic chamber melamine wedges with a thickness between 7.6 and 15.2 cm, depending on available space. The background noise properties of the wind tunnel facility and the transmission loss of the Kevlar window are discussed in detail in Appendix B.

AIRFOIL INSTALLATION

The airfoil model was mounted on a built-in turntable on the test section. The airfoil span of 2.22c could not fully fit in the section as it was constrained by the test section height. The actual aspect ratio of the airfoil therefore became 1.39, with the remaining portion of the span outside the flow. Consequently, the main pressure tap row on the airfoil was positioned at a distance of approximately 1c above the floor. A photograph showing the airfoil installed in the LTT section is provided in Fig. 3.4b. Deviations of the measured surface pressure distribution due to the Kevlar and Melamine walls with respect to the hard-wall configuration [155] are carefully examined and discussed in Section 3.4.2.

3.4. FLOW MEASUREMENT TECHNIQUES

It has been shown in Chapter 2 that the far-field TBL–TE noise is governred by the TBL characteristics at the TE. Therefore, it is of high interest to collect TBL information close to the airfoil TE region for verifying, or even modeling, the TBL–TE noise. Flow measurement techniques employed for this purpose are described in Section 3.4.1.

Furthermore, static pressure distribution on the airfoil surface provides insights on the boundary layer evolution along the stream as well as information for calculating the lift coefficient. On the other hand, the drag coefficient can be calculated from the wake profile downstream of the airfoil. These aerodynamic, i.e. lift and drag, coefficients complement performance assessment of the TBL–TE noise reduction devices. This is because not only is the noise reduction crucial, it is also crucial for industrial applications that the aerodynamic performance of the airfoil should also remain as unaffected as possible. Aerodynamic coefficient measurements are described in Section 3.4.2.

3.4.1. TURBULENT BOUNDARY LAYER MEASUREMENTS

HOT-WIRE ANEMOMETRY

A single-sensor miniature wire probe model 55P15 (boundary-layer type) from Dantec Dynamics was used. The sensitive wire was made of platinum-plated tungsten having a length of 1.25 mm and a diameter of 5 μm. The probe was positioned at $x = -0.02c$ and $z = -0.3c$ and traversed in the $-y$ direction using a Zaber LRQ150HL–DE51T3 traverse controller with 0.15 μm accuracy. Conditioning of the sensor was carried out with a TSI IFA–300 CTA module and acquisition was performed with NI–9234 cards ($\pm$5 V, 24 bits resolution). Data were collected at 71 different points in the $-y$ direction, with more data points collected near the wall. Each acquisition point took 2 seconds using the sampling frequency of 51.2 kHz. The calibration used a fourth-order polynomial curve fitting of the output voltages [156] with data from 17 speed–voltage data points logarithmically spaced

between the lowest and the highest free-stream flow speed u_∞, which was measured upstream from the airfoil, i.e. close to the nozzle lip. The reference velocity information was taken from a Pitot tube installed near the hot-wire probe. The maximum deviation of the actual flow velocity from the flow velocity calculated from the calibrated speed–voltage curve was found to be below 0.2 m/s, or 0.58% of u_∞.

PARTICLE IMAGE VELOCIMETRY

The flow was seeded with SAFEX fog, and a laser sheet was created at $z = -0.04c$, i.e. close to the center of the span, using a Quantel EverGreen 200 (200 mJ, dual pulsed, 15 Hz) laser placed in the opposite wall from the microphone array. Two Imager sCMOS (5.5 MP, 16 bit, 50 fps) cameras were placed at the bottom of the test section, 0.8 m from the illuminated plane. The first camera was positioned along the TE line, to ensure the precision of the in-plane velocities (x– and y directions) while the second camera was fixed 20° in the upstream direction, to allow for stereoscopic PIV post-processing, obtaining the fluctuations of the velocity in the spanwise (z) direction [157]. Figure 3.5 illustrates the set up used for the measurements and Table 3.3 summarizes the set up employed and associated uncertainty for the measurement technique. The uncertainty mentioned in the table refers to the instantaneous velocity estimation. The averaging of the 1,000 uncorrelated velocity fields reduce the uncertainty to about 0.02% of u_∞. The velocity field was extracted on a field of $x \times y = 0.15c \times 0.06c$ centered with the TE. Measurements were carried out only for the forced transition configuration for all the Reynolds number for $\alpha_{\text{geom.}} = 0°$, and additionally $\pm 4°$ for $Re_c = 2 \times 10^6$.

Specifications	Set values
Number of images recorded	1,000
Numerical aperture	$f/11$
Digital image resolution (px/mm)	18
Maximum particle displacement (px)	15
Field of view ($x \times y$ mm)	150×100
Vector resolution (mm)	0.3
Uncertainty in instantaneous velocity (%u_∞)	0.7
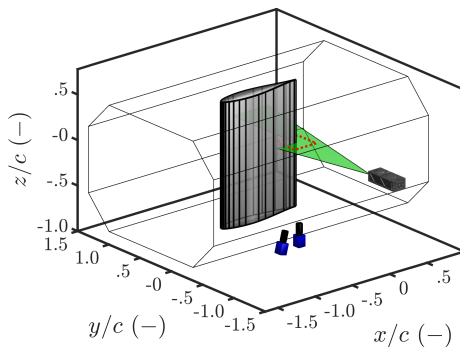
Figure 3.5: Schematics of the PIV set up used for characterizing the boundary layer properties over the NACA 63$_3$–018 airfoil model in the LTT.

Table 3.3: Main parameters of the PIV measurement technique used to capture the boundary-layer profile over the NACA 63$_3$–018 airfoil model in the LTT.

EXTRACTION OF THE BOUNDARY LAYER PARAMETERS

Having obtained the velocity profiles in the direction normal to the wall, the boundary-layer parameters were extracted, e.g. the edge velocity u_e, the TBL integral parameters, the displacement thickness δ^*, momentum thickness θ, and boundary layer thickness δ_{99}. The values of δ_{99} and u_e were obtained from the region where the spanwise vorticity

profile becomes constant [158]. The friction velocity u_τ was obtained from the fitting of the logarithmic layer, following the work of Clauser [159]. The fitting procedure results in an uncertainty of $1.5\% u_\tau$. The wake parameter Π was calculated based on Eq. (3.1) according to the work of Coles [160]:

$$2\Pi - \log(1 + \Pi) = \kappa \frac{u_e}{u_\tau} - \log\left(\frac{\delta^* u_e}{\nu}\right) - \kappa B - \log\kappa.$$
(3.1)

The implicit equation was solved with the Newton–Raphson method. In the equation, the Kármán constant κ and the parameter B have the values of 0.41 and 5, respectively, and ν is the kinematic viscosity.

3.4.2. Aerodynamic coefficient measurements

Static pressure taps for lift and effective angle of attack determination

For the A–Tunnel tests, pressure tap readings were done via Honeywell TruStability HSC-DRRN025MDAA3 differential pressure transducers of ±2.5 kPa range and 0.25% full-scale accuracy (±6 Pa). On the other hand, for the LTT tests, a DTC pressure system featuring 6 ESP–HD scanners with selected ranges for the application (Accuracy ±2 Pa) was used.

The lift coefficient c_l was computed from closed-line integral of the pressure coefficients c_p along the airfoil outline S, following Eq. (3.2):

$$c_l = \frac{\mathbf{n}_\alpha}{c} \cdot \oint_S c_p \mathbf{n}_S \mathrm{d}S,$$
(3.2)

where $\mathbf{n}_\alpha$ and $\mathbf{n}_S$ denote the unit vectors that are orthogonal to the airfoil angle of attack and to the airfoil surface, respectively.

For all of the airfoil models considered, determination of the effective zero-degree angle of attack, i.e. $\alpha = 0°$, is relatively simple, thanks to the symmetric geometry of the airfoil. The effective zero-degree angle was found by matching the pressure distribution on both sides of the model. However, non-zero geometrical angles of attack $\alpha_{\text{geom.}}$ may give $\alpha_{\text{eff.}}$ that deviate drastically from the geometrical one. This is due to the distortions of the jet direction by the airfoil circulation for the semi-open A–Tunnel, or due to the Kevlar–melamine walls for the LTT. These issues are investigated and necessary corrections are presented in the following.

For the A–Tunnel, it is assumed that the relationship between $\alpha_{\text{eff.}}$ and $\alpha_{\text{geom.}}$ is given by:

$$\alpha_{\text{eff.}} = K_B(\alpha_{\text{geom.}} + \epsilon),$$
(3.3)

where $0 < K_B < 1$ is a correction factor and ϵ is an angle offset. Brooks et al. [152] provided an analytical formula to determine the value of K_B based on the geometry of the experiment set up. The formula suggests $K_B = 0.681$ for this particular set up. To determine an exact value for this measurement, a direct search for a combination of K_B and ϵ that minimizes the Sum of Squared Error (SSE) between the actual pressure distribution and that predicted my XFOIL [101] is used. Data from pressure taps close to the leading edge (only upstream of the turbulator strip, in case it is present) at selected

$\alpha_{\text{geom.}}$ are used. The resulting K_B and ϵ for the 0.2-chord NACA 0018 and NACA 63_3–018 airfoils are summarized in Table 3.4.

Table 3.4: Test conditions used for determining $\alpha_{\text{eff.}}$, and resulting K_B and ϵ, for the A–Tunnel tests in the A–Tunnel.

Airfoil model	$\alpha_{\text{geom.}}$ (deg.)	Turbulator	K_B (-)	ϵ (deg.)
NACA 0018	≤10.5	Present	0.670	-0.23
NACA 63_3–018	±6	Absent	-0.670	0.00

It is notable that the resulting $K_B = 0.670$ is very close to the suggested value of 0.681. The negative sign for the NACA 63_3–018 is used to ensure consistency of the sign conventions with its upscaled counterpart in the LTT such that the pressure side of the airfoil always faces the microphone array when $\alpha_{\text{eff.}}$ is positive. Figures 3.6a and 3.6b show the pressure distributions at $\alpha_{\text{geom.}} = 6°$ at $Re_c = 4 \times 10^5$ compared to the pressure distribution predicted by XFOIL at the corresponding estimated $\alpha_{\text{eff.}}$ based on Eq. 3.3 for the NACA 0018 and NACA 63_3–018 airfoils, respectively.
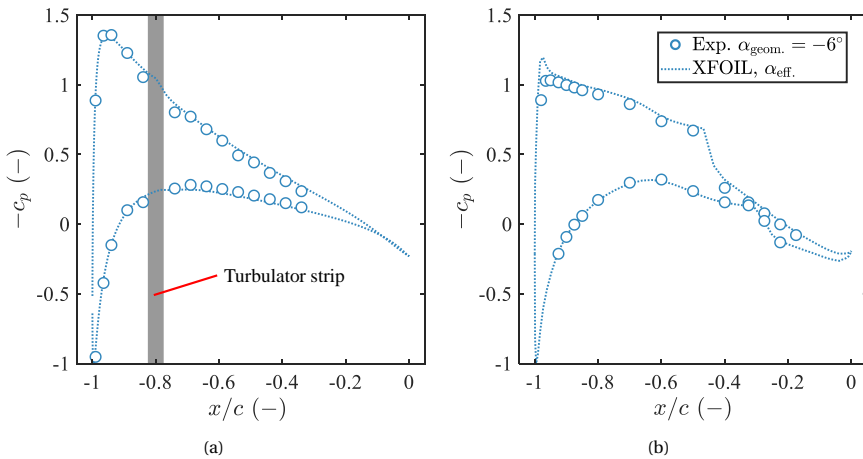
Figure 3.6: Measured pressure distributions at $\alpha_{\text{geom.}} = 6°$ and predicted pressure distributions using XFOIL at the corresponding effective angles of attack $\alpha_{\text{eff.}}$ based on the computed K_B and ϵ values over the (a) NACA 0018 and (b) NACA 63_3–018 airfoils.

For the LTT, the correction for the octagonal hard-wall test section can be found in the works of Timmer and Garner et al. [147, 161]. Aerodynamic measurements of the baseline NACA 63_3–018 airfoil were carried with both Kevlar and hard-wall configurations. Of major concern, while one side (the wall facing the suction side at positive angles of attack) of the test section was the Kevlar–Melamine panel with a solid back plate for the absorption of the acoustic waves, the opposite side (the wall facing the pressure side at positive angles of attack) was left with a single Kevlar panel in order to allow the microphone array measurements. This may cause asymmetry between the positive and negative angles of attack tested. Figure 3.7a shows the comparison of the c_p distributions and c_l polars

$\alpha_{\text{geom.}}$ (deg.)	$\alpha_{\text{eff.}}$ (deg.)
0.002	0.003
4.003	4.255
7.999	8.473

Table 3.5: Summary of $\alpha_{\text{geom.}}$ and their corresponding $\alpha_{\text{eff.}}$ considered in the high-Re_c LTT tests of the NACA 63_3–018 airfoil.

3

obtained in both test sections, and comparison against XFOIL predictions. From Fig. 3.7a where c_p distributions at $\alpha_{\text{eff.}} \approx \pm 8°$ are compared, a slightly smaller suction peak is captured with the Kevlar walls. The permeable walls of the Kevlar section leak air from the ambient room to the test section when the pressure difference is significant, consequently reducing the suction peak. The difference between positive and negative angles of attack is also shown. Using the hard walls as reference, the Kevlar walls cause a small decrease in the lift (c_l in Fig. 3.7b) for angles above $\alpha_{\text{eff.}} \approx 10°$ at the negative condition caused by the relatively lower suction peak. Observable difference in c_l can only be found at $\alpha_{\text{eff.}} < -10°$. Based on this observation, it is motivate to limit the angle range for further data analysis to $\alpha_{\text{geom.}} \leq 8°$. The considered $\alpha_{\text{geom.}}$ and their corresponding $\alpha_{\text{eff.}}$ are summarized in Table 3.5).
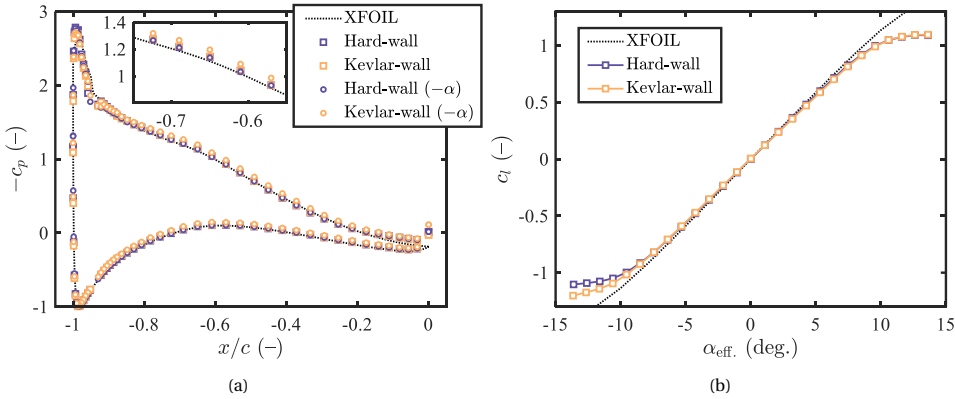
Figure 3.7: Aerodynamic coefficients of the 0.9-m-chord NACA 63_3–018 airfoil in the LTT test section with hard-wall and Kevlar-wall configurations at $Re_c = 3 \times 10^6$ compared to XFOIL predictions: (a) c_p for $\alpha_{\text{eff.}} \approx \pm 8°$ and (b) c_l polar.

Additionally, the two-dimensionality of the flow within the test section, both with the Kevlar and the solid walls, was also verified by comparing pressure distributions from the pressure taps at other spanwise locations to the main one. This comparison is shown in Fig. 3.8 for $\alpha_{\text{eff.}} \approx \pm 10°$ at the highest Re_c. At $\alpha_{\text{eff.}} \approx -10°$, the Kevlar window causes lower static pressures on the suction side relative to when the solid wall is used. This explains the relatively higher magnitude of c_l at large negative angles of attack seen previously in Fig. 3.7b. Notably, this trend is seen regardless of the spanwise location z measured. Therefore, variation of the c_p values along the span are lower than that caused by the difference between the solid and the Kevlar walls. This confirms the two-dimensionality of the flow in the LTT section within the angle of attack range of interest.
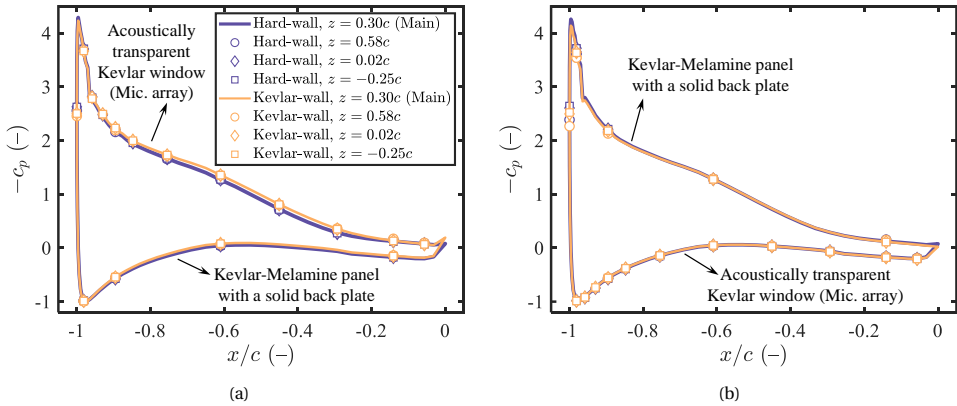
Figure 3.8: Comparison of c_p distribution obtained from multiple spanwise pressure tap rows on the baseline NACA 63_3–018 airfoil in the LTT test section with hard-wall and Kevlar-wall configurations at $Re_c = 3 \times 10^6$ for (a) $\alpha_{\text{eff.}} \approx 10°$ and (b) $\alpha_{\text{eff.}} \approx -10°$.

WAKE SURVEY TECHNIQUE FOR DRAG MEASUREMENT

A wake survey was performed using a wake rake placed downstream of the airfoil model to measure momentum deficits and thus extract the profile drag coefficients c_d [147, 162]. The wake rake set up differs slightly for the different tests, and are specified in Table 3.6. The pressure transducer systems for the wake rake were shared with the surface static pressure taps mentioned in the previous section. It is noteworthy that the wake rake was always absent during acoustic measurements.

Table 3.6: Specifications of the wake rake.

Airfoil model	Wake rake specifications				
	P. tap no. (static + total)	Min. p. tap spacing	Streamwise location	Width in z direction	Traverse in z direction?
NACA 0018 A–tunnel tests ($c = 0.2$ m)	50 + 12	3 mm	$x = 2c$	$1.1c$	Yes 0.5c range
NACA 63_3–018 A–tunnel tests ($c = 0.2$ m)	48 + 12	3 mm	$x = c$	$1.1c$	No
NACA 63_3–018 LTT tests ($c = 0.9$ m)	67 + 16	3 mm	$x = 0.67c$	$0.55c$	Yes 0.32c range

By assuming the incompressible flow and the Bernoulli theorem, the drag coefficient can be calculated by the method of Jones which requires the total and static pressure profiles in the wake [163]. Let c_p denote the pressure coefficients at the wake rake location, the subscripts s and t in $c_{p,s}$ and $c_{p,t}$ indicate that c_p is calculated from the measured

static and total pressures, respectively. The drag is then computed by the following integral across the wake [162–164]:

$$c_d = \frac{2}{c} \int_{\text{wake}} \sqrt{c_{p,t} - c_{p,s}} \left(1 - \sqrt{c_{p,t}}\right) \mathrm{d}y. \tag{3.4}$$

3

4

MICROPHONE ARRAY AND BEAMFORMING TECHNIQUES FOR ACOUSTIC MEASUREMENTS[1]
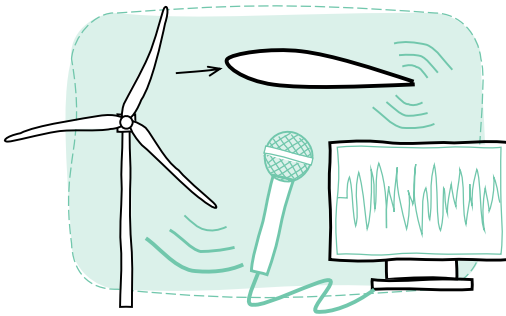
The added value of employing microphone arrays and acoustic beamforming techniques, compared to a single-microphone measurement, is the ability to localize and quantify relevant sound sources. In this thesis, microphone arrays and several acoustic beamforming techniques are employed for measuring trailing-edge noise of airfoil models in a wind tunnel, as well as for field measurements of noise from a real wind turbine. This chapter provides detailed descriptions of the microphone-array setups. Useful beamforming, i.e. post-processing, techniques as well as their applications and limitations are extensively discussed.

---

[1]Section 4.2.1 will be published in the AIAA Journal and parts of Section 4.3 have been published in the International Journal of Aeroacoustics. Please cite the aforementioned sections as shown in the list of peer-reviewed journal articles, number 6 and 3, respectively.

4.1. INTRODUCTION

Quantification of noise reduction provided by trailing-edge noise reduction technologies installed on real wind turbines and on a representative airfoil tested in wind tunnels could be done by a single microphone measurement [165, 166]. In fact, an international procedure for wind turbine noise certification such as that of the International Electrotechnical Commission (IEC61400) [167] employs a single-microphone measurement. However, microphone recording collects sound originated from every sound source in the measurement environment. This restricts researchers from gaining certainty and insights on the origin of the noise production and noise mitigation [138], which are crucial for accelerating understanding of noise production mechanisms and development of noise reduction technologies. For field measurements of a wind turbine, the recorded sound signal could be contaminated by irrelevant noise sources such as from nearby traffic. For wind-tunnel measurements, there are many possible irrelevant noise sources. For closed-section test section such as the LTT, the environment may not be ideal to represent free-field acoustic propagation. This is due to sound reflection from walls [168, 169] and other noise sources from the wind tunnel circuits [170]. Open-jet wind tunnels, such as the A–Tunnel, are designed primarily to minimize the aforementioned effects [171]. The walls are treated with acoustically absorbent foam wedges, and extra efforts are usually made to isolate noise from the wind-tunnel circuit [151]. However, even with good acoustic treatment, there are still unavoidable noise sources such as noise made by the flow leaving the nozzle [172], and the so-called *corner sources* [173] emanating from wall boundary layer interaction with the airfoil model.

To overcome the tendency for a single microphone measurement to record irrelevant sounds in the measurement environment, a microphone array is utilized instead to collect sound signal and the so-called *acoustic beamforming* technique is applied to help quantify the sound originated from a region of interest [174], e.g., for this thesis, the airfoil trailing edge in the wind tunnel and the blade tip on the wind turbine. This chapter explains further components of the microphone-array measurement and acoustic beamforming techniques employed. The chapter is divided in two main parts: description of the microphone array set ups, i.e. hardware, in Section 4.2 and description of various acoustic beamforming techniques, i.e. post-processing software in Section 4.3.

4.2. MICROPHONE ARRAY SET UPS

4.2.1. WIND-TUNNEL MEASUREMENTS OF AIRFOIL MODELS

Arrays of 64 microphones were used for both the low-Re_c tests in the A–Tunnel and the high-Re_c tests in the Low-Turbulence Tunnel (LTT) introduced in Section 3.1. On each array, the microphones were arranged in a scaled optimized multi-arm spiral configuration on a plane parallel to the airfoil planform when placed at zero-degree geometrical angle of attack. This multi-arm spiral microphone arrangement has been optimized to minimize the Maximum Sidelobe Level (MSL) and the Main Lobe Width (MLW), i.e. minimizing the spurious sources and maximizing the spatial resolution (See page 50). Details on this array design can be found in the work of Luesutthiviboon et al. [175]. The microphone specifications, array scaling, and positioning relative to the chord c of the airfoil models

are specified in Table 4.1 and illustrated in Figs. 4.1a and 4.1b for the A–Tunnel and the LTT, respectively. The microphone coordinates are provided in Appendix A.
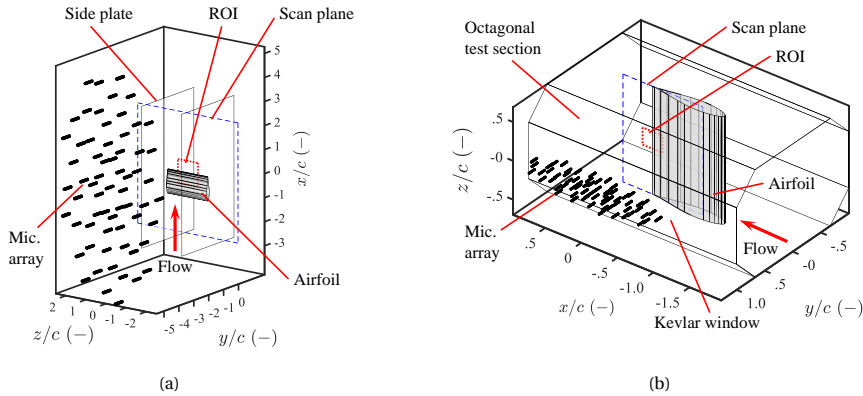
Figure 4.1: Microphone arrays for noise measurements of an airfoil in wind tunnels (a) A–Tunnel and (b) LTT.

Table 4.1: Specifications of the microphone array and the position with respect to the airfoil models.

Specifications	Wind-tunnel facilities and airfoil chords	
	A–Tunnel $c = 200$ mm	LTT $c = 900$ mm
Array width and height in $x \times z$	$10c \times 5c$	$1.75c \times 0.45c$
Array plane y location	$-5.00c$	$1.16c$
Microphone model	G.R.A.S. 40PH	PUI AUDIO 665–POM–2735P–R
Measurement uncertainty (reconstructed spectra from 50 to 5,000 Hz)	± 1 dB	± 2 dB

The microphones for both arrays were calibrated using a G.R.A.S. 42AA Pistonphone with a reference frequency of 250 Hz and a Sound Pressure Level (SPL) of 114 dB. It is worth highlighting that, for the closed-section high-Re_c tests in the LTT, the microphone array was placed behind a stretched Kevlar window (See Fig. 3.4b). Extra transmission correction and background noise level examination are essential for this particular set up and are discussed in Appendix B.

4.2.2. FIELD MEASUREMENT OF A WIND TURBINE

Field measurements were performed to quantify noise emission from an actual wind turbine and to assess performance of a trailing-edge noise reduction device prototype. For this purpose, a 4 m × 4 m array of 64 microphones was placed upwind of a wind turbine of interest (shown later in a schematic in Fig. 4.6, Section 4.3.6). This array is an assembly of 16 1 m × 1 m wooden plates covered by 1.5-cm-thick flamex GU foam.

For this array, the microphones are arranged in the so-called Underbrink multi-arm spiral configuration [176, 177] containing 8 spiral arms and 8 microphones per arm. The microphone specification is identical to that used in the high-Re_c tests in the LTT (See Table 4.1). In addition to acoustic data aquisition, a synchronized Datavision UI–1220 LE optical camera with Kowa LM4NCL lens placed in the center of the array was used to collect optical data with a frame rate of 48 Hz and a resolution of 480 × 752 pixels.

4.3. BEAMFORMING TECHNIQUES

4.3.1. CONVENTIONAL FREQUENCY DOMAIN BEAMFORMING (CFDBF)

Conventional Frequency-Domain Beamforming (CFDBF) [178, 179] is a very popular method, since it is robust, fast, and intuitive. CFDBF is a basis for other advanced beamforming techniques introduced in the subsequent sections.

Relative to a planar array of N microphones, a scan plane is defined as a set of grid points on a parallel plane. A schematic is shown in Fig. 4.2. With a predefined scan grid, the CFDBF method works by assuming a possible sound source at each scan grid point and determining its power.
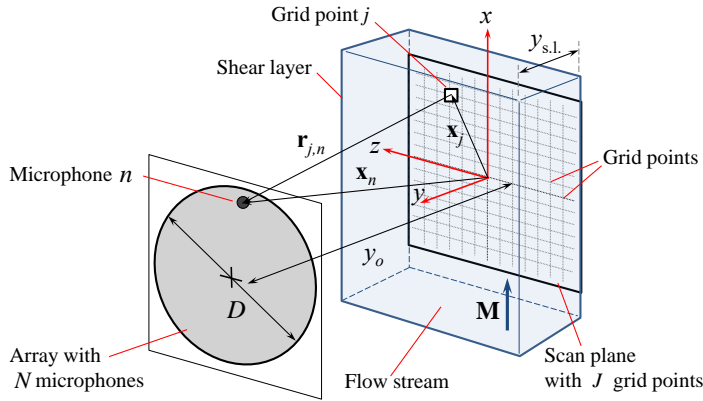
Figure 4.2: Schematic of an acoustic array depicted as a circular disc with aperture D and a scan plane at a distance h away having J grid points. The array consists of N microphones.

Let $\mathbf{p}_{\text{meas.}} \in \mathbb{C}^{N \times 1}$ be a vector consisting of the Fourier transforms of the measured microphone time signals, the $N \times N$ measured *Cross-Spectral Matrix* (CSM), $\mathbf{C}_{\text{meas.}}$, is calculated as

$$\mathbf{C}_{\text{meas.}} = E[\mathbf{p}_{\text{meas.}} \mathbf{p}_{\text{meas.}}^*], \tag{4.1}$$

where $E[*]$ is the ensemble average of snapshots and $(\cdot)^*$ the complex conjugate transpose. The CSM $\mathbf{C}_{\text{meas.}}$ is thus calculated by averaging a large number of Fourier-transformed sample blocks.

To perform beamforming, use is made of steering vectors $\mathbf{g}_j \in \mathbb{C}^{N \times 1}$, which are the modeled complex pressure amplitudes at the microphone locations for a sound source

with unit strength at a given grid point [180]. There are several steering vector formulations in the literature [181], but commonly, the omnidirectional monopole representation is used from the Green's function of the Helmholtz equation.

For this thesis, a case of sound sources in a flow stream is often encountered, e.g. beamforming of trailing-edge noise from an airfoil in a wind tunnel. Let the scan plane in Fig. 4.2 lie within a flow stream with a Mach number vector $\mathbf{M} = [M_x, M_y, M_z]$, for microphone n and grid point j located at $\mathbf{x}_n = [x_n, y_n, z_n]$ and $\mathbf{x}_j = [x_j, y_j, z_j]$, respectively, a component of the vector $\mathbf{g}_j$ reads

$$g_{j,n} = \frac{\exp\left(-2\pi \mathrm{i} f \Delta t_e\right)}{\sqrt{(\mathbf{M} \cdot \mathbf{r}_{j,n})^2 + \beta^2 \|\mathbf{r}_{j,n}\|^2}}, \tag{4.2}$$

where f is the frequency of the sound source, i is the imaginary unit, $\beta = \sqrt{1 - \|\mathbf{M}\|^2}$, and $\mathbf{r}_{j,n} = \mathbf{x}_n - \mathbf{x}_j$ is the distance between grid point j and microphone n. The emission time delay Δt_e is

$$\Delta t_e = \frac{-\mathbf{M} \cdot \mathbf{r}_{j,n} + \sqrt{(\mathbf{M} \cdot \mathbf{r}_{j,n})^2 + \beta^2 \|\mathbf{r}_{j,n}\|^2}}{c_0 \beta^2}, \tag{4.3}$$

where c_0 is the speed of sound.

For some scenarios, only part of the sound ray is within the flow stream. A shear layer is the interface between the moving medium and the still medium. Let the distance $y_{\mathrm{s.l.}}$ denote the distance from the scan plane to the shear layer as shown in Fig. 4.2. Because the scan plane and the microphone array plane are parallel, $|y_n - y_j| = y_o$ is a constant. For beamforming in wind tunnels in this thesis, $\mathbf{M}$ is either $[M, 0, 0]$ or $[0, 0, M]$. To account for the shear layer, M is replaced by $M_{\mathrm{corr.}}$:

$$M_{\mathrm{corr.}} = \frac{y_{\mathrm{s.l.}}}{y_o} M. \tag{4.4}$$

Equation (4.4) provides a rather simple correction for the presence of the shear layer, compared to the more complex approaches such as Amiet's approach [182]. However, based on beamforming simulations, Sijtsma [180] found that the difference between this simple correction and the complex approaches is infinitesimal for $M \leq 0.25$ and the angle between the shear layer and the sound ray $\geq 45°$, which is the case for the scope of this thesis.

It is worth noting that, when the flow is absent, i.e. $\mathbf{M} = \mathbf{0}$, Eq. (4.2) simplifies to

$$g_{j,n} = \frac{1}{\|\mathbf{r}_{j,n}\|} \exp\left(\frac{-2\pi \mathrm{i} f \|\mathbf{r}_{j,n}\|}{c_0}\right). \tag{4.5}$$

The estimated source power $\tilde{A}$ at grid point j is then given by CFDBF:

$$\tilde{A}_j = \mathbf{w}_j^* \mathbf{C}_{\mathrm{meas.}} \mathbf{w}_j, \tag{4.6}$$

where $\mathbf{w}_j$ is the weight vector [180] given by

$$\mathbf{w}_j = \frac{\mathbf{g}_j}{\|\mathbf{g}_j\|^2}. \tag{4.7}$$

Finally, to obtain a source map, Eq. (4.6) is applied to every of grid point. Finally, the SPL at grid point j SPL$_j$ is calculated by

$$\text{SPL}_j = 20\log_{10}\frac{\tilde{A}_j}{p_0}\ \text{dB}, \tag{4.8}$$

where $p_0 = 2 \times 10^{-5}$ Pa.

4

RESOLUTION LIMIT, POINT SPREAD FUNCTION, AND SIDELOBES

For CFDBF, the spatial resolution in the source map, given by an acoustic array, is limited by the Rayleigh resolution limit. Assuming plane-wave propagation, the Rayleigh resolution limit is given by

$$\Delta \ell \approx 1.22 y_o \frac{c_0}{fD} = 1.22 y_o \frac{\lambda}{D}, \tag{4.9}$$

meaning that two sources with a distance less than $\Delta \ell$ cannot be resolved. From Eq. (4.9), it can be derived that the spatial resolution depends on the ratio between the acoustic wavelength λ and the array aperture D, as well as the distance to the scan plane y_o. Equation (4.9) shows that $\Delta \ell$ varies inversely with f.

Apart from the Rayleigh resolution limit, the result of CFDBF is limited by high sidelobe levels, especially at high frequencies. Consequences are that weaker secondary sound sources can be masked by sidelobes of dominant sources. The sidelobe pattern of a source is represented by the Point Spread Function (PSF) of the microphone array, inherent to any imaging system.

For the present microphone array setups for airfoil noise measurements in the wind tunnels shown in Figs. 4.1a and 4.1b, the PSFs of a simulated point source placed at the middle of the airfoil trailing edge, i.e. coordinate origin, are provided in Figs. 4.3a and 4.3b, respectively. The selected frequency range is a 1/3-octave frequency band centered at 1 kHz. These figures therefore represent the idealistic case of source maps for acoustic beamforming in wind-tunnel where no other sound sources is present and can be compared to the more realistic source maps presented later in this thesis such as Fig. 6.11 in Chapter 6. From the figures, qualitative assessments of the resolution and the tendency of sidelobe misinterpretation can be done. For both arrays, this point source appears as an elliptical main lobe in the PSF. This is due to the elliptical-shaped microphone array. The resolution is therefore unequal between the x and z directions [See Eq. (4.9)]. For both setups, the resolution is higher in the streamwise direction than in the spanwise direction. However, the source is axis-symmetric with respect to the x and z axes. The major axis of the elliptical main lobe aligns with the airfoil trailing-edge. It is noteworthy that, at this frequency, the MSL is much lower (-15 dB) compared to the main lobe.
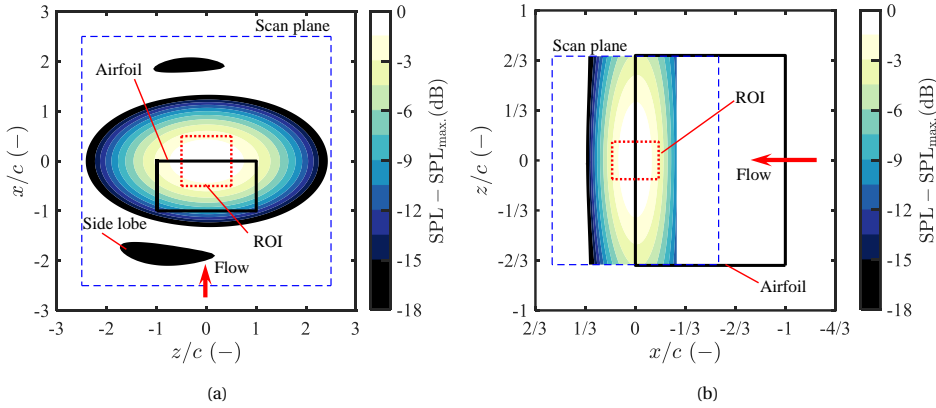
Figure 4.3: PSFs of a simulated point source placed at the origin (airfoil trailing edge center) for a 1/3-octave frequency band centered at 1 kHz for the (a) A–Tunnel set up and (b) LTT set up.

4.3.2. CLEAN-SC

Knowledge of the PSF allows correction of the image by deconvolution. A common deconvolution method in acoustic imaging is CLEAN-SC [183]. This method is based on the CLEAN method used in astronomy [184], where deconvolution is performed by assuming the measurement to be exactly proportional to $\mathbf{g}$. CLEAN-SC finds the so-called source components $\mathbf{h}$ which more closely resemble the measured data contained in $\mathbf{p}_{\text{meas.}}$, using the fact that sidelobes are *spatially coherent* with the main lobe. Both techniques are iterative procedures where source contributions are removed at each step from the CSM and replaced with clean beams in the source map.

In CLEAN-SC, the measured CSM is decomposed as follows:

$$\mathbf{C}_{\text{meas.}} = \sum_{k=1}^{N_S} \mathbf{p}_k \mathbf{p}_k^* + \mathbf{C}_{\text{degraded}}, \tag{4.10}$$

meaning that the measured CSM consists of two parts. The first part represents the contribution of N_S incoherent sound sources. The second part, $\mathbf{C}_{\text{degraded}}$, represents the remaining part in $\mathbf{C}_{\text{meas.}}$, where the source information is not (yet) extracted. Herein, $\mathbf{p}_k$ are the N–dimensional acoustic *source vectors* representing the Fourier components of the signals from the kth source. The assumption of Eq. (4.10) is valid under the following conditions:

- All sound sources present are incoherent.

- The CSM is calculated from a large number of time blocks, so that the ensemble averages of the cross-products $\mathbf{p}_k \mathbf{p}_l^*$, $k \neq l$, can be neglected.

- There is no decorrelation of signals from the same source between different microphones (e.g. due to sound propagation through turbulence).

- There is no additional incoherent noise.

Let the highest power $\tilde{A}_s$ be noted by grid point $s = \mathrm{argmax}_j(\tilde{A}_j)$ with the corresponding weight vector $\mathbf{w}_s$, the source power at any grid point j is spatially coherent with this source power peak [183], or

$$\mathbf{w}_j^* \mathbf{C}_{\text{meas.}} \mathbf{w}_s = \mathbf{w}_j^* \left[\sum_{k=1}^{N_S} \mathbf{p}_k \mathbf{p}_k^* + \mathbf{C}_{\text{degraded}} \right] \mathbf{w}_s. \tag{4.11}$$

At the first iteration step of CLEAN-SC, the exact number of sources N_S is not yet known, and all information is still contained in $\mathbf{C}_{\text{meas.}}$, i.e. $\mathbf{C}_{\text{meas.}} = \mathbf{C}_{\text{degraded}}$. The CLEAN-SC algorithm extracts the constituting source information from $\mathbf{C}_{\text{meas.}}$ and transfers it to the first term on the right hand side of Eq. (4.10). To achieve this, CLEAN-SC starts with the result of CFDBF from Eq. (4.6), focusing at the grid point s where the strongest source is identified as

$$\tilde{A}_s = \mathbf{w}_s^* \mathbf{C}_{\text{meas.}} \mathbf{w}_s = \mathbf{w}_s^* \left[\sum_{k=1}^{N_S} \mathbf{p}_k \mathbf{p}_k^* + \mathbf{C}_{\text{degraded}} \right] \mathbf{w}_s. \tag{4.12}$$

By using the the CSM decomposition assumption introduced in Eq. (4.10) and expanding the summation term on the right hand side of Eq. (4.12), assuming that $\mathbf{C}_{\text{degraded}}$ is small compared to the part resulting from the contribution of the N_S incoherent sound sources, i.e. $\mathbf{C}_{\text{meas.}} \approx \sum_{k=1}^{N_S} \mathbf{p}_k \mathbf{p}_k^*$, we have

$$\mathbf{C}_{\text{meas.}} \mathbf{w}_s \approx (\mathbf{p}_1^* \mathbf{w}_s) \mathbf{p}_1 + \sum_{k=2}^{N_S} (\mathbf{p}_k^* \mathbf{w}_s) \mathbf{p}_k. \tag{4.13}$$

At $j = s$, it can further be assumed that the second term on the right hand side of Eq. (4.13), i.e. the contribution from the other sources, is small compared to the first term, and an approximation can be made:

$$\mathbf{C}_{\text{meas.}} \mathbf{w}_s \approx (\mathbf{p}_1^* \mathbf{w}_s) \mathbf{p}_1. \tag{4.14}$$

In the same manner:

$$\tilde{A}_s \approx |\mathbf{p}_1^* \mathbf{w}_s|^2 + \sum_{k=2}^{N_S} |\mathbf{p}_k^* \mathbf{w}_s|^2 \approx |\mathbf{p}_1^* \mathbf{w}_s|^2. \tag{4.15}$$

Dividing Eq. (4.14) by $|\mathbf{p}_1^* \mathbf{w}_s|^2$ yields

$$\frac{\mathbf{C}_{\text{meas.}} \mathbf{w}_s}{|\mathbf{p}_1^* \mathbf{w}_s|^2} \approx \frac{\mathbf{p}_1}{|\mathbf{p}_1^* \mathbf{w}_s|} \equiv \mathbf{h}_s, \tag{4.16}$$

assuming that the phase of $\mathbf{p}_1^* \mathbf{w}_s$ is irrelevant, and can be written as $|\mathbf{p}_1^* \mathbf{w}_s|$. The so-called *source component*, $\mathbf{h}_s$, representing the identified source's contribution in the measured CSM is now defined. This contribution is to be removed from the measured CSM before proceeding to the next iteration. Equation (4.15) assumes that the source power at $j = s$ is approximately only the result of one source $k = 1$. However, there is also a small contribution from the other unidentified sources at $j = s$ [185]. Therefore, a safety

factor is used to account for their contributions. This is the so-called *loop gain* [183], Φ. As an extension to Eq. (4.15), we define

$$|\mathbf{p}_1^* \mathbf{w}_s|^2 = \Phi \tilde{A}_s. \tag{4.17}$$

The loop gain $0 < \Phi \leq 1$ indicates to which extent we assume the source power at grid point s to contain the influence of the identified source $k = 1$. For example, $\Phi = 0.99$ means that 99% of source power results from the identified source.

Finally, the influence of the source is taken away from the measured CSM by

$$\mathbf{C}_{\text{degraded}} = \mathbf{C}_{\text{meas.}} - \mathbf{p}_1 \mathbf{p}_1^* = \mathbf{C}_{\text{meas.}} - |\mathbf{p}_1^* \mathbf{w}_s|^2 \mathbf{h}_s \mathbf{h}_s^* = \mathbf{C}_{\text{meas.}} - \Phi \tilde{A}_s \mathbf{h}_s \mathbf{h}_s^*, \tag{4.18}$$

yielding $\mathbf{C}_{\text{degraded}}$ which replaces $\mathbf{C}_{\text{meas.}}$ in the next iteration. First, $\mathbf{C}_{\text{degraded}}$ replaces $\mathbf{C}_{\text{meas.}}$ in Eq. (4.6) to identify the next source, i.e. the grid point with the source peak. Then the CLEAN-SC process is repeated.

The stopping criterion for CLEAN-SC is when $\mathbf{C}_{\text{degraded}}$ is *empty* after the source components for all incoherent sources have been taken away. In other words, its norm should be sufficiently small compared to the original CSM: $\|\mathbf{C}_{\text{degraded}}\| < \varepsilon \|\mathbf{C}_{\text{meas.}}\|$, where ε is a small constant usually taken as 0.01 [183, 185].

At this point, the exact number of sources N_S is known. Let the set $\mathbb{S}$ contain the indices of grid points where the sources are identified by CLEAN-SC such that $s \in \mathbb{S}$ and $|\mathbb{S}| = N_S$, the new source map is obtained by the summation of all the clean beams from the N_S identified sources and the remaining degraded CSM as

$$\tilde{A}_j = \sum_{k' \in \mathbb{S}} \Phi \tilde{A}_{k'} 10^{-b d_{j,k'}^2} + \mathbf{w}_j^* \mathbf{C}_{\text{degraded}} \mathbf{w}_j. \tag{4.19}$$

where b is the clean beam shape parameter and $d_{j,k'}$ the distance from grid point j to the identified source location at grid point k'.

The CLEAN-SC method results in the improvement of both the MLW and the MSL in the source map. The MSL is lowered by the elimination of sidelobes which are spatially coherent to the main lobe, improving the dynamic range. The MLW is controlled by b and selected by the user. Selection of b can only provide smaller beam widths for aesthetic purpose, yet it does not provide spatial resolution beyond the Rayleigh resolution limit given in Eq. (4.9). For sources which are spaced closer than this limit, CLEAN-SC locates the source marker in between.

4.3.3. HR-CLEAN-SC

Having applied CLEAN-SC, the exact value for the number of sources N_S is determined. The source locations are marked where their peaks are. For HR-CLEAN-SC, the source markers given by CLEAN-SC are relocated such that the relative contribution of the other $(N_S - 1)$ sources is minimal [185]. The new source marker location which matches this requirement for a given source originally marked at s is determined by searching for m which minimizes the cost function as [185]

$$m = \operatorname{argmin}_j \left\{ F(\mathbf{u}_j) = \frac{\| \sum_{k' \in \mathbb{S}, k' \neq s} (\mathbf{g}_{k'}^* \mathbf{u}_j) \mathbf{g}_{k'} \|^2}{|\mathbf{g}_j^* \mathbf{u}_j|^2 \|\mathbf{g}_j\|^2} \right\}. \tag{4.20}$$

With this, the original weight vector $\mathbf{w}_s$ is replaced by $\mathbf{u}_m$, where m associates with a grid point index where the new source marker is to be placed. At this grid point, the total relative contribution of the other sources located at $k' \in S$, $k' \neq s$ is minimized.

The choices for the marker location are restricted to a predefined set of J grid points representing the scan plane. Therefore, employing the brute force approach, i.e. evaluating Eq. (4.20) for all J grid points, is sufficient to determine $\mathbf{u}_m$ in a short time.

The corresponding source component for the new marker $\mathbf{u}_m$ then becomes

$$\mathbf{h}_m = \frac{\mathbf{C}_{\text{meas.}}\mathbf{u}_m}{\mathbf{u}_m^*\mathbf{C}_{\text{meas.}}\mathbf{u}_m}. \tag{4.21}$$

The corresponding source power estimates for the remaining grid points are calculated by varying $\mathbf{w}_j^*$ to cover the entire scan plane as

$$\tilde{A}_j = (\mathbf{u}_m^*\mathbf{C}_{\text{meas.}}\mathbf{u}_m)|\mathbf{w}_j^*\mathbf{h}_m|^2. \tag{4.22}$$

For this map, the maximum $\tilde{A}_s$ is determined in the same manner as shown previously, $s = \text{argmax}_j(\tilde{A}_j)$, where $j = s$ represents the *actual* location of the source. It is important to highlight that, for HR-CLEAN-SC, it is possible that $m \neq s$, meaning that the source markers are not necessarily at the source's peak.

For the next source, $\mathbf{C}_{\text{meas.}}$ is replaced by $\mathbf{C}_{\text{degraded}}$ calculated as in Eq. (4.18). Then the process from Eq. (4.20) to (4.22) is repeated for all the remaining sources found in CLEAN-SC until all marker locations and actual source locations do not change anymore, or the maximum number of iterations is reached [185]. Finally, the source map is computed using Eq. (4.19).

To avoid division by zero in Eq. (4.20), a constraint has to be set for any arbitrary source marker $\mathbf{u}_j$ as

$$|\mathbf{g}_j^*\mathbf{u}_j|^2 \geq \eta > 0. \tag{4.23}$$

The parameter η will be the source marker constraint of the minimization problem in Eq. (4.20) and limits how far the source marker is allowed to move from the main lobe's peak. It is desirable to stay on the main lobe as actual sources might have different PSFs [183]. Therefore, η should be larger than the MSL. In the work of Sijtsma et al. [185], no improvement in resolution was found for η below 0.25 for the acoustic array configuration used. Therefore, a constant $\eta = 0.25$ was taken, which is equivalent to $10\log_{10}0.25 \approx -6$ dB relative to the main lobe's peak [185].

Figure 4.4 schematically illustrates the aforementioned concepts of the HR-CLEAN-SC algorithm. Supposing that there are two closely-spaced sound sources placed at a distance d apart, which is lower than the Rayleigh resolution limit ($d < \Delta\ell$), these two sources are represented by PSF 1 and 2. Figure 4.4 shows the resolved two sources with the alternated source marker locations at the final iteration of HR-CLEAN-SC. For PSF 1, the source marker is shifted to the grid point where the influence of PSF 2 is minimized, according to Eq. (4.20). The same applies for the source marker of PSF 2. In HR-CLEAN-SC, the source marker is allowed to shift within the source marker constraint η defined in Eq. (4.23).
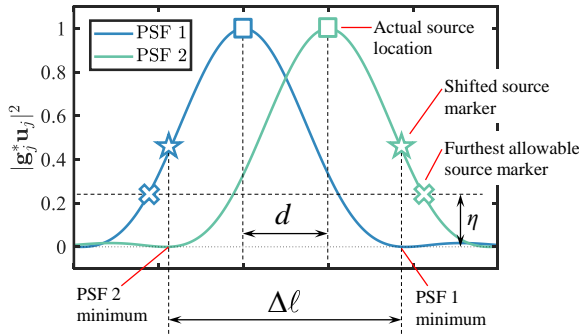
Figure 4.4: Schematic of two closely-spaced sound sources resolved by HR-CLEAN-SC after the source markers have been shifted. The source marker constraint η is also shown.

4.3.4. Enhanced HR-CLEAN-SC

As mentioned in the previous section, the parameter η should be larger than the MSL, which strongly depends on the sound frequency considered f and the acoustic array design. Hence, an Enhanced version of HR-CLEAN-SC[2] was recently proposed [175] in order to benefit from the usage of acoustic arrays with low MSL at low frequencies, where η varies per frequency as

$$\eta(f) = 10^{\text{MSL}(f)/10}. \tag{4.24}$$

Thus, for a finite predefined scan grid, $\text{MSL}(f) < 0$ is calculated for each frequency of interest as the relative level in dB between the main lobe's peak and the maximum sidelobe's peak. As an example, the obtained adaptive values of $\eta(f)$ for a range of frequencies, and for the Underbrink microphone array and the optimized array design used in this thesis are presented in Fig. 4.5 to illustrate the exploitation of the optimized array design on the freedom of selecting η. Additionally, the constant value of $\eta = 0.25$ used by Sijtsma et al. [185] and $\eta(f)$ assuming that the MSL increases linearly with frequency [175] are also presented.

The different side lobe levels make η differ between different arrays. Good agreement can be seen between the values of η determined by the actual MSLs and the approximated values of η based on the assumed MSLs in previous research [175]. Additionally, slightly lower values of η are allowed for the optimized array. It can be seen that η is almost constant for the optimized array from 400 to 2000 Hz. This is due to the low-sidelobe design of the optimized array [175]. Nevertheless, the values of η used by both arrays at higher frequencies are comparable. It is also notable that when the frequency is low, i.e. $f \leq 300$ Hz, the value of adaptive η increases up of more than 0.3. This is because only the main lobe dominates the scan area at low frequency. In this case, the source marker can be moved to any grid point.

In practice, evaluating the PSF per frequency is performed as a part of the HR-CLEAN-SC algorithm where the term $|\mathbf{g}_j^*\mathbf{u}_j|^2$, representing the PSF, is evaluated for all J grid points. Therefore, evaluating the exact value of MSL from the already-existing PSF hardly incurs

---

[2]The method was called *Adaptive* HR-CLEAN-SC in the previous study [175].
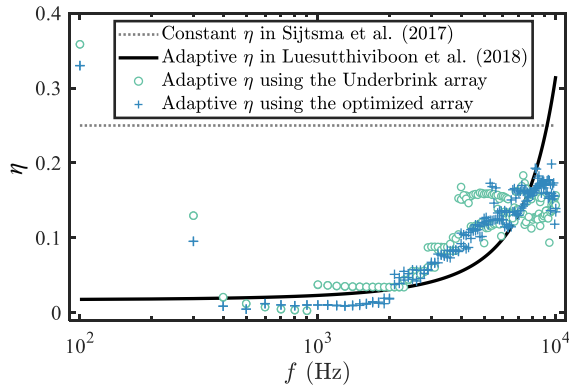
Figure 4.5: Value of η used in the Enhanced HR-CLEAN-SC algorithm versus frequency to resolve two closely-spaced sound sources from synthesized data using the Underbrink and optimized arrays, compared with $\eta = 0.25$ in the HR-CLEAN-SC algorithm [185] and the adaptive η based on the assumed MSL [175].

additional computation time compared to HR-CLEAN-SC. Therefore, it is recommended to derive η from the exact MSLs. However, in case very wide frequency ranges or very fine grids are required, the MSL per frequency can be approximated by empirical formulae [186] to ease the computational effort.

Performances of the HR CLEAN-SC beamforming method as well as the and enhanced version of it have extensively been assessed in the work of Luesutthiviboon et al. [187] using both simulated closely spaced point sound sources, and speakers in a real experiment. The ability of the HR-CLEAN-SC method in resolving sound sources placed closer than the Rayleigh's resolution limit, i.e. super resolution, has been demonstrated. The 'enhanced' performance when the adaptive η together with an optimized array design are used has been shown. This added benefit has also been demonstrated for beamforming using a spherical microphone array in the work of Zhu et al. [188]. Recently, Merino–Martínez et al. [189] also assessed performance of the Enhanced HR-CLEAN-SC beamforming for more diverse experimental cases, including the airfoil trailing-edge noise measurement. It has been shown that, for closely-spaced point sources, deconvolution beamforming techniques such as the Enhanced HR-CLEAN-SC techniques outperforms CFDBF and functional beamforming. However, for airfoil trailing-edge noise where the sources are distributed in a line and the Rayleigh's resolution limit is not the critical issue, deconvolution beamforming techniques such as the Enhanced HR-CLEAN-SC is not necessary.

4.3.5. SOURCE-POWER INTEGRATION (SPI)

The beamforming techniques introduced in the preceeding sections, such as the CLEAN-SC method and its variants, are suitable for quantification of SPLs from multiple point sources as individual sources. However, in some cases, distributed sound sources are encountered and the SPL needs to be quantified collectively. For instance, the trailing-edge noise is a line source, i.e. distribution of point sources [190]. In order to quantify the SPL for such sources, the Source Power Integration (SPI) technique [180, 191] is employed.

The SPI techniques defines a region of interest, integrates the source powers within this region, and represents the source powers by a unit monopole, i.e. omnidirectional point source.

Having applied a beamforming technique, e.g. Eqs. (4.6), (4.19), or (4.22), the source power at grid point j, $\tilde{A}_j$, is obtained. For this section, $\tilde{A}_j$ is denoted as $\tilde{A}_{j,\text{meas.}}$ where the subscript 'meas.' emphasized that the source power is measured. Next, a region of interest containing J grid points where $\tilde{A}_{j,\text{meas.}}$ is to be integrated is defined. This region is called the Region Of Integration (ROI). Within the ROI, there is a grid point k, usually in the middle, where the representative unit monopole is placed. The source power resulting from this unit monopole at any grid point j is $\tilde{A}_{j,\text{sim.}}$ where the subscript 'sim.' means 'simulated'. Let $P_{\text{meas.}}$ and $P_{\text{sim.}}$ represent the sound powers of the measured and simulated sources within the ROI, respectively, the SPI method assumes the following proportionality:

$$\frac{\sum_{j\in J}\tilde{A}_{j,\text{meas.}}}{P_{\text{exp.}}} = \frac{\sum_{j\in J}\tilde{A}_{j,\text{sim.}}}{P_{\text{sim.}}}. \tag{4.25}$$

For the assumed unit monopole, the peak $\tilde{A}_{j,\text{sim.}}$ value is one and therefore $P_{\text{sim.}}$ is one. The representative $P_{\text{meas.}}$ in case $\tilde{A}_{j,\text{exp.}}$ is obtained from CFDBF, i.e. Eq. (4.6), $P_{\text{exp.}}$ becomes

$$P_{\text{meas.}} = \frac{P_{\text{sim.}}\sum_{j\in J}\left(\mathbf{w}_j^*\mathbf{C}_{\text{meas.}}\mathbf{w}_j\right)}{\sum_{j\in J}\left[\mathbf{w}_j^*\left(\mathbf{g}_k\mathbf{g}_k^*\right)\mathbf{w}_j\right]}, \tag{4.26}$$

where $\mathbf{w}_j^*\left(\mathbf{g}_k\mathbf{g}_k^*\right)\mathbf{w}_j$ is an expression for a PSF of a unit monopole at grid point k. For the present thesis, this grid point is the origin. In fact, this term produces the same PSFs as shown in Figs. 4.3a and 4.3b.

For wind-tunnel trailing-edge noise measurements in this thesis, Eq. (4.26) is used. The scan plane and the ROI are shown in Figs. 4.1a and 4.1b. For some cases, the diagonal element of $\mathbf{C}_{\text{meas.}}$ is removed to avoid microphone self-noise [174]. This may result in negative $\tilde{A}_{j,\text{meas.}}$ for some grid points within the ROI. Moreover, spurious sources due to sidelobes might also be found within the ROI. To avoid integrating these sources, a lower integration bound relative to the maximum value within the ROI is usually set [191]. Post-processing settings for the wind-tunnel trailing-edge noise data are specified in Table 4.2.

The SPI technique has shown the ability to provide accurate representation of the overall source power in wind-tunnel measurements [189]. Other advance variants of the SPI technique use alternative terms instead of $\mathbf{g}_k\mathbf{g}_k^*$ in Eq. (4.26) to minimize error between $\mathbf{C}_{\text{meas.}}$ and the simulated source, i.e. to better represent the source characteristics. Interested readers are referred to a publication of Merino–Martínez [191] for further details.

Table 4.2: Specifications the far-field microphone array acoustic signal measurements and processing settings using the SPI beamforming technique.

Specifications	Wind-tunnel facilities and airfoil chords	
	A–Tunnel $c = 200$ mm	LTT $c = 900$ mm
Sampling frequency (kHz)	51.2	50.0
Time-domain data snapshot specifications for CSM averaging	5120 samples Overlap: 50% Hanning weighing function	2048 samples Overlap: 50% Hanning weighing function
Scan plane dimension in $x \times z$, centered at the origin	$5.00c \times 5.00c$	$1.11c \times 1.39c$
Scan plane resolution	$0.05c$	$0.01c$
ROI dimension in x and z, centered at the origin	$1c \times 1c$ Span coverage: 200 mm	$0.31c \times 0.25c$ Span coverage: 200 mm
Integration lower bound (dB, relative to the maximum value)	−6	−6
CSM diagonal removal	No	Yes

4.3.6. Conventional Time Domain Beamforming (CTDBF) and Rotational Source Identifier (ROSI)

The beamforming techniques discussed so far based on the schematic in Fig. 4.2 rely on a stationary scan plane and scan grid points. Nevertheless, for some measurements where the sound sources are moving, imposing the stationary scan plane may result in inaccurate representation of the source location and level. Therefore, for rotational sources such as wind turbines, a special beamforming technique is needed to help accurately identify the sound sources.

The ROtational Source Identifier (ROSI) [25] beamforming rotates the scan grid with the source. The ROSI technique is based on Conventional Time Domain Beamforming (CTDBF) [178], i.e. delay-and-sum beamforming. For a scan point x_j of interest, the time acoustic signal from this point requires to travel to a microphone n at point x_n on the array, denoted as the emission time delay Δt_e is known. For the most simple case, this is the distance between x_j and x_n divided by the speed of sound c_0, i.e. $\Delta t_e = \|x_j - x_n\|/c_0$. If $\chi_n(t_q)$ is the recorded acoustic signal by microphone n at time t_q, the effective acoustic pressure from the scan point x_j, $p_{j,\text{eff.}}^2$ can be reconstructed from $\chi_n(t_q)$ by accounting for Δt_e. This reconstruction is averaged over a set of consecutive samples Q and all N microphones as:

$$p_{j,\text{eff.}}^2 = \frac{1}{N^2 Q} \sum_{q \in Q} \sum_{n=1}^{N} \left[\chi_n(t_q + \Delta t_e) \right]^2 \tag{4.27}$$

Equation (4.27) is the basis for the ROSI beamforming. Next, a proper formulation for

Δt_e which accounts for the rotational grid and possibly the non-stationary medium is needed. Here, an upwind microphone array noise measurement of a wind turbine shown in a schematic in Fig. 4.6 is considered. The origin of the reference coordinate is placed at the center of the microphone array as shown. Let $\mathbf{x}_c = [x_c, y_c, z_c]$ denote the rotational hub of the wind turbine. The following assumptions are made for this set up:
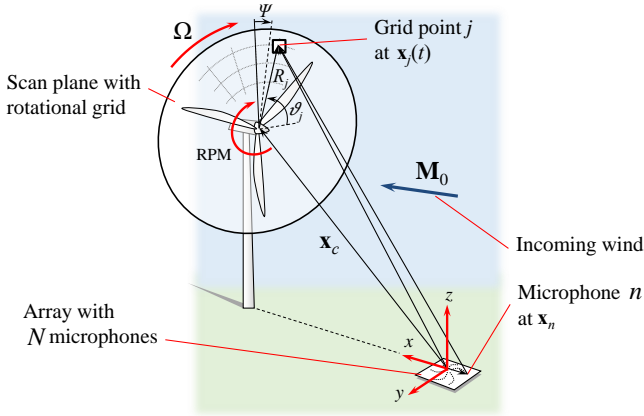
Figure 4.6: Schematic of a microphone-array noise measurement of a wind turbine and notations used in the ROSI beamforming.

- The rotational plane of the wind turbine is parallel to the y–z plane.

- The hub aligns with the array center, i.e. $\mathbf{x}_c = [x_c, 0, z_c]$.

- The wind turbine rotates at a constant rotational speed of Ω rad/s, where $\Omega = 2\pi\mathrm{RPM}/60$ and RPM is the rotational speed in rounds per minute.

- The incoming wind speed profile is uniform and constant, i.e. the atmospheric boundary layer is neglected.

- The Mach number vector of the incoming wind $\mathbf{M}_0$ is perfectly normal to the rotational plane, i.e. $\mathbf{M}_0 = [M_0, 0, 0]$.

In order to perform the ROSI beamforming of this wind turbine, a set of rotational scan points rotating at the same rotational speed of the wind turbine is defined. Based on the assumptions, the instantaneous location of a scan point $\mathbf{x}_j(t)$ at time t is

$$
\begin{aligned}
\mathbf{x}_j(t) &= [x_j(t), y_j(t), z_j(t)] \\
&= [x_c, R_{j,0}\cos(\Omega t + \vartheta_0), z_c + R_{j,0}\sin(\Omega t + \vartheta_0)]
\end{aligned}, \tag{4.28}
$$

where $R_{j,0} = \|\mathbf{x}_c - \mathbf{x}_j(0)\|$ and $\vartheta_{j,0} = \arctan[z_j(0)/y_j(0)]$.

Having determined the instantaneous scan point location $\mathbf{x}_j(t)$, Δt_e is calculated in a similar manner to Eq. (4.3):

$$\Delta t_e(\mathbf{x}_n, \mathbf{x}_j(t)) = \frac{-M_0(x_n - x_j(t)) + \sqrt{M_0^2(x_n - x_j(t))^2 - \beta^2 \|\mathbf{x}_n - \mathbf{x}_j(t)\|^2}}{c_0 \beta^2}. \tag{4.29}$$

It is noteworthy that when $\mathbf{M}_0 \to \mathbf{0}$, Eq. (4.29) simplifies to

$$\Delta t_e(\mathbf{x}_n, \mathbf{x}_j(t)) = \frac{\|\mathbf{x}_n - \mathbf{x}_j(t)\|}{c_0}. \tag{4.30}$$

By substituting $t_e(\mathbf{x}_n, \mathbf{x}_j(t))$ in Eq. (4.27), $p_{j,\text{eff.}}^2$ is determined. The source map is obtained by evaluating $p_{j,\text{eff.}}^2$ for every grid point j. This is represented in terms of SPL in dB as

$$\text{SPL}_j = 10 \log_{10} \frac{p_{j,\text{eff.}}^2}{p_0^2} \text{ dB}. \tag{4.31}$$

The expressions shown so far are used to calculate the far-field (wind-turbine) noise as perceived by an observer, i.e. the microphone array in this case. To demonstrate the benefit of the ROSI beamforming compared to CTDBF, the wind-turbine noise measurement presented in Section 1.3 is revisited. Source maps for this wind obtained by CTDBF ($\Omega = 0$ rad/s) and ROSI ($\Omega = 1.42$ rad/s) beamforming calculated for a full rotation are presented in Figs. 4.7a and 4.7b, respectively, where the circles mark the inner part of the scan grid, the blade tip, and the outer part of the scan grid. For CTDBF, the noise source is seen only for the downward-moving portion. This noise source reaches its peak level at the azimuth angle $\Psi \approx 120°$. This result using the stationary scan grid implies that, in average, the wind turbine is perceived as the noisiest when a blade is at $\Psi \approx 120°$. However, noise level from each individual blade cannot be visualized and quantified by this technique.

The rotating grid employed in the ROSI beamforming overcomes this limitation. The source map in Fig. 4.7b reveals the noise origin from all of the three blades. This is therefore beneficial for quantifying each blade's contribution to the overall perceived noise.

Convective amplification and directionality effects on the perceived noise

Movement of the wind turbine blade relative to the observer affects the SPL perceived by the observer. For a stationary observer, movement of the blade toward the observer amplifies the SPL. This effect is called *convective amplification*. Moreover, it has been discussed in Section 2.2.1 that the trailing-edge noise is directional. Therefore, depending on the location of the blade relative to the observer, the perceived SPL also varies due to this *directivity*.

Combination of the convective amplification and the directivity explains the asymmetry of the noise source shown in Fig. 4.7a. SPL deviations in dB due to these effects can analytically be quantified by the following function [23, 192]:
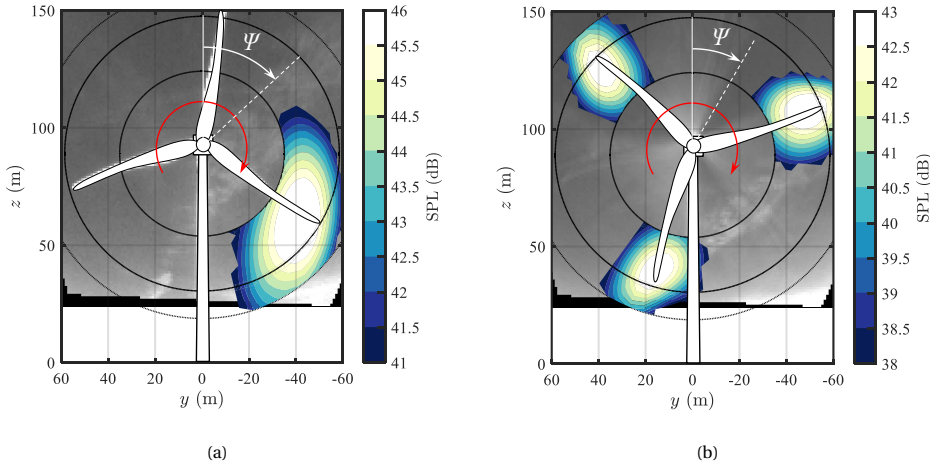
Figure 4.7: Source maps for a wind turbine obtained by (a) CTDBF ($\Omega = 0$ rad/s) and (b) ROSI ($\Omega = 1.42$ rad/s) beamforming calculated for a full rotation.

$$\text{SPL deviation} = 10 \log_{10} \frac{2 \sin^2(\Theta/2) \sin^2 \xi}{(1 - M_{\text{tot.}} \cos \zeta)^4} \text{ dB} \qquad (4.32)$$

The two sine functions in the numerator of Eq. (4.32) account for the directionality effect. The angle Θ is defined as shown in Fig. 2.1. In Eq. (4.32) the wind turbine blade is assumed to be acoustically non-compact (See Section 2.2.1). For the acoustically compact case, $2 \sin^2(\Theta/2)$ is replaced by $\sin^2 \Theta$. Next, the angle ξ, defined as the angle between the plane of the blade planform and the plane intersecting the chord and the observer, accounts for the out-of-plane observer. The SPL deviation due to the numerator of Eq. (4.32) for the present wind turbine is shown in Fig. 4.8a. It is assumed that the blade plane is the same as the rotational plane. It can be seen that the SPL is amplified to the highest level at $\Psi \approx 120°$ and the highest SPL reduction is found at $\Psi \approx 300°$. Therefore, due to the directionality, the trailing-edge noise from the wind turbine blade is highly amplified as the leading edge of the blade moves toward the observer. This is mainly because of the cardioid directivity of the trailing-edge noise which reaches the peak level in the direction of the observer when the leading edge moves towards them.

The denominator of Eq. (4.32) accounts for the convective amplification. Here, the 4th power amplification is assumed [192]. The term $M_{\text{tot.}}$ is the Mach number based on the flow velocity relative to the blade and the angle ζ is the angle between this velocity vector and the source–observer line. Again, the SPL deviation due to this term is shown in Fig. 4.8b. For this set up, the SPL from downward-moving blade is expected to be amplified while the opposite happens as the blade moves upward.

Combining the directionality and the convective amplification effects, the SPL deviation from the full Eq. (4.32) is shown in Fig. 4.8c. Since both effects increase and decrease the SPL at approximately the same Ψ, it is expected that the blade will be perceived the loudest at the azimuth angle of $\Psi \approx 120°$ as it moves towards the observer on the ground
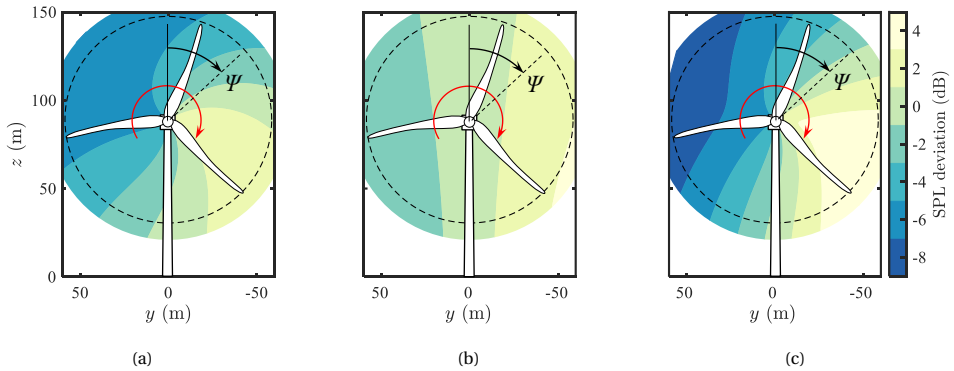
Figure 4.8: SPL deviation of the noise perceived from a wind turbine due to (a) the directionality (b) the convective amplification (c) the directionality and the convective amplification combined.

and will become more quiet when it moves upward, away from the ground. The present result is in-line with Oerlemans et al. [23] where a similar set up is considered.

This explains the *swishing* characteristics discussed in Chapter 1 and also the beamforming source map in Fig. 4.7a. For the rest of this thesis however, the wind turbine noise as perceived by an observer is of interest. Therefore, these SPL deviations will not be accounted for and the data will be shown as measured by the microphone array.

5

AEROACOUSTIC CHARACTERIZATION OF TRAILING-EDGE NOISE FROM A NACA 63₃–018 AIRFOIL[1]
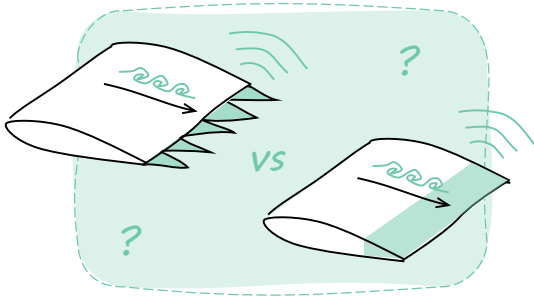
This chapter presents aeroacoustic measurements of a NACA 63₃–018 airfoil with a baseline Trailing Edge (TE) and TE add-ons for noise reduction, namely TE serrations and perforated TE inserts. The measurements are performed in a broad chord-based Reynolds number Re_c range using two NACA 63₃–018 airfoils in two wind tunnels. At zero-lift condition, the TE add-ons hardly alter the boundary-layer characteristics at the TE. Noise reduction varies with the TE serrations geometry and the perforated TE insert permeability. The perforated TE inserts provide approximately 4 dB higher maximum noise reduction than the best-performing 'iron-shaped' TE serrations. Increasing airfoil loading and surface roughness cause noise increase for the TE serrations and the perforated TE inserts, respectively. Overall, noise reduction performance of both add-ons worsens with the increasing airfoil loading.

---

[1]Parts of this chapter will be published in the AIAA Journal. Please cite as shown in the list of peer-reviewed journal articles, number 6.

5.1. INTRODUCTION

Previous Turbulent Boundary Layer Trailing-Edge (TBL–TE) noise studies have indicated needs to validate modeling strategies and new computational simulation algorithms [193–195] against reference experimental datasets with well-characterized inputs and inaccuracies [193]. One of the most remarkable collaborative benchmarking initiatives is the Benchmark problems for Airframe Noise Computations (BANC) workshop (category I, TE noise). Up to the fifth edition of the workshop (BANC–V), the presented datasets feature aeroacoustic data of a symmetric NACA 0012 airfoil, and cambered DU96–W180 and NACA 64_3–618 airfoils with a straight TE in the chord-based Reynolds number (Re_c) range from 1×10^6 to 1.5×10^6 [194, 195].

The published BANC results still left several open questions, as the need to explain the influence of Re_c on the measured TE noise. The narrow Re_c range of the benchmark dataset (1×10^6 to 1.5×10^6) is neither representative of industrial airfoil applications (usually $\geq 3 \times 10^6$) nor covers the range where existing semi-empirical TE noise prediction methods are based upon, or where academic studies are carried out [193]. For example, semi-empirical prediction methods such as the one of Brooks, Pope, and Marcolini [29], or anechoic wind-tunnel measurements [174] are based on data acquired at $Re_c \leq 1 \times 10^6$. This issue has partially been addressed in the work of Ferret Gasch et al. [193] where the aeroacoustic data of two cambered airfoil models from Siemens Gamesa are tested up to $Re_c = 3.7 \times 10^6$. However, there are still some unexplainable phenomena, e.g. a noise increase hump in the far-field noise spectra, which could be attributed to the self-noise noise of the airfoil, and differences in wind-tunnel setups, i.e. blockage effects and aspect ratios. The authors hypothesized that the noise increase hump resulted from the post-processing method of the far-field acoustic signals. To date, the BANC dataset is available for a scattered Re_c range where the available data and post-processing protocols differ per campaign. Moreover, boundary-layer parameters at the TE are not consistently available in every dataset, being insufficient for analytical TE noise prediction models. Therefore, Ferret Gasch et al. [193] recommended testing an airfoil with known aerodynamic characteristics with the same post-processing technique among different institutions. Additionally, the growing application of trailing-edge noise mitigation devices, such as TE serrations [47, 52, 196], have also presented the needs for a benchmarking dataset of noise reduction provided by such technologies.

Referring to the airfoil profiles considered in this thesis, which have been presented in Section 3.2.1, the NACA 63_3–018 airfoil profile is considered as a benchmarking airfoil for the aforementioned purposes. This is due to its known [145] and predictable [146] change of the aerodynamic characteristics in relation to the flow features, e.g. Re_c and angle of attack. Additionally, the symmetric geometry of the airfoil helps defining an accurate zero-lift angle, at the same time allows studying very similar pressure distributions to the ones of profiles usually employed on wind turbines, once placed at a different angle of attack [144]. As one NACA 63_3–018 airfoil model has recently been manufactured during the course of this thesis, this chapter presents an extensive aeroacoustic characterization of this airfoil profile, both with a baseline TE configuration, and with noise mitigation add-ons, namely TE serrations and permeable TE inserts, installed at the TE.

Characterization is done in a broad Re_c range thanks to the low-Re_c and high-Re_c

tests introduced in Section 3.3 carried out in the A–Tunnel and the Low-Turbulence Tunnel (LTT), respectively. For convenience, in this chapter, the 200-mm-chord and the 900-mm-chord NACA 63_3–018 airfoil models are named as the Low-Re_c Model (LRM) and the High-Re_c Model (HRM), respectively. Extensive descriptions of the experimental setups and the measurement techniques employed are provided in Chapters 3 and 4. The airfoil models were tested both without and with the turbulators installed on them (See Section 3.2.3) to force the laminar-to-turbulent boundary layer transition location. The test configurations without and with the turbulator are denoted hereinafter as the *clean* and *forced* configurations, respectively.

The LRM and the HRM have also been tested in various other facilities, such as the Stability Tunnel of Virginia Tech [148], the Pour La Cour Tunnel at DTU, and the Acoustic Wind Tunnel in Braunschweig in collaboration with the German Aerospace Center (DLR). An extensive endeavor to extend the comparison to different facilities in Europe is on course. This dataset is additionally presented and employed in the Hybrid Anechoic Wind Tunnel (HAWT) yearly activities. The noise reduction data given by various TE serration configurations also fits in the International Energy Association (IEA) Wind Technology Collaboration Programme (TCP) Task 39 framework which focuses on accelerating research and developments of quiet wind turbines.

5.2. Specifications of the TE add-ons

5.2.1. TE serrations

TE serrations were installed on the airfoils and tested under forced transition location only. Two geometries shown in Fig. 5.1 are considered: namely the *sawtooth* and the *iron* serrations. These serrations geometries are chosen from a numerical study of Avallone et al. [141] which found an additional noise attenuation given by the iron serrations compared to the more conventional sawtooth counterpart, due to minimized scattering at the curved and (almost) tangent roots. The serrations have wavelength $\lambda = 0.05c$, and $2h = 0.1c$, where h is the serration peak amplitude, following the guidelines given by Gruber et al. [47]. For the experiments, the serrations for both airfoils were produced from a 1-mm thick stainless steel plate using wire cutting. The serrations feature minimum manufacturing corner radii of $2 \times 10^{-3}c$ and $2 \times 10^{-4}c$ (See Fig. 5.1). Both serrations were installed with a zero-degree flap angle φ, i.e. parallel to the chord. The sawtooth serration was also tested with flap angles: $\varphi = \pm 8°$ on the LRM and $\varphi = 4°$ on the HRM with respect to the chordline, where the positive φ denotes deflection towards the pressure side [197].

Installation of the serrations on the airfoil models differ for the LRM and the HRM. For the LRM, the TE insert starting at $x = -0.2c$ was removed and replaced by the serration clampers which support the serrations on the airfoil. The serration clampers are shown in Fig. 5.2a. For the HRM, the serrations have an upstream extension of 45 mm which was used to side mount the inserts to the airfoil using double-sided tapes and Aluminum tapes. Note that the actual chord extension is slightly less than $0.1c$ due to the aforementioned minimum radius criteria. Details of the serration installation on the HRM are illustrated in Fig 5.2c.

(a) Sawtooth serrations
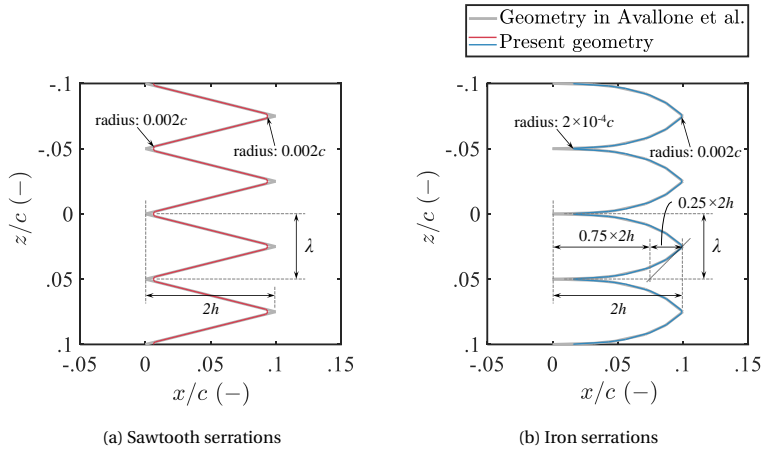
(b) Iron serrations

Figure 5.1: Drawings of the TE serrations used on the airfoil compared to the geometry used in the simulation of Avallone et al. [141].

(a) Serrations installation on the LRM

(b) Perforated TE insert on the LRM

(c) Serrations installation on the HRM
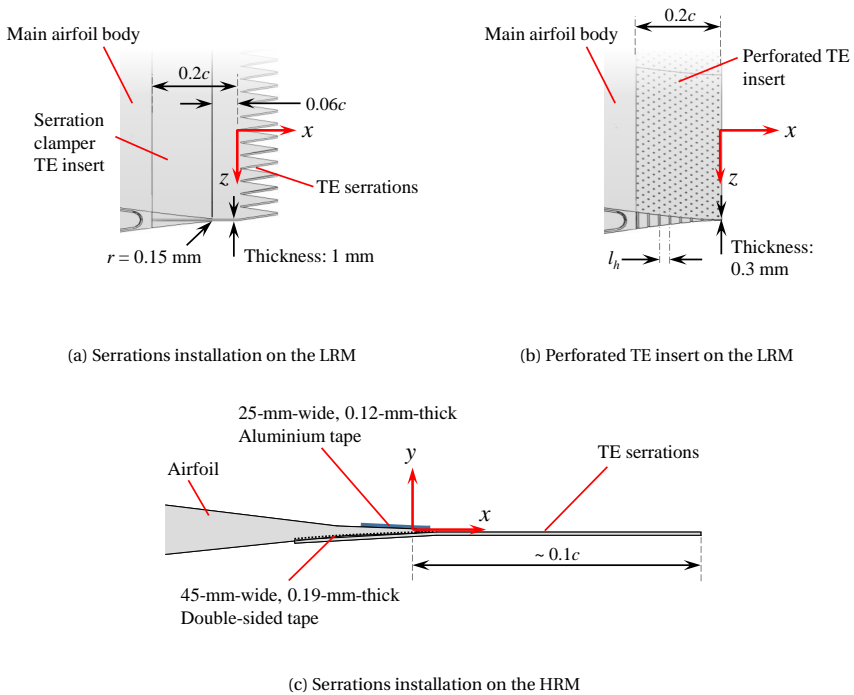
Figure 5.2: TE add-on installations on the airfoils.

5.2.2. PERFORATED TE INSERTS

The impermeable baseline TE insert of the LRM (See Fig. 3.2b) was also replaced by TE inserts with perforations as shown in Fig. 5.2b. The length of the TE insert is 20% of the

chord. Cylindrical holes with a diameter of 0.8 mm connects the suction and the pressure sides in the direction normal to the chord y are distributed on the TE insert with a hole spacing defined by l_h. In this chapter, $l_h = 2.5$ and 5.0 mm are considered.

The perforated TE inserts were manufactured by 3D printing using the so-called digital-light-projector printing technique. The printing material was high-temperature photopolymer. Perforated TE inserts manufactured by this method having the same hole diameter and hole spacing dimensions were formerly tested on a 200-mm-chord NACA 0018 airfoil model in a previous study of Rubio–Carpio et al. [108]. Interested readers are referred to their publication for detailed specifications and characterization of the perforated structure.

5.3. TEST MATRIX

The test matrix is presented in Table 5.1. The chord-based Reynolds numbers Re_c and geometrical angle of attack $\alpha_{\text{geom.}}$ sweeps where the LRM and the HRM were tested are specified. Measurement techniques employed are specified with respect to $\alpha_{\text{geom.}}$ where data are collected. It is worth emphasizing that the TE serrations were tested on both the LRM and the HRM while the perforated TE inserts were tested on the LRM only.

It can be seen that the tests involve testing the two scaled airfoils in multiple facilities and configurations in order to achieve a broad Re_c range from 0.2×10^6 to 3×10^6. This testing strategy is visualized in Fig. 5.3. It is also worth highlighting that the tests were carried out at several overlapping Re_c between different nozzles/facilities.
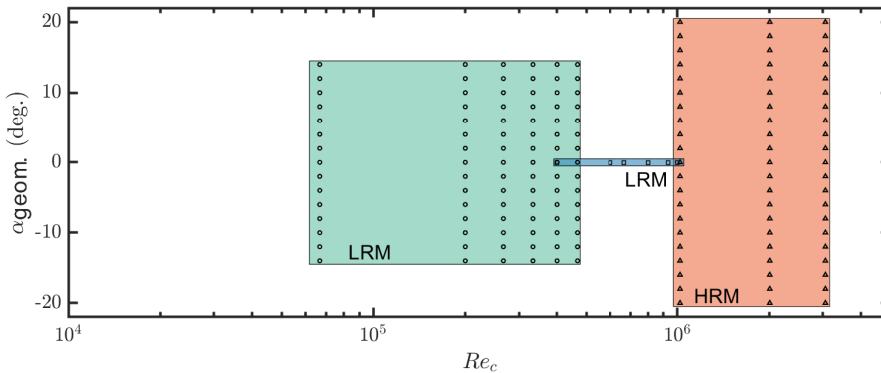

Figure 5.3: Illustration of the conditions tested in the test campaigns. The circle and square marks represent the conditions measured during the campaigns with LRM using the $3.5c \times 2c$ nozzle and the $1.25c \times 2c$ nozzle in the A–Tunnel, respectively. The triangular marks represent the experiments carried out with the HRM in the LTT.

Table 5.1: Test matrix.

Airfoil model	Wind tunnel facility	Re_c ($\times 10^6$, -)	u_∞ (m/s)	$\alpha_{geom.}$ sweep [start:increment:end] (deg.)	Measurements with respect to $\alpha_{geom.}$ (deg.)				
					Aerodynamics		TBL profiles		Acoustics
					Static pressure taps	Wake-rake drag	Hot-wire	PIV	
LRM	A–tunnel, 3.5c × 2c nozzle	0.20	15	±[0:3:9], ±[9:1.5:24], ±[24:-1.5:12]	For baseline TE, available at all $\alpha_{geom.}$; For TE add-ons, at $\alpha_{geom.}$ for acoustics	[0:3:18]	0	N/A	±[0,6,12,15,18]
		0.26	20	±[0,6,12,15,18]		0	0	N/A	[0,6,12,15]
		0.39	30	±[0:3:9], ±[9:1.5:24], ±[24:-1.5:12]		[0:3:18]	0	N/A	±[0,6,12,15,18]
		0.46	35	±[0,6,12,15,18]		N/A	N/A	N/A	[0,6,12,15]
LRM	A–tunnel, 1.25c × 2c nozzle	0.39	30	0	0	N/A	0	N/A	0
		0.59	45	0	0	N/A	0	N/A	0
		0.66	50	0	0	N/A	N/A	N/A	0
		0.79	60	0	0	N/A	0	N/A	0
		0.92	70	0	0	N/A	N/A	N/A	0
		1.00	75	0	0	N/A	0	N/A	0
HRM	LTT, Kevlar-walled section	1.00	16	±[0:2:20]	For baseline TE, available at all $\alpha_{geom.}$; For serrations, available up to ± 16	Same as p. taps	N/A	[0,4]	±[0:2:8], ±[8:4:16]
		2.00	34	±[0:2:20]		Same as p. taps	N/A	[0,4]	±[0:2:8], ±[8:4:16]
		3.00	51	±[0:2:20]		Same as p. taps	N/A	[0,4]	±[0:2:8], ±[8:4:16], except -2

5

5.4. Results: Baseline TE

5.4.1. Pressure distributions

Effects of Re_c variation

Figure 5.4 shows the pressure distribution over the two models at $\alpha_{\text{eff.}} \approx 0°$ in the clean and forced configurations. The selected Re_c are 0.4×10^6 and 2×10^6 for the LRM and the HRM, respectively. The results are plotted together with XFOIL predictions at each given condition.

(a) Clean, $\alpha_{\text{eff.}} \approx 0°$ (b) Forced, $\alpha_{\text{eff.}} \approx 0°$

Figure 5.4: Comparison of c_p distributions from the A–Tunnel and the LTT tests of the baseline NACA 63_3–018 airfoil with XFOIL predictions at various Re_c and $\alpha_{\text{eff.}} \approx 0°$.

At $\alpha_{\text{eff.}} \approx 0°$, the clean configuration in Fig. 5.4a reveals a laminar separation bubble. For the LRM, the laminar separation bubble starting at $x/c \approx -0.6$ and ending where the flow reattaches at $x/c \approx -0.35$ is clearly visible. This region is shown in the plot inset. However, in this region, the laminar separation bubble is not as visible on the HRM where Re_c is relatively higher. On the other hand, when the turbulator strip is applied to force the transition location, similar c_p distributions between the different models and Reynolds numbers can be seen as shown in Fig. 5.4b. The laminar separation bubble is no longer visible. Additionally, the c_p distribution trends for both the clean and forced configurations are in good agreement with the XFOIL predictions, for both the LRM and the HRM.

Several additional Re_c from both models are included in Fig. 5.5 to more clearly illustrate the change of the c_p distribution with respect to Re_c. The XFOIL predictions are now omitted. It can be seen from the clean configuration in Fig. 5.5a that the laminar separation bubble shortens as Re_c increases. This shows that the Re_c effect on the c_p distribution can be seen by joining data from two different wind tunnels. For the forced configuration in Fig. 5.5b, there is no indication of the laminar separation bubble at any Re_c.

Effects of the angle of attack

The pressure distributions on the LRM and the HRM at $\alpha_{\text{eff.}} \approx 4°$ and $8°$ for the clean and forced configurations are shown in Fig. 5.6. Again, the selected Re_c are 0.4×10^6 and

(a) Clean, $\alpha_{\text{eff.}} \approx 0°$ (b) Forced, $\alpha_{\text{eff.}} \approx 0°$

Figure 5.5: Comparison of c_p distributions from the A–Tunnel and the LTT tests of the baseline NACA 63_3−018 airfoil at various Re_c and $\alpha_{\text{eff.}} \approx 0°$.

2×10^6 for the LRM and the HRM, respectively. The results are plotted together with XFOIL predictions at the given conditions.

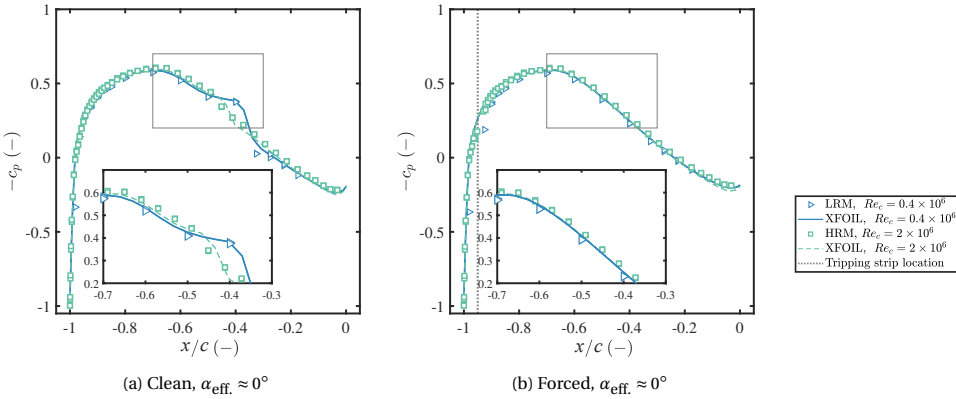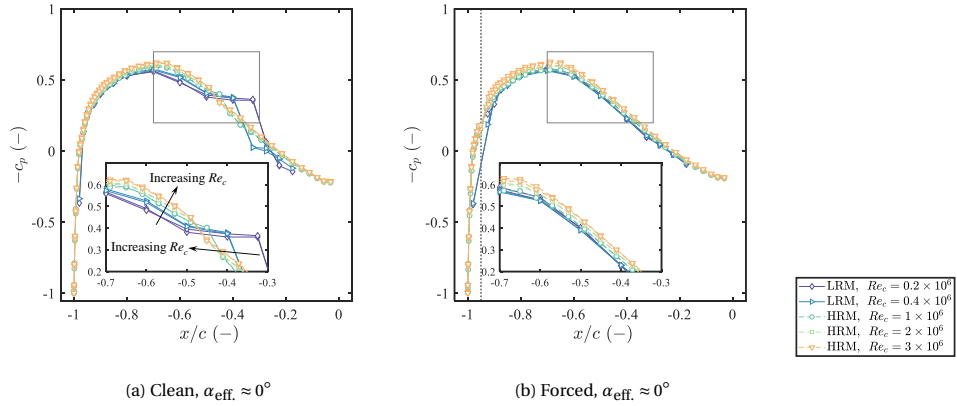For the clean configuration, the laminar separation bubble is still visible for $\alpha_{\text{eff.}} \approx 4°$, especially for $Re_c = 0.4 \times 10^6$ where it is visible on both the suction and the pressure sides. This is in good agreement with the XFOIL prediction. However, the laminar separation bubble is no longer present for $\alpha_{\text{eff.}} \approx 8°$, except for the pressure side of the LRM for $Re_c = 0.4 \times 10^6$.

For the forced configuration, a small deviation of the c_p distribution is observed between the HRM and the LRM on the suction side. The measurements of the HRM feature a slightly lower pressure on the suction side, compared to the LRM. This difference is larger as the angle of attack is increased. Moreover, for the LRM at $\alpha_{\text{eff.}} \approx 8°$, the c_p distribution close to the TE on the suction side flattens, indicating flow separation. Therefore, a lower c_l for the LRM is expected for the forced configuration. This is discussed in the next section. Interestingly, for the LRM at $\alpha_{\text{eff.}} \approx 8°$, the c_p distribution on the pressure side does not seem to differ from the clean configuration. It is therefore expected that at higher angles of attack, the forced transition on the pressure side is not effective.

5.4.2. LIFT CURVES AND DRAG POLARS

The aerodynamic coefficients give an overall picture of the comparisons between the two campaigns. Figure 5.7 shows the lift and drag coefficients, c_l and c_d, measured on the two models at different $\alpha_{\text{eff.}}$. From the lift curve, the effect of the smaller Re_c at high angles of attack is noticeable. The lift curve for this model exits the linear regime for $\alpha_{\text{eff.}} > 6°$. Lower values of c_l beyond the linear regime are observed for the forced transition condition, where the flow separation is seen (See $\alpha_{\text{eff.}} \approx \pm 8°$). The stall angle increases with Re_c. In general, the curves agree well with the theoretical $c_l = 2\pi\alpha$.

Similarly, the drag coefficient (c_d) decreases with the increasing Re_c [198]. The curves follow closely the predictions obtained from XFOIL. For the clean configuration, the critical amplification factor for natural laminar to turbulent transition of 9 and 14 were chosen
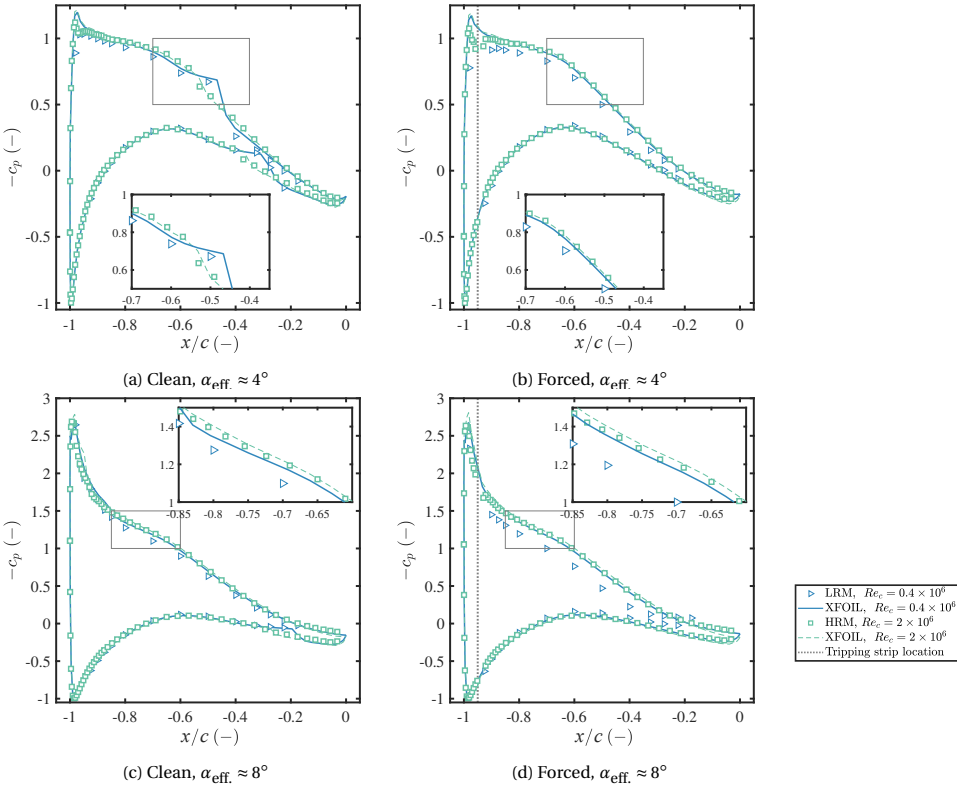
Figure 5.6: Comparison of c_p distributions from the A–Tunnel and the LTT tests of the baseline NACA 63_3–018 airfoil at various Re_c and non-zero $\alpha_{\text{eff.}}$.

for the LRM and the HRM, respectively, based on the expected turbulent intensity of the each wind-tunnel facility [151]. Especially for the HRM, the measured drag compares well with the predicted one for small angles of attack ($-8° \leq \alpha_{\text{eff.}} \leq 8°$). For higher angles the measured drag departs from the ones predicted with XFOIL. At such conditions, the boundary layer separation is observed sooner than predicted. This is likely because the flow is no longer two dimensional at those angles.

5.4.3. BOUNDARY-LAYER PARAMETERS AT THE TE REGION
The extensive summary of the extracted boundary-layer parameters for the clean and forced configurations are provided in Tables 5.2 and 5.3, respectively.

5

(a) Clean, c_l curves

(b) Forced, c_l curves

(c) Clean, c_d polars

(d) Forced, c_d polars
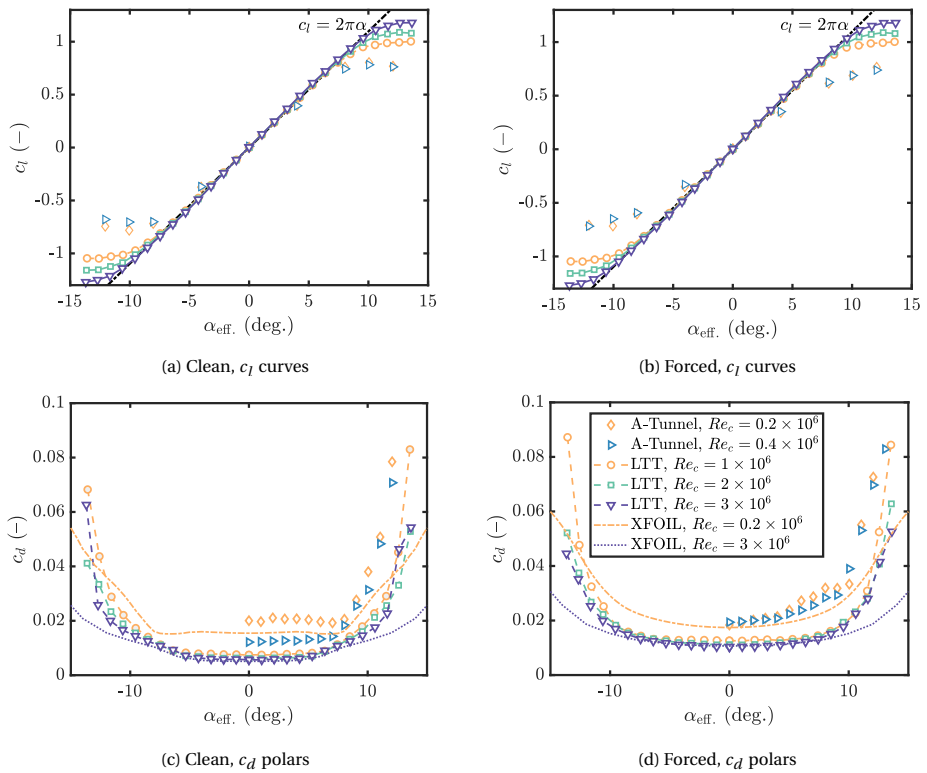
Figure 5.7: Comparison of c_l curves and c_d polars from the A–Tunnel and the LTT tests of the baseline NACA 63_3-018 airfoil at various Re_c.

Table 5.2: Boundary-layer properties measured at the TE of the airfoil at $\alpha_{\mathrm{eff.}} \approx 0°$, clean configuration.

Model	u_∞ (m/s)	$\alpha_{\mathrm{eff.}}$ (deg.)	Re_c (–)	δ_{99} (mm)	δ^* (mm)	θ (mm)	u_e (m/s)	u_T (m/s)	Π (–)
LRM 3.5c nozzle	15	0	0.2×10^6	13.0	2.40	1.65	14.1	0.61	0.54
	20		0.3×10^6	12.1	1.89	1.33	18.6	0.82	0.35
	30		0.4×10^6	11.2	1.58	1.12	27.8	1.18	0.47
LRM 1.25c nozzle	30	0	0.4×10^6	10.9	1.70	1.07	29.1	1.25	0.25
	45		0.6×10^6	9.2	1.21	0.75	41.8	1.87	-0.14
	60		0.8×10^6	9.0	1.31	0.84	56.7	2.37	0.14
	75		1.0×10^6	8.5	1.25	0.77	69.9	2.77	0.45

Table 5.3: Boundary-layer properties measured at the TE of the airfoil, forced configuration.

Model	u_∞ (m/s)	$\alpha_{\mathrm{eff.}}$ (deg.)	Re_c (–)	δ_{99} (mm)	δ^* (mm)	θ (mm)	u_e (m/s)	u_T (m/s)	Π (–)
LRM 3.5c nozzle	15	0	0.2×10^6	9.2	2.23	1.33	14.2	0.52	1.7
	20		0.3×10^6	9.1	2.40	1.36	18.8	0.62	2.3
	30		0.4×10^6	8.9	2.54	1.37	28.1	0.81	3.0
LRM 1.25c nozzle	30	0	0.4×10^6	8.7	2.20	1.20	27.7	0.91	2.1
	45		0.6×10^6	7.7	1.93	1.05	41.4	1.28	2.4
	60		0.8×10^6	7.3	1.78	1.01	55.1	1.69	2.3
	75		1.0×10^6	6.8	2.02	1.13	70.9	2.03	2.7
HRM	17	0	1.0×10^6	28	6.6	4.1	15.3	0.45	2.6
	34	0	2.0×10^6	27	6.1	3.9	31.5	0.91	2.5
	34	4 (s.s.)	2.0×10^6	30	9.0	4.8	31.5	0.69	4.8
	34	4 (p.s.)	2.0×10^6	17	3.4	2.8	31.0	1.08	1.4
	51	0	3.0×10^6	26	5.5	3.5	47.6	1.34	2.4

5

The natural transition location condition causes a thicker boundary layer at the TE. This boundary layer presents a relatively lower shape factor $H = \delta^*/\theta$. The forced-to-transition boundary-layer velocity profile departs from the logarithmic one [159], resulting in the higher wake parameter Π.

As $\alpha_{\text{eff.}}$ increases, the boundary layer on the pressure side becomes thinner while the one on the pressure side becomes thicker. The wake parameter is also strongly influenced by this condition, decreasing on the pressure side and increasing on the suction side.

The variation of the boundary-layer thicknesses at $x/c = -0.02$ at $\alpha_{\text{eff.}} \approx 0°$ with Re_c is shown in Fig. 5.8a for δ_{99} and in Fig. 5.8b for δ^*. The graphs contain the data of the LRM (A–Tunnel) experiment with the two different nozzles and of the HRM (LTT) experiment. For Fig. 5.8a, two trend lines are created for visualization purposes based on the scaling laws shown in Eqs. (5.1) and (5.2). These equations come respectively from the Blasius solution for the laminar boundary layer and the generic solution of the differential equation of the boundary layer growth in Schlichting [198]:

$$\delta_{99,\text{lam.}} = 5\frac{x_{\text{tr.}}}{\sqrt{Re_{x_{\text{tr.}}}}}, \tag{5.1}$$

$$\delta_{99,\text{turb.}} = K_{\delta_{99}}\left\{0.29\frac{(c - x_{\text{tr.}})^{5/4}}{\left[\left(\frac{c-x_{\text{tr.}}}{c}\right)Re_c\right]^{1/4}} + \delta_{99,\text{lam.}}^{5/4}\right\}^{4/5}. \tag{5.2}$$
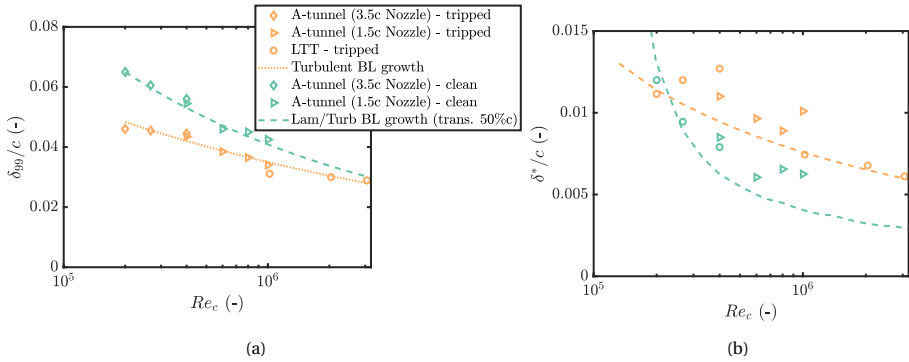
Figure 5.8: (a) δ_{99}/c measured at $X/c = -0.02$ and $\alpha_{\text{eff.}} \approx 0°$ compared against (corrected) scaling laws for turbulent and transitional boundary layers over a plate. The scaling laws are provided to guide the reader to the expected trend from the theory. (b) δ^*/c measured at $x/c = -0.02$ and $\alpha_{\text{eff.}} \approx 0°$ compared against predictions obtained with XFOIL.

where $x_{\text{tr.}}$ and $Re_{x_{\text{tr.}}}$ represent the distance from the leading edge along the chord line where the transition occurs and the Reynolds number based on this distance, respectively. For the clean configuration, the transition is assumed at $x/c = -0.5$, where the separation bubble is observed for most of the Reynolds numbers (See Fig. 5.4). The boundary-layer thickness computed from Eq. (5.2) needs to be scaled with an empirical factor $K_{\delta_{99}} = 2.7$ and 1.5 for the natural and forced transition configurations, respectively. This is necessary as the equations are based on the boundary layer development on a flat plate, i.e. they do not account for the pressure gradients over the airfoil. The value of the empirical

$K_{\delta_{99}} = 2.7$ of the configuration without forced transition is greater due to the effect of the separation bubble on the estimated thickness.

For Fig. 5.8b, the displacement thickness δ^* variation with Re_c and the tripping condition is compared to XFOIL predictions. The predicted δ^* from XFOIL in Fig. 5.8b are well in agreement with the measurements. Discrepancies are larger for δ^* for the LRM due to the relatively lower measurement resolution near the wall. The higher shape factor of the boundary-layer profiles for the clean condition case contributes to the fact that the displacement thickness is smaller although the boundary-layer thickness is larger.

5.4.4. TE NOISE SPECTRA

MEASURED TE NOISE COMPARED TO BACKGROUND NOISE AND BPM MODEL

Firstly, the measured far-field noise spectra are compared against the prediction from the semi-empirical model of Brooks, Pope, and Marcolini (BPM) [29] and the background flow noise level measured when the models were absent to assess the reliability. It is worth emphasizing that the BPM model is developed based on an extensive experimental dataset of a NACA 0012 airfoil, a slightly thinner symmetric airfoil. Therefore, the BPM model predictions provide good reference trend lines on the expected far-field Sound Pressure Levels (SPLs) spectra variations with Re_c and the clean and forced configurations. However, exact matches are not expected. The extracted boundary-layer properties shown in Tables 5.2 and 5.3 are used directly as inputs for the BPM model rather than the scaling laws or XFOIL outputs described previously to avoid additional uncertainties.

Figure 5.9a shows the comparisons for the LRM measured in the A–Tunnel for the two nozzles (one Re_c per nozzle). The measured far-field SPL spectra, both with and without the LRM, i.e. empty section, are expressed in the 1/3-octave band format (SPL$_{1/3}$) in order to compare with the BPM model. For the LRM, the SPL$_{1/3}$ spectra of the empty section are obtained by applying exactly the same SPI beamforming technique as described in Section 4 to the measured pressure–time signals.

For the low $Re_c = 0.4 \times 10^6$, the measured SPL$_{1/3}$ levels for the entire frequency range considered are higher than the flow noise in the empty section. The smallest SPL$_{1/3}$ difference of approximately 2 dB is found at the highest frequency: $f = 4$ kHz. The relative spectral slopes and trends between the measured and the predicted SPL$_{1/3}$ spectra are satisfactory for $f \geq 1$ kHz for both the clean and forced configurations. At lower frequencies, the SPL$_{1/3}$ spectral levels tend to exceed the predicted values. Careful analysis of the source maps (not shown for conciseness) indicates that this results from the worsened resolution of the source map at relatively low frequencies. Consequently, the sound source at the TE can no longer be discerned from the flow noise from the nozzle. This analysis also shows that the noise from the flow interaction with the side plates is stronger than the TE noise at the relatively higher frequencies. For the high $Re_c = 1 \times 10^6$, the measured noise levels are shown to be more severely affected by the background flow noise levels. It is important to note that when the LRM was removed, the stiffness of the side plates reduced. This caused them to vibrate more freely and thereby cause additional noise, especially at relatively high u_∞. Therefore, the noise levels from the empty section shown in the plots are likely to be overestimated. Nevertheless, at frequencies above $f = 1.6$ kHz, good agreement between the measured and predicted SPL$_{1/3}$ is found. It can be
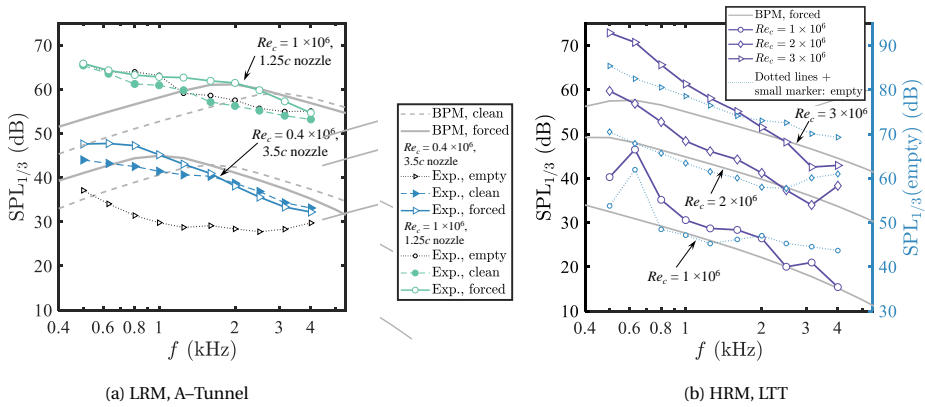
(a) LRM, A–Tunnel

(b) HRM, LTT

Figure 5.9: SPL spectra for the airfoils with baseline TE at various Re_c and $\alpha_{\text{eff.}} \approx 0°$ considering natural and forced transition configurations compared to the background flow noise levels and the BPM model. The different Re_c and facilities are annotated in the plots.

5

inferred that the spectra for the forced configuration are more trustworthy, since the levels in average are higher than the clean configuration, and therefore, the background flow noise.

A similar comparison for the HRM measurements in the LTT is shown in Fig. 5.9b. For the HRM cases, only the forced configuration is shown for all Re_c. Since the measurement of the empty section noise level was performed using only one microphone at preselected u_∞, the empty-section $\text{SPL}_{1/3}$ spectra from the closest measured speeds used for each Re_c are shown with a separated vertical axis on the right. For $Re_c = 1 \times 10^6$, a tonal peak is found in the measured $\text{SPL}_{1/3}$ at $f = 0.6$ kHz. The comparison indicates that this can be attributed to the background noise. Therefore, due to the strong background noise, this lowest $Re_c = 1 \times 10^6$ is omitted in further analyses to avoid confusion. Variations of $\text{SPL}_{1/3}$ with Re_c are in line with the prediction for $f > 1$ kHz. It can also be seen that the slopes of the $\text{SPL}_{1/3}$ spectra from the airfoil TE region are higher than those of the single-microphone empty-section noise measurement. This could be attributed to the spatial filtering of the beamforming which improves with increasing f.

EFFECTS OF TRANSITION LOCATION AND Re_c

Figures 5.10a and 5.10b show the measured $\text{SPL}_{1/3}$ for the clean and forced configurations with the baseline TE measured in the A–Tunnel (LRM) and the LTT (HRM), respectively. Only $\alpha_{\text{eff.}} = 0°$ is considered, while the nonzero $\alpha_{\text{eff.}}$ will be discussed in upcoming figures.

For the frequency range considered, the effects of the forced transition location on $\text{SPL}_{1/3}$ spectra become visible from $Re_c = 0.4 \times 10^6$ onward. At this Re_c, Fig. 5.8b indicates that the tripping strip applied causes a thicker δ^* at the TE compared to the case without it. This causes a noise increase on the former configuration of up to 5 dB compared to the clean configuration. This trend is in good agreement with the BPM prediction (See Fig. 5.9a). The frequencies where the noise increase is found are higher for larger Re_c.
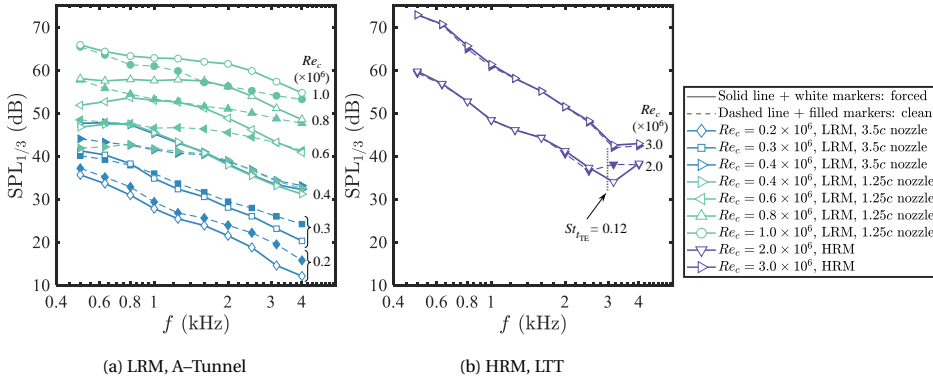
Figure 5.10: SPL spectra for the airfoils with baseline TE at various Re_c and $\alpha_{\text{eff.}} \approx 0°$ considering natural and forced transition configurations.

Additionally, it can be seen that at the overlapping $Re_c = 0.4 \times 10^6$ where the spectra are measured using two different nozzles, both the clean and forced configurations SPL$_{1/3}$ collapse well; this confirms that the results from the wide Re_c range can be obtained and interpreted continuously, regardless of the different nozzles.

Similarly, the LTT data are shown in Fig. 5.10b. For the HRM, the forced transition location does not produce clearly visible difference from the natural one, as the boundary-layer thickness produced for both conditions are similar.

For the LTT measurements of the HRM, the noise created by the vortex shedding from a blunt TE [29] is also observed. Using the suggested Strouhal number based on the TE thickness $St_{t_{\text{TE}}} = 0.12$, where $t_{\text{TE}} = 1.35$ mm, the frequencies at which the peak is expected are marked in Fig. 5.10b. These frequencies are in line with the frequencies where the measured SPL$_{1/3}$ from the clean configuration is higher than that of the forced configuration. This is expected because the SPL of the TE bluntness noise varies with $10\log_{10}(t_{\text{TE}}/\bar{\delta}^*)$ [29], where $\bar{\delta}^*$ is the averaged displacement thickness at the TE from the suction and the pressure sides. The ratio $t_{\text{TE}}/\bar{\delta}^*$ is larger for the clean case as the expected $\bar{\delta}^*$ is smaller than the forced configuration (See Fig. 5.8b).

EFFECTS OF THE ANGLE OF ATTACK

The effects of the varying effective angle of attack $\alpha_{\text{eff.}}$ on the SPL$_{1/3}$ spectra are investigated in Figs. 5.11a and 5.11b for the A–Tunnel and LTT measurements, respectively. In the same manner as Figs. 5.10a and 5.10b, the baseline TE with the clean and forced configurations are considered. Three different $\alpha_{\text{eff.}}$ are considered and the readers are referred back to Figs. 5.4 and 5.6 for the c_p distributions at these angles.

For the A–Tunnel data in Fig. 5.11a, $Re_c = 0.4 \times 10^6$ is considered. For the forced transition configuration, it can be seen that the low-frequency SPL$_{1/3}$ levels ($f < 1$ kHz) increases with $\alpha_{\text{eff.}}$. This can be attributed to the thicker δ^* at the suction side. On the other hand, for the clean configuration, a noise increase is observed when $\alpha_{\text{eff.}}$ increases. The narrow-band spectra (omitted for conciseness) indicate that this noise increase is

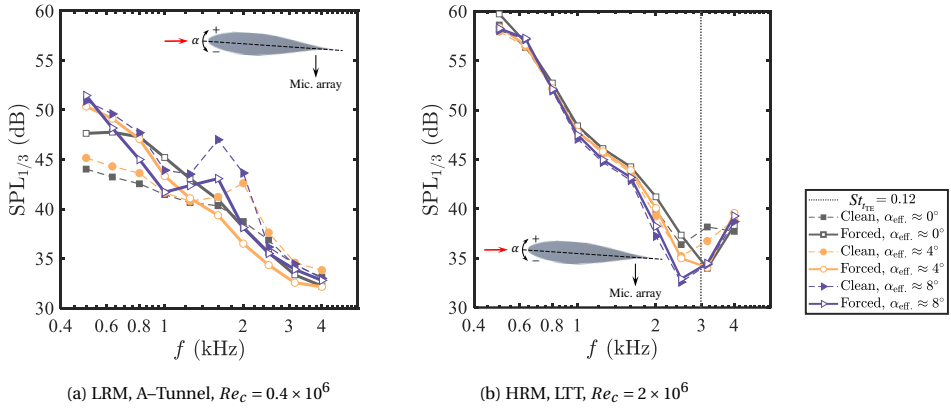(a) LRM, A–Tunnel, $Re_c = 0.4 \times 10^6$ (b) HRM, LTT, $Re_c = 2 \times 10^6$

Figure 5.11: SPL spectra for the airfoils with baseline TE considering natural and forced transition configurations at various $\alpha_{\text{eff.}}$.

5

tonal. This is likely due to the acoustic feedback loop of the laminar boundary layer vortex shedding noise occurring on the pressure side of the airfoil. This effect can also partially be seen for the highest $\alpha_{\text{eff.}}$ in the forced configuration. This could be because, at high angles, the forced transition was not effective as discussed in Fig. 5.6d. Due to the thin TE geometry of the small model ($t_{\text{TE}} = 0.3$ mm), the lowest possible frequency for the tonal blunt TE vortex shedding noise is expected to be at $f \approx 6$ kHz. This is beyond the observed frequency range.

For the LTT measurements, shown in Fig. 5.11b, the Re_c case of 2×10^6 is selected due to the clearest difference between the clean and forced configurations as discussed in Fig. 5.10b. The values of $\alpha_{\text{eff.}}$ are selected consistently with Fig. 5.6. Within the frequency range 1 kHz < f < 3.5 kHz, noise reduction of up to 5 dB due to the increasing $\alpha_{\text{eff.}}$ can be seen. However, the noise increase at lower frequencies is not observed. This could be caused by the LTT wind tunnel background noise at lower frequencies that hampers the TE noise and all the spectra seem to collapse. This also applies to the higher frequency range at $f > 3.5$ kHz. Figures 5.10b and 5.11b therefore imply a reliable frequency range for the LTT measurement at this Re_c. Again, the frequency associated with the blunt TE vortex shedding noise is marked by a line. This frequency agrees with the one where the SPLs of the clean configuration exceed those of the forced configuration and can be seen for $\alpha_{\text{eff.}} \approx 0°$ and $4°$.

5.5. RESULTS: TE ADD-ONS

5.5.1. LIFT CURVES AND DRAG POLARS

Figures 5.12a and 5.12b compare the lift curves of the baseline (straight and impermeable) TE configuration to TE add-on configurations for the LRM and HRM, respectively. The selected Re_c for the LRM and HRM are 0.4×10^6 and 3×10^6, respectively, and only the forced transition location configuration is considered. The full overview on the baseline

lift coefficients can be found in Fig. 5.7b.

(a) c_l curves, LRM, $Re_c = 0.4 \times 10^6$

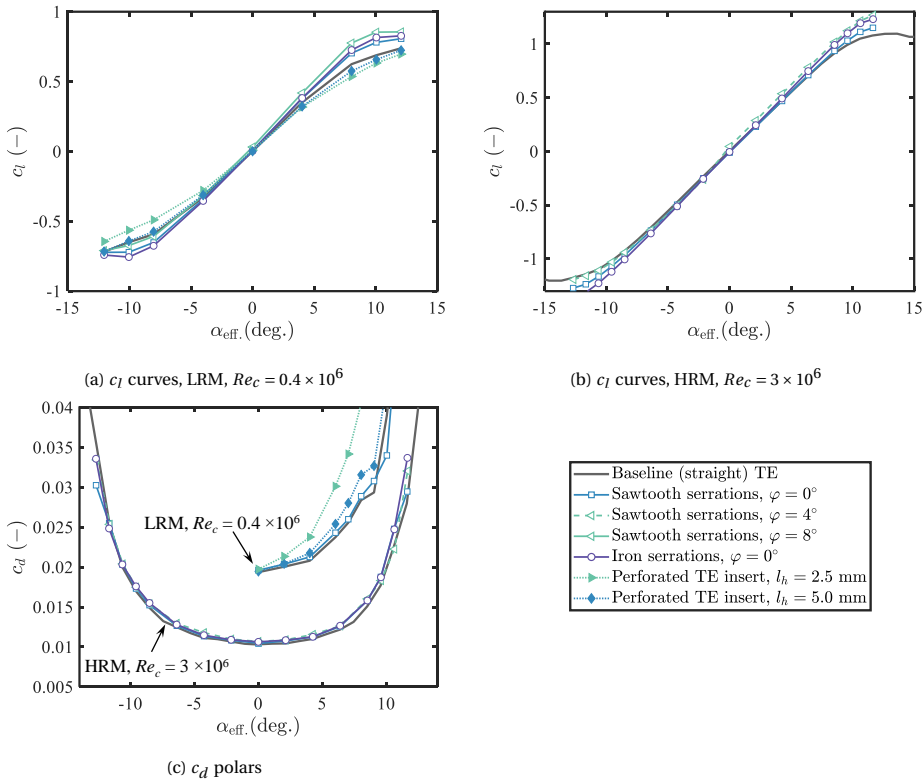(b) c_l curves, HRM, $Re_c = 3 \times 10^6$

(c) c_d polars

Figure 5.12: Measured aerodynamic coefficients with different TE add-ons installed. Only the forced transition location configuration is considered.

At $\alpha_{\text{eff.}} = 0°$, most TE add-ons do not affect the baseline zero-lift due to symmetry, with an exception for the flapped sawtooth serrations where a slightly higher c_l is found. For nonzero $\alpha_{\text{eff.}}$, the airfoil with the serrated TE provides a slightly higher lift curve slope due to the extended effective chord. For $\varphi = 0°$, the lift increase provided by the iron serrations is slightly larger than the sawtooth counterpart. This is expected since the iron geometry has a relatively larger wetted area (See Fig. 5.1). However, the trend is symmetric for both the positive and negative $\alpha_{\text{eff.}}$. On the other hand, for the flapped sawtooth serrations, the airfoil effectively behaves as a cambered airfoil with the relatively higher lift for the positive $\alpha_{\text{eff.}}$, and the trend is no longer symmetric.

In contrast, lift reduction is seen for perforated TE inserts at nonzero $\alpha_{\text{eff.}}$. This is due to (partial) balancing of the static pressures between the suction and the pressure sides enabled by the permeability [54, 130]. Evidence of this partial balancing is observed by pressure taps in the region close to the TE insert (omitted for conciseness). The perforated TE insert with $l_h = 2.5$ mm, thus denser perforation distribution than $l_h = 5.0$ mm, losses more lift due to the higher permeability [108]. The c_l curves for the perforated TE inserts are noticeably less symmetric with respect to $\alpha_{\text{eff.}} = 0°$. A careful investigation

showed that local bendings at the thin part close to the perforated TE insert tip caused by manufacturing limitations are responsible for this asymmetry.

Correspondingly, Fig. 5.12c compares the drag polars of the baseline TE configuration to TE add-ons configurations for both the LRM and the HRM. Again, the full overview on the baseline drag coefficients can be found in Fig. 5.7d. The results from both the LRM and the HRM consistently show a slight increase in drag when the TE serrations are installed. However, the difference in the c_d increments among the different TE serration geometries cannot be discerned by the present experimental approach. This could be limited by the resolution of the wake rake, i.e. the thickness of the serrations (1 mm) is lower than the spacing between the adjacent total pressure probes on the wake rake (3 mm).

On the other hand, for the perforated TE insert on the LRM, a clear increase of c_d is observed, especially for nonzero $\alpha_{\text{eff.}}$. This could be caused by the surface roughness of the perforated TE inserts where the flow encounters an array of 0.8-mm pore openings [109, 122]. More drag increase is found for l_h = 2.5 mm than l_h = 5.0 mm due to the more concentration of pores.

5.5.2. BOUNDARY-LAYER PARAMETERS AT THE TE REGION

The boundary-layer parameters measured with the hot-wire on top of the LRM with different TE add-ons in the forced configuration at $\alpha_{\text{eff.}}$ = 0° for two selected Re_c are shown in Table 5.4. Because the perforated TE insert cases are also considered, extraction of the boundary-layer parameters following the method described in Section 3.4.1 may not be suitable as it requires determination of the friction velocity and the distance to the wall. To still allow for comparisons between the baseline TE and the TE add-ons, the so-called *diagnostic plot* method described in the work of Vinuesa et al. [199, 200] is employed instead. This method is an iterative method that does not require information on the wall friction and the wall distance. The diagnostic plot method has been proven to be robust for turbulent boundary layers subjecting to pressure gradient [199] and has shown potential to also be suitable for boundary layers over rough walls [201]. Compared to Table 5.3, the extracted edge velocities u_e for the baseline TE cases are approximately 1 m/s lower and the estimated boundary layer thicknesses δ_{99} are approximately 6% lower. Nevertheless, relative comparisons between the baseline TE and the TE add-on cases would still be meaningful.

For the serrated TE, when $\varphi = 0°$, the boundary layer thickness at $x = -0.02c$ is comparable to the baseline TE case. Notably, the serrations are responsible for a local decrease of the boundary-layer momentum and displacement thicknesses. This might be caused by the favorable pressure gradient induced by flow deceleration due to the presence of the serrations. Under a more favourable pressure gradient, the boundary-layer growth rate is smaller.

The change of the boundary layer thickness over the perforated TE insert compared to the baseline TE for the range of Re_c and $\alpha_{\text{eff.}}$ considered is also small, i.e. approximately the same order as that caused by the serrations.

A stronger influence is observed when serrations are put at an angle with respect to the airfoil symmetry line, i.e. flapped serrations, $\varphi \neq 0°$. From the suction side, the

boundary layer develops thicker, while, from the pressure side, the boundary layer is thinner.

5

5

Table 5.4: Boundary-layer properties measured at the TE of the LRM with different TE add-ons at various Re_c and $\alpha_{\text{eff.}} \approx 0°$.

TE configuration	u_∞ (m/s)	Re_c (–)	δ_{99} (mm)	δ^* (mm)	θ (mm)	u_e (m/s)
Baseline	30	0.4×10^6	8.3	2.59	1.33	28.7
Sawtooth serrations, $\varphi = 0°$			7.8	2.32	1.23	27.6
Iron serrations, $\varphi = 0°$			7.9	2.37	1.25	27.6
Sawtooth serrations, $\varphi = 8°$ (s.s.)			8.0	2.56	1.31	27.2
Sawtooth serrations, $\varphi = 8°$ (p.s.)			7.4	2.06	1.15	28.2
Perforated TE insert, $l_h = 5.0$ mm			7.7	2.31	1.21	27.3
Perforated TE insert, $l_h = 2.5$ mm			7.4	2.06	1.15	27.7
Baseline	75	1.0×10^6	6.5	1.81	1.01	69.0
Sawtooth serrations, $\varphi = 0°$			6.5	1.73	0.95	67.6
Iron serrations, $\varphi = 0°$			6.6	1.78	1.03	67.8
Sawtooth serrations, $\varphi = 8°$ (s.s.)			6.7	1.95	1.03	67.0
Sawtooth serrations, $\varphi = 8°$ (p.s.)			6.6	1.69	0.95	69.3
Perforated TE insert, $l_h = 5.0$ mm			6.7	1.76	0.96	69.2
Perforated TE insert, $l_h = 2.5$ mm			6.6	1.80	0.97	67.7

5.5.3. TE NOISE SPECTRA RELATIVE TO THE BASELINE TE

EFFECTS OF GEOMETRIES AND Re_c

Figures 5.13 and 5.14 show the noise reduction with respect to the baseline TE in 1/3-octave bands $\Delta\text{SPL}_{1/3}$ obtained with the different TE add-ons in the A–Tunnel and in the LTT, respectively. In the figures, $\Delta\text{SPL}_{1/3} = \text{SPL}_{1/3} - \text{SPL}_{1/3,\text{ref.}}$ dB, where $\Delta\text{SPL}_{1/3}$ is the noise level for the modified TE cases, and $\text{SPL}_{1/3,\text{ref.}}$ is the baseline TE noise level at the corresponding Re_c and $\alpha_{\text{eff.}}$ (see the absolute levels in Figs. 5.10 and 5.11). The negative $\Delta\text{SPL}_{1/3}$ indicates noise reduction. The effects of increasing Re_c on the $\Delta\text{SPL}_{1/3}$ are investigated in the figures where each subfigure accounts for a specific TE add-on. Only $\alpha_{\text{eff.}} = 0°$ is considered.

For the TE serrations, the frequency where the maximum noise reduction is found appears to increase with the increasing Re_c. This frequency shift follows the work of Gruber et al. [47] who suggested that the $\Delta\text{SPL}_{1/3}$ scales with the Strouhal number based on the TBL thickness, thus decreasing with the increasing Re_c. As also presented in other works [47, 202], the noise reduction has a maximum that depends on the flow velocity. This maximum is around 5 dB for the sawtooth and 7 dB for the iron-shaped serrations. The results also confirm the higher noise reduction observed for iron-shaped serrations in numerical studies by Avallone et al. [141].

Figures 5.13a to 5.13d show that $\Delta\text{SPL}_{1/3}$ measured with the large $3.5c$ and the small $1.25c$ nozzles is similar up to $f = 2$ kHz. Beyond this frequency, approximately 1 dB additional noise reduction is found when measuring with the small ($1.5c$) nozzle. This is likely caused by the lower background noise of the fan operating at a smaller mass flow rate with the smaller nozzle (See the A–Tunnel characterization by Merino–Martinez et al. [151]). For the lowest Re_c tested, the measurements show a second peak of noise reduction around $f = 2$ kHz. This feature is observed for both the sawtooth and the iron serration and is also found in the study of Zhou et al. [51] where the sawtooth and the iron-shaped TE serrations were tested on a flat-plate at similar Re_c to the LRM. This additional noise reduction at relatively higher frequencies could be due to the destructive interference of the high-frequency content in the surface pressure fluctuation occurring close to the serration tip [51, 137]. For the flapped sawtooth serration, a lower noise reduction is found compared to the zero-flap one. This is because the airfoil is effectively cambered when the flapped serrations are installed, and the nonzero airfoil loading (See the change in c_l in Figs. 5.12a) induces formation of a pair of vortices along the edge of the serrations which hinder the noise reduction [197].

Results for the perforated TE inserts are shown in Figs. 5.13e and 5.13f. In average, both perforated TE inserts show a higher maximum noise reduction than the serrations: 5 dB for $l_h = 5.0$ mm and up to 12 dB for $l_h = 2.5$ mm. The magnitude of the maximum noise reduction varies directly with the number of cylindrical holes per unit area. This is because when the number of cylindrical holes per unit area increases, the permeability increases [108]. It is known that the pressure release process (See Section 2.3.1) and therefore the noise mitigation are facilitated when the permeability is higher [54, 109]. Similar to the serrations, the frequency at which the maximum noise reduction is found increases with Re_c. Interestingly, unlike the TE serrations, there are higher frequency ranges with noise increase (positive ΔSPL) for the perforated TE inserts. This is most likely

(a) Sawtooth serrations, $\varphi = 0°$

(b) Iron serrations, $\varphi = 0°$

(c) Sawtooth serrations, $\varphi = -8°$

(d) Sawtooth serrations, $\varphi = 8°$

(e) Perforated TE insert, $l_h = 5.0$ mm
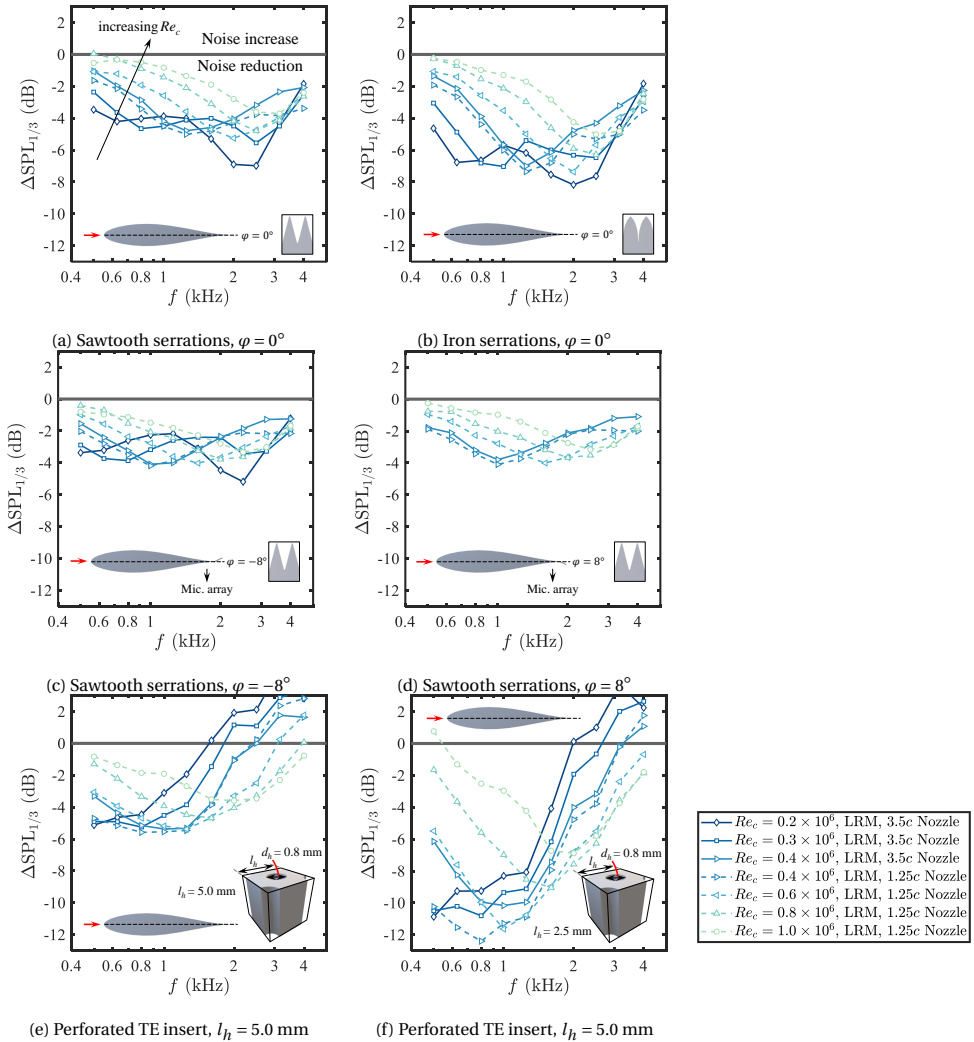
(f) Perforated TE insert, $l_h = 5.0$ mm

Figure 5.13: One-third octave band SPL noise reduction spectra for the LRM under forced transition condition with serrated TEs at various Re_c and $\alpha_{\text{eff.}} \approx 0°$.

to be caused by the surface roughness [105, 106, 109, 125]. Finally, in the same manner as for the TE serrations cases, slightly higher maximum noise attenuation is found when the smaller (1.25c) nozzle is used. This is due to the smaller mass flow rate required by the small nozzle to reach the same flow speed as the larger nozzle (3.5c), and therefore the lower background noise [151].

For the LTT where only the TE serrations are considered, it is worth highlighting that the background noise levels vary largely with the flow speed. In Fig. 5.9b, it can be observed that at $Re_c = 2 \times 10^6$, the spectra are least affected by the LTT background noise. This implies that, for $Re_c = 2 \times 10^6$, the noise reduction can most clearly and completely
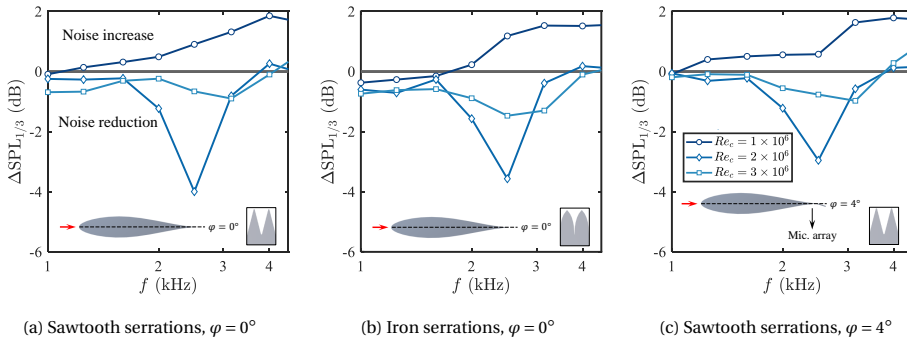
(a) Sawtooth serrations, $\varphi = 0°$ (b) Iron serrations, $\varphi = 0°$ (c) Sawtooth serrations, $\varphi = 4°$

Figure 5.14: One-third octave band SPL noise reduction spectra for the HRM under forced transition condition with TE add-ons at various Re_c and $\alpha_{\text{eff.}} \approx 0°$.

be seen. For the available data, the maximum noise reduction of approximately 4 dB is observed at $f = 2.5$ kHz. The influence of the serration shape on the maximum noise reduction cannot be seen as clearly as for the LRM data from the A–Tunnel. Nevertheless, it can be observed that a slightly lower noise reduction is obtained for the flapped sawtooth serrations compared to the zero-flap counterpart. This is consistent with the finding for the LRM.

EFFECTS OF THE ANGLES OF ATTACK

The influence of increasing $\alpha_{\text{eff.}}$ on $\Delta \text{SPL}_{1/3}$ provided by the TE add-ons are shown in Fig. 5.15 for the LRM. The $\alpha_{\text{eff.}}$ selection is consistent with Fig. 5.11a as well as the selected $Re_c = 0.4 \times 10^6$. As the angle of attack increases, the noise reduction promoted by both the serrations and the perforated TE inserts decreases. For the TE serrations, this phenomenon is attributed to the formation of the vortex pairs, which is present for both the flapped and the non-flap serrations for nonzero $\alpha_{\text{eff.}}$ [48, 197], due to the nonzero c_l (See the change in c_l in Figs. 5.12a and 5.12b). Therefore, this effect is more pronounced for the sawtooth serration with positive flap angle ($\varphi = 8°$), since the aerodynamic loading over the serration is the highest. This configuration shows noise increase at $\alpha_{\text{eff.}} = 4.02°$. On the other hand, the noise reduction spectra provided by the sawtooth serrations with the negative flap angle ($\varphi = -8°$) is least affected when the angle of attack increases due to the least altered airfoil loading, i.e. smallest change in c_l. This can be confirmed from the lift curves in Figs. 5.12a and 5.12b for the positive φ at negative $\alpha_{\text{eff.}}$. It is worth highlighting that, for $\alpha_{\text{eff.}} = 8.04°$, the pronounced noise reduction at $f = 1.6$ kHz may be misleading. This is because the baseline airfoil produces extra tonal noise from the feedback loop caused by the laminar boundary instability (See Fig. 5.11a). This feedback loop and tonal noise are not present for the TE add-on cases. The same variations of $\Delta \text{SPL}_{1/3}$ with $\alpha_{\text{eff.}}$ are also captured by the experiment with the HRM (See Fig. 5.16).

Similarly, noise reduction by the perforated TE inserts also decreases with the increasing angle of attack. This trend has been observed in previous works and could be attributed to the less efficient pressure release process when the angle of attack increases [105, 109, 122]. Interestingly, the noise increase due to roughness appears to be less

sensitive to the increasing angle of attack and is lower than the noise increase due to the flapped serrations.

(a) $\alpha_{\text{eff.}} = 0°$

(b) $\alpha_{\text{eff.}} = 4°$

(c) $\alpha_{\text{eff.}} = 8°$

Figure 5.15: One-third octave band sound pressure level noise reduction spectra for the LRM under forced transition condition with TE add-ons at $Re_c = 0.4 \times 10^6$ and various $\alpha_{\text{eff.}}$.

(a) $\alpha_{\text{eff.}} \approx 0°$

(b) $\alpha_{\text{eff.}} \approx 4°$
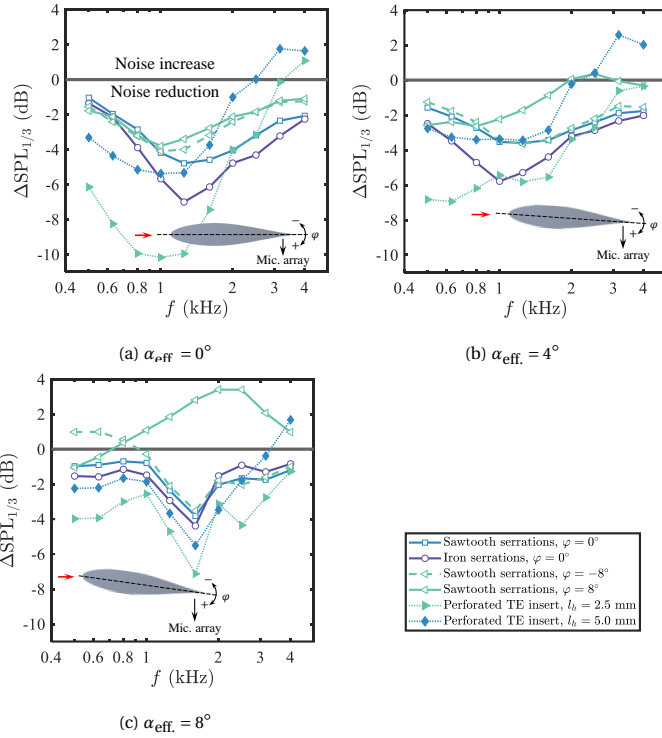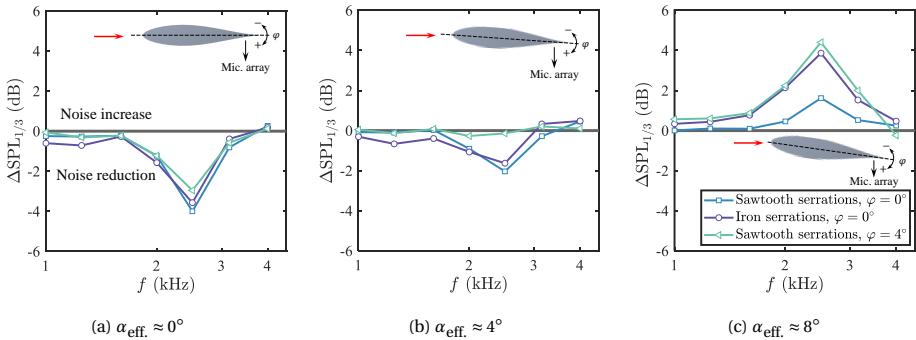
(c) $\alpha_{\text{eff.}} \approx 8°$

Figure 5.16: One-third octave band sound pressure level noise reduction spectra for the HRM under forced transition condition with serrated TEs at $Re_c = 2 \times 10^6$ and various $\alpha_{\text{eff.}}$.

5.6. CONCLUSIONS

This chapter presents aeroacoustic characterization of the NACA 63_3–018 airfoil, which is a profile in an airfoil family commonly employed on wind turbines, in a broad chord-based Reynolds number Re_c range from 0.2×10^6 to 3×10^6. Experiments were carried out using two scaled NACA 63_3–018 airfoil in two wind-tunnel facilities: 0.2-m-chord low-Re_c model (LRM) for low-Re_c tests in the A–Tunnel and 0.9-m-chord high-Re_c model (HRM) for high-Re_c tests in the Low-Turbulence Tunnel (LTT). The airfoils were tested with and without turbulator strips applied to force the laminar-to-turbulent transition location denoted as the forced and clean configurations, respectively. For the forced configurations, trailing-edge (TE) add ons, namely TE serrations and perforated TE inserts are also considered.

For the baseline 63_3–018 airfoil, results show expected variations of the aerodynamic coefficients with Re_c, increase of the maximum lift coefficient and reduction of the drag coefficient with the increasing Re_c. Boundary layer thicknesses at the TE also reduce with the increasing Re_c. The forced configuration increases the boundary layer displacement thickness at the TE compared to the clean configuration. This, in turn, increases the far-field Sound Pressure Level (SPL) of the TE noise for the forced configuration for approximately 5 dB compared to the clean one.

TE serrations increase the lift coefficient compared to the baseline TE. The lift increase depends on the serrations wetted area and flap angle. On the contrary, the perforated TE inserts cause lift reduction. The lift loss varies directly with the permeability. The TE serrations slightly increase the aerodynamic drag and the difference among the different TE serrations geometry is not discernible. On the other hand, the perforated TE insert increases the aerodynamic much more outstandingly, especially at nonzero angles of attack due to surface roughness. At zero-lift condition, the TE add ons hardly alter the boundary-layer characteristics at the TE, compared to the baseline TE.

Iron-shaped serrations provides 2 dB extra maximum noise reduction compared to the conventional sawtooth shape. The noise reduction provided by the TE serrations is also sensitive to the increasing airfoil loading. At relatively higher airfoil loading, noise increase is found. In average, the perforated TE inserts provide higher noise reduction compared to the TE serrations. However, roughness noise increase is found at higher frequencies. The noise reduction capability of the perforated TE insert also deteriorates when the airfoil loading increases.

5

6

AN ALTERNATIVE PERMEABLE TOPOLOGY DESIGN SPACE FOR TRAILING-EDGE NOISE ATTENUATION[1]
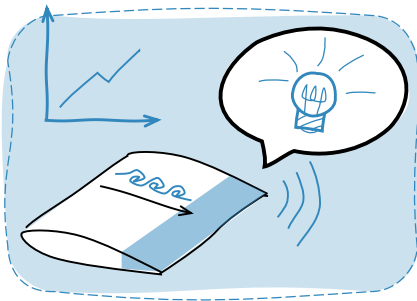
This chapter focuses upon a new permeable topology design concept for Turbulent Boundary Layer Trailing-Edge (TBL–TE) noise attenuation. The present permeable topology has unconventional characteristics with respect to metal foams: a combination of a low flow resistivity r and a high form drag coefficient C, realized by a Kevlar-covered 3D-printed perforated structure. An experimental study featuring a NACA 0018 airfoil model with a Kevlar-covered 3D-printed TE insert is carried out. A broadband TBL–TE noise reduction up to approximately 5 dB, compared to a solid TE, is found. This reduction varies only slightly with airfoil loading (lower than 1 dB variation), in contrast to the porous metal foams (up to 3 dB variation). The variation given by all the permeable materials considered is found to decrease with the increasing C. Additionally, the aerodynamic drag as well as the roughness noise increase of the airfoil equipped with the present TE insert are infinitesimal compared to the fully solid airfoil. Finally, design guidelines for permeable TE are proposed: the permeable material shall have a combination of a low flow resistivity and a high form drag coefficient as well as a negligible surface roughness.

6.1. INTRODUCTION

Literature review presented in Section 2.3.1 has shown that there are still downsides of the permeable Trailing Edge (TE) technology for Turbulent Boundary Layer Trailing-Edge (TBL–TE) noise reduction that make this technology unappealing for practical implementations. These are, for instance, the rough surface of the metal foams that causes the roughness noise and the aerodynamic drag increase, and the tendency of the perforated channels to produce tonal noise. To overcome these issues, this chapter considers an alternative design for a permeable TE insert. Performance of this design is assessed experimentally by wind-tunnel tests of a NACA 0018 airfoil with an unconventional permeable TE insert. TBL–TE noise reduction and aerodynamic performances of this design are compared against those of the conventional porous metal foams. Extensive descriptions of the NACA 0018 airfoil model, the wind-tunnel facility, and the flow measurement techniques are provided in Chapter 3. Acoustic measurement and post-processing techniques are described in Chapter 4. The rest of this chapter focuses on the specifications of the alternative permeable TE design (Section 6.2), the results and discussion (Section 6.3), the conclusions and further possible applications (Sections 6.4).

6.2. SPECIFICATIONS AND CHARACTERIZATION OF THE ALTERNATIVE PERMEABLE TOPOLOGY DESIGN SPACE

An unconventional combination of the flow resistivity and form drag coefficient is proposed. The concept is realized by combining two permeable materials: a 3D-printed perforated structure covered by a Kevlar fabric. The present study focuses on the use of a highly permeable 3D-printed insert with straight channels to form a simple perforated structure. The pores directly connect regions of the suction and the pressure sides, allowing a point-to-point communication between both sides. On the other hand, a stretched Kevlar fabric, which has widely been used in aeroacoustic applications to replace hard walls of closed-section wind tunnels to allow for acoustic measurements [153, 155, 203] due to their ability to be acoustically transparent while being aerodynamically impermeable [153, 155], is used to cover the surface of the 3D-printed perforated structure. There are two main purposes; first, the relatively smooth texture of the Kevlar fabric is expected to mitigate the roughness noise; second, the flow-impermeable Kevlar fabric is used to cover the regular highly permeable 3D-printed pattern to prevent the tonal noise generation. Overall, this present permeable material combination is expected to provide a mixture of low resistivity (given by the highly permeable 3D-printed pattern) and high form drag coefficient (given by the Kevlar sheet). Aeroacoustic characteristics of a NACA 0018 airfoil with Kevlar-covered 3D printed TE insert is investigated with a close comparison to two other metal-foam TE inserts of which well-established characteristics are available in literature [105, 122, 125].

Figure 6.1 shows the 3D-printed permeable TE insert covered by the Kevlar sheet installed on the NACA 0018 airfoil model together with close-up views of the 3D-printed TE insert and the Kevlar fabric alone. The 3D-printed permeable TE insert was produced using an *Ultimaker 3* 3D printer. Polylactic Acid (PLA) was used as printing material. The honeycomb-like pattern was obtained by replicating the unit pattern shown in Fig. 6.1.

The hexagonal voids were surrounded by 0.8-mm-width 3D-printed PLA edges, forming a perforation parallel to the y-direction connecting the pressure and the suction sides of the airfoil.
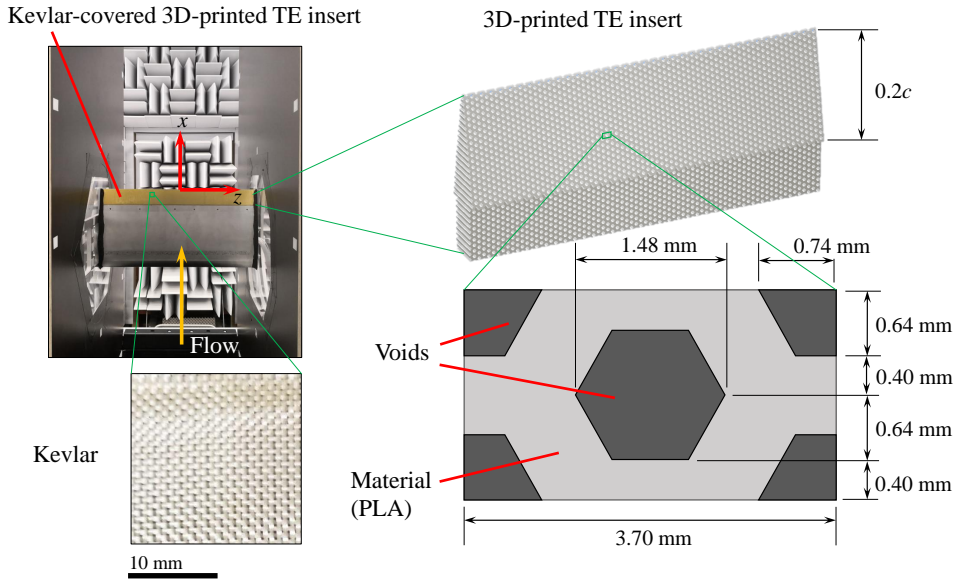

Figure 6.1: 3D-printed permeable TE insert covered by a Kevlar fabric, installed on a NACA 0018 airfoil model with a close-up view on the Kevlar fabric, the 3D-printed TE insert, and the perforated pattern.

The wind-tunnel tests were carried out both with and without the Kevlar sheet covering the 3D-printed TE insert. For the Kevlar-covered 3D-printed TE insert case as shown in Fig. 6.1, the Kevlar sheet was glued to adhere on the surface of the 3D-printed permeable TE insert. The aviation-standard Kevlar *49 T 965* fabric provided by *Engineered Cramer Composites* [154] was used. The Kevlar foil has a weight-to-area ratio of 61 ± 3 g/m^2, a density of 1.45 ± 0.05 g/m^3, and a thickness of 0.12 ± 0.02 mm.

Porous metal-foam TE inserts were also tested on the airfoil as baseline references. The porous metal-foam made of NiCrAl was manufactured by *Alantum*, featuring dodecahedron-shaped cells. Due to the well-established characterization and experimental data in the literature, the porous metal-foam TE with a cell diameter d_c of 0.8 mm and 0.45 mm were chosen. Details on these porous metal-foam TE inserts, as well as their extensive test results can be found in previous literature [105, 122, 125].

A plot showing the measured static pressure drop Δp across the 3D-printed perforated Polylactic Acid (PLA) material sample having the thickness $t_s = 60$ mm with and without the Kevlar sheet for 15 different Darcy velocities v_D is shown in Fig. 6.2 (left). The curves obtained by fitting the measured data to Eq. (2.23) to determine the air flow resistivity r, the permeability K, and the form drag coefficient C are also given in solid and dashed lines.

The resulting r, K, and C are given in Table 6.1. The parameters obtained from metal-foam samples with the same thickness t_s from the previous studies are also provided for comparison.
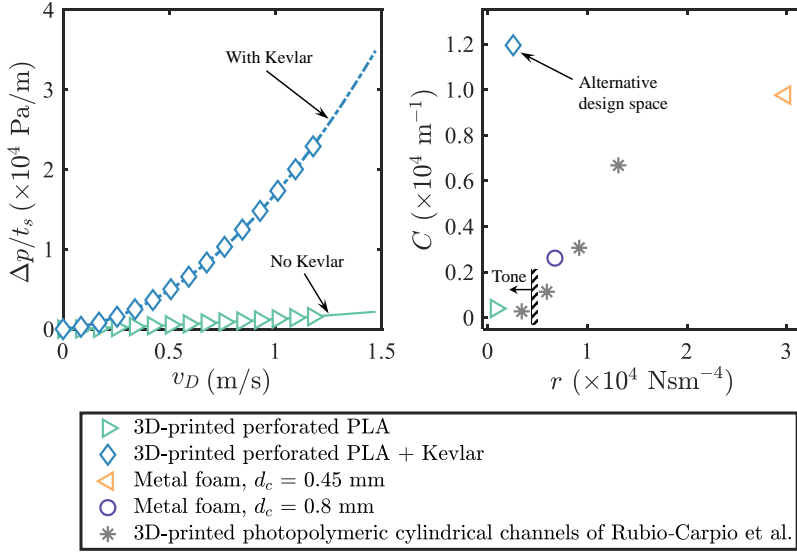

Figure 6.2: Left: measured static pressure drop Δp across the 3D-printed perforated PLA samples having the thickness t_s = 60 mm with and without the Kevlar sheet for 15 different Darcy velocities v_D, including the curve-fitting of Eq. (2.23) to the measured data. Right: measured r versus C for the permeable material samples tested and those from permeable materials in literature.

Table 6.1: Measured properties of the permeable material samples and metal-foam materials.

Material sample	r (Nsm^{-4})	K ($\times 10^{-10}$m^2)	C (m^{-1})
3D-printed perforated PLA	787	233	404
3D-printed perforated PLA + Kevlar	2,537	72	11,945
Metal foam, d_c = 0.45 mm [105, 122]	29,850	6	9,758
Metal foam, d_c = 0.8 mm [105, 122]	6,728	27	2,613

For the perforated 3D-printed PLA sample without the Kevlar sheet, a relatively low static pressure drop is observed, resulting in the lowest r. This is mainly due to the alignment of the straight pores with the flow direction in the permeability test section which facilitates the air flow. On the other hand, the 3D-printed perforated material sample with the Kevlar sheet shows an increase of the static pressure drop as well as a higher sensitivity of the static pressure drop with the increasing v_D. This results in an increase of r and a drastic increase of the form drag coefficient C, the coefficient of v_D^2 in Eq. (2.23), which dictates the dependence of the static pressure drop on v_D.

A scatter plot visualizing the measured r and C of the permeable material samples tested and those from the metal-foam samples is given in Fig. 6.2 (right). Apart from the

present (Kevlar-covered) 3D-printed perforated material and metal-foam samples, the values of r and C of multiple 3D-printed photopolymeric cylindrical channel samples used in the work of Rubio–Carpio et al. [108, 133] are also shown. It is important to note that, for these particular cases, the material sample thickness t_s are 10 mm instead of 60 mm. Nevertheless, the values of r and C if the thickness t_s would be 60 mm are not likely to differ drastically from the values shown since t_s is already much larger than the pore sizes and cell diameters [125]. Thus, the relative trends are still worth being compared to the present materials. The readers are referred to the original publication [108, 133] for detailed specifications of these particular material samples. For the 3D-printed perforated material without the Kevlar sheet as well as the metal-foam materials, the increase of C seems to correlate with the increase of r in a similar fashion. The increase of C with respect to r for the 3D-printed photopolymeric material having cylindrical channels also appears to follow the aforementioned trend in a slightly less gradual manner. Distinctively, the 3D-printed perforated material with the Kevlar sheet is far different from this trend; for a relatively low value of r, the value of C is around the same order of the metal foam sample with d_c = 0.45 mm, which has the highest r. This means that the application of the Kevlar sheet on a highly permeable 3D-printed perforated topology creates a rather unconventional combination of r and C.

The present topology of the 3D-printed perforated material sample with and without the Kevlar sheet give lower values of r than the lowest value of r found in the collection of 3D-printed photopolymeric materials. In the literature [133], tonal noise increase by the airfoil equipped with the 3D-printed TE insert with the lowest r has been reported, suggesting that there exists a threshold of r below which the tonal noise would occur. The location of this threshold lies somewhere between the case with the lowest r and the case next to it, where the tonal noise was no longer found. An approximated location of this threshold is also illustrated in Fig. 6.2 (right). Thus, in the present investigation, one could certainly expect the airfoil equipped with the 3D-printed perforated trailing-edge insert without the Kevlar sheet to also produce the tonal noise. However, for the 3D-printed perforated insert with the Kevlar sheet, despite also having a lower value of r than the identified threshold, production of the tonal noise is less certain. This is because the high value of C which does not follow the aforementioned general trend may play a role. Noise emission characteristics of the airfoil equipped with these materials as permeable trailing-edge inserts are investigated in the coming sections.

6.3. Results and Discussion

6.3.1. Narrow-band noise spectra

The measured narrow-band Sound Pressure Level (SPL) spectra (frequency resolution of 10 Hz) at $Re_c = 2.6 \times 10^5$ and 4.6×10^5, both at $\alpha_{\text{geom.}} = 0°$, of the airfoil with the solid TE, the 3D-printed perforated TE inserts with and without the Kevlar sheet, as well as the metal-foam TE inserts are shown in Fig. 6.3. An alternative frequency axis is also given in terms of the non-dimensional Strouhal number based on the displacement thickness at the trailing edge on the suction side of the solid NACA 0018 airfoil $St_{\delta_s^*|\text{TE,ref.}}$, where $\delta_s^*|_{\text{TE,ref.}}$ represents the displacement thickness of the boundary layer at the trailing edge (TE) on the suction side of the solid (reference) NACA 0018 airfoil, calculated by XFOIL [101],

i.e. $St_{\delta_s^*|_{\text{TE,ref.}}} = (f\delta_s^*|_{\text{TE,ref.}})/u_\infty$. Calculation with XFOIL was done by setting a forced transition at the same chordwise location $x/c = -0.8$ as on the actual airfoil on both the suction and the pressure sides. In previous studies, frequency scaling with $\delta_s^*|_{\text{TE,ref.}}$ has been found to provide a good collapse of the spectra [29], and a good agreement between $\delta_s^*|_{\text{TE,ref.}}$ calculated from XFOIL and the actual value has been demonstrated [36, 105, 204]. In addition, for each Re_c, a spectrum of the measured empty test section noise, i.e. without the airfoil, obtained by the identical beamforming methodology is also shown.

Comparing the spectra with the measured noise from the empty test section, a signal to noise ratio between 5 and 15 dB is obtained up to $f \approx 3$ kHz. Above this frequency, the signal to noise ratio is lower. Therefore, it is motivated to exclude the portion of the spectra above 3 kHz in further analysis of this chapter.

For the metal-foam TEs, up to 10 dB broadband attenuation at low frequencies as well as a broadband noise increase at high frequencies are observed. The magnitudes of noise attenuation and noise increase follow the dimension of the cell diameter d_c. As explained in previous studies, increasing d_c reduces the flow resistivity r (see the previous section) which in turns increases noise attenuation [82, 109]. However, increasing d_c also increases the surface roughness which results in the increasing roughness noise at high frequencies [54, 106, 109, 122].

For the 3D-printed perforated TE insert without the Kevlar sheet, despite having a broadband noise attenuation compared to the solid counterpart, a series of strong tonal peaks are observed as anticipated. In addition, noise increase due to roughness at high frequencies can also be seen. The magnitude of the roughness noise is higher than that given by the metal-foam TE with the largest d_c, thus implying the 3D-printed permeable TE has a higher equivalent roughness than that of the metal foam. This is reasonable since the hexagonal 3D-printed pore has a larger diameter than the largest d_c of 0.8 mm of the metal foam. Additionally, the pores extend to the opposite side of the airfoil, creating a much larger effective depth than the pore cells in the metal foams.

When the Kevlar sheet is applied on the 3D-printed perforated insert, the tonal peaks as well as the roughness noise are mitigated. A broadband noise reduction of approximately 5 dB with respect to the solid TE is observed. The spectra of the Kevlar-covered 3D-printed perforated TE insert case seem to be comparable to those of the metal-foam TE insert with $d_c = 0.45$ mm; the Kevlar-covered 3D-printed perforated TE insert gives approximately 2 dB less noise attenuation at low frequencies and 2 dB more roughness noise attenuation at high frequencies. Noticeably, despite having much lower flow resistivity r than the metal-foam material with $d_c = 0.45$ mm, the Kevlar-covered 3D-printed TE does not give additional noise attenuation compared to this metal foam case. This suggests that the ranking according to r may not be a good indicator of the ranking of noise attenuation when permeable materials with different topologies are considered altogether [133]. In the upcoming sections, dependence of noise attenuation magnitude on different material characteristics is further discussed to identify a better indicator for noise attenuation based on the permeable material characteristics.

Interestingly, although the value of r for the Kevlar-covered 3D-printed permeable material is lower than the threshold below which the tonal noise is expected, the material
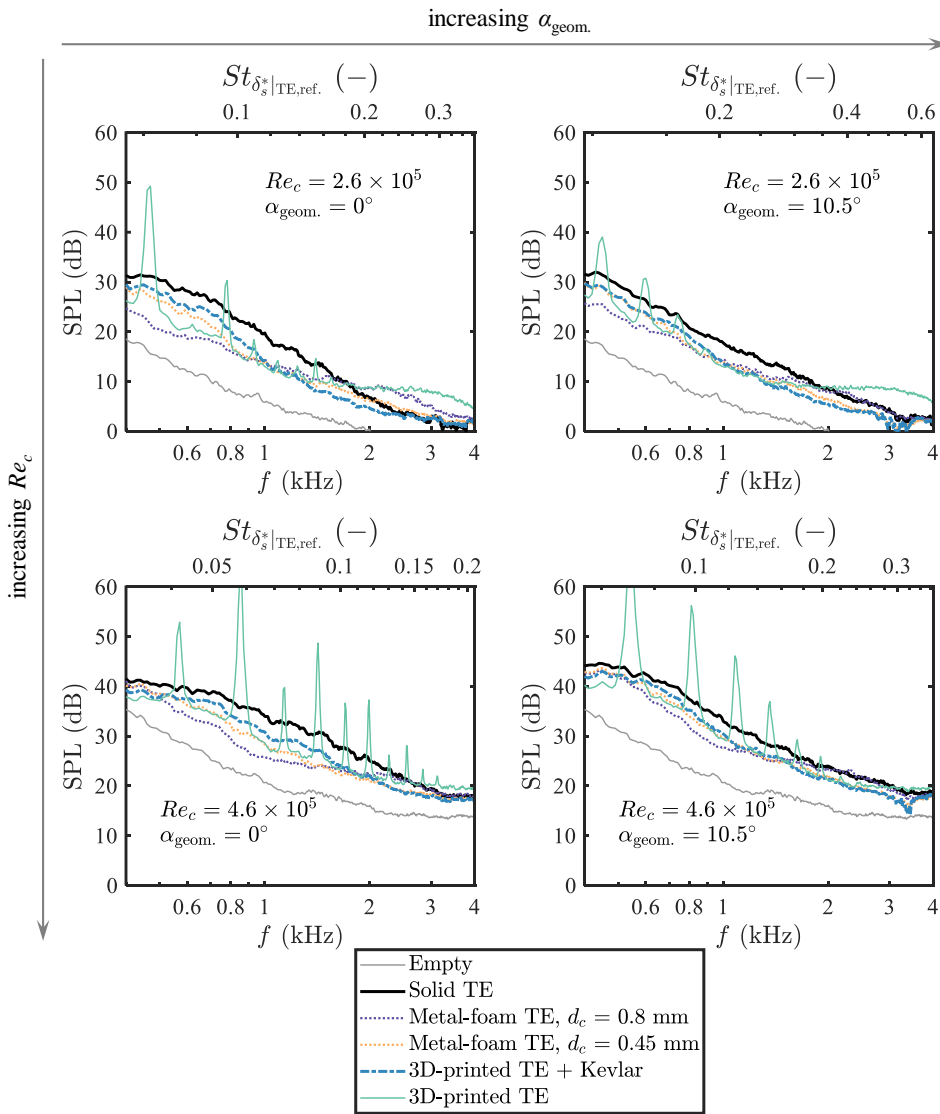
Figure 6.3: Narrow-band SPL spectra of the NACA 0018 airfoil with various permeable TE inserts at different given combinations of chord-based Reynolds numbers and geometrical angles of attack, compared to the reference solid TE insert and empty test section background noise.

has a high value of C, and, evidently, this characteristic helps to mitigate the tonal noise. Therefore, with a slight modification, it is possible to still maintain a low value of r while preventing the tonal noise. One possible way is by increasing the form drag coefficient C across the permeable topology, e.g. by applying the Kevlar sheet on the surface.

To further address the tonal noise, the spectra from the 3D-printed perforated TE
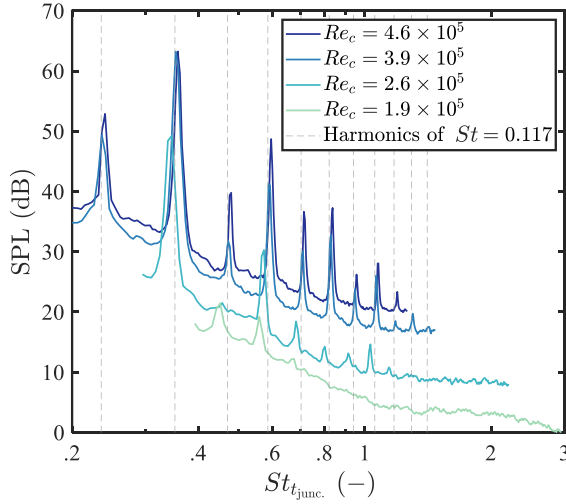
Figure 6.4: Narrow-band SPL spectra of the NACA 0018 airfoil with the 3D-printed perforated TE insert at different chord-based Reynolds numbers and zero-degree geometrical angles of attack presented in terms of the Strouhal number based on the thickness of the airfoil at x/c = -0.2, together with vertical lines marking harmonics of the fundamental Strouhal number.

6

without the Kevlar sheet are exclusively examined. The highly permeable 3D-printed perforated pattern may cause a sudden streamwise impedance jump, creating effectively a blunt trailing edge [29] at the junction between the solid and the permeable part of the airfoil at x/c = -0.2. This could promote tonal noise resulting from vortex shedding [108, 109]. Figure 6.4 shows exclusively the measured spectra of the 3D-printed perforated TE insert case, from which the tonal noise is produced, for all the Re_c considered at $\alpha_{\text{geom.}} = 0°$. The frequencies are non-dimensionalized to Strouhal numbers based on the thickness of the airfoil at the junction $St_{t_{\text{junc.}}} = f\,t_{\text{junc.}}/u_\infty$, where $t_{\text{junc.}} = 16$ mm is the thickness of the airfoil at at x/c = -0.2. Noticeably, the tonal peaks from all the Re_c collapse. The fundamental Strouhal number $St \approx 0.117$ has been found by linear regression analysis [108] of the tonal peaks ($R^2 = 0.9975$). This value is in line with the peak Strouhal number between 0.11 and 0.17 anticipated by Brooks et al. [29] for the blunt trailing edge noise. The harmonics of $St = 0.117$ are marked by the vertical lines which show good alignments with the tonal peaks. The presence of the vortex shedding is confirmed by the wake survey to be presented in Fig. 6.14 on page 106. However, due to the presence of the tonal noise, the 3D-printed perforated TE insert case without the Kevlar is excluded in the upcoming noise analysis in 1/3-octave bands.

6.3.2. Broadband noise attenuation variability with angle of attack

To further highlight the broadband attenuation of TBL–TE noise, Fig. 6.5 shows the values of $\Delta\text{SPL}_{1/3}$ which are the difference between the 1/3-octave SPL of each case and the 1/3-octave SPL of the solid TE (reference) case, i.e. $\Delta\text{SPL}_{1/3} = \text{SPL}_{1/3} - \text{SPL}_{1/3,\,\text{ref.}}$

dB. Thus the positive and negative values of $\Delta\text{SPL}_{1/3}$ represent noise increase and noise attenuation, respectively. The values of $\Delta\text{SPL}_{1/3}$ are shown for $Re_c = 2.6 \times 10^5$ and 4.6×10^5, at $\alpha_{\text{geom.}} = 0°$ and $10.5°$. An alternative non-dimensional frequency axis in terms of $St_{\delta_s^*|\text{TE,ref.}}$ is also given in the same manner as in Fig 6.3.

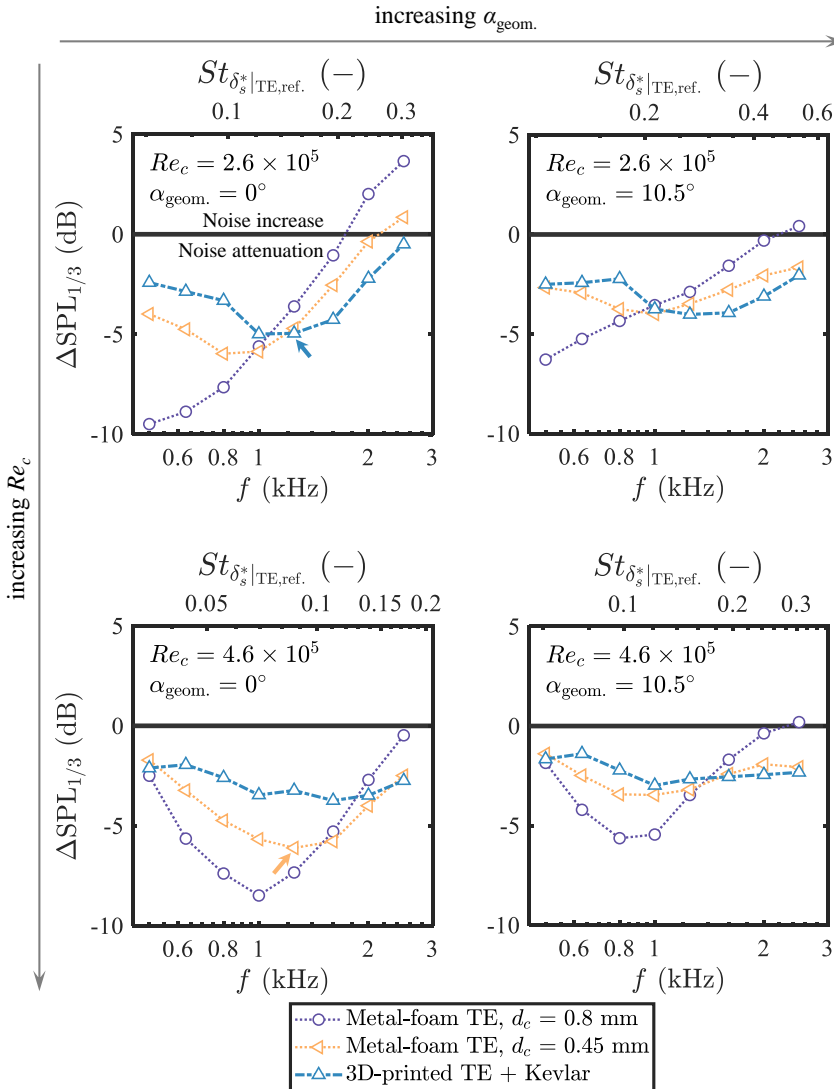Figure 6.5: 1/3-octave band SPL spectra of various permeable TE inserts at different combinations of chord-based Reynolds numbers and geometrical angles of attack relative to those of the reference solid TE case ($\Delta\text{SPL}_{1/3} = \text{SPL}_{1/3} - \text{SPL}_{1/3,\,\text{ref.}}$ dB).

For $\alpha_{\text{geom.}} = 0°$, the noise attenuation trend follows what has been discussed in Fig. 6.3.

Maximum noise reduction of approximately 9 dB at $St_{\delta_s^*}|_{\text{TE,ref.}} \approx 0.06$ and 6 dB at $St_{\delta_s^*}|_{\text{TE,ref.}} \approx 0.1$ are found for the metal-foam TE insert cases with $d_c = 0.8$ and 0.45 mm, respectively. Observably, the higher the noise attenuation, the more variation of $\Delta\text{SPL}_{1/3}$ with the frequency, and the lower the frequency (i.e. Strouhal number) where the maximum noise attenuation occurs. For the Kevlar-covered 3D-printed TE insert, the maximum noise reduction of 3-5 dB is seen at a slightly higher $St_{\delta_s^*}|_{\text{TE,ref.}} \approx 0.12$. Among the permeable TE inserts considered, the Kevlar-covered 3D-printed TE insert appears to give the lowest roughness noise increase at high frequencies.

When $\alpha_{\text{geom.}}$ increases to 10.5°, the magnitudes of the maximum noise attenuation given by the metal-foam TE insert in the frequency range considered reduce by approximately 4 dB and 2 dB, for $d_c = 0.8$ mm and 0.45 mm, respectively, meaning that when the angle of attack increases, the metal foams become relatively less effective in noise attenuation. In other words, there is a *variability* of noise attenuation by the metal-foam TE insert with the increasing angle of attack, and the variability is larger when d_c is larger. This observation is in line with a previous study [125]. Interestingly, the Kevlar-covered 3D-printed TE exhibits around 1 dB variability, i.e. less than that of the metal foams.

To address the noise attenuation variability, let ΔOSPL denote the difference between the Overall Sound Pressure Level (OSPL) of a considered case and the reference solid TE case, i.e. $\Delta\text{OSPL} = \text{OSPL} - \text{OSPL}_{\text{ref.}}$ dB, the variability of ΔOSPL with the angle of attack is taken as the relative value between ΔOSPL at a particular geometrical of attack $\alpha_{\text{geom.}}$ and that at the lowest geometrical angle of attack $\alpha_{\text{geom.,min.}}$. For convenience, a parameter $V_{\Delta\text{OSPL}}^{\alpha_{\text{geom.}}}$ is used to denote this variability, where

$$V_{\Delta\text{OSPL}}^{\alpha_{\text{geom.}}} = \Delta\text{OSPL} - \Delta\text{OSPL}_{\alpha_{\text{geom.,min.}}} \text{ dB}. \tag{6.1}$$

Thus, by definition, a positive value of $V_{\Delta\text{OSPL}}^{\alpha_{\text{geom.}}}$ represents a less effective noise attenuation capability than at $\alpha_{\text{geom.,min.}}$. As an attempt to exclude the contribution of the roughness noise increase, summation of $\Delta\text{SPL}_{1/3}$ to obtain the OSPL is done only when $\Delta\text{SPL}_{1/3} < 0$, i.e. at the sound frequencies where the noise attenuation is achieved.

Examination of $V_{\Delta\text{OSPL}}^{\alpha_{\text{geom.}}}$ of the permeable TE inserts is given in Fig. 6.6 between $Re_c = 2.6 \times 10^5$ and 4.6×10^5. The trend confirms the noise attenuation variability up to 3 dB for the metal-foam TE insert cases for the range of $\alpha_{\text{geom.}}$ considered. The variability is larger for a larger d_c. The minimum noise reduction variability (lower than 1 dB) is found for the Kevlar-covered 3D-printed TE. Noticeably, the magnitude of $V_{\Delta\text{OSPL}}^{\alpha_{\text{geom.}}}$ seems to vary inversely with the form drag coefficient C of the permeable material used, i.e. the higher C, the lower $V_{\Delta\text{OSPL}}^{\alpha_{\text{geom.}}}$. This is likely because when $\alpha_{\text{geom.}}$ increases, a stronger pressure gradient between the suction and the pressure sides is present. To illustrate this, the curves showing the pressure gradient between the suction and the pressure sides of the airfoil at the junction between the solid and the permeable extent $|\Delta c_p|_{\text{junc.}}$, where 'junc.' denotes the chordwise location of this junction (x/c = -0.2), calculated from XFOIL [101] are also given Fig. 6.6. These results are associated to the right vertical axes. The increase of the pressure gradient may induce cross flow through the permeable material. This cross flow is likely to reduce the effectiveness of the pressure release mechanism [122] which contributes to the noise attenuation. Therefore, since the value of C indicates the ability of the material to withstand the cross flow resulting from the pressure gradient
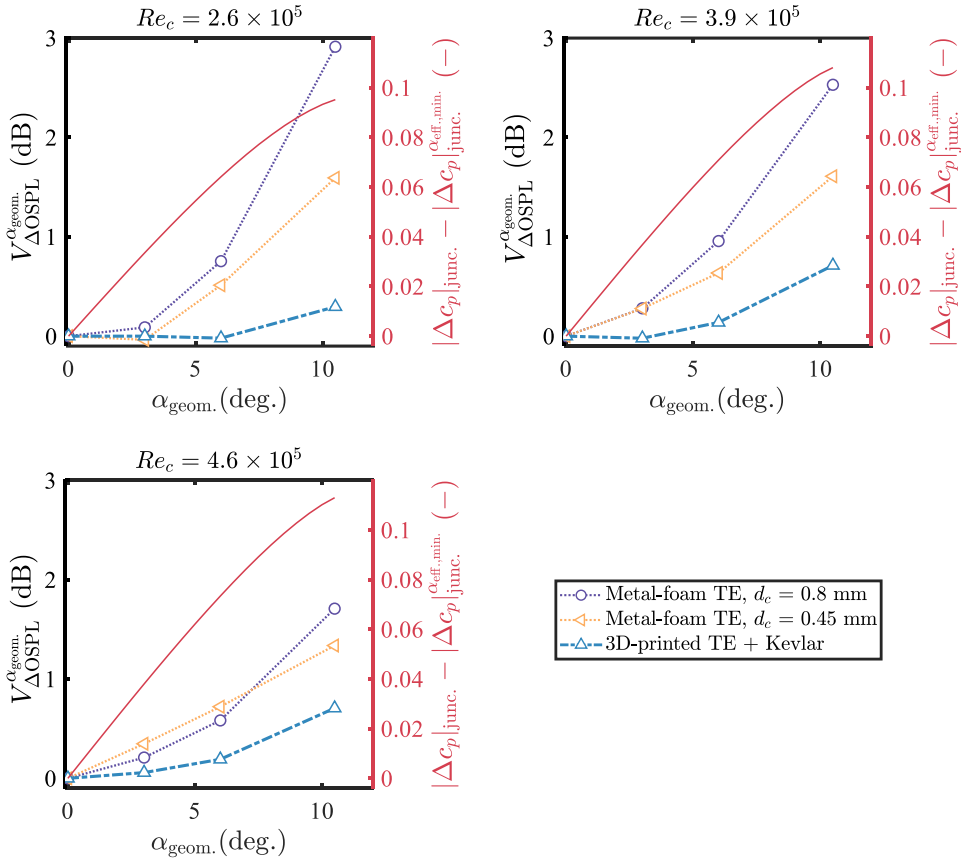
Figure 6.6: Noise reduction variability with respect to the angle of attack of various permeable TE inserts at different chord-based Reynolds numbers relative to the noise reduction at zero-degree geometrical angle of attack.

[205], the noise attenuation capability provided by a permeable material with a larger C will have a lower tendency to become less effective when the angle of attack, i.e. the pressure gradient, increases.

Similarly, an increase of $|\Delta c_p|_{junc.}$ can also be seen as the chord-based Reynolds number Re_c increases as visualized in Fig. 6.7, where the noise attenuation variability with Re_c, $V_{\Delta OSPL}^{Re_c}$, is examined. The definition of $V_{\Delta OSPL}^{Re_c}$ is analogous to that of $V_{\Delta OSPL}^{\alpha_{geom.}}$ [See Eq. (6.1)]. For conciseness, only one case (at $\alpha_{geom.} = 6°$) is given in Fig. 6.7 as an example. It can clearly be seen that the metal-foam TE with $d_c = 0.8$ mm shows the largest $V_{\Delta OSPL}^{Re_c}$ while the Kevlar-covered 3D-printed TE insert gives the lowest $V_{\Delta OSPL}^{Re_c}$. Again, as $|\Delta c_p|_{junc.}$ increases with Re_c, the magnitude of $V_{\Delta OSPL}^{Re_c}$ seems to vary inversely with the form drag coefficient C of the permeable material as for $V_{\Delta OSPL}^{\alpha_{geom.}}$ discussed previously. To further address this observation, the next section examines the links between the characterized permeable material properties and the broadband noise attenuation, including its
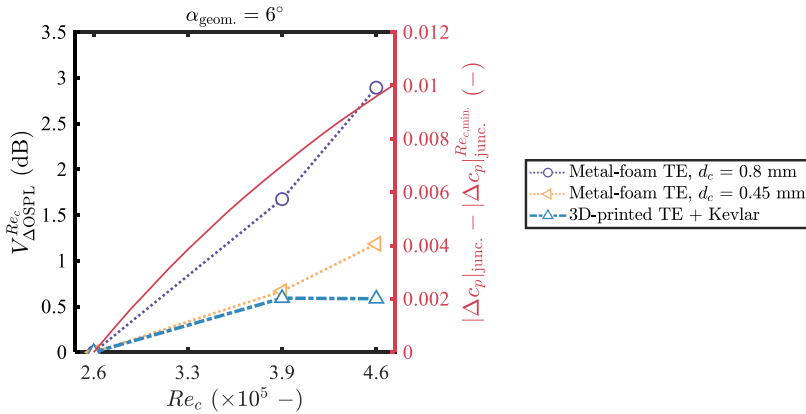
Figure 6.7: Noise reduction variability with respect to the chord-based Reynolds number of various permeable TE inserts at a geometrical angle of attack of 6 degree relative to the noise reduction at the lowest chord based Reynolds number.

variability with $\alpha_{\text{geom.}}$ and Re_c.

6.3.3. MATERIAL PROPERTIES AND NOISE ATTENUATION CHARACTERISTICS

In Fig. 6.8, the parameter ΔOSPL indicating the overall noise attenuation with respect to the reference solid TE is plotted as functions of r (left) and C (right) for the permeable TE inserts examined. In this case, data is taken from $Re_c = 4.6 \times 10^5$. When only the metal-foam TE inserts are considered, it can be seen that the parameter ΔOSPL varies proportionally with r and C, meaning that when the flow resistivity r or the form drag coefficient C increases, less noise attenuation is obtained. However, once the Kevlar-covered 3D-printed TE insert is considered together with the metal-foam TE inserts, the same observation no longer holds for the flow resistivity r as shown in Fig. 6.8 (left). Interestingly, the lower noise attenuation capability can still be related to the increase of the form drag coefficient C when the different permeable material topologies are considered altogether.

Following the same format as Fig. 6.8, Figs. 6.9 and 6.10 relate the material properties to the maximum noise attenuation variability with $\alpha_{\text{geom.}}$ and Re_c, $V_{\Delta\text{OSPL,max.}}^{\alpha_{\text{geom.}}}$ and $V_{\Delta\text{OSPL,max.}}^{Re_c}$, respectively. A clear increase of $V_{\Delta\text{OSPL,max.}}^{\alpha_{\text{geom.}}}$ and $V_{\Delta\text{OSPL,max.}}^{Re_c}$ with the inverse of C can be seen in the right subfigures, confirming the observation made in the previous section. Increasing the form drag coefficient C increases the material's ability to withstand the cross flow due to the pressure gradient between the suction and the pressure sides, which strengthens as $\alpha_{\text{geom.}}$ and/or Re_c increase as illustrated in Figs. 6.6 and 6.7. Prevention of this possible cross flow could help to sustain the effectiveness of the noise attenuation mechanisms and therefore keep the variability low. Again, when comparing all the permeable TE insert cases, no clear relations of $V_{\Delta\text{OSPL,max.}}^{\alpha_{\text{geom.}}}$ and $V_{\Delta\text{OSPL,max.}}^{Re_c}$ can be drawn to the inverse of r as shown in the left subfigures.

This section has demonstrated that, while the flow resistivity may be related to the
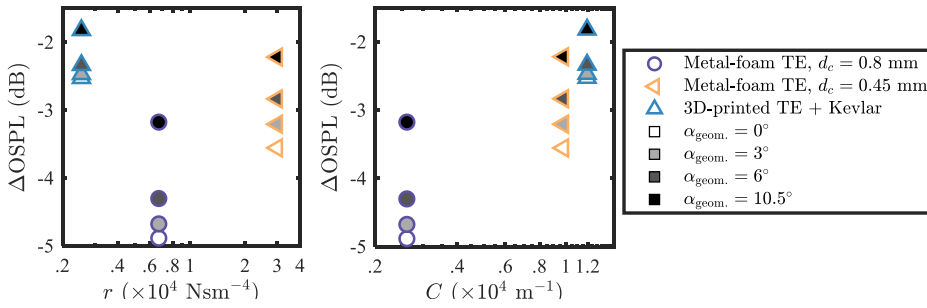
Figure 6.8: Noise attenuation of the airfoil with various permeable TE inserts at the chord-based Reynolds number of $Re_c = 4.6 \times 10^5$ and various geometrical angles of attack as functions of the flow resistivity (left) and form drag coefficient (right).

Figure 6.9: Noise attenuation variability with the geometrical angle of attack of the airfoil with various permeable TE inserts at various chord-based Reynolds numbers as functions of the flow resistivity (left) and form drag coefficient (right).

Figure 6.10: Noise attenuation variability with the chord-based Reynolds number of the airfoil with various permeable TE inserts at various geometrical angles of attack as functions of the flow resistivity (left) and form drag coefficient (right).

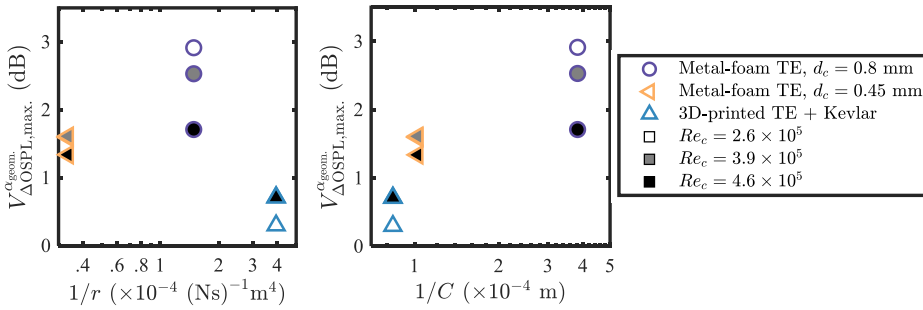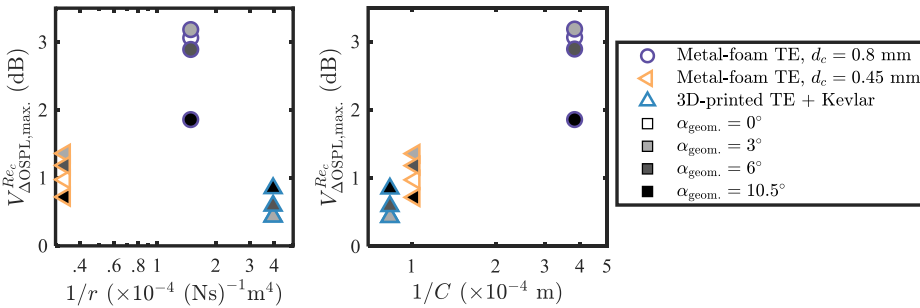ΔOSPL and its variabilities for materials belonging to the same topological group, e.g. porous metal-foams, at a given Re_c and $\alpha_{\text{geom.}}$, it cannot directly be linked to the ΔOSPL

nor its variability with $\alpha_{\text{geom.}}$ and Re_c when multiple types of the permeable material topology are considered altogether. Instead, the form drag coefficient C shows a clearer link to the overall noise attenuation ΔOSPL, including its variability with $\alpha_{\text{geom.}}$ and Re_c, which can be generalized even though the permeable material topologies are different.

Therefore, a design implication with regards to the permeable material characteristics could be drawn from this finding. The permeable material topology for the permeable TE should be realized such that a high form drag coefficient C is achieved in order to ensure its low variability of noise attenuation performance. Then, without major alterations to the topology, the overall permeability (inverse of r) shall carefully be increased to maximize the broadband noise attenuation. As an example, for the present Kevlar-covered 3D-printed topology, the latter could be achieved by enlarging the size of the 3D-printed hexagonal voids.

From the material characterization perspective, considering the pressure drop curve in Fig. 6.2 (left), the 'ideal' permeable material based on the design implication is represented by any material that provides a slow increase of $\Delta p / t_s$ for low values of v_D (dominated by the low r), similar to the 'No Kevlar' curve. When v_D increases, $\Delta p / t_s$ shall increase more rapidly due to the influence of the high C, similar to the 'With Kevlar' curve.

6.3.4. Source map analysis

The source maps for the 1/3-octave frequency band centered at 1 kHz, $Re_c = 2.6\times10^5$ ($St_{\delta_s^*}|_{\text{TE,ref.}} \approx 0.12$), are presented in Fig. 6.11 at $\alpha_{\text{geom.}} = 0°$. The SPLs shown are ΔSPLs relative to the 'Reference' maximum SPL for the solid TE case, i.e. $\Delta\text{SPL} = \text{SPL} - \text{SPL}_{\text{ref.,max.}}$ dB. In addition, a source map of the empty test section at the same flow condition and 1/3-octave frequency band is shown.

The most dominant noise source can clearly be seen around the TE region in all the source maps where the airfoil is present. The relative levels among the maps visualize the TBL–TE noise attenuation as discussed previously. Additionally, the chordwise locations where the maximum SPL is found $\bar{x}_{\text{SPL}_{1/3}^{\text{max.}}}/c$ are marked by the solid lines for the spanwise extent as wide as the ROI.

Prior to further discussions, it is important to note that the Rayleigh resolution limit at this particular condition is approximately $1.1c$, meaning that sound sources with a physical spacing of less than $1.1c$ cannot be discerned. This distance is much larger than the TE insert extent of $0.2c$. Therefore, one must not deduce that the noise source seen is the only actual source. However, all the presented cases are subjected to the same uncertainty, and the apparent source localization shown in the maps still gives a good implication of the chordwise location where the noise scattering is dominant. Thus, relative comparisons of these locations among the different cases are still valid.

For the solid TE, the dominant noise source appears to align with the trailing edge. However, the dominant noise source appears to shift upstream to a location close to the junction between the solid and the permeable extents of the airfoil for the metal-foam TE cases. The distance with the dominant noise source shifts upstream for the metal-foam TE cases seems to increase with the increasing d_c, i.e. permeability. The observation confirms what has been reported in a previous study [122], suggesting that scattering of noise on metal-foam TE inserts is distributed along the TE insert, resulting in a relatively
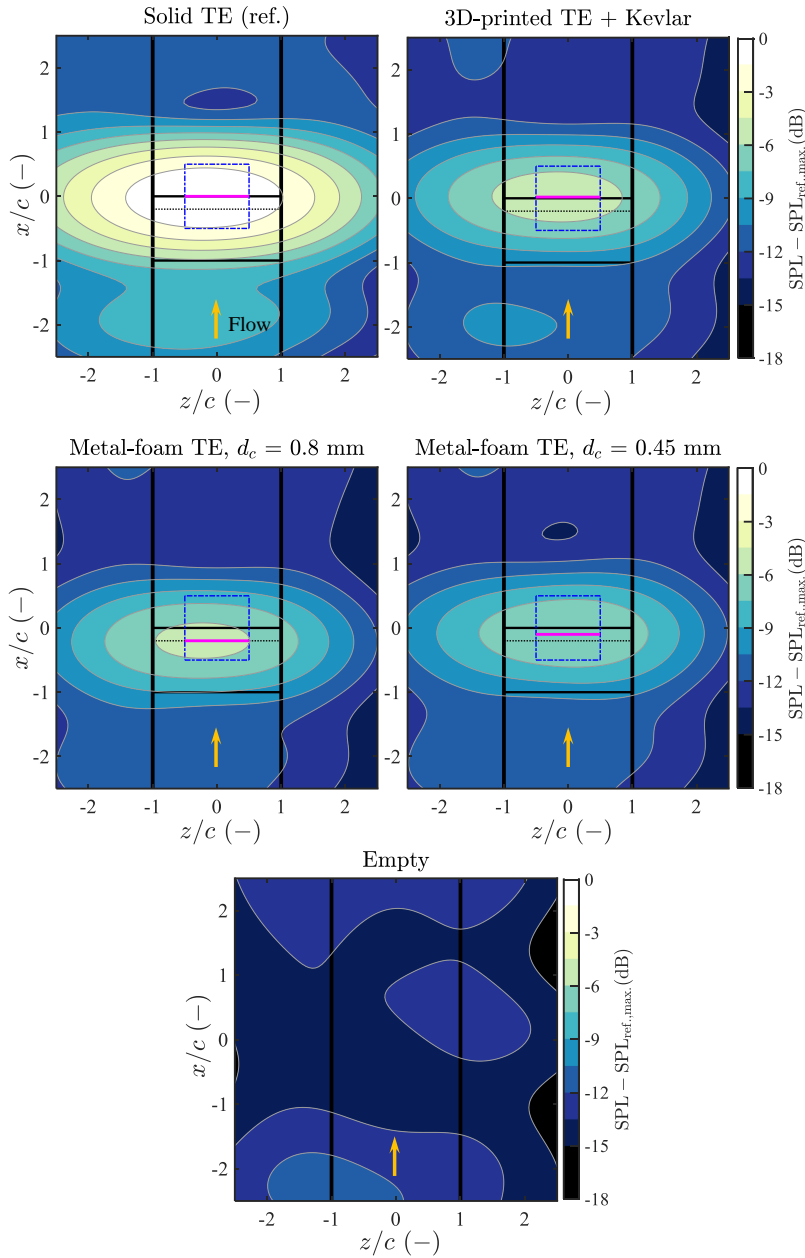
Figure 6.11: Source maps showing the relative SPL at $Re_c = 2.6 \times 10^5$ ($St_{\delta_s^*|\text{TE,ref.}} \approx 0.12$) and $\alpha_{\text{geom.}} = 0°$ for various permeable TE inserts. The levels are relative to the maximum SPL of the 'reference' solid TE case ($\text{SPL}_{\text{ref.,max.}}$), i.e. $\Delta\text{SPL} = \text{SPL} - \text{SPL}_{\text{ref.,max.}}$ dB. The colorbars are identical and apply to all of the maps.

weaker scattering at the edge. On the other hand, for the Kevlar-covered 3D-printed TE case, the dominant noise source still appears to be at the trailing edge in a more similar way to the solid TE case. This suggests that, although noise scattering along the permeable Kevlar-covered 3D-printed TE insert may exist, the noise still scatters most dominantly from the trailing edge.

Figure 6.12: Streamwise locations of the maximum SPL from the source maps per frequency at different combinations of chord-based Reynolds numbers and geometrical angles of attack relative to the locations of the trailing edge (TE) and the junction between the solid and the permeable extents of the airfoil.

To broaden the observation, the plots in Fig. 6.12 show the averaged chordwise distance where the maximum SPL is found, $\bar{x}_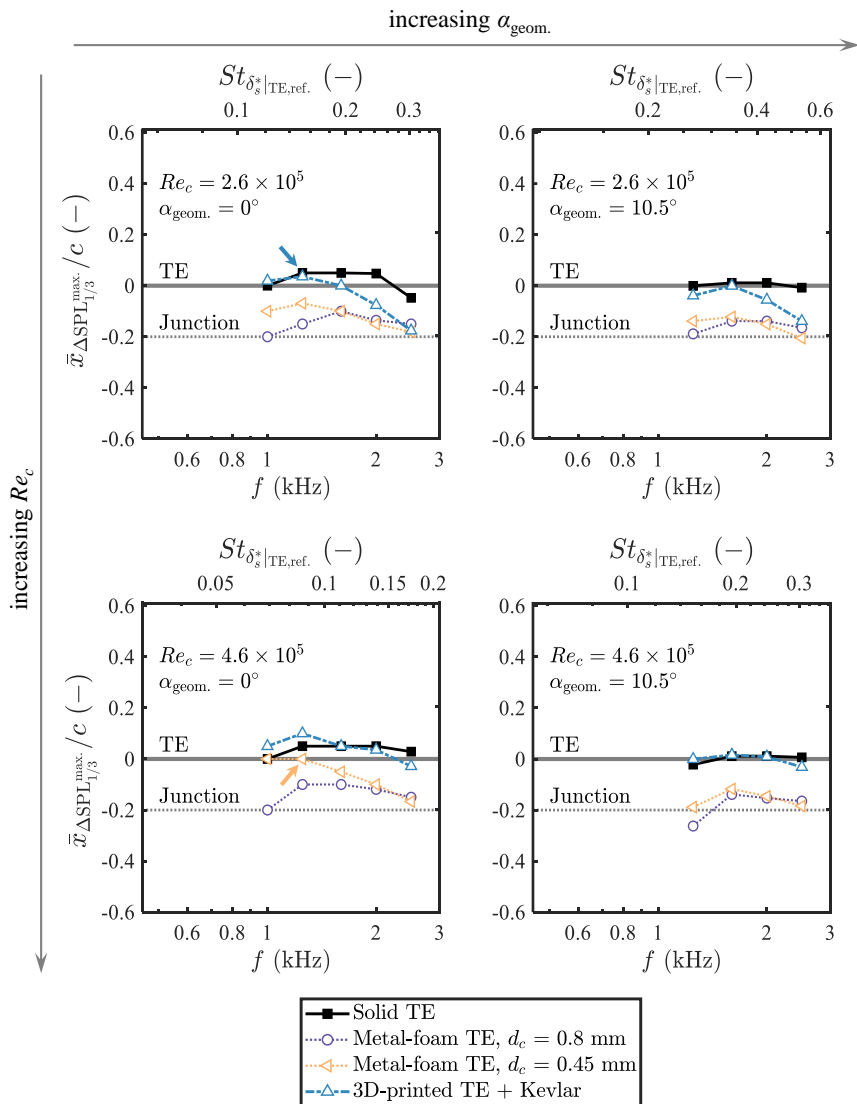{\mathrm{SPL}_{1/3}^{\max}}/c$, with respect to the frequency for $Re_c = 2.6 \times 10^5$ and 4.6×10^5, and $\alpha_{\mathrm{geom.}} = 0°$ and $10.5°$. The locations of the trailing edge and the junctions are marked for reference. To avoid interference of the noise source from the nozzle due to the resolution limit, only the results at sound frequencies above 1 kHz are presented.

For the solid TE case, $\bar{x}_{\mathrm{SPL}_{1/3}^{\max.}}/c$ aligns approximately with the trailing edge. However, for the metal-foam TE cases, $\bar{x}_{\mathrm{SPL}_{1/3}^{\max}}/c$ is still localized relatively more upstream as observed previously. For most frequencies, $\bar{x}_{\mathrm{SPL}_{1/3}^{\max.}}/c$ of the Kevlar-covered 3D-printed TE follows that of the solid TE case closely.

The trend still holds for $\alpha_{\mathrm{geom.}} = 10.5°$. Noticeably, for the metal-foam TE insert case with $d_c = 0.45$ mm, $\bar{x}_{\mathrm{SPL}_{1/3}^{\max.}}/c$ appears to shift even slightly further upstream. This is likely because of the relatively more dominant noise scattering close to the junction induced by the larger pressure gradient between the suction and the pressure sides at nonzero $\alpha_{\mathrm{geom.}}$.

Therefore, localization of the dominant sound source could again be linked to the ability of the permeable material to withstand the pressure gradient, characterized by the form drag coefficient C. To confirm this, Fig. 6.13 shows the averaged streamwise location at the frequency where the maximum noise attenuation (ΔSPL) is obtained $\bar{x}_{\Delta\mathrm{SPL}_{1/3}^{\max}}/c$ with respect to the flow resistivity r and the form drag coefficient C. In analogy to the observations in the previous section, a clear dependence of the distance of the dominant noise source from the junction and C is identified, meaning that the more form drag coefficient of the permeable material, the further the dominant noise scattering source from the impermeable-permeable junction.
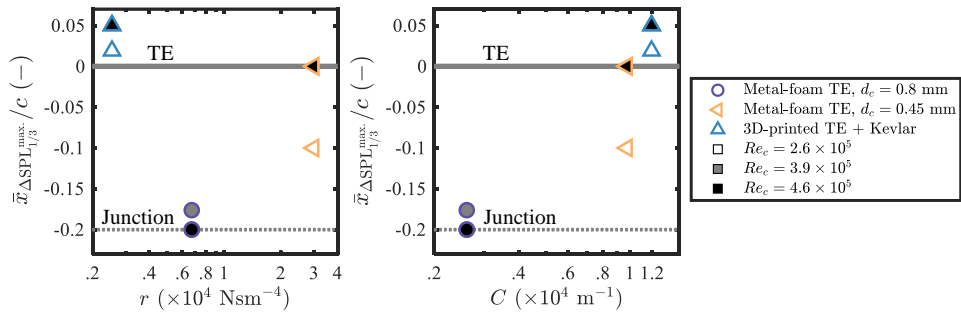
Figure 6.13: Streamwise locations of the maximum ΔSPL given by various permeable TE inserts at various chord-based Reynolds numbers at zero-degree geometrical angle of attack as functions of the flow resistivity (left) and form drag coefficient (right).

By examining the locations of the dominant noise scattering source with respect to the frequency, an observation can also be made regarding the roughness noise. Figure 6.12 is arranged in accordance with Fig. 6.5. For the permeable TE cases at high frequencies, it is notable that the frequency at which the $\Delta\mathrm{SPL}_{1/3}$ starts to inflect to the noise increase direction in Fig. 6.5 is approximately the same as the frequency at which $\bar{x}_{\mathrm{SPL}_{1/3}^{\max.}}/c$ starts to inflect from the TE to a more upstream location in Fig. 6.12. For example, for the metal-

foam TE insert case with $d_c = 0.45$ mm at $Re_c = 4.6 \times 10^5$ and $\alpha_{\text{geom.}} = 0°$, the $\Delta\text{SPL}_{1/3}$ curve in Fig. 6.5 starts to inflect at $f \approx 1.25$ kHz, approximately the same frequency as the frequency at which $\bar{x}_{\text{SPL}_{1/3}^{\max.}}/c$ in Fig. 6.12 starts to inflect from the TE to the upstream direction. Similarly, the Kevlar-covered 3D-printed TE insert also exhibits this behavior at the same frequency when $Re_c = 2.6 \times 10^5$ and $\alpha_{\text{geom.}} = 0°$. The frequencies where these mutual inflections are found are annotated by the arrows in both Fig. 6.12 and Fig. 6.5. This correlation interestingly visualizes the gradual dominance of the surface roughness noise over the noise scattered at the trailing edge as the frequency increases.

6.3.5. DRAG COEFFICIENTS

The wake profiles measured by the wake rake at a distance of $2c$ downstream of the airfoil trailing edge along a $0.5c$ spanwise traversing distance are shown in Fig. 6.14. The profiles are shown in terms of $c_{p,t} - c_{p,s}$, in accordance with Eq. (3.4), representing the measured dynamic pressure deficit, where $c_{p,t}$ and $c_{p,s}$ are the total and static pressure coefficients measured at the wake rake, respectively. The profiles are measured at $Re_c = 4.6 \times 10^5$ and $\alpha_{\text{geom.}} = 0°$. Only the cases for the solid TE, Kevlar-covered 3D-printed TE, and 3D-printed TE are given to clearly demonstrate the effect of Kevlar application.
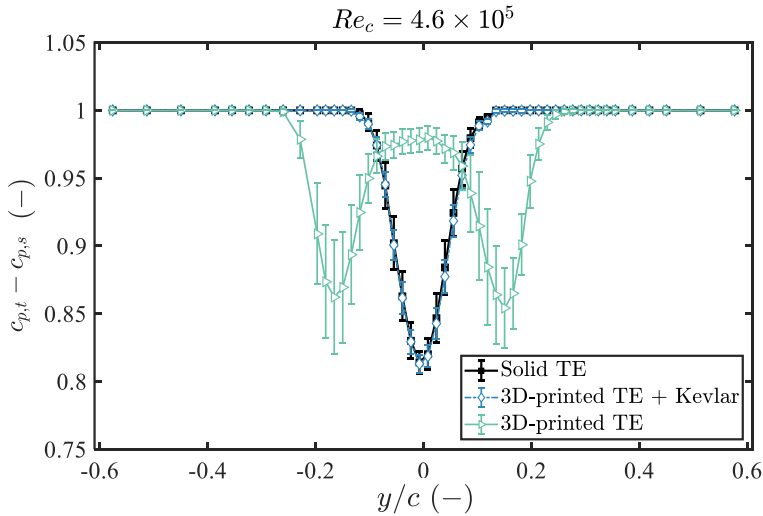
Figure 6.14: Wake profiles captured downstream of the airfoil with different TE inserts at $Re_c = 4.6 \times 10^5$ and $\alpha_{\text{geom.}} = 0°$.

Notably, the wake profile downstream of the airfoil with the 3D-printed TE insert without the Kevlar sheet shows two regions with dynamic pressure deficit: downstream of the suction and pressure sides of the airfoil. The regions with the dynamic pressure deficit are likely to result from vortices traveling downstream. In addition, the relatively high deviations suggest that the two regions with the dynamic pressure deficit may probably not exist at the same instance of time. Instead, the dynamic pressure deficit region

location alternates between positive and negative y/c, i.e. downstream of the suction and the pressure sides. Combining this speculation with the previously discussed tonal noise generation unique to this TE insert case, the wake profile strongly suggests existence of the vortex shedding [29, 108, 109] starting from the junction between the solid and the permeable parts of the airfoil. In turn, the c_d cannot be derived from the momentum deficit in the wake for this particular case due to this unsteadiness. For the remaining cases, the drag coefficient for any given spanwise measurement location is calculated by Eq (3.4).

Figure 6.15: Drag coefficients of the NACA 0018 airfoil with various TE inserts for four different chord-based Reynolds number and geometrical angles of attack of $0°$ (upper) and $10.5°$ (lower).

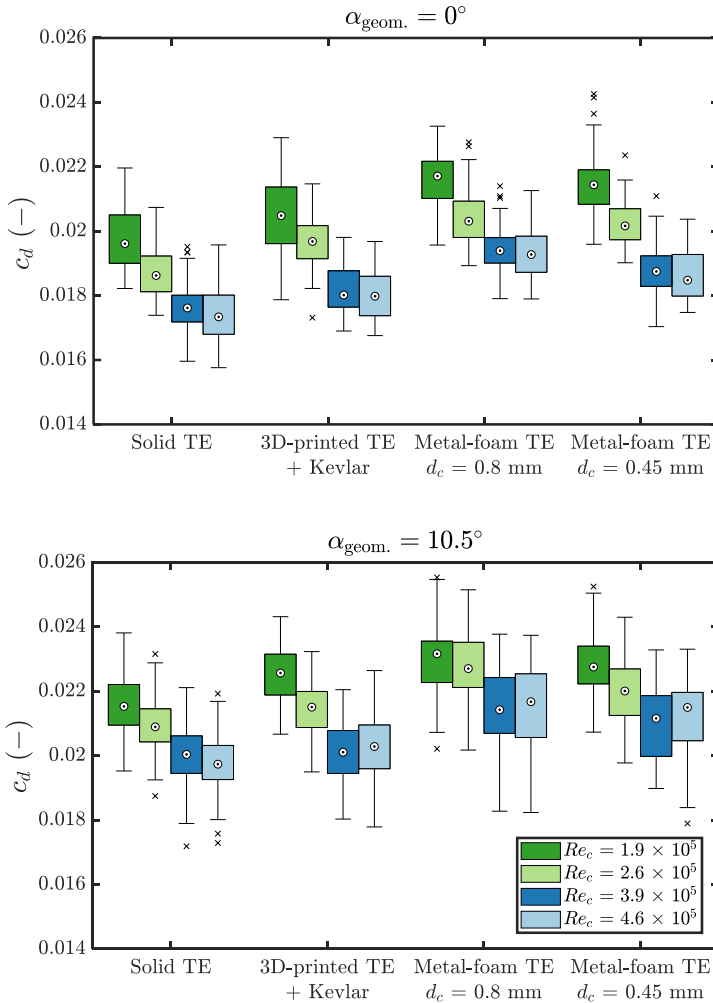The box plots in Fig. 6.15 show the measured drag coefficients for all the TE insert

cases considered and all Re_c collected along the spanwise traversing range of the wake rake. The geometrical angles of attack are $\alpha_{\text{geom.}} = 0°$ and $\alpha_{\text{geom.}} = 10.5°$ for the upper and lower subfigures, respectively. For a reasonable comparison, the distribution of the measured c_d from all the spanwise location is given in the box plot format rather than a single average value since the measured c_d may vary in the spanwise direction for the permeable TE, especially the porous metal foams which have a random topology. The metal-foam TE with $d_c = 0.8$ mm shows the highest values of c_d followed by the metal-foam TE with $d_c = 0.45$ mm. This can be attributed to the friction drag caused by the rough surface of the metal foams; a larger d_c leads to a rougher surface and thus a higher c_d. Analysis of Variance [206] and, subsequently, pairwise t-tests [207] within a confidence interval of 95% (with the Bonferroni correction [208] applied) have been carried out to objectively assess the difference of the c_d distribution presented in Fig. 6.15. It is found that the c_d of the airfoil with both metal-foam TE insert cases are significantly higher than that of the solid airfoil (P-value < .01). Among all the permeable TE insert cases tested, the Kevlar-covered 3D-printed TE seems to give the slightest increase of c_d compared to the solid TE due to the relatively smooth Kevlar surface covering the rather large 3D-printed pores under the Kevlar sheet. In some cases, such as for $Re_c \leq 2.6 \times 10^5$ and $\alpha_{\text{geom.}} = 10.5°$, this increment of c_d is insignificant (P-value > .05) compared to the solid TE. The c_d of the Kevlar-covered 3D-printed TE case is significantly lower than those of the metal-foam TE cases (P-value < .01). This confirms that the relatively smooth Kevlar surface provides an evident mitigation of surface drag compared to the metal foams. The mitigation of the surface drag could be achieved by the Kevlar sheet to an extent that the the difference of the friction drag between the baseline solid TE and the Kevlar-covered permeable TE insert is negligible.

6.4. CONCLUSIONS AND DERIVATION OF THE PERMEABLE TE DESIGN CONCEPT

The noise attenuation and the aerodynamic drag results are combined in Fig. 6.16 where scatter plots of the drag coefficient c_d and the difference of the Overall A-weighted Sound Pressure Levels (OASPL), ΔOASPL, of every TE insert case for $Re_c = 2.6 \times 10^5$ and 4.6×10^5, and $\alpha_{\text{geom.}} = 0°$ and $10.5°$ are presented. In this plot, ΔOASPL, defined in the same manner as ΔOSPL, is used to give an implication on perception of noise attenuation in real applications. Nevertheless, for the given frequency range, the A-weighting does not alter the SPL for more than 2 dB and the same observations as discussed previously still hold. The plots visualize the trade-off between the noise attenuation and the aerodynamics performance, the drag in this case. For the metal-foam TE cases tested, additional noise reduction comes at a cost of increasing c_d. The metal-foam TE insert case with $d_c = 0.8$ mm attenuates approximately 3.5 to 6.5 dB(A) of noise while $d_c = 0.45$ mm attenuates approximately 2.5 to 4.5 dB(A). The aforementioned large variability of the noise attenuation with the angle of attack found in the metal-foam cases can also be seen clearly in the figure. This variability is observably larger than that of the Kevlar-covered 3D-printed TE case which gives a rather constant noise attenuation of 2 to 3 dB(A) over the considered range of $\alpha_{\text{geom.}}$. This results in a comparable noise attenuation between the Kevlar-covered 3D-printed TE insert and the metal-foam TE inserts with $d_c = 0.45$

mm at $\alpha_{\text{geom.}} = 10.5°$. It has been found that the ranking of the noise attenuation and its variability are inversely proportional to the form drag coefficient C of the permeable materials. The plots also visualize the significant reduction of c_d by the Kevlar-covered 3D-printed TE compared to the metal-foam TE insert cases. At $\alpha_{\text{geom.}} = 10.5°$, it can be seen that the increment of c_d by the Kevlar-covered 3D-printed TE insert is infinitesimal, compared to the solid TE.
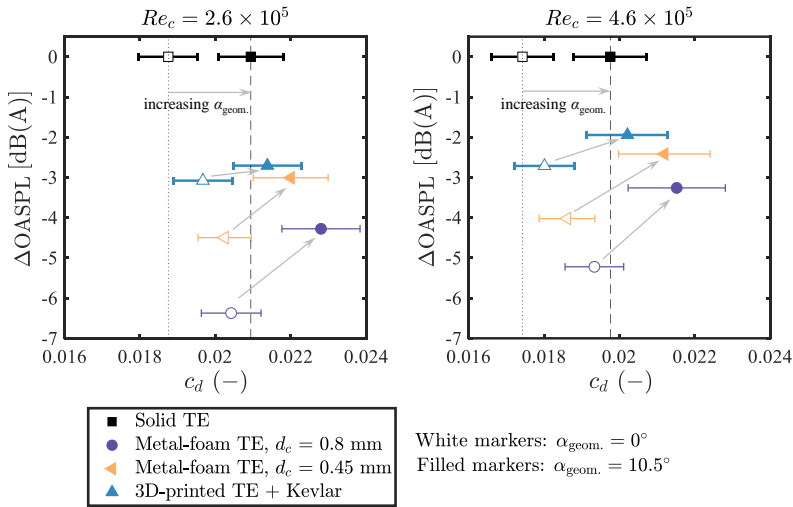

Figure 6.16: Comparison of noise attenuation and drag coefficients provided by all the permeable TE inserts at different combinations of the chord based Reynolds numbers and geometrical angles of attack.
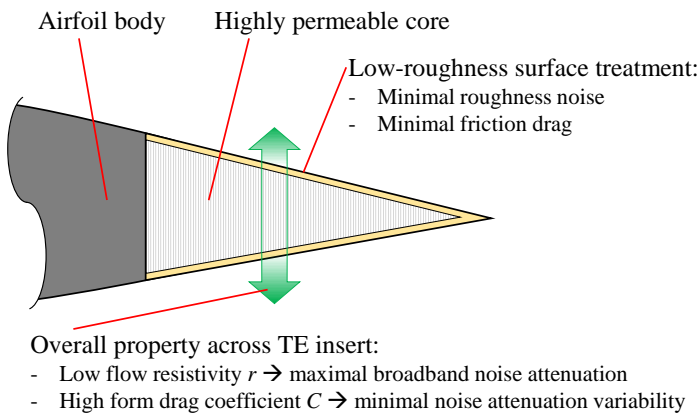

Figure 6.17: Proposed TE insert design concept for TBL–TE noise attenuation based on findings in the present study.

By taking into account all the findings discussed so far, a general design guideline for the permeable TE insert topology is derived in Fig. 6.17. This concept features a low-roughness surface treatment which has been proven to help mitigate the surface roughness noise and the friction drag increase. In addition, across the TE insert, a combination of a low flow resistivity r for maximal broadband noise attenuation and high form drag coefficient C for minimal variability of the noise attenuation with $\alpha_{\text{geom.}}$ and Re_c shall be realized. One way to achieve these features is by covering a highly permeable core material with a smooth material having a high form drag coefficient. This chapter has shown that the present Kevlar-covered 3D-printed perforated topology is a possible topology which could provide the aforementioned features altogether. Nevertheless, the investigations of the links between the permeable material characteristics and the aeroacoustic characteristics of an airfoil equipped with it presented in this chapter have helped to formulate a generic guideline for the permeable TE insert topological design. Therefore, any permeable material combinations other than the Kevlar-covered 3D-printed perforated channels could also be employed to achieve the same effects, as long as the features prescribed in Fig. 6.17 are fulfilled.

This chapter studies an approach of Turbulent Boundary Layer Trailing-Edge (TBL–TE) noise mitigation by integrating a simple permeable topology design concept represented by the Kevlar-covered 3D-printed structure into the trailing-edge of an airfoil. An experimental study in an open-jet anechoic wind tunnel featuring a NACA 0018 airfoil with a TE insert made of the Kevlar-covered 3D-printed perforated structure was carried out. The results have been compared to those for the same airfoil with a solid TE insert and conventional porous metal-foam TE inserts. The chord-based Reynolds number Re_c was within 1.9×10^5 and 4.6×10^5 and the geometrical angle of attack $\alpha_{\text{geom.}}$ was varied between $0°$ and $10.5°$.

Characterization of the Kevlar-covered 3D-printed permeable topology has shown that the present topology gives an unconventional combination of flow resistivity r and form drag coefficient C. Unlike other conventional permeable materials of which C increases gradually with increasing r, the Kevlar-covered 3D-printed permeable topology gives a drastic increase of C (the highest value among all the permeable materials tested) while the value of r is minimal.

The Kevlar-covered 3D-printed TE provides a broadband TBL–TE noise reduction up to approximately 5 dB as compared to the reference solid airfoil. Although the reduction is not as much as that achieved by the porous metal-foam TE inserts, the reduction is found in a wider range of frequency considered. This is the consequence of the Kevlar sheet exhibiting negligible surface roughness as compared to the metal-foam surface. Apart from the mitigation of the roughness noise, the Kevlar sheet is also found to play an important role in mitigating the tonal noise. This finding suggests that a permeable material with a low r can still be employed as a TE insert for an airfoil without a risk of producing the tonal noise, as long as C is large enough.

Unlike the airfoil with the porous metal-foam TE inserts of which the noise attenuation capability varies strongly with increasing airfoil loading, the airfoil with the Kevlar-covered 3D-printed TE insert clearly gives a lower variability. Within the range of Re_c and $\alpha_{\text{geom.}}$ considered, this TE insert gives a noise attenuation variability lower than 1 dB, while the metal-foam TE inserts give a maximum variability up to 3 dB.

When relating the characterized permeable material properties to the noise attenuation and its variability, it has been found that, when different permeable topologies are compared, the form drag coefficient C shows a clearer relation to those aeroacoustic behaviors than the resistivity r. The broadband noise attenuation as well as the noise attenuation variabilities are found to vary inversely with C. Additionally, analysis of the source maps has also shown the dominant noise scattering source shifts further away from the solid-permeable junction when C of the permeable material increases.

Lastly, the drag coefficients provided by the airfoil with the Kevlar-covered 3D-printed TE insert is significantly lower than that provided by the metal-foam TE inserts due to the relatively lower surface roughness. In many cases, especially at high Re_c and $\alpha_{\text{geom.}}$, the drag increment given by this proposed TE insert compared to a solid airfoil is insignificant.

The aeroacoustic findings, in combination with their links to the material properties, have led to a design guideline for a permeable TE insert topology for TBL–TE noise attenuation. The features that the design needs to fulfill are:

- In the direction linking the suction and the pressure sides, the permeable material shall have a combination of a low flow resistivity but a high form drag coefficient to achieve maximal broadband noise attenuation while having a low variability of noise attenuation with the airfoil loading.

- The surface roughness of the permeable insert shall be negligible, compared to the solid extent of the airfoil, in order to have a minimal increment of the friction drag as well as the roughness noise.

When these requirements are fulfilled, a promising trade-off between the noise attenuation and the aerodynamics penalty, i.e. drag increase, is obtained. Apart from the significantly low surface roughness, noise attenuation by a topology as such also appears to be less sensitive to the increasing airfoil loading, compared to the conventional porous metal-foams. A simple permeable material combination such as the Kevlar-covered 3D-printed permeable structure considered in this chapter could be one, but indeed not only, possible realization to fulfill those requirements.

The aforementioned permeable TE concept has also been extrapolated for aircraft applications, subjecting to a chord-based Reynolds number in the same order as the modern wind turbines. The permeable TE concept is integrated with an acoustic liner to be applied at the TE of an aircraft wing downstream of an engine/ propeller to mitigate various aircraft noise sources. Interested readers are referred to Appendix C for more details.

Crucial elements for future studies include identification of strong, yet highly permeable, topologies and materials for the inner part of the proposed TE insert design concept. In addition, performance of the proposed concept on a realistic wind turbine to verify its noise attenuation capability as well as effects of the streamwise permeable TE insert length on both aerodynamic and aeroacoustic performances shall also be investigated.

7

EFFECTS OF AIRFOIL GEOMETRY AND PERMEABLE MATERIAL TYPES ON TRAILING-EDGE NOISE ATTENUATION: A STUDY USING SYMBOLIC REGRESSION MODELING
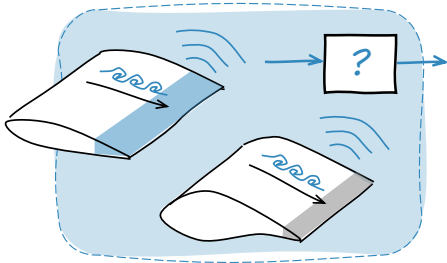
This chapter attempts to formulate an expression to predict the maximum trailing-edge (TE) noise attenuation by airfoils with a permeable TE. Experimental dataset featuring two different airfoils and three different permeable material types are considered. Symbolic regression modeling supported by genetic programming is employed for the present work. Results suggest that for a given permeable material, the noise attenuation is maximized when the permeable TE geometry is long and/or thin. When multiple permeable material types are considered together, the maximum noise attenuation varies with a generic parameter called the Brinkman screening distance, which is the square-root of the permeability in the streamwise direction.

7.1. Introduction

Permeable materials are usually characterized by porosity and permeability [118, 205, 209]. When they are installed on an airfoil, Turbulent Boundary Layer Trailing-Edge (TBL–TE) noise attenuation given by permeable materials belonging to the same type, e.g. porous foams or perforated channels, are found to vary directly with those parameters. In other words: the more porous/permeable, the more noise attenuation [54, 106, 109]. However, as has been shown in Chapter 6, when different types of permeable materials are considered, the maximum noise attenuation could differ largely, even though they share a very close permeability. Another supporting evidence has been presented in the work of Rubio–Carpio et al. [133] which compared the TBL–TE noise attenuation of a NACA 0018 airfoil with a porous metal-foam TE and a 3D-printed perforated TE with very similar permeability values. They found that the metal-foam TE attenuates up to 3 dB more than the 3D-printed perforated TE.

Not only does the noise attenuation depend on the permeable material properties, it also depends on the geometry of the material installation on the airfoil, i.e. the local TE shape [210, 211]. For instance, Zhang and Chong [211] studied a NACA 65(12)–10 having an array of perforations close to the TE region. They found an increase in the broadband TBL–TE noise attenuation as the number of perforation rows increases in the chordwise direction. Thus, there is a dependency of the achievable noise reduction on the permeable material properties and the geometry of the material installed on the airfoil.

The past findings have indicated the need for a relevant and more generic set of parameters that help predict the TBL–TE noise attenuation provided by permeable materials. For this purpose, by incorporating symbolic regression modeling supported by genetic programming, Sarradj and Geyer [124] formulated a function that links the noise emissions to some relevant parameters. An extensive experimental dataset was utilized to help formulate the function. It was found that the noise emission is driven by the flow resistivity r of the permeable material (inversely proportional to the permeability K). A function based on the flow resistivity was proposed to describe the noise emission. However, the permeable materials considered were limited to the porous foam or wool felt types and did not include permeable materials from more modern manufacturing techniques such as 3D-printed metamaterials. In Chapter 6, the unconventional Kevlar-covered 3D-printed permeable TE was considered together with several porous metal foams. Figure 6.8. has shown that, for this consideration where two completely different permeable material types are considered together, the form drag coefficient C correlates better to the noise attenuation compared to r. Nonetheless, neither the work of Sarradj and Geyer nor the results in Chapter 6 considers noise reduction provided by the same permeable materials installed on different airfoils.

Based on the more recent studies of the pressure release mechanism [109, 110], the mechanism that drives the TBL–TE noise attenuation on the permeable airfoils, most noise attenuation occurs in the thin region close to the TE tip [107]. Thus, it could be hypothesized that for two airfoils with similar TBL-induced surface pressure fluctuations in the TE region, the one with a more slender (long and thin) TE cross-sectional shape would enable more communication of the surface pressure fluctuations, facilitate more the pressure release mechanism, and achieve more TBL–TE noise attenuation. Studies

of grazing flow over different permeable walls also have shown that the depth within the material where the hydrodynamic fluctuations are influenced by the external flow is proportional to the material permeability in the direction of the flow [128, 212, 213]. Therefore, for the airfoil application, it is of high interest to include the permeability in the streamwise direction in the consideration, and separate it from the permeability in the chord-normal direction (the one that is usually characterized and is inversely proportional to r).

This chapter attempts to identify generic parameters that helps predict the TBL–TE noise attenuation provided when a permeable material is installed on an airfoil. The same symbolic regression modeling framework of Sarradj and Geyer is followed. Wind-tunnel experimental dataset [108, 214] featuring two airfoils and three different material types are considered. For the model, a set of parameters describing the airfoil geometry as well as a set of parameters describing the permeable materials are considered. It is worth highlighting that the permeability in the chord-normal and the streamwise directions are considered here as two separate parameters.

The dataset is described in Section 7.2. The symbolic regression modeling approach is presented in Section 7.3. Finally, results are discussed in Section 7.4.

7.2. EXPERIMENTAL DATASET

7.2.1. AIRFOIL MODELS

Experimental datasets featuring two symmetric airfoil models: a NACA 0018 airfoil and a NACA 63_3–018 airfoil with permeable TE inserts are considered. Both models were tested in the A–Tunnel, an anechoic open–jet vertical wind tunnel at Delft University of Technology. Extensive details of the airfoil models and the wind-tunnel facility are provided in Chapter 3. In this chapter, only data for the zero-degree angle of attack are considered in the chord-based Reynolds number Re_c range between 0.2×10^6 and 0.45×10^6.

The chordwise permeable TE length covers up to 20 % of the chord c. For the present study, two geometrical parameters are defined as a preliminary attempt to describe the *slenderness* of the permeable TE insert, namely, the length of the permeable TE extent $x_{\mathrm{per.}}$, and the cross-sectional area of the permeable material $A_{\mathrm{per.}}$. Cross–sectional profiles of the airfoils as well as $x_{\mathrm{per.}}$ and $A_{\mathrm{per.}}$ are shown in Fig. 7.1. Note that the x and y directions denote the direction parallel to the chord and normal to the chord, respectively. In Fig. 7.1, it can be seen that despite the identical $x_{\mathrm{per.}}/c = 0.2$, $A_{\mathrm{per.}}$ of the NACA 63_3–018 airfoil is smaller than that of the NACA 0018 airfoil due to the overall thinner permeable TE shape.

7.2.2. PERMEABLE MATERIALS

Three different permeable material types are considered in this chapter, namely porous metal foams, 3D-printed perforated channels, and an open-cell diamond-lattice structure. Each type may be subdivided further based on geometrical parameters. Each permeable material type is described in the following.
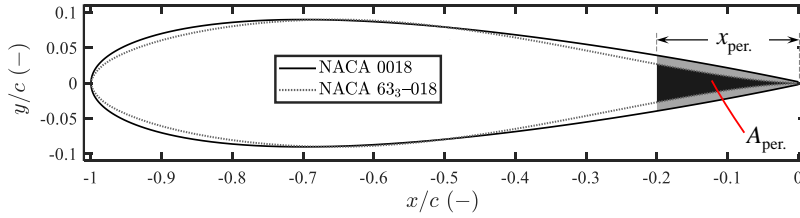
Figure 7.1: Airfoil profiles with a permeable TE insert considered.

1. **Porous metal foams**: Porous metal foams from Alantum are considered. The metal foams were manufactured by electrical discharge machining creating homogeneous dodecahedral open-cells within NiCrAl alloy. The foams are described by their nominal cell diameter d_c. A schematic of a representative cubic metal foam with a definition of d_c is illustrated in Fig. 7.2a. In this chapter, $d_c = 0.80$, 0.58, and 0.45 mm are considered.

2. **3D-printed perforated channels**: The 3D-printed perforated channels were manufactured using digital light projector printing of high-temperature photopolymer. Cylindrical channels having a diameter d_h of 0.8 mm were formed in the direction perpendicular to the airfoil chord, connecting the suction and the pressure sides. Perforation was achieved by replicating the unit perforation pattern illustrated in Fig. 7.2b next to one another. The distance between two adjacent pores is defined as l_h. Thus, when applied on the airfoil, the number of pores per unit area, hence the permeability, is varied by varying l_h. In this paper, $l_h = 1.5, 2.0, 2.5, 3.0$, and 5.0 mm are considered.

3. **Open-cell diamond-lattice structure**: Finally, an open-cell diamond-lattice structure is considered. This structure was produced using an *Ultimaker 3* 3D-printer. Polylactic acid was used as printing material. The diamond structure has a unit–cell size $D = 6.36$ mm and a mean pore size $d_p = 1.20$ mm as shown in Fig. 7.2c. The actual diamond TE insert on the airfoil constitutes of multiple small unit cells.

For convenience, the porous metal foams, the perforated channels, and the diamond-lattice structure are in this chapter denoted by 'mf.XXX', 'pf.XpX', and 'dmnd.', respectively, where 'X' is replaced by numbers specifying their geometrical parameters. These notations are specified in Table 7.1.

Table 7.1 also presents several additional permeable material properties. First, the permeable materials are characterized by their porosity ϕ. Definition of the porosity is provided in Section 2.3.1. The values of ϕ for each material are provided in Table 7.1. It is noteworthy that, for the perforated channels, an analytical formula is used to determine ϕ: $\phi = \pi d_h^2/(2l_h^2)$ [108].

Furthermore, the permeable materials are characterized according to the ISO 9053 standard [115, 116] where pressure drops across a sample permeable material are measured. The sampled pressure drop data are used to calculate the permeability K and
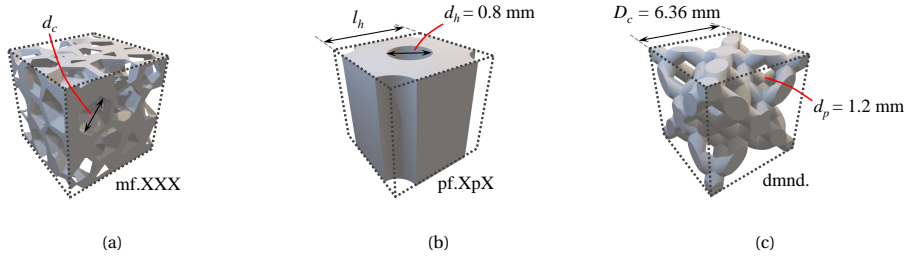
Figure 7.2: Schematic of the permeable materials: (a) Porous metal foam, (b) Perforated channels, and (c) Diamond-lattice structure.

Table 7.1: Permeable materials considered and their characteristics.

Notation	Geometrical parameter	ϕ (-)	K_y (m^2)	K_x (m^2)	C (m^{-1})
mf.800	d_c = 0.80 mm	0.92	3.2×10^{-9}	$\approx K_y$	2,333
mf.580	d_c = 0.58 mm	0.90	1.5×10^{-9}	$\approx K_y$	3,939
mf.450	d_c = 0.45 mm	0.89	5.0×10^{-10}	$\approx K_y$	10,335
pf.1p5	l_h = 1.5 mm	0.40	5.4×10^{-9}	5.2×10^{-10}	279
pf.2p0	l_h = 2.0 mm	0.22	3.1×10^{-9}	2.8×10^{-10}	1,138
pf.2p5	l_h = 2.5 mm	0.14	2.0×10^{-9}	1.8×10^{-10}	3,065
pf.3p0	l_h = 3.0 mm	0.10	1.4×10^{-9}	1.3×10^{-10}	6,681
pf.5p0	l_h = 5.0 mm	0.04	5.0×10^{-10}	5.2×10^{-11}	55,189
dmnd.	See Fig. 7.2c	0.62	2.4×10^{-8}	$\approx K_y$	2,923

the form drag coefficient C through the so-called Forchheimer Equation. Details on this characterization method as well as physical explanations of K and C are discussed in detail in Section 2.3.1.

The resulting K and C are also shown in Table 7.1. It is important to highlight that the flow direction in the pressure-drop characterization penetrates through the material sample. Correspondingly, the resulting K rather represents the permeability in the direction normal to the airfoil chord, i.e. the y direction. Thus, the characterized K is denoted by K_y for clarity. However, the permeability in the direction normal to K_y, K_x, may better represent the flow interaction with the permeable material on the airfoil.

For the porous metal foams and the diamond-lattice structure, the permeability K can be assumed to be isotropic, meaning that K is approximately constant regardless of the flow direction. Therefore, for those cases, $K_x \approx K_y$. On the other hand, for the perforated TE, the flow direction x is approximately perpendicular to the channel direction y. Thus, $K_x \ll K_y$. This paper utilizes the following expression for determining K_x of a perforated channels provided by Bae and Kim [132] based on their direct numerical simulations of flow over perforated plates:

$$K_x = \phi(0.07 d_h - 0.002 t_s)^2, \tag{7.1}$$

where t_s = 10 mm is the material sample thickness. It is important to highlight that this material sample thickness, which is consistent with the sample thickness used in the characterization described in Section 2.3.1, is a representative value which is in the same order of magnitude of the average permeable material thickness on the airfoil. Nevertheless, the permeable material thickness, and therefore its permeability, varies along the chord. This is beyond the current consideration and the permeability for each permeable material is represented by one constant value. The resulting K_x and K_y are shown in Table 7.1. It can be seen that, for the perforated channels, K_x is approximately one order of magnitude lower than K_y.

7.2.3. Dataset summary

Extraction of ΔSPL$_{\text{MAX}}$.
Far-field Sound Pressure Level (SPL) spectra SPL(f) in decibels were measured during wind-tunnel measurements of these airfoils with permeable TE inserts. Additionally, the airfoils with a reference, i.e. solid, TE inserts were tested at the same condition and the reference SPL$_{\text{ref.}}$(f) were also measured. Subsequently, the noise reduction spectra were calculated from

$$\Delta\text{SPL}(f) = \text{SPL}(f) - \text{SPL}_{\text{ref.}}(f) \text{ dB.} \tag{7.2}$$

By convention, noise reduction is represented by negative values, the lower the ΔSPL(f) the more the noise reduction. This chapter focuses on the maximum noise reduction ΔSPL$_{\text{max.}}$. A method employed by Rubio–Carpio et al. [108] in which cubic B–splines were fitted to the ΔSPL(f) spectra was used to extract ΔSPL$_{\text{max.}}$. Rubio–Carpio et al. showed that, for the range of Re_c considered, ΔSPL$_{\text{max.}}$ is a very weak function of Re_c and an averaged ΔSPL$_{\text{max.}}$ can be used to represent the noise reduction given by a specific combination of airfoil and permeable material at a specific angle of attack.

The considered cases and the corresponding ΔSPL$_{\text{max.}}$ values are shown in Table 7.2. Each case is therefore a unique data point, and 18 data points in total are considered. These data points are represented by specific markers in the rest of the plots in this chapter, unless indicated.

It is noteworthy that most of the data points presented in this chapter have formerly been discussed in previous publications of Luesutthiviboon et al. [214], Rubio–Carpio et al. [108], and Teruna et al. [107].

Effects varying permeable TE shapes on ΔSPL$_{\text{MAX}}$.
Some selected data points in Table 7.2 are presented in Fig. 7.3 to highlight the effect of different airfoil installations on ΔSPL$_{\text{max.}}$ given by a particular material. The plot shows ΔSPL$_{\text{max.}}$ for several perforated TE inserts installed on the different airfoils at different $x_{\text{per.}}/c$. Notably, ΔSPL$_{\text{max.}}$ provided by a given permeable material, such as pf.5p0, installed at an identical $x_{\text{per.}}/c$ = 0.2 but on different airfoils differs drastically. On the NACA 0018 airfoil, pf.5p0 provides ΔSPL$_{\text{max.}}$ = −2.2 dB while it provides a larger noise reduction of ΔSPL$_{\text{max.}}$ = −5.3 dB on the NACA 63$_3$–018 airfoil. This clearly shows that the noise reduction does not depend solely on the permeable material, but also the
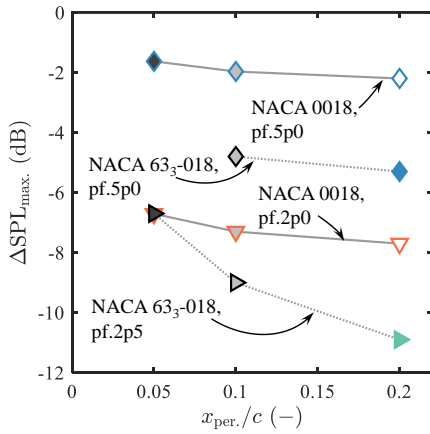
Figure 7.3: $\Delta SPL_{max.}$ versus $x_{per.}/c$ for various airfoil geometries.

airfoil permeable TE shape. By considering Fig. 7.1, where the NACA 0018 and NACA 63_3–018 airfoils are compared, one could anticipate that a thinner permeable TE may provide more noise reduction. The thickness of the permeable TE may be only one out of many other factors which are beyond the scope of this chapter. The boundary layer evolution along the chord, the pressure gradient, and the TBL-induced surface pressure fluctuations may also play a role. However, one may assume that those factors for the two airfoils considered are rather similar to each other (See, for example, the pressure distribution comparison in Figs. 3.6a and 3.6b).

The effect of $x_{per.}/c$ is also demonstrated in Fig. 7.3. It can generally be seen that the magnitude of $\Delta SPL_{max.}$ increases with $x_{per.}/c$. In other words: the longer the permeable TE insert, the more the noise reduction. However, $\Delta SPL_{max.}$ seems to reach a plateau beyond a certain $x_{per.}/c$ value [108]. This suggests that the noise attenuation efficiency is not uniform along the chord. Instead, most of the noise attenuation is contributed by the region very close to the TE tip [107, 123]. Teruna et al. [107] confirmed this statement in their simulation of a NACA 0018 airfoil with a permeable 'dmnd.' TE. They showed that noise attenuation at the last 4 % of the chord, i.e. very close to the TE, contributes substantially to the overall noise attenuation. Further analysis of the flow field showed that there exists a certain depth inside the permeable material where the pressure fluctuation magnitudes are comparable to that at the surface. This distance is the so-called *entrance length* [118, 126, 127] and is closely linked to the pore diameter for the foam-material type [126, 128]. Interactions of the surface pressure fluctuations between both sides, and therefore the pressure release process discussed in Section 2.3.1, would occur most effectively only where the entrance lengths from the suction and the pressure sides of the airfoil overlap. Because of this, the region close to the TE, where the local airfoil geometry is thinner than approximately two times the entrance length, contributes the most to the overall noise attenuation [107].

7

Table 7.2: Data points considered in each trial of the symbolic regression modeling; ✓ = included and ✗ = excluded.

Airfoil	Permeable material	$\frac{x_{per.}}{c}$ (-)	$\frac{A_{per.}}{c^2}$ (-)	$\Delta SPL_{max.}$ (dB)	Data marker in plots	Trial 1	Trial 2	Trial 3
NACA 0018	mf.800	0.2	0.008538	-9.1	○	✗	✓	✓
NACA 0018	mf.580	0.2	0.008538	-8.6	□	✗	✓	✓
NACA 0018	mf.450	0.2	0.008538	-6.1	▽	✗	✓	✓
NACA 0018	pf.1p5	0.2	0.008538	-9.0	◁	✓	✓	✓
NACA 0018	pf.2p0	0.2	0.008538	-7.7	▷	✓	✓	✓
NACA 0018	pf.2p5	0.2	0.008538	-6.0	△	✓	✓	✓
NACA 0018	pf.3p0	0.2	0.008538	-4.4	□	✓	✓	✓
NACA 0018	pf.5p0	0.2	0.008538	-2.2	◇	✓	✓	✓
NACA 0018	pf.2p0	0.1	0.002399	-7.3	▷	✓	✓	✗
NACA 0018	pf.5p0	0.1	0.002399	-2.0	◈	✓	✓	✗
NACA 0018	pf.2p0	0.05	0.000704	-6.7	▶	✓	✓	✗
NACA 0018	pf.5p0	0.05	0.000704	-1.6	◆	✓	✓	✗
NACA 0018	dmnd.	0.2	0.008538	-13.5	◇	✗	✓	✓
NACA 63$_3$–018	pf.2p5	0.2	0.004427	-10.9	▲	✓	✓	✗
NACA 63$_3$–018	pf.5p0	0.2	0.004427	-5.3	◆	✓	✓	✗
NACA 63$_3$–018	pf.2p5	0.1	0.000809	-9.0	△	✓	✓	✗
NACA 63$_3$–018	pf.2p5	0.05	0.000158	-6.7	▲	✓	✓	✗
NACA 63$_3$–018	pf.5p0	0.1	0.000809	-4.8	◈	✓	✓	✗

7.3. SYMBOLIC REGRESSION MODELING SUPPORTED BY GENETIC PROGRAMMING

Symbolic regression modeling assumes that there is a function g that describes the relationship between an output variable Y and N input variables X_i: X_1, X_2, ..., and X_N. The predicted value of the output variable $\hat{Y}$, where the hat represents the prediction of Y is therefore expressed mathematically as

$$\hat{Y} = g(X_1, X_2, \ldots, X_N). \qquad (7.3)$$

In reality, it is not fully known a priori whether each X_i is actually related to Y. The function g may also contain fewer than N elements X_i. A suitable expression for g is searched for by applying symbolic regression [124].

One strategy to search for g is by applying genetic programming which is a bio-inspired evolutionary algorithm. The procedures involved in genetic programming are summarized in Fig. 7.4. The numbers shown in the diagram correspond to the following steps:

Figure 7.4: Flow diagram of the genetic programming.

1. Generate a population which contains a number of individuals. Each individual represents a possible candidate for the function g. Algorithmically, the function g is represented in form of *trees* with multiple *nodes*, where each node represents an occurrence of X_i or a primitive mathematical operation, e.g. plus, minus, etc., in the function.

2. Evaluate the fitness of each individual. Criteria for evaluating the fitness could be the prediction accuracy, i.e. deviation of $\hat{Y}(X_i)$ from $Y(X_i)$, and/or functional complexity, e.g. number of nodes.

3. Select a portion of the population with the highest fitness to continue on to the next generation.

4. Generate new individuals for the next population by applying genetic operations, such as reproduction, crossover, and mutation.

5. Repeat steps 2 to 4 until the fitness of the population converges, or the maximum number of generation or the maximum runtime is reached.
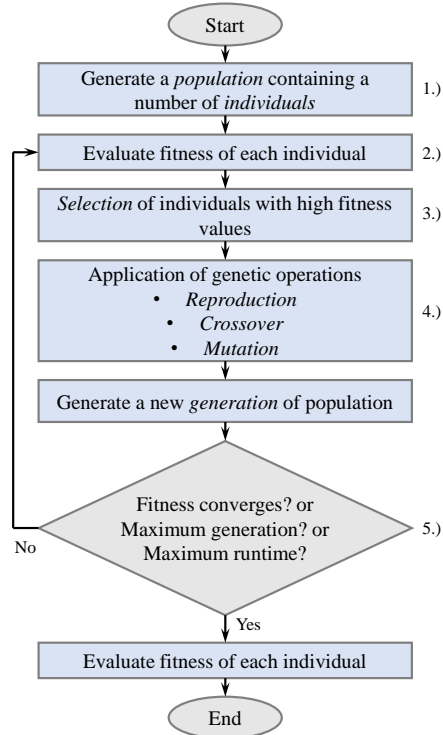
Table 7.3: Input and output variables considered in the present symbolic regression modeling.

Y	X_1	X_2	X_3	X_4	X_5	X_6	X_7	X_8	X_9
$\Delta\mathrm{SPL_{max.}}$	ϕ	$x_{\mathrm{per.}}C$	$\dfrac{A_{\mathrm{per.}}}{x_{\mathrm{per.}}^2}$	$\dfrac{x_{\mathrm{per.}}}{\sqrt{K_x}}$	$\dfrac{A_{\mathrm{per.}}}{K_x}$	$\sqrt{K_x}C$	$\dfrac{x_{\mathrm{per.}}}{\sqrt{K_y}}$	$\dfrac{A_{\mathrm{per.}}}{K_y}$	$\sqrt{K_y}C$

For the present application, the output variable to be predicted is $\Delta\mathrm{SPL_{max.}}$. The input variables are selected based on the variables that have been observed to be related to $\Delta\mathrm{SPL_{max.}}$. For the present data, it has been assumed that $\Delta\mathrm{SPL_{max.}}$ is a weak function of Re_c. Furthermore, the fluid properties, such as the temperature and viscosity, do not vary largely among the different data points. Therefore, $\Delta\mathrm{SPL_{max.}}$ may be linked to two variable groups: the material properties ϕ, K_x, K_y, and C, and the airfoil permeable TE geometry represented by $x_{\mathrm{per.}}$ and $A_{\mathrm{per.}}$ in this case.

Because the algorithm has no knowledge in the physical unit of each variable, dimensionless input variables are employed to avoid physically incorrect functions [124]. The Buckingham–Pi theorem is utilized to formulate dimensionless quantities based on the input variables. The dimensionless input and output variables for the present problem are summarized in Table 7.3. In combination with these input variables, the following primitive mathematical operations are allowed in formulating the function g: $(.) + (.)$, $(.) - (.)$, $(.) \times (.)$, $(.) \div (.)$, $\sqrt{(.)}$, $(.)^2$, and $\log_{10}(.)$, where $(.)$ is any X_i or any combination of X_i and the mathematical operations.

In this study, three different trial runs are performed. By carefully selecting a dedicated set of data points in each trial run, the effects of airfoil geometry and permeable material types can be isolated. Inclusion and exclusion of each data point in each trial are specified in Table 7.2. Each trial is explained below.

- Trial 1: Same material type, varying airfoils: This trial only includes the perforated channel type but on both the NACA 0018 and NACA 63$_3$–018 airfoils to study the effect of airfoil geometry on the noise reduction.

- Trial 2: All cases: This trial is the most generic case, and therefore the most challenging case since it contains every data point.

- Trial 3: Same airfoil, varying material types: This trial only considers the NACA 0018 airfoil with $x_{\mathrm{per.}}/c = 0.2$ as an attempt to find a generic material-related parameter that could describe $\Delta\mathrm{SPL_{max.}}$ regardless of the permeable material type.

An open-source MATLAB-based software 'GPTIPS 2' developed by Searson [215] for symbolic data mining was used for the present problem. For each trial, five independent runs are performed. Each run contains a population of 100 individuals. The runs are terminated after 20,000 generations. This is sufficient since it is found that the lowest Root-mean-square (RMS) error of $\Delta\mathrm{SPL_{max.}}$ converges (lower than 0.5% further change) after approximately 8,000 generations for the second trial, which is the most challenging trial.

7.4. RESULTS AND DISCUSSION

7.4.1. TRIAL 1: SAME MATERIAL TYPE, VARYING AIRFOILS

A scatter plot in Fig. 7.5 shows every individual in the final-generation population of the trial 1 run. Each point represents a unique regression model for predicting $\Delta SPL_{max.}$. The points are plotted according to the regression model complexity, i.e. number of nodes, in the horizontal axis, and the RMS error of the $\Delta SPL_{max.}$ prediction in the vertical axis.
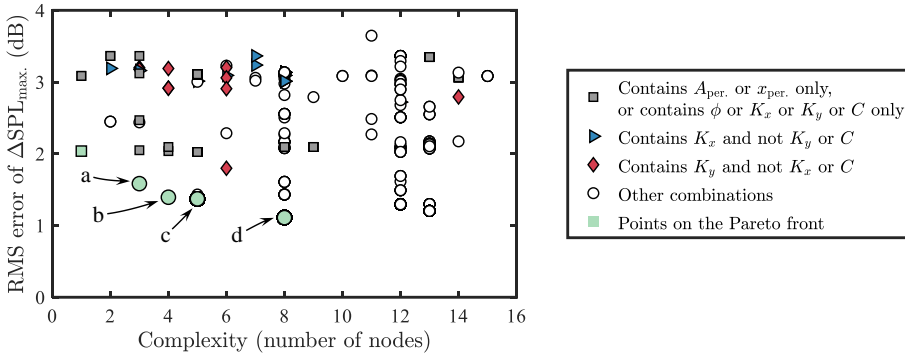

Figure 7.5: Functional complexity and prediction accuracy of the final-generation population of the symbolic regression modeling trial 1.

Furthermore, to gain further insights into parameters that are included in each model, i.e. individual, in the population, the point markers vary according to the following conditions (See the legend of Fig. 7.5):

- Models that contain either the parameters describing the airfoil geometry ($A_{per.}$ or $x_{per.}$), or the parameters describing the material properties (ϕ or K_x or K_y or C). When multiple airfoils are considered altogether, i.e. trials 1 and 2, it is obviously impossible to be able to predict $\Delta SPL_{max.}$ by disregarding the airfoil geometry and using parameters that account for the material properties alone. These models are therefore incomplete and shall not be considered further in trials 1 and 2.

- Models that contain the permeability in the x direction K_x and neither K_y nor C.

- Models that contain the permeability in the y direction K_y and neither K_x nor C. The latter two conditions help to gain further insights on the comparative importance between K_x and K_y in predicting $\Delta SPL_{max.}$.

- Models that do not fall within any criteria above are marked by a generic point.

- Models on the so-called *Pareto front*, where potentially the best trade-offs between the modeling complexity and the prediction accuracy are found are highlighted by slightly bigger markers with a different color.

According to Fig. 7.5, there are five models on the Pareto front. Since this trial considers the perforated channels on multiple airfoils, one model on the Pareto front where only the airfoil- or material-related parameters are considered is definitely incomplete. Logically, this model is the least accurate model (RMS error $\approx$ 2 dB) out of all models on the Pareto front. Interestingly, for the other incomplete models, the RMS errors are never lower than 2 dB.

The four remaining models on the Pareto front are examined further. These models are marked by the letters a to d ordered from the least-accurate and least-complex to the most-accurate and most-complex models. The expressions for these models are shown in Eqs. 7.4a to 7.4d.

$$\Delta SPL_{\text{max.}} = 9.8 \times 10^5 \frac{A_{\text{per.}} \sqrt{K_y} C}{x_{\text{per.}}^2} - 8.3 \text{ dB} \tag{7.4a}$$

$$\Delta SPL_{\text{max.}} = 3.4 \times 10^3 \frac{\sqrt{A_{\text{per.}} \sqrt{K_y} C}}{x_{\text{per.}}} - 11 \text{ dB} \tag{7.4b}$$

$$\Delta SPL_{\text{max.}} = 266 \left(\frac{A_{\text{per.}} \sqrt{K_y} C}{x_{\text{per.}}^2} \right)^{1/4} - 15 \text{ dB} \tag{7.4c}$$

$$\Delta SPL_{\text{max.}} = 2.7 \log_{10} \left(\frac{A_{\text{per.}} \sqrt{K_x} C}{x_{\text{per.}}^2} - \frac{0.074 K_x}{A_{\text{per.}}} \right) - 36 \text{ dB} \tag{7.4d}$$

7

Despite the increasing complexity from Eq. (7.4a) to Eq. (7.4d), a common trend among these models is observed. All of the models contain a rather specific selection of the dimensionless parameters, namely a multiplication between $A_{\text{per.}}/x_{\text{per.}}^2$ relating to the permeable TE geometry and $\sqrt{K} C$ relating to the permeable material properties. This confirms the dependence of $\Delta SPL_{\text{max.}}$ on the airfoil geometry $A_{\text{per.}}/x_{\text{per.}}^2$ and implies that, for a given material property $\sqrt{K} C$, more noise reduction is expected if the permeable TE is long and/or thin. This could be linked to the previously discussed findings of Teruna et al. [107] which pointed out that the noise reduction driven by the pressure release mechanism is better facilitated when the permeable TE is thin enough so that the surface pressure fluctuations on the opposite sides are able to communicate. Therefore, the long and/or thin permeable TE promotes the pressure release mechanism.

The corresponding $\Delta SPL_{\text{max.}}$ prediction accuracies of the four models in Eqs. (7.4a) to (7.4d) are shown in Figs. 7.6a to 7.6d. The data point markers correspond to the data points in Table 7.2. The RMS error of $\Delta SPL_{\text{max.}}$ prediction as well as the ± 2 dB accuracy margins are indicated. Although the prediction accuracies of the models in Eqs. (7.4a) to (7.4c) for most data points lie within ± 2 dB, the models do not seem to predict the deterioration of the maximum noise reduction when $x_{\text{per.}}/c$ decreases, especially for the relatively more permeable variants of the perforated channels, e.g. pf2p5. This is improved in the more complicated model in Eq. (7.4d) for which the smallest RMS error of 1.11 dB is found.
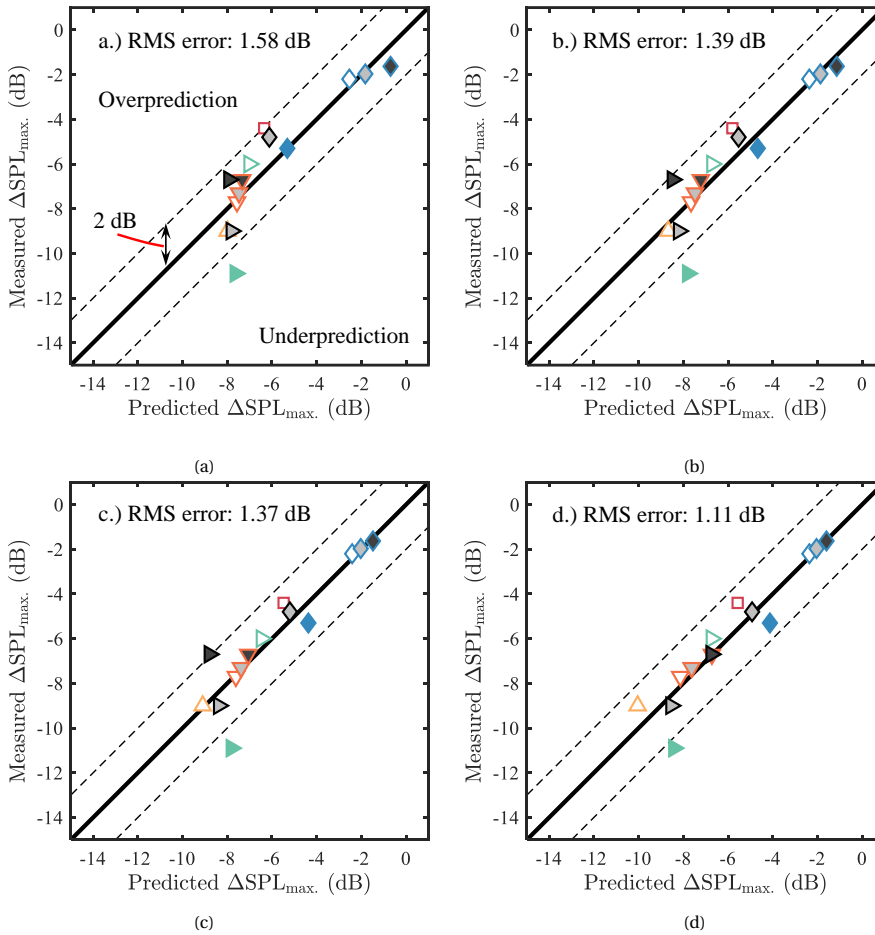
Figure 7.6: Prediction accuracy of the selected individuals in the Pareto front of the symbolic regression modeling trial 1.

7.4.2. Trial 2: All cases

Figure 7.7 presents the scatter plot of the population in the final generation from trial 2 run where all the data points in Table 7.2 are considered in the symbolic regression modeling. Because this trial contains all airfoil and material type variations. It is the most complex case, and logically, the resulting models entail a relatively higher RMS error of $\Delta SPL_{max.}$ than the first trial, ≈ 2 dB in average. Again, the models that only contain the material- or airfoil-related dimensionless groups are disregarded. These models give relatively higher RMS errors of $\Delta SPL_{max.}$ (2.5 dB or more). Therefore, only four out of six models on the Pareto front denoted by the letters a to d are examined further. Interestingly, these four selected models are noticeably more complicated than the models examined in trial 1. The lowest number of nodes is 9 while the highest number of nodes in trial 1 is
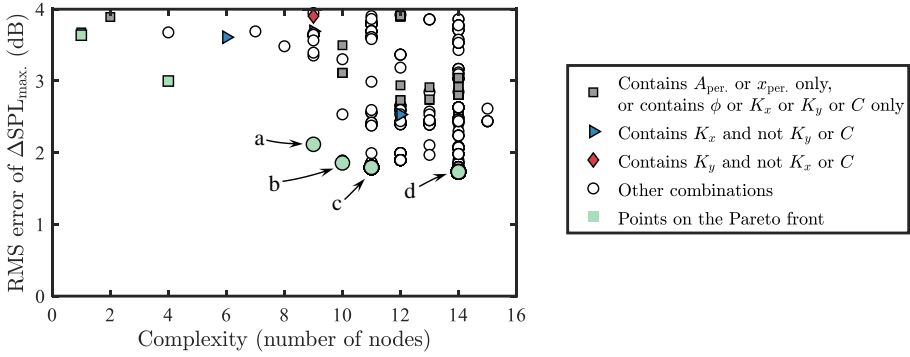
8.

Figure 7.7: Functional complexity and prediction accuracy of the final-generation population of the symbolic regression modeling trial 2.

The expressions for the selected models from the Pareto front are shown in Eqs. (7.5a) to (7.5d). Their corresponding prediction errors are shown in Figs. 7.8a to 7.8d.

$$\Delta\text{SPL}_{\text{max.}} = 9.4(\phi - A_{\text{per.}}/x_{\text{per.}}^2)\log_{10}\phi - 7.7 \text{ dB} \tag{7.5a}$$

$$\Delta\text{SPL}_{\text{max.}} = -9.8 \times 10^4 \sqrt{K_y} C \log_{10}\left(\frac{\phi x_{\text{per.}}^2}{A_{\text{per.}}}\right) - 7.2 \text{ dB} \tag{7.5b}$$

$$\Delta\text{SPL}_{\text{max.}} = -\frac{3.1 \times 10^5 \sqrt{K_x} C \log_{10}\left(\frac{\phi x_{\text{per.}}^2}{A_{\text{per.}}}\right)}{1.7\phi - 2.7} - 7.5 \text{ dB} \tag{7.5c}$$

$$\Delta\text{SPL}_{\text{max.}} = 580\frac{(\phi - A_{\text{per.}}/x_{\text{per.}}^2)\log_{10}\phi}{23\phi + 7\sqrt{K_y/K_x}} - 7.3 \text{ dB} \tag{7.5d}$$

The least complicated model in Eq. (7.5a) contains only two dimensionless groups, ϕ representing the material property and $A_{\text{per.}}/x_{\text{per.}}^2$ representing the permeable TE geometry. Interestingly, this model provides a rather accurate prediction of $\Delta\text{SPL}_{\text{max.}}$ for the perforated channels with varying $x_{\text{per.}}/c$ on the NACA 0018 airfoil. However, when considered together with the more porous metal foams and diamond-lattice structure, the prediction becomes inaccurate. The error of the predicted $\Delta\text{SPL}_{\text{max.}}$ for the diamond-lattice structure case is almost 4 dB. This leads to a relatively high RMS error of the predicted $\Delta\text{SPL}_{\text{max.}}$ of 2.12 dB for this model.

The more complicated models in Eqs. (7.5b) to (7.5d) gradually improve the prediction accuracy as shown in the corresponding Figs. 7.8b to 7.8d. Again, these models contain $\sqrt{K}C$, $A_{\text{per.}}/x_{\text{per.}}^2$, as well as ϕ.

It has been shown that predicting the $\Delta\text{SPL}_{\text{max.}}$ for an arbitrary airfoil with an arbitrary permeable TE type is a non-trivial problem. This trial indicates the need to combine

multiple material characteristics to be able to predict $\Delta \text{SPL}_{\text{max.}}$. In the next trial, the dependency on the airfoil TE shape is eliminated to simplify the problem as an attempt to identify the most relevant parameter that governs $\Delta \text{SPL}_{\text{max.}}$.

Figure 7.8: Prediction accuracy of the selected individuals in the Pareto front of the symbolic regression modeling trial 2.

7.4.3. TRIAL 3: SAME AIRFOIL, VARYING MATERIAL TYPES

The resulting final-generation plot for the trial 3 run is shown in Fig. 7.9. For this trial where the permeable TE shape on the airfoil is identical for every data point and only the permeable material type varies, the models provide relatively low RMS errors compared to the first two trials, lower than 1 dB for most points on the Pareto front.

Another interesting observation from Fig. 7.9 is that two models on the Pareto front contains only K_x. This has not been observed in the previous two trials. This result

Figure 7.9: Functional complexity and prediction accuracy of the final-generation population of the symbolic regression modeling trial 3.

suggests that K_x may be used to as an alternative to the more well-known K_y to predict $\Delta\mathrm{SPL_{max.}}$ when multiple permeable material types are considered altogether. Possible explanation for this finding is given later in this section.

Due to the relatively high accuracy, and for brevity, only two models from the Pareto front are examined in this trial. These models are again indicated by the letters a and b. The corresponding models and their prediction accuracies are shown in Eq. 7.6a and Fig. 7.10a for point a, and Eq. 7.6b and Fig. 7.10b for point b.

$$\Delta\mathrm{SPL_{max.}} = 3.3\log_{10}\left(\frac{x_{\mathrm{per.}}}{\sqrt{K_x}}\right) - 37 \text{ dB} \tag{7.6a}$$

$$\Delta\mathrm{SPL_{max.}} = -0.97\log_{10}\left(\frac{\phi K_y\sqrt{K_x K_y}}{x_{\mathrm{per.}}^2 A_{\mathrm{per.}}}\right) - 40 \text{ dB} \tag{7.6b}$$

The model in Eq. 7.6a is indeed a very interesting model due to its simplicity and accuracy (RMS error within ± 2 dB according to Fig. 7.10a). In this trial, $x_{\mathrm{per.}}/c = 0.2$ is a constant. Therefore, the model in Eq. 7.6a suggests that $\Delta\mathrm{SPL_{max.}}$ varies inversely with $\sqrt{K_x}$. In fact, $\sqrt{K_x}$ is a well-known parameter in permeable material studies called the *Brinkman screening distance* [128, 212, 213]. It is known that the depth within the permeable material where the hydrodynamic fluctuation is influenced by fluid flows over it, is proportional to $\sqrt{K_x}$. This distance should be proportional to the entrance length introduced previously. Therefore, this model implies that the maximum noise attenuation may be achieved by maximizing $\sqrt{K_x}$ of the permeable material.

The model in Eq. 7.6b and Fig. 7.10b provides a better fit with the data as well as an impressively low RMS error of 0.36 dB. In addition to K_x, this model includes ϕ and K_y. However, this model may rather be too complicated for the given problem. Interestingly, unlike the models examined in trials 1 and 2, for both models examined in trial 3, and, in fact, also for the other remaining models on the Pareto front which are omitted, the airfoil-dependent dimensionless group $A_{\mathrm{per.}}/x_{\mathrm{per.}}^2$ are not found. This is reasonable because

the permeable TE geometry in this trial is kept constant. This implies that the present symbolic regression modeling is able to prioritize the relevant dimensionless group for each specific problem.
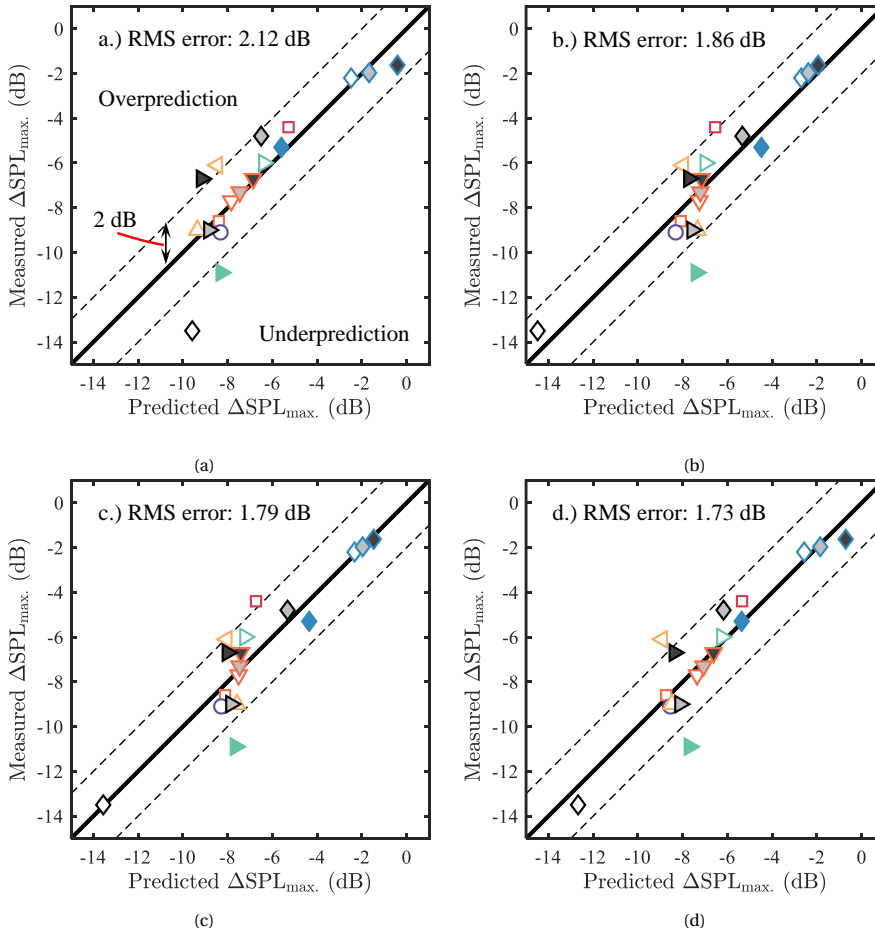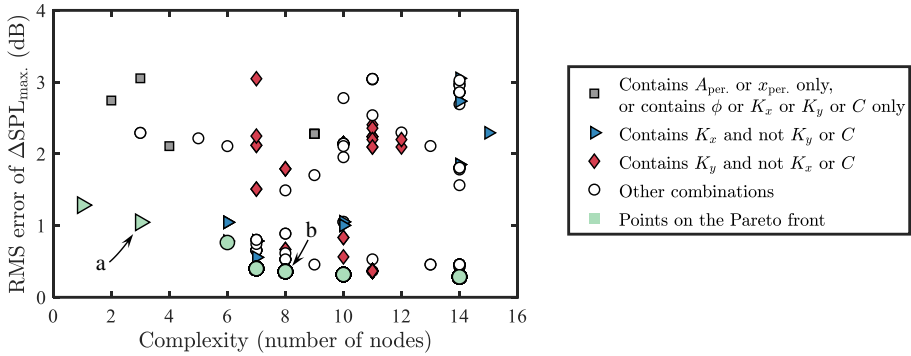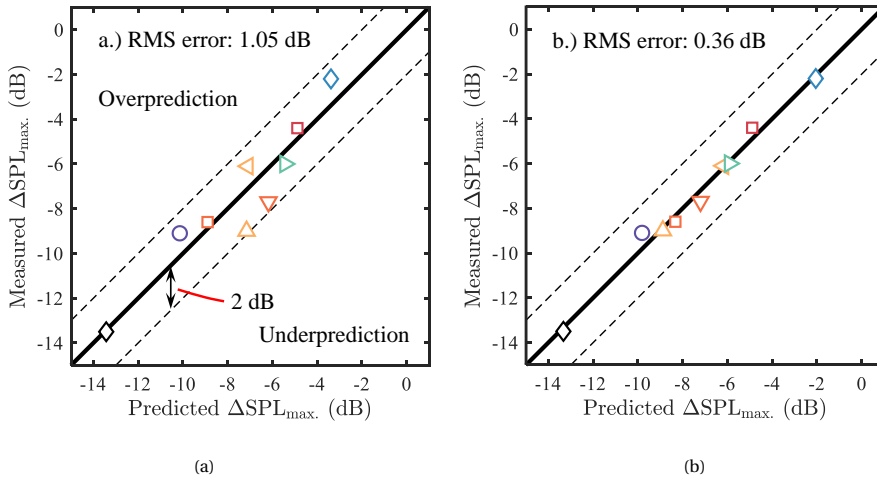

Figure 7.10: Prediction accuracy of the selected individuals in the Pareto front of the symbolic regression modeling trial 3.

7.5. CONCLUSIONS

This chapter seeks for parameters that govern the maximum noise attenuation $\Delta SPL_{max.}$ provided by airfoils with a permeable Trailing Edge (TE). It has been hypothesized that a slender, i.e. long and thin, permeable TE shape helps to maximize the magnitude of $\Delta SPL_{max.}$ because the pressure release mechanism is facilitated. Additionally, it is motivated to separate the permeable material permeability K in the chord-normal and the streamwise direction as the latter may better correlate to $\Delta SPL_{max.}$.

Experimental datasets featuring two airfoils and three permeable material types with varying permeabilities K installed at varying chordwise permeable extent lengths $x_{per.}$ are considered. A so-called symbolic regression modeling approach in combination with genetic programming is employed to formulate a function that helps to predict $\Delta SPL_{max.}$ based on the input parameters describing the permeable material characteristics and the local permeable material geometry on the airfoil.

It is found that, for a given permeable material, more noise reduction is expected if the permeable TE shape is long and/or thin. This could be because the thin permeable material shape promotes the surface pressure communications in the pressure release mechanism, which is the driving mechanism for the noise attenuation.

When multiple permeable material types are considered altogether, $\Delta SPL_{max.}$ is a complicated function that contains multiple material properties, such as the porosity ϕ, the permeability K, and the form drag coefficient C. Nevertheless, it has been found that

$\Delta SPL_{max.}$ given by multiple permeable material types can be predicted with a very good accuracy $\pm$ 2 dB by an outstandingly simple formula containing only the square-root of the permeability in the streamwise direction $\sqrt{K_x}$ known as the Brinkman screening distance. This is likely because the Brinkman screening distance is proportional to the depth within the permeable material where the hydrodynamic fluctuations are comparable to that on its surface.

7

8

APPLICATION, CONCLUSIONS, AND RECOMMENDATIONS
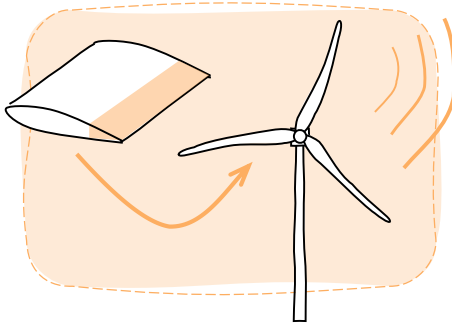
This chapter presents the first attempt to implement a novel permeable trailing-edge extension for trailing-edge noise reduction on a real wind turbine. Far-field noise measurements of a blade equipped with this novel technology are compared to a baseline blade and a blade with trailing-edge serrations. Finally, conclusions and recommendations based on the entire thesis are presented.

8.1. WIND-TURBINE APPLICATION OF A NOVEL PERMEABLE TE EXTENSION

Novel perforated Trailing-Edge (TE) extensions are applied on a real wind turbine. The acoustic performance of a blade equipped with this novel design is compared to that provided by more conventional serrated and baseline (straight and impermeable) TEs. This is an attempt to advance the technological readiness level of the permeable TE concept for TE noise reduction, as well as to advance the understanding of how the perforated TE extensions behave, compared to the more mature TE serrations, when applied on a real wind turbine. It is worth highlighting that the permeable TE concept is applied as TE extensions instead of TE inserts shown in most parts of this thesis. The reason for this design is twofold: first, to keep the blade loading as close as possible to when the TE serrations are applied; second, the extensions can be applied as an add-on to avoid major blade modifications. Practically, this add-on concept is more preferred by wind-turbine operators because it can be applied directly on existing wind turbines, similar to the TE serrations.

8.1.1. MEASUREMENT SET UP

A measurement was carried out at Windpark Wieringermeer administrated by ECN Wind Energy Facilities B.V. (EWEF) on the 'Prototype 6' wind turbine. The Prototype 6 wind turbine has a base-to-hub height of 110 m and a rotor diameter of 130 m. The power rating of this turbine is 3.6 MW.

A schematic of the set up is shown in Fig. 8.1a. The same array of microphones as described in Section 4.2.2 was placed at 71 m away from the base in the upwind direction. Each of the three blades was treated differently as follows: one blade with a baseline TE, one blade with commercial sawtooth-shaped TE serrations (details are omitted due to confidentiality), and one blade with perforated TE extensions.

A close-up view of the perforated TE extension during the installation is shown in Fig. 8.1b. The extensions were applied close to the blade tip with a spanwise portion of approximately 11 m (17 % of the span). The chordwise extension length is approximately 10 % of the local chord. This installation geometry is identical to the TE serrations installation on the other blade. The extensions comprise of arrays of 1.4-mm-diameter cylindrical perforations having 3.5-mm spacing. Based on a wind-tunnel measurement of a DU93 airfoil, a profile close to that on the actual wind-turbine blade, this particular perforation pattern is expected to give an airfoil loading very close to the TE serrations. A drawing of the permeable TE extension is also shown in Fig. 8.1b. It is worth noting that the interface where the extensions were attached to the blade via a double-sided tape has a three-dimensional wave-like pattern on the surface, identical to that of the serrations (to be shown further in Fig. 8.4), and the tip of the extensions is tapered.

The demonstrator measurement was carried out in December 2021. During the measurement, the wind speed was approximately 8 m/s and the yaw angle (See Fig. 8.1a) was 345 degrees. The turbine was rotating at 9.8 Rotations Per Minute (RPM). The local temperature was 8°C and the relative humidity was 86 % according to the Royal Netherlands Meteorological Institute (KNMI) [22].
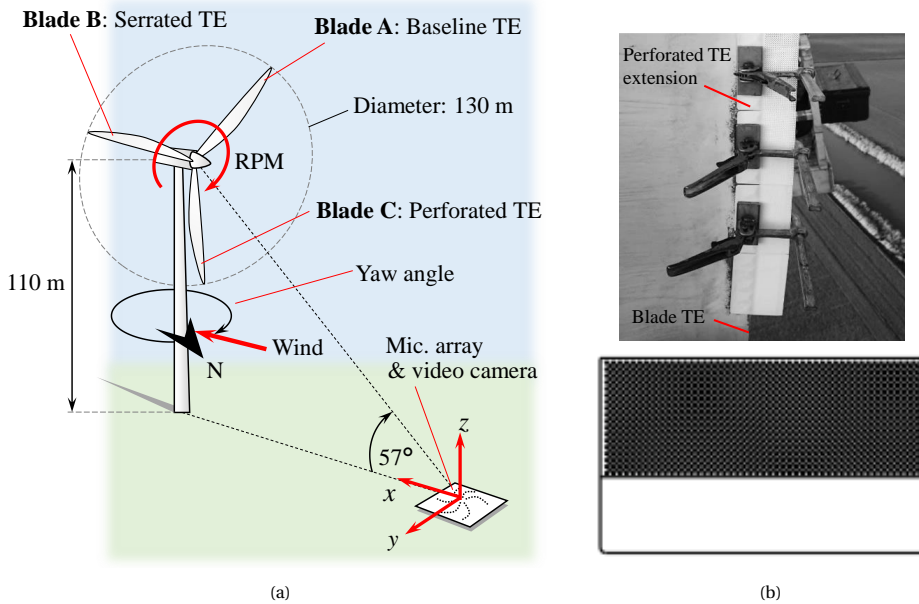
Figure 8.1: Noise measurement set up of a wind turbine with the three different blade TE configurations: (a) Schematic (not to scale) and (b) photograph and drawing of the perforated TE extension.

8.1.2. RESULTS AND DISCUSSIONS

Time-series of the Overall A-weighted Sound Pressure Level (OASPL) from a 20-second recording averaged over all microphones are shown in Fig. 8.2a. Unlike the plot presented in Fig. 1.5a, periodic patterns synchronizing with blade passes clearly shows OASPL difference among the three blades. To quantify the noise levels of each blade, a Savitzky–Golay filter 'sgolayfilt' [216] is applied to smoothen the pressure-time data and each blade pass is treated as a noise event as shown in Fig. 8.2a and the Sound Exposure Levels (SELs) are extracted. Box plots of the extracted SELs are shown in Fig. 8.2b. In average, the TE serrations give a clear noise reduction of approximately 2.5 dB(A) compared to the baseline untreated blade. Unexpectedly, the blade with the perforated TE extensions increases the noise with 1.5 dB(A), compared to the untreated blade.

Further investigations are done by analysing the Sound Pressure Level (SPL) spectra shown in Fig. 8.3. The baseline blade has an SPL peak level of approximately 55 dB at around 0.3 kHz. It also shows a distinct noise increase at approximately 8 kHz. Further calculations suggest that this noise increase is likely due to vortex shedding from the blunt TE of the baseline blade. The frequency translates to the thickness of 1.4 – 2 mm which is in the same order as the actual baseline TE thickness. The TE serrations give noise reduction in the frequency range below 1 kHz and the tonal peak is absent. The perforated TE inserts give noise increase in two frequency ranges. At relatively low frequencies (below 0.7 kHz), this noise increase is likely due to flow separation. On the other hand, noise increase at high frequencies (from 3 kHz) could be attributed to surface roughness, i.e.
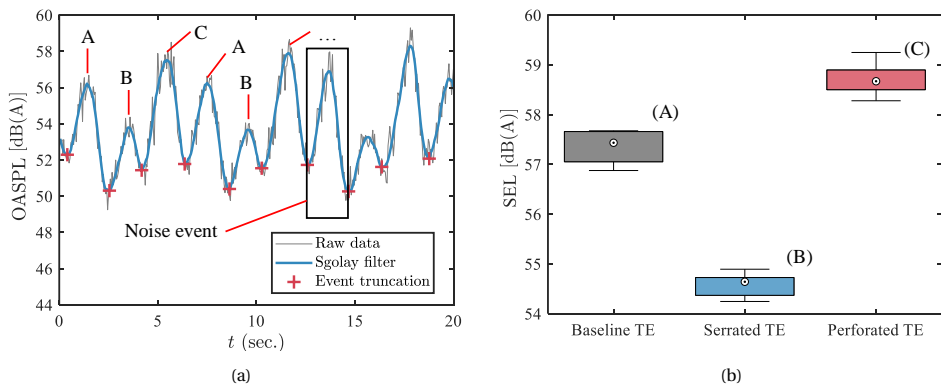
Figure 8.2: (a) Time-series OASPL data of 20-second recording from the Prototype 6 wind turbine where the three blades are treated differently and (b) SEL given by each blade of the Prototype 6 wind turbine.
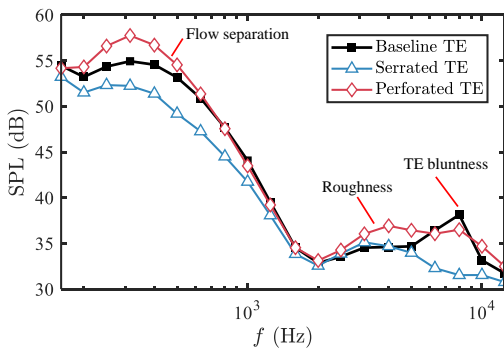
Figure 8.3: SPL spectra of noise emission from each blade of the Prototype 6 wind turbine.

flow interaction with the array of pore openings.

8.1.3. INSPECTION OF THE INSTALLED PERMEABLE TE EXTENSIONS

The results have shown that the perforated TE extensions do not reduce noise as expected. In January 2022, a drone inspection was carried out to gather evidence that could be useful for explaining the results. Photographs were taken by a Sony 65 Megapixel camera mounted on a DJI Matrice 600 Pro drone operated by Euro Drone Inspections. High-resolution photographs of the perforated TE extensions are shown in Fig. 8.4. The photographs show that the pores are not clogged. However, there is a clear pattern of darker color in the upstream part of the extension which ends close to the extension tip. Some of them exhibit a clear pattern resembling the wave-like structure at the interface surface (See, for instance, S2). This pattern might result from dust or dirt transported by the wind or water droplets. The absence of this pattern close to the tip suggests that the flow might separate where the extensions taper. This phenomenon may be responsible for the absent of the noise reduction, i.e. the downstream pores are not interacting with

the flow.

Figure 8.4: Drone photographs of the perforated TE extensions approximately one month after installation.

Therefore, to conclude this application part, the TE serrations are very robust in mitigating the TE noise. On the other hands, for the novel perforated TE extension, despite being successful in noise reduction when tested in wind tunnels, it still needs to be more carefully designed to ensure its work-ability and robustness on real wind turbines.

8.2. CONCLUSIONS

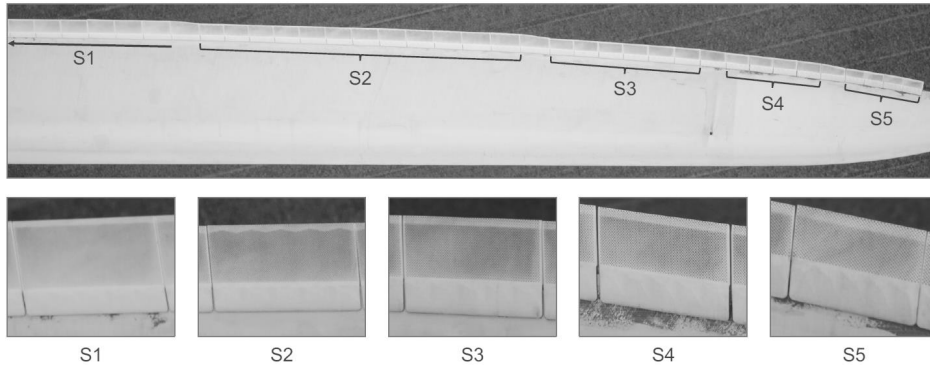It is worth beginning this conclusion section by briefly restating the objectives of this thesis represented by the title 'Assessing and improving trailing-edge noise reduction technologies for industrial wind-turbine applications'.

This thesis aims to advance technological readiness level of TE noise reduction technologies for industrial wind-turbine applications. There are therefore two consecutive research objectives of this thesis: first, to thoroughly *assess* aerodynamic and acoustic performance of an airfoil with TE noise reduction technologies, namely TE serrations and permeable TE. Next, based on the assessment, to *improve* the performance of the permeable TE which is a less mature technology compared to the TE serrations, but shows potential to achieve a higher maximum noise reduction than the TE serrations. The entire framework of this thesis focuses on industrial wind-turbine applications. It is aimed to raise the technological readiness level of such technologies by ultimately implementing them on a real wind turbine.

The conclusions are provided in the following with regard to each aspect of the research objectives:

1. *Assessment* of the TE noise reduction technologies is presented in Chapter 5. Extensive characterization of NACA 63_3–018 airfoil models equipped with TE serrations and perforated TE inserts in a broad range of chord-based Reynolds number Re_c and angle of attack range led to the following conclusions:

    (a) The TE noise reduction varies with the TE serrations geometry and the perfo-

rated TE insert permeability. The perforated TE inserts provide approximately 4 dB higher maximum noise reduction than the TE serrations. Increasing airfoil loading and surface roughness cause noise increase for the TE serrations and the perforated TE inserts, respectively. Overall, the TE noise reduction performance of both add ons deteriorates with the increasing airfoil loading.

(b) Regarding to the aerodynamic performances, the TE serrations increase lift and drag of the airfoil slightly. On the other hand, the perforated TE inserts reduce the lift and increase the drag more substantially, especially at high angles of attack.

2. *Improvement* of the TE noise reduction by the permeable TE is presented in Chapters 6 and 7. Chapter 6 examines an alternative permeable topology design for TE noise attenuation. This permeable topology, realized by a Kevlar-covered 3D-printed perforated channels, has a high form drag coefficient C and a low air flow resistivity r, unlike the conventional porous metal foams where C varies directly with r. An extensive experimental investigation featuring aerodynamic drag and far-field noise measurements of a NACA 0018 airfoil with this alternative permeable TE design was carried out. Results were compared to the porous metal-foam TE inserts. The study led to the following conclusions:

(a) The proposed permeable topology design provides a broadband TE noise mitigation of up to 5 dB. The proposed topology overcomes the tonal noise increase that would occur when the 3D-printed perforated channels are employed alone. Furthermore, the smooth surface of the proposed topology helps mitigate the roughness noise, and, correspondingly, the aerodynamic drag increase, compared to the porous metal foams.

(b) Unlike the metal foams, the high-C and low-r property helps to sustain the noise mitigation performance when the airfoil loading increases.

Next, Chapter 7 compiles the past wind-tunnel noise measurement data of two airfoil profiles and three different permeable material types to investigate effects of airfoil installation and permeable material types on the maximum noise reduction. A symbolic regression modeling method was employed to identify relevant parameters that drive the maximum noise reduction. The study led to the following conclusions:

(a) For a given permeable material, the noise reduction is maximized with a long and/or thin permeable material.

(b) For multiple permeable material types, the maximum noise reduction is driven by a generic parameter called the Brinkman screening distance, which is the square-root of the permeability in the streamwise direction $\sqrt{K_x}$.

3. *Wind-turbine application* of the novel permeable TE extension presented in this chapter led to the following conclusions:

(a) For the considered real wind-turbine set up, the TE serrations mitigate approximately 2.5 dB(A) of noise. However, 1.5 dB(A) of noise increase is found for the novel perforated TE extension.

(b) Noise spectra and visual inspections of the perforated TE extension suggest that flow separation may have occurred. Due to this, the pores may not be interacting with the flow as intended.

8.3. RECOMMENDATIONS

Chapter 5 of this thesis has shown that the permeable TE insert can achieve up to 4 dB extra noise reduction, compared to the best-performing TE serrations. This thesis has attempted to overcome aerodynamic shortcomings of the permeable TE technology as well as increase its practicality and technological readiness level. The conclusions from this thesis motivate recommendations for future *fundamental* and *applied* research works into permeable TEs for wind-turbine noise reduction, presented in Sections 8.3.1 and 8.3.2, respectively.

8.3.1. RECOMMENDATIONS FOR FUNDAMENTAL RESEARCH

DETERMINATION OF K_x

Chapter 7 has shown that the permeability in the streamwise direction K_x may be a more suitable more parameter for describing the TE noise attenuation given by a permeable TE compared to the more frequently used permeability in the direction normal to the chord K_y. Therefore, the present permeable material characterization method shown in Section 2.3.1, where flow is forced to penetrate the material sample, may not be suitable for characterizing permeable materials for the TE noise reduction because it does not represent the actual flow–material interaction.

An alternative set up for permeable material characterization to extract K_x may be realized as a channel flow set up as shown in Fig. 8.5 where the flow passes a channel with a permeable material layer. Within the permeable material, the flow velocity equals to the Darcy velocity v_D. At the fluid and permeable material interface $y = 0$, there is a finite slip velocity v_S and the interface boundary layer thickness δ_i where v_S approaches v_D. Past literature has derived expressions showing that the parameters v_S and δ_i are correlated [217] and vary directly with $\sqrt{K_x}$ [213, 218]. Thus K_x can be determined experimentally or numerically by measuring v_S and/or δ_i using this set up.

OPTIMIZING K_x AND K_y

Subsequently, it is further recommended to consider anisotropic permeable materials, i.e. $K_x \neq K_y$, in future studies. The goal of this is to find an optimal combination of K_x and K_y. While the maximum noise reduction is driven by K_x, the loss of lift for permeable airfoils due to balancing of steady surface pressures between the suction and the pressure sides is governed by K_y. Therefore, a parametric study may be carried out experimentally and/or numerically to maximize the noise reduction and minimize the aerodynamic impacts provided by the permeable TE.

One tool that may be suitable for such a parametric study is the so-called Mimetic
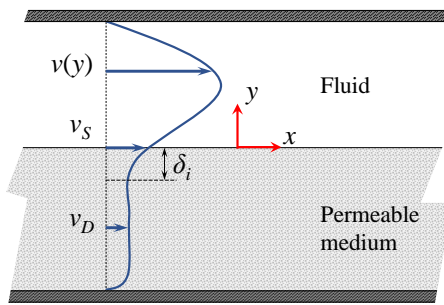
Figure 8.5: A typical velocity profile in a channel flow with a permeable medium layer.

Spectral Element Method (MSEM), a variant of the Finite Element Method (FEM) which is able to provide machine-precision solution in a relatively short time [219]. Thus, this tool may be suitable to be incorporated in a design routine to search for an optimal K_x and K_y combination. A preliminary effort in modeling a NACA 0018 airfoil with a permeable TE insert having anisotropic permeability using the MSEM is briefly presented in Appendix D.

8.3.2. RECOMMENDATIONS FOR APPLIED RESEARCH

For *applied* research works, it is likely that permeable TE extensions such as that presented in Section 8.1 will gain more industrial acceptance than permeable TE inserts. This is because, similarly to the TE serrations, they can be applied directly on existing wind-turbine blades without major geometrical and/or structural modifications. Future wind-tunnel tests of permeable TE prototypes shall focus on such extensions. Moreover, robustness of the permeable TE extensions shall be improved. Future permeable TE extensions shall be designed to be more resilient to flow separation and to avoid excessive lift. A parametric study on the noise reduction performance of permeable TE extensions in relation to their flap angle, for instance, may be beneficial. Moreover, frequent tests of permeable TE extension prototypes on real wind turbines would help to accelerate the industrial acceptance and the technological readiness level of this technology.

8

A

SUPPLEMENTARY COORDINATES[1]

A.1. PRESSURE TAP COORDINATES

The chordwise locations of the pressure taps on the NACA 0018 and NACA 63_3–018 airfoil models are provided in Tables A.1 to A.3. The superscript * indicates the pressure taps that may be blocked or interfered by the tripping strip.

A.2. MICROPHONE ARRAY COORDINATES

The microphone array coordinates used in the A–Tunnel and the LTT are provided in Tables A.4 and A.5, respectively.

---

[1]Parts of this appendix will be published in the AIAA Journal. Please cite as shown in the list of peer-reviewed journal articles, number 6.

A

Table A.1: Chordwise pressure tap locations on the 200-mm chord NACA 0018 airfoil for both the suction and pressure sides.

x/c (−)	-0.99	-0.965	-0.94	-0.89	-0.84	-0.79*	-0.74	-0.69	-0.64	-0.59
	-0.54	-0.49	-0.44	-0.39	-0.37					

Table A.2: Chordwise pressure tap locations on the 200-mm chord NACA 63_3–018 airfoil model (LRM).

x/c (−)	-0.98	-0.965*	-0.95*	-0.925*	-0.9	-0.875	-0.85	-0.8	-0.7	-0.6	-0.5	-0.4
Presence		suction side only					suction and pressure sides					

x/c (−)	-0.325	-0.275	-0.225	-0.175
Presence	suction and pressure sides			suction side only

Table A.3: Chordwise pressure tap locations on the 900-mm chord NACA 63_3–018 airfoil model (HRM) for both the suction and pressure sides.

x/c (−)									
-1.0000	-0.9996	-0.9984	-0.9963	-0.9934	-0.9898	-0.9858	-0.9812	-0.9760	-0.9705
-0.9646	-0.9583	-0.9516	-0.9446*	-0.9373*	-0.9296*	-0.9215	-0.9131	-0.9044	-0.8953
-0.8859	-0.8762	-0.8635	-0.8478	-0.8291	-0.8074	-0.7826	-0.7548	-0.7239	-0.6899
-0.6499	-0.6099	-0.5700	-0.5302	-0.4904	-0.4508	-0.4113	-0.3719	-0.3325	-0.2933
-0.2540	-0.2147	-0.1754	-0.1409	-0.1113	-0.0816	-0.0568	-0.0319	0.0000	

A

Table A.4: Microphone coordinates used in the A–Tunnel.

Mic. No. (–)	x (m)	z (m)	Mic. No. (–)	x (m)	z (m)	Mic. No. (–)	x (m)	z (m)	Mic. No. (–)	x (m)	z (m)
1	-0.410	0.030	17	0.640	0.030	33	-0.125	0.120	49	-0.005	-0.180
2	-0.545	-0.030	18	0.745	-0.120	34	-0.230	0.195	50	-0.080	-0.270
3	-0.605	0.120	19	0.730	0.105	35	-0.020	0.315	51	-0.350	-0.150
4	-0.605	-0.135	20	0.880	-0.030	36	-0.410	0.195	52	-0.380	-0.240
5	0.040	0.420	21	0.910	-0.210	37	-0.245	0.330	53	-0.290	-0.345
6	-0.755	0.030	22	0.970	0.105	38	-0.500	0.300	54	-0.605	-0.270
7	-0.695	0.240	23	1.045	-0.105	39	0.460	0.435	55	-0.110	-0.435
8	-0.830	-0.090	24	0.955	0.210	40	-0.185	0.435	56	-0.515	-0.375
9	0.355	0.120	25	0.265	-0.105	41	0.115	0.000	57	0.295	-0.270
10	0.115	0.165	26	0.355	-0.030	42	0.115	-0.135	58	0.025	-0.345
11	0.475	0.195	27	0.325	0.045	43	0.040	0.105	59	0.460	-0.300
12	0.130	0.255	28	0.190	0.105	44	-0.095	0.045	60	0.235	-0.390
13	0.430	0.285	29	0.235	-0.180	45	-0.125	-0.030	61	0.685	-0.270
14	0.715	0.225	30	0.430	-0.105	46	-0.035	-0.105	62	0.490	-0.420
15	0.265	0.360	31	0.475	0.015	47	-0.245	0.015	63	0.715	-0.390
16	0.625	0.345	32	0.580	-0.150	48	-0.200	-0.105	64	0.100	-0.495

A

Table A.5: Microphone coordinates used in the LTT.

Mic. No. (–)	x (m)	z (m)	Mic. No. (–)	x (m)	z (m)	Mic. No. (–)	x (m)	z (m)	Mic. No. (–)	x (m)	z (m)
1	0.068	0.014	17	0.417	-0.038	33	-0.328	0.004	49	0.240	0.069
2	0.059	-0.021	18	0.520	0.021	34	-0.271	0.035	50	0.331	-0.006
3	0.124	0.046	19	0.424	-0.089	35	-0.409	0.032	51	0.118	0.128
4	0.183	-0.005	20	0.512	0.098	36	-0.262	0.070	52	0.388	0.059
5	0.097	-0.054	21	0.611	-0.029	37	-0.333	0.103	53	0.315	0.121
6	0.208	-0.079	22	0.365	-0.142	38	-0.266	0.138	54	0.114	0.178
7	0.192	-0.118	23	0.645	0.060	39	-0.396	0.176	55	0.311	0.172
8	0.070	-0.157	24	0.619	-0.079	40	-0.228	0.202	56	0.244	-0.181
9	-0.424	-0.022	25	-0.175	-0.050	41	-0.688	-0.011	57	-0.126	0.000
10	-0.564	-0.034	26	-0.289	-0.030	42	-0.762	0.036	58	-0.147	0.051
11	-0.547	0.045	27	-0.094	-0.078	43	-0.704	-0.076	59	-0.013	0.042
12	-0.584	0.083	28	-0.299	-0.065	44	-0.779	0.091	60	-0.037	-0.046
13	-0.529	-0.100	29	-0.376	-0.097	45	-0.858	-0.037	61	-0.051	0.076
14	-0.523	0.131	30	-0.181	-0.142	46	-0.719	0.138	62	-0.022	0.113
15	-0.376	-0.152	31	-0.110	-0.188	47	-0.769	-0.123	63	-0.071	-0.115
16	-0.593	-0.147	32	-0.304	-0.199	48	-0.933	0.010	64	-0.097	0.165

B

KEVLAR TRANSMISSION LOSS AND BACKGROUND NOISE OF THE LTT[1]

This appendix describes the characterization of the Transmission Loss (TL) and background noise properties of the Low–Turbulence Tunnel (LTT) facility. These properties were measured using a speaker in the empty test section for the TL and with the fully empty test section for the background noise.

A Visaton K50 SQ speaker was used to assess the Kevlar properties. The speaker was positioned at $(x, y, z) = (0.5c, 0, 0.12c)$. Synthesized white-noise signal generated in MATLAB was fed to the speaker. To record the sound signal emitted from the speaker, a LinearX M53 microphone was installed at the center of the microphone array, $(x, y, z) = (0.5c, 1.16c, 0)$. Prior to installation, this microphone was calibrated using a G.R.A.S. Type 42AA pistonphone. Tests were carried out with and without the stretched Kevlar panel between the speaker and the microphone to determine the TL. Figures B.1a and B.1b show the set up with and without the Kevlar panel, respectively.
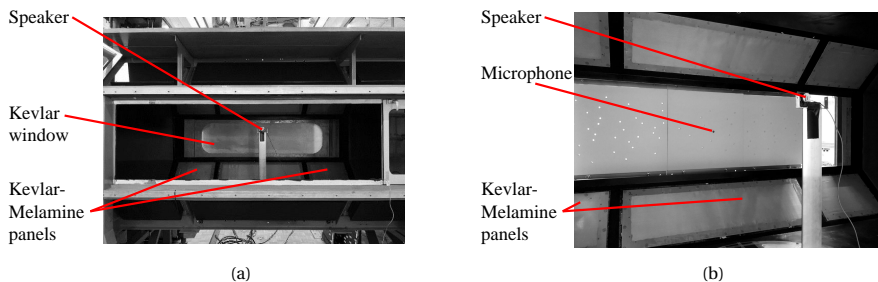

Figure B.1: Set up of the speaker and microphone in the empty LTT test section (a) viewed from outside of the test section and (b) viewed from inside of the test section.

Data was recorded with a sampling frequency of 51.2 kHz for 2.7 seconds. Post-processing in the frequency domain was done by averaging the spectra obtained from fast-Fourier-transformed time domain data snapshots having a length of 0.0625 second,

---

[1]This appendix will be published in the AIAA Journal. Please cite as shown in the list of peer-reviewed journal articles, number 6.

weighted with the Hanning weighting function with 50% data overlap between adjacent time-domain snapshots. The process resulted in a frequency resolution of 16 Hz.

The TL is calculated following the procedure described in Devenport et al. [153] for the Stability Wind Tunnel at Viginia Tech and Mayer et al. [220] for the Kevlar-walled test section at the University of Bristol. The latter uses the same Kevlar cloth type, 49 plain cloth with a weight-per-area ratio of 61 g/m^2 [154], as the one selected for the LTT test section. The values of TL versus frequency f are shown in Fig. B.2a. The periodic pattern of the TL with respect to f is observed in the measured narrow-band TL. This is in accordance with previous works [153, 221, 222]. The following equation is fitted to the data to represent the frequency-dependent TL:

$$\text{TL} = K_{\text{TL}}\left(\frac{f}{1000}\right)^2 \text{ dB,} \tag{B.1}$$

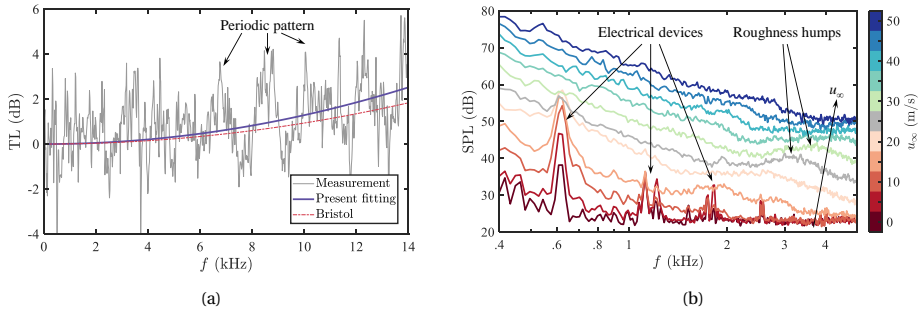
Figure B.2: (a) Transmission losses (TL) through the Kevlar sheet and (b) Background noise SPL spectra measured in the LTT versus flow speeds u_∞.

where a least-square fitting procedure was used to determine the empirical coefficient K_{TL}. This results in $K_{\text{TL}} = 12.9 \times 10^{-3}$, close to the work of Mayer et al. [220] for the Kevlar section at Bristol ($K_{\text{TL}} = 9.4 \times 10^{-3}$). These curves are also shown in Fig. B.2a.

The measured narrow-band background noise SPL spectra for varying free-stream flow speeds u_∞ are shown in Fig. B.2b. The levels have been corrected for the TL and the distance from the center of the test section is assumed to be 1 m (1.11c). Strong tones are captured for $u_\infty \leq 20$ m/s, predominantly at 0.6 kHz. These are attributed to background noise from the motor inverter in the LTT. The same tone is also observed for the measurements of the airfoil at the lowest Re_c case in the LTT (Fig. 5.10b), indicating that the measured tone is not a self noise from the airfoil model. For $u_\infty > 20$ m/s, the flow noise dominates, overshadowing the tones, and the background noise levels increase with the increasing u_∞. Another notable feature of the spectra is the broadband hump which becomes visible for $u_\infty \geq 25$ m/s. At $u_\infty = 25$ m/s, the hump reaches its peak at $f \approx 3$ kHz. This part of the spectrum is attributed to the so-called roughness humps, as investigated by Stephens [223] and other studies [224]. This roughness comes from imperfections on the wind-tunnel walls, such as opening gaps between the test section and the LTT circuit.

C

AIRCRAFT APPLICATION OF THE PERMEABLE TE DESIGN CONCEPT[1]

The permeable TE design having a permeable core and a smooth surface from Chapter 6 may be integrated with an acoustic liner which is a noise mitigation for modern aircraft. A possible design is a hybrid-permeable liner design. A schematic of the design concept is shown in Fig. C.1.

The present design concept is an actively-controlled structure with the goal of attenuating multiple aeroacoustic sources of noise from an aircraft. The structure is integrated into the TE region of an aircraft wing, downstream of the engine or propeller. It targets both the airfoil self-noise generated by a TBL on the flap surface, and interaction noise due to the proximity between the wing and the exhaust flow from the engine or the impinging vortices from the propeller. The active control allows the structure properties to shift among different operational modes to tackle different aircraft noise sources occurring during different flight phases. Moreover, the use of smooth, flow-impermeable, and acoustically-permeable materials on the structure surface allows for minimal change in aerodynamic performance, i.e. minimal decrease of lift and increase of friction drag.

The structure is similar to a conventional acoustic liner. The main difference is in the back plate which is usually rigid and impermeable. In this case, the permeability of the back plate is actively controlled, resulting in a hybrid characteristic between two well-known passive noise attenuation devices: an acoustic liner and an open-cell permeable structure.

The structure comprises of five main layers (starting from the side of the wing which faces the engine/propeller):

1. A fixed micro-perforated plate that serves as a face-sheet for the acoustic liner, whose surface may also be covered by a wire-mesh. The perforations of this layer remain open in all flight conditions;

2. An array of honeycomb channels;

3. A sliding micro-perforated plate, featuring a special perforation pattern for opening and closing the micro-perforated pattern of layer 4;

---

[1]This appendix has been filed as a patent. Please cite as shown in patent application number 1.
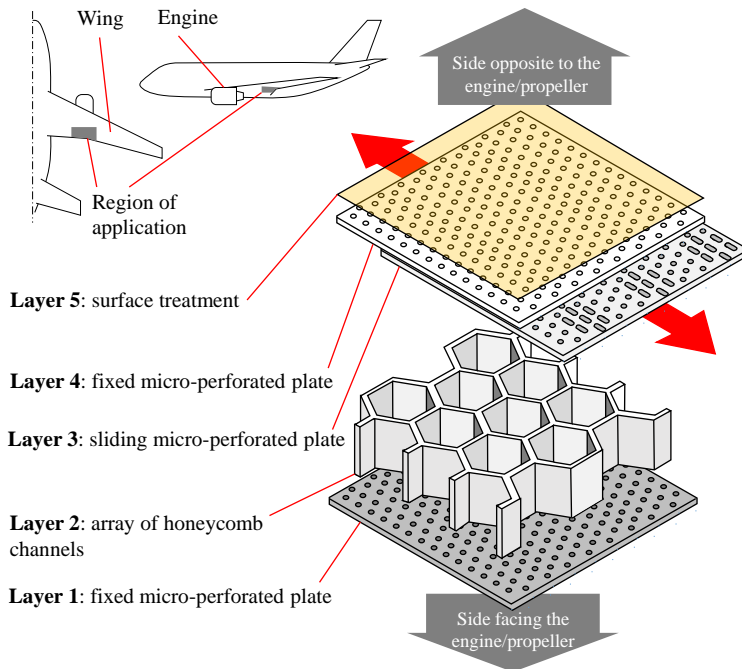
Figure C.1: Schematic of the hybrid permeable liner design concept.

4. A fixed micro-perforated plate, similar to layer 1, which acts as solid back-plate, when the perforations are not aligned with those of layer 3;

5. A surface treatment layer made of a smooth, acoustically permeable material with a high form drag coefficient, for maintaining the aerodynamic performance of the wing, as well as mitigating possible additional surface roughness.

Layers 1 and 2 may be manufactured in multiple layers inside the honeycomb structure to increase the number of degrees-of-freedom of the acoustic liner. Different operational modes of the structure can be obtained by sliding layer 3, which controls alignment of the pores between layers 3 and 4. The control to activate the different pore alignments to shift among the different operational modes as shown in Figs. C.2a to C.2c may be coupled with flap deployment mechanism as follows:

1. All pores are closed, providing no permeability through any of the honeycomb channels: the structure is operated fully as an acoustic liner. This mode is activated when the flaps are fully retracted during the cruise phase;

2. Some pores are open, providing permeability through some of the honeycomb channels: the structure is a hybrid between the acoustic liner and the permeable
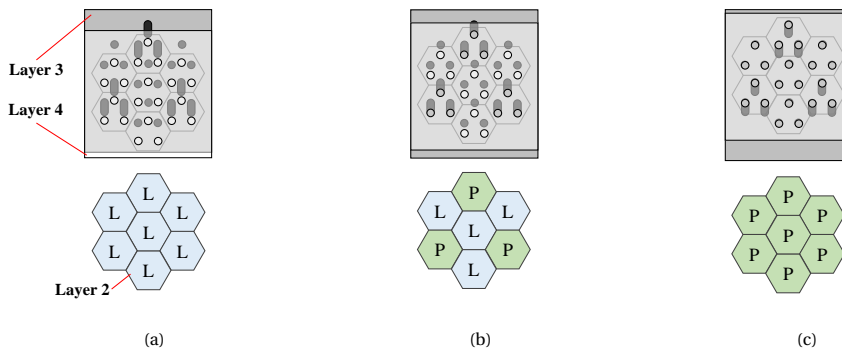
Figure C.2: Operational modes of the hybrid permeable liner (L = liner and P = permeable structure).

structure. This mode is activated when the flaps are partially deployed during the take-off phase;

3. All pores are open, providing permeability through all of the honeycomb channels: the structure is operated fully as a permeable structure. This mode is activated when the flaps are fully deployed during the approach phase.

The characteristics of the liner and the permeable structure may also be fine-tuned by locally varying the distribution of the perforation, i.e. layers 1 ,3, and 4, or sizes of the honeycomb channels, i.e. layer 2. A *gradient permeability* on the surface, where the number of open-cell permeable structures increases towards the TE of the wing, may be realized. In this way, an optimized permeability can be achieved with respect to the surface pressure distribution on the flap, thus avoiding a sudden change in impedance between solid and permeable surfaces, as well as reducing possible losses to the performance due to lift decrease and drag increase.

C

D

MSEM APPLICATION TO AN AIRFOIL WITH AN ANISOTROPICALLY PERMEABLE TE

The so-called Mimetic Spectral Element Method (MSEM) is a variant of the Finite Element Method (FEM) which is able to provide machine-precision solution in a relatively short time [219]. This appendix presents a preliminary effort in modeling a NACA 0018 airfoil with a permeable trailing-edge (TE) insert having anisotropic permeability using the MSEM.

A flow domain containing the NACA 0018 airfoil with a permeable TE having a length of 20 % of the chord is governed by the hybrid Darcy equation [225]. This equation contains a permeability tensor $\mathbb{K}(x, y)$ where $K_x(x, y)$ and $K_y(x, y)$ can be varied. Figures D.1a to D.1d show the normalized mean flow velocities u/u_∞ for various combinations of K_x and K_y within the permeable TE insert of this airfoil at zero-degree angle of attack. It can be seen that, for the permeable TEs with anisotropic permeabilities (Figs. D.1b and D.1c), u/u_∞ within the permeable TE inserts are infinitestimal. Only for the permeable TE insert with isotropic permeability, there are finite u/u_∞ within the permeable TE insert which increases toward the TE tip.

The corresponding pressure distribution over the airfoils considered in Figs. D.1a to D.1d are shown in Fig. D.2. The pressure distribution of an impermeable NACA 0018 airfoil (corresponds to Case A) obtained from the Vortex Panel Method (VPM) is also shown for verification. It is evident that, while there is a change of lift over the TE insert with an isotropic permeability (Case D), the pressure distributions over the TE insert with anisotropic permeabilities (Cases B and C) hardly alter from the impermeable airfoil (Case A). This implies that there are possibilities to realize anisotropic permeable TEs that have minimal impacts on the airfoil's lift.

Referring to the results in this thesis, Case B where $K_y \gg K_x$ is analogous to the perforated channels, while Case D where $K_y \approx K_x$ is analogous to the porous metal foams. Both of the aforementioned permeable materials are able to mitigate the TE noise. However, considering the aerodynamic benefits, anisotropic permeable materials such as the perforated channels are more preferred than the porous metal foams.
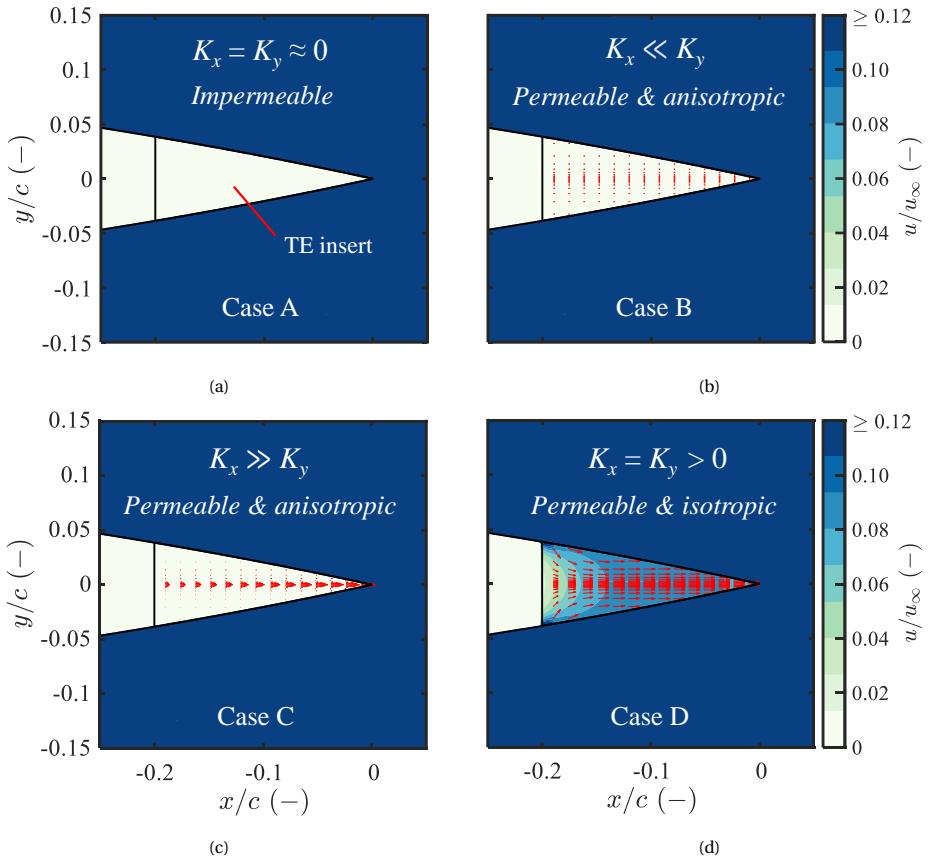
D

(a)

(b)

(c)

(d)

Figure D.1: Close-up view of the velocity field within a permeable TE insert having different permeabilities on a NACA 0018 airfoil predicted by the MSEM for zero-degree angle of attack.
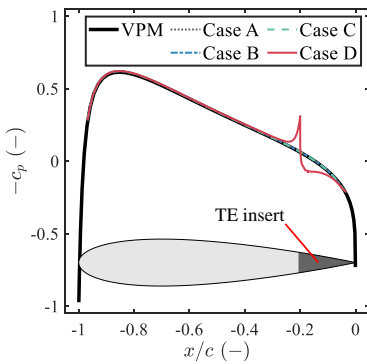

Figure D.2: Pressure distributions on a NACA 0018 airfoil with TE inserts having different permeabilities predicted by the MSEM for zero-degree angle of attack.

REFERENCES

[1] S. Bull, *Renewable energy today and tomorrow,* Proceedings of the IEEE **89**, 1216–1226 (2001).

[2] J. K. Kaldellis and D. Zafirakis, *The wind energy (r)evolution: A short review of a long history,* Renewable Energy **36**, 1887–1901 (2011).

[3] International Renewable Energy Agency (IRENA), *Renewable capacity statistics 2021*, Tech. Rep. (International Renewable Energy Agency (IRENA), Abu Dhabi, 2021).

[4] IEA Wind, *IEA Wind TCP annual report 2020*, Tech. Rep. (International Energy Association Wind Technology Collaboration Programme, 2020).

[5] WindEurope, *Wind energy in Europe 2020 Statistics and the outlook for 2021-2025*, Tech. Rep. (Wind Europe, 2021).

[6] E. I. Konstantinidis and P. N. Botsaris, *Wind turbines: current status, obstacles, trends and technologies,* IOP Conference Series: Materials Science and Engineering **161**, 012079 (2016).

[7] A. Untaroiu, A. Raval, H. G. Wood, and P. E. Allaire, *Boundary layer control for a vertical axis wind turbine using a secondary-flow path system,* in *Volume 1: Aircraft Engine Ceramics Coal, Biomass and Alternative Fuels Wind Turbine Technology* (ASMEDC, 2011).

[8] A. Betz, *Behavior of vortex systems*, Tech. Rep. (National Advisory Committee for Aeronautics (NACA), Washington D.C., 1933).

[9] European Wind Energy Association, *Wind energy-the facts: a guide to the technology, economics and future of wind power* (Routledge, 2012).

[10] International Renewable Energy Agency (IRENA), *Renewable capacity statistics 2019*, Tech. Rep. (International Renewable Energy Agency (IRENA), Abu Dhabi, 2019).

[11] R. van Haaren and V. Fthenakis, *GIS-based wind farm site selection using spatial multi-criteria analysis (SMCA): Evaluating the case for New York State,* Renewable and Sustainable Energy Reviews **15**, 3332–3340 (2011).

[12] M. Harper, B. Anderson, P. James, and A. Bahaj, *Assessing socially acceptable locations for onshore wind energy using a GIS-MCDA approach,* International Journal of Low-Carbon Technologies **14**, 160–169 (2019).

[13] L. D. Knopper, C. A. Ollson, L. C. McCallum, M. L. W. Aslund, R. G. Berger, K. Souweine, and M. McDaniel, *Wind turbines and human health,* Frontiers in Public Health **2** (2014), 10.3389/fpubh.2014.00063.

[14] World Health Organization, *Environmental noise guidelines for the European region*, Tech. Rep. (World Health Organization, 2018).

[15] M. Basner, W. Babisch, A. Davis, M. Brink, C. Clark, S. Janssen, and S. Stansfeld, *Auditory and non-auditory effects of noise on health,* The Lancet **383**, 1325–1332 (2014).

[16] A. L. Hansell, M. Blangiardo, L. Fortunato, S. Floud, K. de Hoogh, D. Fecht, R. E. Ghosh, H. E. Laszlo, C. Pearson, L. Beale, *et al.*, *Aircraft noise and cardiovascular disease near Heathrow airport in London: small area study,* BMJ **347** (2013), 10.1136/bmj.f5432.

[17] J. L. Davy, K. Burgemeister, and D. Hillman, *Wind turbine sound limits: Current status and recommendations based on mitigating noise annoyance,* Applied Acoustics **140**, 288–295 (2018).

[18] S. Oerlemans and P. Fuglsang, *Low-noise wind turbine design,* in *EWEA Workshop on Sound* (2012).

[19] Netherlands Enterprise Agency (RVO), *Installing wind turbines,* (Accessed 10 Feb 2022).

[20] J. E. Ffowcs-Williams and L. H. Hall, *Aerodynamic sound generation by turbulent flow in the vicinity of a scattering half plane,* Journal of Fluid Mechanics **40**, 657–670 (1970).

[21] S. Deshmukh, S. Bhattacharya, A. Jain, and A. R. Paul, *Wind turbine noise and its mitigation techniques: A review,* Energy Procedia **160**, 633–640 (2019).

[22] Royal Netherlands Meteorological Institute (KNMI), *Weerstations uurwaarnemingen,* (Accessed 10 Feb 2022).

[23] S. Oerlemans, P. Sijtsma, and B. M. López, *Location and quantification of noise sources on a wind turbine,* Journal of Sound and Vibration **299**, 869–883 (2007).

[24] F. van den Berg, E. Pedersen, J. Bouma, and R. Bakker, *WINDFARMperception. Visual and acoustic impact of wind turbine farms on residents. Final report*, Tech. Rep. (2008).

[25] P. Sijtsma, S. Oerlemans, and H. Holthusen, *Location of rotating sources by phased array measurements,* in *7th AIAA/CEAS Aeroacoustics Conference and Exhibit, May 28–30 2001, Maastricht, the Netherlands* (2001) AIAA 2001–2167.

[26] S. Wagner, R. Bareiß, and G. Guidati, *Wind Turbine Noise* (Springer Berlin Heidelberg, 1996).

[27] W. K. Blake, *Mechanics of flow-induced sound and vibration, Volume 2: Complex flow-structure interactions* (Academic Press, 2017).

[28] M. V. Lowson, *Applications of aero-acoustic analysis to wind turbine noise control,* Wind Engineering **16**, 126–140 (1992).

[29] T. F. Brooks, D. S. Pope, and M. A. Marcolini, *Airfoil self-noise and prediction* (NASA Reference Publication, 1989).

[30] K. Braun, A. Gordner, F. Hailer, B. Huurdeman, H. Arnold, and M. Müller, *Some blade tip modifications and their influence on aeroacoustics,* Tech. Rep. (1996).

[31] H. Klug, T. Osten, and M. Lowson, *Aerodynamic noise from wind turbines and rotor blade modification,* Tech. Rep. (1996).

[32] H. Wagner, M. Weger, M. Klaas, and W. Schröder, *Features of owl wings that promote silent flight,* Interface Focus **7**, 20160078 (2017).

[33] S. Lee, L. Ayton, F. Bertagnolio, S. Moreau, T. P. Chong, and P. Joseph, *Turbulent boundary layer trailing-edge noise: Theory, computation, experiment, and application,* Progress in Aerospace Sciences **126**, 100737 (2021).

[34] Y. Wang, K. Zhao, X.-Y. Lu, Y.-B. Song, and G. J. Bennett, *Bio-inspired aerodynamic noise control: A bibliographic review,* Applied Sciences **9**, 2224 (2019).

[35] A. Finez, M. Jacob, E. Jondeau, and M. Roger, *Broadband noise reduction with trailing edge brushes,* in *16th AIAA/CEAS Aeroacoustics Conference, June 7–9 2010, Stockholm, Sweden* (2010) AIAA 2010–3980.

[36] C. A. Arce-León, *A study on the near-surface flow and acoustic emissions of trailing edge serrations: For the purpose of noise reduction of wind turbine blades,* Ph.D. thesis, Delft University of Technology (2017).

[37] S. Oerlemans, M. Fisher, T. Maeder, and K. Kögler, *Reduction of wind turbine noise using optimized airfoils and trailing-edge serrations,* AIAA Journal **47**, 1470–1481 (2009).

[38] M. Gruber, M. Azarpeyvand, and P. F. Joseph, *Airfoil trailing edge noise reduction by the introduction of sawtooth and slitted trailing edge geometries,* in *20th International Congress on Acoustics, August 23–27 2010, Sydney, Australia* (2010).

[39] S. Buck, S. Oerlemans, O. H. Mascarell, P. Joseph, W. N. Alexander, and S. Letica, *Active control of trailing edge noise,* in *AIAA AVIATION 2021 Forum, August 2–6 2021, Virtual event* (2021).

[40] M. Szőke, D. Fiscaletti, and M. Azarpeyvand, *Uniform flow injection into a turbulent boundary layer for trailing edge noise reduction,* Physics of Fluids **32**, 085104 (2020).

[41] S. Oerlemans, J. Schepers, G. Guidati, and S. Wagner, *Experimental demonstration of wind turbine noise reduction through optimized airfoil shape and trailing-edge serrations,* Tech. Rep. (National Aerospace Laboratory NLR, 2001).

[42] G. Guidati and S. Wagner, *Design of reduced noise airfoils for wind turbines,* in *Proc. of the ECCOMAS 2000 Conference, September 11–14 2000, Barcelona, Spain* (2000).

[43] G. Lilley, *A study of the silent flight of the owl,* in *4th AIAA/CEAS Aeroacoustics Conference, June 2–4 1998, Toulouse, France* (1998) AIAA 1998–2340.

[44] T. Bachmann and H. Wagner, *The three-dimensional shape of serrations at barn owl wings: towards a typical natural serration as a role model for biomimetic applications,* Journal of Anatomy **219**, 192–202 (2011).

[45] M. Barone, *Survey of techniques for reduction of wind turbine blade trailing edge noise*, Tech. Rep. (Sandia National Laboratories, 2011).

[46] T. Dassen, R. Parchen, J. Bruggeman, and F. Hagg, *Results of a wind tunnel study on the reduction of airfoil self-noise by the application of serrated blade trailing edges*, Tech. Rep. (National Aerospace Laboratory NLR, 1996).

[47] M. Gruber, P. Joseph, and T. Chong, *On the mechanisms of serrated airfoil trailing edge noise reduction,* in *17th AIAA/CEAS Aeroacoustics Conference, June 5–8 2011, Portland, OR, USA* (2011) AIAA 2011–2781.

[48] M. Gruber, P. Joseph, and M. Azarpeyvand, *An experimental investigation of novel trailing edge geometries on airfoil trailing edge noise reduction,* in *19th AIAA/CEAS Aeroacoustics Conference, May 27–29 2013, Berlin, Germany* (2013) p. 2011, AIAA 2013–2011.

[49] F. Avallone, C. A. Arce-León, S. Pröbsting, K. P. Lynch, and D. Ragni, *Tomographic-PIV investigation of the flow over serrated trailing-edges,* in *54th AIAA Aerospace Sciences Meeting, January 4–8 2016, San Diego, CA, USA* (2016).

[50] C. A. Arce-León, R. Merino-Martínez, D. Ragni, F. Avallone, and M. Snellen, *Boundary layer characterization and acoustic measurements of flow-aligned trailing edge serrations,* Experiments in Fluids **57**, 1–22 (2016).

[51] P. Zhou, Q. Liu, S. Zhong, Y. Fang, and X. Zhang, *A study of the effect of serration shape and flexibility on trailing edge noise,* Physics of Fluids **32**, 127114 (2020).

[52] S. Oerlemans, M. Fisher, T. Maeder, and K. Kögler, *Reduction of wind turbine noise using optimized airfoils and trailing-edge serrations,* AIAA Journal **47**, 1470–1481 (2009).

[53] S. Oerlemans, *Reduction of wind turbine noise using blade trailing edge devices,* in *22nd AIAA/CEAS Aeroacoustics Conference, May 30–June 1 2016, Lyon, France* (2016) AIAA 2016–3018.

[54] T. F. Geyer, E. Sarradj, and C. Fritzsche, *Measurement of the noise generation at the trailing edge of porous airfoils,* Experiments in Fluids **48**, 291–308 (2010).

[55] M. Herr and J. Reichenberger, *In search of airworthy trailing-edge noise reduction means,* in *17th AIAA/CEAS Aeroacoustics Conference, June 5-8 2011, Portland, OR, USA* (2011) AIAA 2011–2780.

[56] M. Herr and W. Dobrzynski, *Experimental investigations in low-noise trailing edge design,* AIAA Journal **43**, 1167–1175 (2005).

[57] M. Herr, *Design criteria for low-noise trailing-edges,* in *13th AIAA/CEAS Aeroacoustics Conference, 21–23 May 2007, Rome, Italy* (2007) AIAA 2007–3470.

[58] J. Schepers, A. Curvers, S. Oerlemans, K. Braun, T. Lutz, A. Herrig, W. Wuerz, A. Mantesanz, L. Garcillan, M. Fischer, *et al.*, *Sirocco: silent rotors by acoustic optimisation,* in *second international meeting on wind turbine noise, September 20–21, Lyon, France,* Vol. 2021 (2007).

[59] I. A. Clark, W. N. Alexander, W. Devenport, S. Glegg, J. W. Jaworski, C. Daly, and N. Peake, *Bioinspired trailing-edge noise control,* AIAA Journal **55**, 740–754 (2017).

[60] A. Afshari, M. Azarpeyvand, A. A. Dehghan, M. Szőke, and R. Maryami, *Trailing-edge flow manipulation using streamwise finlets,* Journal of Fluid Mechanics **870**, 617–650 (2019).

[61] D. Fiscaletti, S. Luesutthiviboon, F. Avallone, and D. Casalino, *Streamwise fences for the reduction of trailing-edge noise in a NACA633018 airfoil,* in *AIAA SciTech 2022 Forum, January 3–7, 2022, San Diego, CA, USA, & Virtual* (2022).

[62] L. Kamps, C. Brücker, T. F. Geyer, and E. Sarradj, *Airfoil self noise reduction at low Reynolds numbers using a passive flexible trailing edge,* in *23rd AIAA/CEAS Aeroacoustics Conference, June 5–9 2017, Denver, CO, USA* (2017) AIAA 2017–3496.

[63] E. Talboys, T. F. Geyer, and C. Brücker, *An aeroacoustic investigation into the effect of self-oscillating trailing edge flaplets,* Journal of Fluids and Structures **91**, 102598 (2019).

[64] E. Talboys, T. F. Geyer, F. Prüfer, and C. Brücker, *A parametric study of the effect of self-oscillating trailing-edge flaplets on aerofoil self-noise,* Applied Acoustics **177**, 107907 (2021).

[65] A. Vathylakis, T. P. Chong, and P. F. Joseph, *Poro-serrated trailing-edge devices for airfoil self-noise reduction,* AIAA Journal **53**, 3379–3394 (2015).

[66] T. P. Chong and A. Vathylakis, *On the aeroacoustic and flow structures developed on a flat plate with a serrated sawtooth trailing edge,* Journal of Sound and Vibration **354**, 65–90 (2015).

[67] C. A. Arce-León, R. Merino-Martínez, S. Pröbsting, D. Ragni, and F. Avallone, *Acoustic emissions of semi-permeable trailing edge serrations,* Acoustics Australia **46**, 111–117 (2017).

[68] R. Amiet, *Acoustic radiation from an airfoil in a turbulent stream,* Journal of Sound and Vibration **41**, 407–420 (1975).

[69] R. K. Amiet, *Noise due to turbulent flow past a trailing edge,* Journal of sound and vibration **47**, 387–393 (1976).

[70] N. Curle, *The influence of solid boundaries upon aerodynamic sound,* Proc. R. Soc. Lond. A **231**, 505–514 (1955).

[71] M. J. Lighthill, *On sound generated aerodynamically I. General theory,* Proceedings of the Royal Society of London. Series A. Mathematical and Physical Sciences **211**, 564–587 (1952).

[72] M. J. Lighthill, *On sound generated aerodynamically II. Turbulence as a source of sound,* Proceedings of the Royal Society of London. Series A. Mathematical and Physical Sciences **222**, 1–32 (1954).

[73] H. M. Macdonald, *A class of diffraction problems,* Proceedings of the London Mathematical Society **s2_14**, 410–427 (1915).

[74] S. Pröbsting, *Airfoil self-noise investigation with particle image velocimetry,* Ph.D. thesis, Delft University of Technology (2015).

[75] B. Noble, *Methods based on the Wiener-Hopf technique for the solution of partial differential equations,* Vol. 332 (Taylor & Francis US, 1958).

[76] K. Schwarzschild, *Die Beugung und Polarisation des Lichts durch einen Spalt. I,* Mathematische Annalen **55**, 177–247 (1901).

[77] C. J. Bouwkamp, *Diffraction theory,* Reports on progress in physics **17**, 35 (1954).

[78] S. Moreau and M. Roger, *Back-scattering correction and further extensions of Amiet's trailing-edge noise model. Part II: Application,* Journal of Sound and Vibration **323**, 397–425 (2009).

[79] M. Roger and S. Moreau, *Back-scattering correction and further extensions of Amiet's trailing-edge noise model. Part I: theory,* Journal of Sound and Vibration **286**, 477–506 (2005).

[80] M. E. Goldstein, *Aeroacoustics* (McGraw-Hill International Book Company, 1976).

[81] R. D. Sandberg and N. D. Sandham, *A modification of Amiet's classical trailing edge noise theory for strictly two dimensional flows,* Tech. Rep. (University of Southampton, 2007).

[82] S. A. S. Ali, M. Azarpeyvand, and C. R. I. da Silva, *Trailing-edge flow and noise control using porous treatments,* Journal of Fluid Mechanics **850**, 83–119 (2018).

[83] A. Afshari, M. Azarpeyvand, A. A. Dehghan, and M. Szőke, *Trailing edge noise reduction using novel surface treatments,* in *22nd AIAA/CEAS Aeroacoustics Conference, May 30–Jun 1 2016, Lyon, France* (2016) AIAA 2016–2834.

[84] F. Q. Hu, M. E. Pizzo, and D. M. Nark, *On the use of a Prandtl-Glauert-Lorentz transformation for acoustic scattering by rigid bodies with a uniform flow,* Journal of Sound and Vibration **443**, 198–211 (2019).

[85] S. Glegg and W. Devenport, *Aeroacoustics of low Mach number flows: fundamentals, analysis, and measurement* (Academic Press, 2017).

[86] M. S. Howe, *Acoustics of fluid-structure interactions* (Cambridge University Press, 1998).

[87] T. Brooks and T. Hodgson, *Trailing edge noise prediction from measured surface pressures,* Journal of Sound and Vibration **78**, 69–117 (1981).

[88] J. M. R. Graham, *Similarity rules for thin aerofoils in non-stationary subsonic flows,* Journal of Fluid Mechanics **43**, 753–766 (1970).

[89] J. W. Jaworski and N. Peake, *Aerodynamic noise from a poroelastic edge with implications for the silent flight of owls,* Journal of Fluid Mechanics **723**, 456–479 (2013).

[90] A. Kisil and L. J. Ayton, *Aerodynamic noise from rigid trailing edges with finite porous extensions,* Journal of Fluid Mechanics **836**, 117–144 (2017).

[91] L. J. Ayton, *Bioinspired aerofoil adaptations: the next steps for theoretical models,* Philosophical Transactions of the Royal Society A: Mathematical, Physical and Engineering Sciences **377**, 20190070 (2019).

[92] Y. Hwang, W. K. Bonness, and S. A. Hambric, *Comparison of semi-empirical models for turbulent boundary layer wall pressure spectra,* Journal of Sound and Vibration **319**, 199–217 (2009).

[93] S. Lee, *Empirical wall-pressure spectral modeling for zero and adverse pressure gradient flows,* AIAA Journal **56**, 1818–1829 (2018).

[94] D. Chase, *Modeling the wavevector-frequency spectrum of turbulent boundary layer wall pressure,* Journal of Sound and Vibration **70**, 29–67 (1980).

[95] E. Cohen and X. Gloerfelt, *Effect of pressure gradients on turbulent boundary layer noise and wall-pressure fluctuations,* in *21st AIAA/CEAS Aeroacoustics Conference, June 22–26 2015, Dallas, TX, USA* (2015) AIAA 2015–3117.

[96] Y. Rozenberg, G. Robert, and S. Moreau, *Wall-pressure spectral model including the adverse pressure gradient effects,* AIAA Journal **50**, 2168–2179 (2012).

[97] M. Goody, *Empirical spectral model of surface pressure fluctuations,* AIAA Journal **42**, 1788–1794 (2004).

[98] M. Kamruzzaman, D. Bekiropoulos, T. Lutz, W. Würz, and E. Krämer, *A semi-empirical surface pressure spectrum model for airfoil trailing-edge noise prediction,* International Journal of Aeroacoustics **14**, 833–882 (2015).

[99] M. R. Catlett, J. M. Anderson, J. B. Forest, and D. O. Stewart, *Empirical modeling of pressure spectra in adverse pressure gradient turbulent boundary layers,* AIAA Journal **54**, 569–587 (2016).

[100] N. Hu and M. Herr, *Characteristics of wall pressure fluctuations for a flat plate turbulent boundary layer with pressure gradients*, in *22nd AIAA/CEAS Aeroacoustics Conference, May 30–Jun 1 2016, Lyon, France* (2016) AIAA 2016–2749.

[101] M. Drela, *XFOIL: An analysis and design system for low Reynolds number airfoils*, in *Low Reynolds number aerodynamics* (Springer, 1989) pp. 1–12.

[102] S. Oerlemans, *Wind turbine noise: primary noise sources*, Tech. Rep. (National Aerospace Laboratory NLR, 2011).

[103] W. W. Willmarth and C. E. Wooldridge, *Measurements of the fluctuating pressure at the wall beneath a thick turbulent boundary layer*, Journal of Fluid Mechanics **14**, 187–210 (1962).

[104] G. M. Corcos, *The structure of the turbulent pressure field in boundary-layer flows*, Journal of Fluid Mechanics **18**, 353 (1964).

[105] A. Rubio-Carpio, R. Merino-Martínez, F. Avallone, D. Ragni, M. Snellen, and S. van der Zwaag, *Experimental characterization of the turbulent boundary layer over a porous trailing edge for noise abatement*, Journal of Sound and Vibration **443**, 537–558 (2019).

[106] E. Sarradj and T. Geyer, *Noise generation by porous airfoils*, in *13th AIAA/CEAS Aeroacoustics Conference, 21–23 May 2007, Rome, Italy* (2007) AIAA 2007–3719.

[107] C. Teruna, F. Avallone, D. Ragni, A. Rubio-Carpio, and D. Casalino, *Numerical analysis of a 3-D printed porous trailing edge for broadband noise reduction*, Journal of Fluid Mechanics **926**, A17 (2021).

[108] A. Rubio-Carpio, F. Avallone, D. Ragni, M. Snellen, and S. van der Zwaag, *Quantitative criteria to design optimal permeable trailing edges for noise abatement*, Journal of Sound and Vibration **485**, 115596 (2020).

[109] M. Herr, K.-S. Rossignol, J. Delfs, N. Lippitz, and M. Mößner, *Specification of porous materials for low-noise trailing-edge applications*, in *20th AIAA/CEAS Aeroacoustics Conference, June 16–20 2014, Atlanta, Georgia* (2014) AIAA 2014–3041.

[110] J. Delfs, B. Faßmann, N. Lippitz, M. Lummer, M. Mößner, L. Müller, K. Rurkowska, and S. Uphoff, *SFB 880: aeroacoustic research for low noise take-off and landing*, CEAS Aeronautical Journal **5**, 403–417 (2014).

[111] B. Tjaden, D. J. L. Brett, and P. R. Shearing, *Tortuosity in electrochemical devices: a review of calculation approaches*, International Materials Reviews **63**, 47–67 (2016).

[112] J. van Brakel and P. Heertjes, *Analysis of diffusion in macroporous media in terms of a porosity, a tortuosity and a constrictivity factor*, International Journal of Heat and Mass Transfer **17**, 1093–1103 (1974).

[113] N. Epstein, *On tortuosity and the tortuosity factor in flow and diffusion through porous media*, Chemical engineering science **44**, 777–779 (1989).

[114] H. Iwai, N. Shikazono, T. Matsui, H. Teshima, M. Kishimoto, R. Kishida, D. Hayashi, K. Matsuzaki, D. Kanno, M. Saito, H. Muroyama, K. Eguchi, N. Kasagi, and H. Yoshida, *Quantification of SOFC anode microstructure based on dual beam FIB-SEM technique,* Journal of Power Sources **195**, 955–961 (2010).

[115] International Organization for Standardization, *ISO 9053-1:2018 Acoustics — Determination of airflow resistance — Part 1: Static airflow method,* (2018).

[116] International Organization for Standardization, *ISO 9053-1:2020 Acoustics — Determination of airflow resistance — Part 2: Alternating airflow method,* (2020).

[117] P. Forchheimer, *Wasserbewegung durch Boden,* Zeitschrift des Vereines Deutscher Ingenieuer **45**, 1782–1788 (1901).

[118] D. B. Ingham and I. Pop, *Transport phenomena in porous media* (Elsevier, 1998).

[119] F. M. White and I. Corfield, *Viscous fluid flow,* Vol. 3 (McGraw-Hill New York, 2006).

[120] H. P. G. Darcy, *Les Fontaines publiques de la ville de Dijon. Exposition et application des principes à suivre et des formules à employer dans les questions de distribution d'eau, etc* (V. Dalamont, 1856).

[121] N. Dukhan, Özer Bağcı, and M. Özdemir, *Experimental flow in various porous media and reconciliation of Forchheimer and Ergun relations,* Experimental Thermal and Fluid Science **57**, 425–433 (2014).

[122] A. Rubio-Carpio, F. Avallone, D. Ragni, M. Snellen, and S. van der Zwaag, *Mechanisms of broadband noise generation on metal foam edges,* Physics of Fluids **31**, 105110 (2019).

[123] C. Teruna, F. Manegar, F. Avallone, D. Ragni, D. Casalino, and T. Carolus, *Noise reduction mechanisms of an open-cell metal-foam trailing edge,* Journal of Fluid Mechanics **898** (2020), 10.1017/jfm.2020.363.

[124] E. Sarradj and T. F. Geyer, *Symbolic regression modeling of noise generation at porous airfoils,* Journal of Sound and Vibration **333**, 3189–3202 (2014).

[125] A. Rubio-Carpio, R. Merino-Martínez, F. Avallone, D. Ragni, M. Snellen, and S. van der Zwaag, *Broadband trailing-edge noise reduction using permeable metal foams,* in *INTER-NOISE Conference, August 27–30 2017, Hong Kong* (Institute of Noise Control Engineering, 2017).

[126] C. Naaktgeboren, P. S. Krueger, and J. L. Lage, *Inlet and outlet pressure-drop effects on the determination of permeability and form coefficient of a porous medium,* Journal of Fluids Engineering **134** (2012), 10.1115/1.4006614.

[127] E. Baril, A. Mostafid, L.-P. Lefebvre, and M. Medraj, *Experimental demonstration of entrance/exit effects on the permeability measurements of porous materials,* Advanced Engineering Materials **10**, 889–894 (2008).

[128] M. Kaviany, *Principles of heat transfer in porous media* (Springer, 1995).

[129] T. F. Geyer, E. Sarradj, and C. Fritzsche, *Porous airfoils: noise reduction and boundary layer effects,* in *15th AIAA/CEAS Aeroacoustics Conference, May 11-13 2009, Miami, FL, USA* (2009) AIAA 2009–3392.

[130] T. F. Geyer and E. Sarradj, *Trailing edge noise of partially porous airfoils,* in *20th AIAA/CEAS Aeroacoustics Conference, June 16–20 2014, Atlanta, Georgia* (2014) AIAA 2014–3039.

[131] R. Hajian and J. W. Jaworski, *The steady aerodynamics of aerofoils with porosity gradients,* Proc. R. Soc. A **473**, 20170266 (2017).

[132] Y. Bae and Y. J. Moon, *Effect of passive porous surface on the trailing-edge noise,* Physics of Fluids **23**, 126101 (2011).

[133] A. Rubio-Carpio, F. Avallone, D. Ragni, M. Snellen, and S. van der Zwaag, *3D-printed perforated trailing edges for broadband noise abatement,* in *25th AIAA/CEAS Aeroacoustics Conference, May 20–23 2019, Delft, the Netherlands* (2019) AIAA 2019–2458.

[134] M. S. Howe, *Aerodynamic noise of a serrated trailing edge,* Journal of Fluids and Structures **5**, 33–45 (1991).

[135] M. S. Howe, *Noise produced by a sawtooth trailing edge,* The Journal of the Acoustical Society of America **90**, 482–487 (1991).

[136] B. Lyu, M. Azarpeyvand, and S. Sinayoko, *Prediction of noise from serrated trailing edges,* Journal of Fluid Mechanics **793**, 556–588 (2016).

[137] F. Avallone, S. Pröbsting, and D. Ragni, *Three-dimensional flow field over a trailing-edge serration and implications on broadband noise,* Physics of Fluids **28**, 117101 (2016).

[138] G. Raman, R. C. Ramachandran, and M. R. Aldeman, *A review of wind turbine noise measurements and regulations,* Wind Engineering **40**, 319–342 (2016).

[139] B. Lyu and L. J. Ayton, *Serrated leading-edge and trailing-edge noise prediction models for realistic wavenumber frequency spectra,* in *25th AIAA/CEAS Aeroacoustics Conference, May 20–23 2019, Delft, the Netherlands* (2019) AIAA 2019–2674.

[140] P. Kholodov and S. Moreau, *Optimization of serrations for broadband trailing-edge noise reduction using an analytical model,* in *25th AIAA/CEAS Aeroacoustics Conference, May 20–23 2019, Delft, the Netherlands* (2019) AIAA 2019–2655.

[141] F. Avallone, W. van der Velden, and D. Ragni, *Benefits of curved serrations on broadband trailing-edge noise reduction,* Journal of Sound and Vibration **400**, 167–177 (2017).

[142] S. M. Hasheminejad, T. P. Chong, P. Joseph, and G. Lacagnina, *Airfoil self-noise reduction using fractal-serrated trailing edge,* in *24th AIAA/CEAS Aeroacoustics Conference, June 25–29 2018, Atlanta, GA, USA* (2018) AIAA 2018–3132.

[143] P. Fuglsang and C. Bak, *Development of the Risø wind turbine airfoils,* Wind Energy: An International Journal for Progress and Applications in Wind Power Conversion Technology **7**, 145–162 (2004).

[144] W. A. Timmer and R. P. J. O. M. van Rooij, *Summary of the Delft University wind turbine dedicated airfoils,* in *41st AIAA Aerospace Sciences Meeting and Exhibit, January 6–9 2003, Reno, NV, USA* (2003) AIAA 2003–352.

[145] I. H. Abbott and A. E. von Doenhoff, *Theory of wing sections: Including a summary of airfoil data* (Courier Corporation, 2012).

[146] W. A. Timmer, *An overview of NACA 6-digit airfoil series characteristics with reference to airfoils for large wind turbine blades,* in *47th AIAA Aerospace Sciences Meeting and Exhibit, January 5–8 2009, Orlando, FL, USA* (2009) p. 268, AIAA 2009–268.

[147] W. A. Timmer, *Two-dimensional low-Reynolds number wind tunnel results for airfoil NACA 0018,* Wind Engineering **32**, 525–537 (2008).

[148] A. Borgoltz, N. Intaratep, and W. J. Devenport, *Aerodynamic effects of boundary layer trip strips on the flow over a DU91W250 airfoil* (2019).

[149] Q. Ye, F. Avallone, D. Ragni, M. Choudhari, and D. Casalino, *Effect of surface roughness geometry on boundary-layer transition and far-field noise,* AIAA Journal **59**, 2396–2408 (2021).

[150] International Organization for Standardization, *ISO 3382-2:2008 Acoustics — Measurement of room acoustic parameters — Part 2: Reverberation time in ordinary rooms,* (2008).

[151] R. Merino-Martínez, A. Rubio-Carpio, L. T. Lima Pereira, S. van Herk, F. Avallone, D. Ragni, and M. Kotsonis, *Aeroacoustic design and characterization of the 3D-printed, open-jet, anechoic wind tunnel of Delft University of Technology,* Applied Acoustics **170**, 107504 (2020).

[152] T. F. Brooks, M. A. Marcolini, and D. S. Pope, *Airfoil trailing edge flow measurements and comparison with theory, incorporating open wind tunnel corrections,* in *9th AIAA/CEAS Aeroacoustics Conference, October 10-15 1984, Williamsburg, VA, USA* (1984) AIAA 1984–2266.

[153] W. J. Devenport, R. A. Burdisso, A. Borgoltz, P. A. Ravetta, M. F. Barone, K. A. Brown, and M. A. Morton, *The Kevlar-walled anechoic wind tunnel,* Journal of Sound and Vibration **332**, 3971–3991 (2013).

[154] *Technisches Datenblatt, Style 120,* ECC (2009).

[155] W. J. Devenport, R. A. Burdisso, A. Borgoltz, P. A. Ravetta, and M. F. Barone, *Aerodynamic and acoustic corrections for a Kevlar-walled anechoic wind tunnel,* in *16th AIAA/CEAS Aeroacoustics Conference, June 7–9 2010, Stockholm, Sweden* (2010) AIAA 2010–3749.

[156] H. H. Bruun, *Hot wire anemometry: principles and signal analysis* (Oxford University Press, 1995).

[157] M. Raffel, C. E. Willert, F. Scarano, C. J. Kähler, S. T. Wereley, and J. Kompenhans, *Particle Image Velocimetry* (2018).

[158] P. R. Spalart and J. H. Watmuff, *Experimental and numerical study of a turbulent boundary layer with pressure gradients,* Journal of Fluid Mechanics **249**, 337 (1993).

[159] F. H. Clauser, *The turbulent boundary layer,* Advances in Applied Mechanics **4**, 1–51 (1956).

[160] D. Coles, *The law of the wake in the turbulent boundary layer,* Journal of Fluid Mechanics **1**, 191–226 (1956).

[161] H. C. Garner, E. W. E. Rogers, W. E. A. Acum, and E. C. Maskell, *Subsonic wind tunnel wall corrections,* Tech. Rep. (AGARD Report, 1996).

[162] J. B. Barlow, W. H. Rae, and A. Pope, *Low-speed wind tunnel testing* (John Wiley & Sons, 1999).

[163] G. P. Russo, *Aerodynamic measurements: From physical principles to turnkey instrumentation* (Elsevier, 2011).

[164] E. L. Houghton and P. W. Carpenter, *Aerodynamics for engineering students* (Elsevier, 2003).

[165] S. Oerlemans and P. Migliore, *Aeroacoustic wind tunnel tests of wind turbine airfoils,* in *10th AIAA/CEAS Aeroacoustics Conference, May 10–12 2004, Manchester, UK* (2004) AIAA 2004–3042.

[166] P. Migliore, J. van Dam, and A. Huskey, *Acoustic tests of small wind turbines,* in *42nd AIAA Aerospace Sciences Meeting and Exhibit, January 5–8 2004, Reno, NV, USA* (2004) AIAA 2004–1185.

[167] *IEC 61400-11 wind turbine generator systems part 11: Acoustic noise measurement techniques,* Geneva, Switzerland: International Electrotechnical Commission (2012).

[168] S. Guidati, C. Brauer, and S. Wagner, *The reflection canceller - Phased array measurements in a reverberating environment,* in *8th AIAA/CEAS Aeroacoustics Conference & Exhibit, June 17–19 2002, Breckenridge, CO, USA* (2002) AIAA 2002–2462.

[169] P. Sijtsma and H. Holthusen, *Corrections for mirror sources in phased array processing techniques,* in *9th AIAA/CEAS Aeroacoustics Conference and Exhibit, May 12–14 2003, Hilton Head, SC, USA* (2003) AIAA 2003–3196.

[170] L. Koop and K. Ehrenfried, *Microphone-array processing for wind-tunnel measurements with strong background noise,* in *14th AIAA/CEAS Aeroacoustics Conference (29th AIAA Aeroacoustics Conference), May 5–8 2008, Vancouver, British Columbia, Canada* (2008) p. 2907, AIAA 2008–2907.

[171] M. P. Sanders, L. Botero, L. D. de Santana, and C. Venner, *Airfoil trailing edge noise measurements in an open-jet, hard-wall and Kevlar-wall test section: A benchmark exercise,* in *AIAA AVIATION 2021 Forum, August 2–6 2021, Virtual Event* (2021) AIAA 2021–2253.

[172] S. Kroeber and L. Koop, *Comparison of microphone array measurements of an airfoil with high-lift devices in open and closed wind tunnels,* in *17th AIAA/CEAS Aeroacoustics Conference (32nd AIAA Aeroacoustics Conference), June 5–8 2011, Portland, OR, USA* (2011) p. 2721, AIAA 2011–2721.

[173] M. Tuinstra and P. Sijtsma, *Suppression of spurious noise sources in airfoil self-noise measurements,* in *21st AIAA/CEAS Aeroacoustics Conference, June 22–26 2015, Dallas, TX, USA* (2015) p. 2689, AIAA 2015–2689.

[174] T. J. Mueller, *Aeroacoustic measurements* (Springer Science & Business Media, 2002) p. 313.

[175] S. Luesutthiviboon, A. M. N. Malgoezar, M. Snellen, P. Sijtsma, and D. G. Simons, *Improving source discrimination performance by using an optimized acoustic array and adaptive high–resolution CLEAN–SC beamforming,* in *7th Berlin Beamforming Conference, March 5–6 2018, Berlin, Germany* (2018) BeBeC–2018–D07.

[176] J. R. Underbrink, *Aeroacoustic phased array testing in low speed wind tunnels,* in *Aeroacoustic Measurements* (Springer Berlin Heidelberg, 2002) pp. 98–217.

[177] J. R. Underbrink, *Circularly symmetric, zero redundancy, planar array having broad frequency range applications,* (U.S. Patent number 6,205,224 B1. 2001).

[178] B. D. van Veen and K. M. Buckley, *Beamforming: A versatile approach to spatial filtering,* IEEE ASSP Magazine **5**, 4–24 (1988).

[179] D. H. Johnson and D. E. Dudgeon, *Array signal processing, concepts and techniques* (P T R Prentice Hall, Englewood Cliffs, 1993).

[180] P. Sijtsma, *Phased array beamforming applied to wind tunnel and fly-over tests,* Tech. Rep. (National Aerospace Laboratory NLR, 2010).

[181] E. Sarradj, *Three-dimensional acoustic source mapping with different beamforming steering vector formulations,* Advances in Acoustics and Vibration **2012**, 1–12 (2012).

[182] R. K. Amiet, *Refraction of sound by a shear layer,* Journal of Sound and Vibration **58**, 467–482 (1978).

[183] P. Sijtsma, *CLEAN based on spatial source coherence,* International Journal of Aeroacoustics **6**, 357–374 (2007).

[184] J. A. Högbom, *Aperture synthesis with a non-regular distribution of interferometer baselines,* Astronomy and Astrophysics Supplement Series **15**, 417–426 (1974).

[185] P. Sijtsma, R. Merino-Martínez, A. M. N. Malgoezar, and M. Snellen, *High-resolution CLEAN-SC: Theory and experimental validation,* International Journal of Aeroacoustics **16**, 274–298 (2017).

[186] J. J. Christensen and J. Hald, *Beamforming*, Tech. Rep. (Brüel & Kjær, 2004).

[187] S. Luesutthiviboon, A. M. N. Malgoezar, R. Merino-Martínez, M. Snellen, P. Sijtsma, and D. G. Simons, *Enhanced HR-CLEAN-SC for resolving multiple closely spaced sound sources,* International Journal of Aeroacoustics **18**, 392–413 (2019).

[188] Z. Chu, S. Yin, Y. Yang, and P. Li, *Filter-and-sum based high-resolution CLEAN-SC with spherical microphone arrays,* Applied Acoustics **182**, 108278 (2021).

[189] R. Merino-Martínez, S. Luesutthiviboon, R. Zamponi, A. Rubio-Carpio, D. Ragni, P. Sijtsma, M. Snellen, and C. Schram, *Assessment of the accuracy of microphone array methods for aeroacoustic measurements,* Journal of Sound and Vibration **470**, 115176 (2020).

[190] E. Sarradj, G. Herold, P. Sijtsma, R. Merino-Martínez, , A. M. N. Malgoezar, M. Snellen, T. F. Geyer, C. J. Bahr, R. Porteous, D. Moreau, and C. J. Doolan, *A microphone array method benchmarking exercise using synthesized input data,* in *23rd AIAA/CEAS Aeroacoustics Conference, June 5–7 2016, Denver, CO, USA* (2017) AIAA 2017–3719.

[191] R. Merino-Martínez, P. Sijtsma, A. Rubio-Carpio, R. Zamponi, S. Luesutthiviboon, A. M. N. Malgoezar, M. Snellen, C. Schram, and D. G. Simons, *Integration methods for distributed sound sources,* International Journal of Aeroacoustics **18**, 444–469 (2019).

[192] C. L. Burley and T. F. Brooks, *Rotor broadband noise prediction with comparison to model data,* Journal of the American Helicopter Society **49**, 28–42 (2004).

[193] O. Ferret Gasch, S. Oerlemans, F. Bertagnolio, A. Fischer, B. Arnold, T. Lutz, B. W. Fassmann, and M. Herr, *Trailing edge noise prediction of wind turbine airfoils: A benchmark exercise,* in *25th AIAA/CEAS Aeroacoustics Conference, May 20–23 2019, Delft, the Netherlands* (2019) p. 2675, AIAA 2019–2675.

[194] M. Herr and M. Kamruzzaman, *Benchmarking of trailing-edge noise computations—Outcome of the BANC-II workshop,* in *19th AIAA/CEAS Aeroacoustics Conference, May 27–29 2013, Berlin, Germany* (2013) AIAA 2013–2123.

[195] M. Herr, R. Ewert, C. Rautmann, M. Kamruzzaman, D. Bekiropoulos, R. Arina, A. Iob, P. Batten, S. Chakravarthy, and F. Bertagnolio, *Broadband trailing-edge noise predictions—Overview of BANC-III results,* in *21st AIAA/CEAS Aeroacoustics Conference, June 22–26 2015, Dallas, TX, USA* (2015) AIAA 2015–2847.

[196] B. Lyu and L. J. Ayton, *Rapid noise prediction models for serrated leading and trailing edges,* Journal of Sound and Vibration **469**, 115136 (2020).

[197] C. Arce-León, R. Merino-Martínez, D. Ragni, F. Avallone, F. Scarano, S. Pröbsting, M. Snellen, D. G. Simons, and J. Madsen, *Effect of trailing edge serration–flow misalignment on airfoil noise emission,* Journal of Sound and Vibration **405**, 19 – 33 (2017).

[198] H. Schlichting and K. Gersten, *Boundary-layer theory* (Springer Science & Business Media, 2003).

[199] R. Vinuesa, A. Bobke, R. Örlü, and P. Schlatter, *On determining characteristic length scales in pressure-gradient turbulent boundary layers,* Physics of Fluids **28**, 055101 (2016).

[200] P. H. Alfredsson, A. Segalini, and R. Örlü, *A new scaling for the streamwise turbulence intensity in wall-bounded turbulent flows and what it tells us about the "outer" peak,* Physics of Fluids **23**, 041702 (2011).

[201] I. P. Castro, A. Segalini, and P. H. Alfredsson, *Outer-layer turbulence intensities in smooth- and rough-wall boundary layers,* Journal of Fluid Mechanics **727**, 119–131 (2013).

[202] D. J. Moreau and C. J. Doolan, *Noise-reduction mechanism of a flat-plate serrated trailing edge,* AIAA Journal **51**, 2513–2522 (2013).

[203] B. Smith, H. Camargo, R. Burdisso, and W. J. Devenport, *Design and testing of a novel acoustic wind tunnel concept,* in *11th AIAA/CEAS Aeroacoustics Conference, May 23–25 2005, Monterey, CA, USA* (2005) AIAA 2005–3053.

[204] F. Avallone, W. C. van der Velden, R. Merino Martinez, and D. Ragni, *Near-wall pressure fluctuations over noise reduction add-ons,* in *23rd AIAA/CEAS Aeroacoustics Conference, June 5–7 2016, Denver, CO, USA* (2017) AIAA 2017–4171.

[205] N. Dukhan and K. P. Patel, *Entrance and exit effects for fluid flow in metal foam,* in *AIP Conference Proceedings*, Vol. 1254 (AIP, 2010) pp. 299–304.

[206] H. Scheffe, *The analysis of variance*, Vol. 72 (John Wiley & Sons, 1999).

[207] Student, *The probable error of a mean,* Biometrika **6**, 1–25 (1908).

[208] G. Rupert Jr *et al.*, *Simultaneous statistical inference* (Springer Science & Business Media, 2012).

[209] R. E. Danielson and P. L. Sutherland, *Porosity,* in *SSSA Book Series* (Soil Science Society of America, American Society of Agronomy, 2018) pp. 443–461.

[210] T. F. Geyer and E. Sarradj, *Self noise reduction and aerodynamics of airfoils with porous trailing edges,* Acoustics **1**, 393–409 (2019).

[211] M. Zhang and T. P. Chong, *Effects of porous trailing edge on aerodynamic noise characteristics,* International Journal of Aeroacoustics **19**, 254–271 (2020).

[212] H. Tan and K. M. Pillai, *Finite element implementation of stress-jump and stress-continuity conditions at porous-medium, clear-fluid interface,* Computers & Fluids **38**, 1118–1131 (2009).

[213] M. Le Bars and M. G. Worster, *Interfacial conditions between a pure fluid and a porous medium: implications for binary alloy solidification,* Journal of Fluid Mechanics **550**, 149 (2006).

[214] S. Luesutthiviboon, D. Ragni, F. Avallone, and M. Snellen, *An alternative permeable topology design space for trailing-edge noise attenuation,* International Journal of Aeroacoustics **20**, 221–253 (2021).

[215] D. P. Searson, D. E. Leahy, and M. J. Willis, *GPTIPS: an open source genetic programming toolbox for multigene symbolic regression,* in *International MultiConference of Engineers and Computer Scientists 2010 (IMECS), March 17–19 2010, Hong Kong,* Vol. 1 (Citeseer, 2010) pp. 77–80.

[216] W. H. Press and S. A. Teukolsky, *Savitzky-Golay smoothing filters,* Computers in Physics **4**, 669 (1990).

[217] C. Carotenuto and M. Minale, *Shear flow over a porous layer: Velocity in the real proximity of the interface via rheological tests,* Physics of Fluids **23**, 063101 (2011).

[218] G. S. Beavers and D. D. Joseph, *Boundary conditions at a naturally permeable wall,* Journal of Fluid Mechanics **30**, 197–207 (1967).

[219] M. Gerritsma, A. Palha, V. Jain, and Y. Zhang, *Mimetic spectral element method for anisotropic diffusion,* in *Numerical Methods for PDEs* (Springer, 2018) pp. 31–74.

[220] Y. D. Mayer, H. K. Jawahar, M. Szőke, S. A. S. Ali, and M. Azarpeyvand, *Design and performance of an aeroacoustic wind tunnel facility at the University of Bristol,* Applied Acoustics **155**, 358–370 (2019).

[221] L. Li, P. Liu, H. Guo, Y. Hou, X. Geng, and J. Wang, *Aeroacoustic measurement of 30P30N high-lift configuration in the test section with Kevlar cloth and perforated plate,* Aerospace Science and Technology **70**, 590–599 (2017).

[222] S. Jaeger, W. Horne, and C. Allen, *Effect of surface treatment on array microphone self-noise,* in *6th AIAA/CEAS Aeroacoustics Conference, June 12–14 2000, Lahaina, HI, USA* (2000) AIAA 2000–1937.

[223] D. Stephens, *The acoustic environment of the NASA Glenn 9- by 15-foot low-speed wind tunnel,* in *21st AIAA/CEAS Aeroacoustics Conference, June 22–26 2015, Dallas, TX, USA* (2015) AIAA 2015–2684.

[224] W. N. Alexander, *Sound from rough wall boundary layer,* Ph.D. thesis, Virginia Polytechnic Institute and State University (Virginia Tech) (2011).

[225] V. Jain, J. Fisser, A. Palha, and M. Gerritsma, *A conservative hybrid method for Darcy flow,* in *Lecture Notes in Computational Science and Engineering*, Vol. 134 (Springer International Publishing, 2020) pp. 215–227.

ACKNOWLEDGEMENTS

I would like to express my gratitude for the immense amount of trust and support provided by my promotors and supervisors. This is necessary for the opportunity to start the PhD journey at all, and also indispensable throughout the entire PhD trajectory. Firstly, I would like to thank Prof.dr. Dick G. Simons, the Aircraft Noise & Climate Effects (ANCE) section chair. Every contact with him reminds me as a researcher to always have a top-level and pragmatic view of my work. Next, I would like to express my gratitude to Prof.dr.ir. Mirjam Snellen. Despite her unimaginably large amount of responsibility, her presence and support have been consistent since I started my MSc thesis. Her reflections on both my strengths and weaknesses as a researcher have inspired me to become a better one. Finally, I would like to thank Dr. Daniele Ragni from the Wind Energy group. I am grateful for his trust and patience, especially, in letting me handle challenging tasks, such as the patent application and the benchmark campaign. Those tasks honestly seemed impossible to me at first, but eventually have led to fruitful outcomes, and more importantly, have made me grow.

Beyond my supervisory team, I would like to acknowledge Dr. Francesco Avallone and Dr. Pieter Sijtsma. Their expertise and support have greatly contributed to the research outputs presented in this thesis as well as in my journal publications.

Many parts of this thesis are not my individual work. They are, in fact, outcomes of great teamwork involving the following colleagues: Alejandro and Christopher are experts in trailing-edge noise reduction using permeable materials. Discussions with them always result in new ideas and insights for my studies. Tercio has immensely helped in testing the NACA 63_3–018 airfoil and documenting the results in the benchmark paper. The patent application would not have been accomplished without Leandro as a perfect IPER-MAN teammate. I am also proud of the advanced beamforming algorithm development and benchmarking I carried out together with Anwar, Roberto, and Riccardo. Varun and his supervisor, Dr. Marc Gerritsma, have introduced me to the interesting world of Mimetic Spectral Element Method (MSEM). I am truly grateful for all our pleasant collaborations and I have learned a lot from working with all of you.

It has been a pleasure to be part of the ANCE section. The perfect combination of colleagues and their cheerful spirits make ANCE a unique and special place. It would be difficult to name all of you but please know that I am grateful for all the fun moments we have shared. I would like to specially mention my long-term officemate, Tannaz. I am lucky to be sharing my office with a caring and empathetic person like you. I would like to thank Bieke for helping me make this thesis summary and propositions available in Dutch. I also enjoyed the fun running, cycling, and brewing sessions with Colin and Timo.

Above all, I would like to thank our kindest secretary, Lisette, for facilitating incredibly diverse sorts of practical matters, and for making everything happen.

At the low-speed laboratory (A–Tunnel and LTT), I have received a great amount of technical support from many colleagues who work there, especially from Marios, Stefan, and Emiel. It would be impossible to name everyone who has helped me at the wind tunnels because every small favor, such as helping me lift the nozzles, counts. I feel thankful for all the help.

The wind-turbine noise measurement campaigns would not have been possible (and fun) without my Dimple–MuteSkin colleagues: Michiel, Olaf, Friso, and Bastiaan. I also would like to thank the staffs at the test site, Andreas, Norbert, Johannes, and Pedro for their facilitation.

Another group of colleagues who have greatly contributed to my experimental campaigns is from the Dienst Electronisch en Mechanisch Ontwikkeling (DEMO). I would like to acknowledge the very professional help from Steve, Frank, Pieter, Peter, and Ed which has brought my computer-aided designs of airfoils, serrations, permeable trailing edges, and many more, to real life.

Apart from my own research, I am grateful to have been involved in many BSc and MSc projects, and have had contact with a lot of students. Their enthusiasms and curiosities, which are common among students in our faculty, are contagious. I would like to especially thank Sidharth and Jonathan who have helped me in my past wind-tunnel campaigns.

I am grateful for all sorts of distractions provided by all my friends, and every workout session with my workout groups throughout the past years, which are essential for my sanity and fitness. Especially, I would like to thank my roommates, Juanito and Ginger, for helping me create the PhD research video that won the 1st prize in the PhD academic event in 2021, and indeed for their unconditional emotional support. I am truly grateful for our f(ur)riendship.

Lastly, I would like to express my love and gratitude to my parents in Thailand. Thank you for always being supportive of every life choice I made. Thank you for letting me face challenges and grow, yet being my most beloved and very much needed 'comfort zone'.

Salil,
Delft, May 2022

CURRICULUM VITÆ

Salil LUESUTTHIVIBOON

Salil Luesutthiviboon was born in March 1993 in Bangkok, Thailand. Since a young age, Salil has been a true fan of airplanes and has always wanted to become an airline pilot. Unfortunately, being nearsighted has made it impossible to pursue this dream. Therefore, he shifted his goal and decided to become an aerospace engineer instead.

In 2015, Salil moved to Delft, the Netherlands, to start his MSc study in Aerospace Engineering at Delft University of Technology (TU Delft). He found the topic of aircraft noise interesting and was fascinated by insights that a microphone-array noise measurement and acoustic beamforming can provide. He joined the Aircraft Noise and Climate Effects (ANCE) research group to carry out his MSc graduation project in 2017. The project was about optimizing microphone locations on a microphone array to improve acoustic beamforming performance, and was supervised by Prof.dr. Dick G. Simons, Prof.dr.ir. Mirjam Snellen, Dr. Pieter Sijtsma, and Dr.ir. Anwar M.N. Malgoezar.

Upon his MSc graduation, Salil was offered an opportunity to continue his PhD research in the collaborative Innovative PERmeable Materials for Airfoil Noise reduction (IPER-MAN) project at TU Delft, funded by the Dutch Research Council (NWO) and industrial partners. His PhD research focused on assessing and improving trailing-edge noise reduction technologies for industrial wind-turbine applications. He was supervised by Dr. Daniele Ragni from the Aeroacoustic research group together with his former supervisors (Prof. Simons and Prof. Snellen) from the ANCE group. The outcomes of this PhD research are presented in this thesis.

In 2022, Salil started as a Postdoctoral researcher for TU Delft and the Dutch Ministry of Defense. His project focuses on acoustic and optical detection of drones.

Outside of work, Salil has several active hobbies. Salil is a group fitness trainer at the Sports Center ('X') of TU Delft and is also a fan of road biking. One of his favorite biking destinations is Schiphol Airport in Amsterdam, where he can do some planespotting.
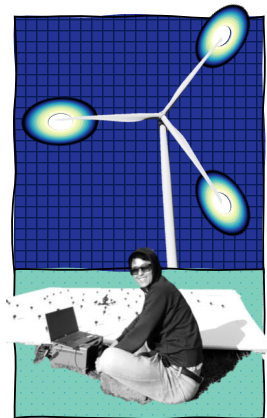
LIST OF PUBLICATIONS

PEER-REVIEWED JOURNAL ARTICLES

6. **S. Luesutthiviboon**, L. T. Lima Pereira, D. Ragni, F. Avallone, M. Snellen, *Aeroacoustic benchmarking of trailing-edge noise from a NACA 63_3–018 airfoil with trailing-edge serrations*, Accepted for publication in the AIAA Journal (2022).

5. **S. Luesutthiviboon**, D. Ragni, F. Avallone, M. Snellen, *An alternative permeable topology design space for trailing-edge noise attenuation*, International Journal of Aeroacoustics **20**, 3–4, 221–253 (2021).

4. R. Merino–Martínez, **S. Luesutthiviboon**, R. Zamponi, A. Rubio–Carpio, D. Ragni, P. Sijtsma, M. Snellen, C. Schram, *Assessment of the accuracy of microphone array methods for aeroacoustic measurements*, Journal of Sound and Vibration **470**, 115176 (2020).

3. **S. Luesutthiviboon**, A. M. N. Malgoezar, R. Merino–Martínez, P. Sijtsma, M. Snellen, D. G. Simons, *Enhanced HR-CLEAN-SC for resolving multiple closely spaced sound sources*, International Journal of Aeroacoustics **18**, 4–5, 392–413 (2019).

2. R. Merino–Martínez, P. Sijtsma, A. Rubio–Carpio, R. Zamponi, **S. Luesutthiviboon**, A. M. N. Malgoezar, M. Snellen, C. Schram, D. G. Simons, *Integration methods for distributed sound sources*, International Journal of Aeroacoustics **18**, 4–5, 444–469 (2019).

1. R. Hedayati, A. Rubio–Carpio, **S. Luesutthiviboon**, D. Ragni, F. Avallone, D. Casalino, S. van der Zwaag, *Role of polymeric coating on metallic foams to control the aeroacoustic noise reduction of airfoils with permeable trailing edges*, Materials **12**(7), 1087 (2019).

PATENT APPLICATION

1. **S. Luesutthiviboon**, L. Rego, F. Avallone, D. Ragni, M. Snellen, S. van der Zwaag, D. Casalino. *A hybrid permeable liner for attenuation of multiple aircraft noise sources*, International application No. PCT/NL2021/050561, International filing date 16/09/2021.

CONFERENCE CONTRIBUTIONS

9. G. Verges i Plaza, A. Fischer, O. Lylloff, C. Bak, A. Smærup Olsen, F. Bertagnolio, **S. Luesutthiviboon**, L. T. Lima Pereira, D. Ragni, F. Avallone, A. Suryadi, M. Herr, *Benchmarking of the NACA 63_3–018 trailing-edge noise in a broad reynolds number range as part of the IEA task 39*, Hybrid Anechoic Wind Tunnel (HAWT) workshop in 28th AIAA/CEAS Aeroacoustics Conference, Southampton, UK, 2022.

8. D. Fiscaletti, **S. Luesutthiviboon**, F. Avallone, D. Casalino, *Streamwise fences for the reduction of trailing-edge noise in a NACA 63_3–018 airfoil*, AIAA SciTech 2022 Forum, San Diego, CA, USA & Virtual, 2022.

7. **S. Luesutthiviboon**, L. T. Lima Pereira, D. Ragni, F. Avallone, M. Herr, A. Suryadi, A. Fischer, O. Lyllof Ackermann, A. Smærup Olsen, C. Bak, *Aeroacoustic characterization of a NACA 63₃–018 airfoil with trailing-edge serrations: benchmarking study across facilities over a wide Reynolds number range*, Hybrid Anechoic Wind Tunnel (HAWT) workshop in 27th AIAA/CEAS Aeroacoustics Conference, Online, 2021.

6. **S. Luesutthiviboon**, D. Ragni, *Characterization of the acoustically treated Low-Turbulence Tunnel (LTT) of TU Delft*, Hybrid Anechoic Wind Tunnel (HAWT) workshop in 26th AIAA/CEAS Aeroacoustics Conference, Online, 2020.

5. **S. Luesutthiviboon**, D. Ragni, *Aeroacoustics characterization of a NACA 63₃–018 airfoil with trailing-edge serrations: A benchmarking aeroacoustics study*, Hybrid Anechoic Wind Tunnel (HAWT) workshop in 26th AIAA/CEAS Aeroacoustics Conference, Online, 2020.

4. A. Rubio–Carpio, **S. Luesutthiviboon**, R. Hedayati, F. Avallone, S. van der Zwaag, M. Hosseini, *3D-printed permeable trailing edges for broadband noise abatement permeable materials for noise reduction*, 23rd workshop of the aeroacoustics specialists committee of the CEAS, Rome, Italy, 2019.

3. D. Ragni, **S. Luesutthiviboon**, C. P. van DerCreek, *Turbulent boundary-layer trailing-edge noise measurements in closed test-sections with hybrid Kevlar and melamine installations*, Hybrid Anechoic Wind Tunnel (HAWT) workshop in 25th AIAA/CEAS Aeroacoustics Conference, Delft, the Netherlands, 2019.

2. **S. Luesutthiviboon**, D. Ragni, F. Avallone, M. Snellen, *Assessment of the thin-airfoil method for predicting steady pressure distribution on partially-porous airfoils*, 25th AIAA/CEAS Aeroacoustics Conference, Delft, the Netherlands, 2019.

1. **S. Luesutthiviboon**, A. M. N. Malgoezar, P. Sijtsma, M. Snellen, D. G. Simons, *Improving source discrimination performance by using an optimized acoustic array and adaptive high-resolution CLEAN-SC beamforming*, 7th Berlin Beamforming Conference (BeBeC), Berlin, Germany, 2018.